

Earth's structure from a Bayesian analysis of seismic signals and noise

Mallory Kay Young

A thesis submitted for the degree of
Doctor of Philosophy at
The Australian National University

March 2014

Earth's structure from a Bayesian
analysis of seismic signals and noise

Mallory Kay Young

© Mallory Kay Young

Typeset in Times by T_EX and L^AT_EX 2_ε.



March 2014

Acknowledgements

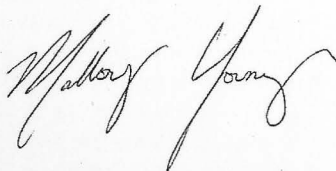
I thank my principal supervisor, Hrvoye Tkalčić, for his support, advice, patience and encouragement throughout the course of this thesis.

I thank special thanks to my co-supervisor Nick Rawlinson, whose generous support and advice throughout the thesis was invaluable to my progress.

I thank my friends and my family for their support, advice and encouragement throughout the thesis.

I wish to thank Nick Brown for much needed advice and technical assistance over the course of this thesis.

Except where otherwise indicated, the research described in this thesis is my own original work. The work comprising Chapter 2 was published in 2012 in *Geophysical Journal International*. The work comprising Chapter 3 was published in 2011 in *Geophysical Research Letters*. In 2013 I published the research presented in Chapter 4 in *Geophysics* and the research presented in Chapter 5 in *Geophysical Research Letters*. The research in Chapter 6 was published in 2013 in the *Journal of Geophysical Research*. In all cases I am first author, performed the data processing, and wrote the manuscripts. The appendix includes work published in *Nature Geoscience* in 2013. In this case I was second author. I received advice, support, and assistance from the following co-authors: Nicholas Rawlinson, Hrvoye Tkalčić, Thomas Bodin, Anya Reading, Malcolm Sambridge, Pierre Arroucau, Ross Cayley, Mark McLean, Silvie Ngo, and Michelle Salmon. Further details about publications are provided in the publication schedule at the end of Chapter 1. These co-authors have given formal consent for the papers to be presented in this thesis.



Mallory Kay Young
March 20, 2014

Acknowledgements

I thank my principal supervisor Hrvoje Tkalčić, for his unparalleled passion and dedication have been a constant source of motivation.

I owe equal thanks to my co-supervisor Nick Rawlinson, whose generous support and continual patience has been invaluable to my progress.

I am also grateful to my advisors Malcolm Sambridge and Brian Kennett for their support, advice, and immense knowledge.

I wish to thank Nick Direen for much needed advice and helpful discussions, especially concerning life beyond my PhD.

I thank Anya Reading for introducing me to Tasmania. I will forever remember with gratefulness her kind hospitality.

I thank Sherryl Kløver for rescuing me when I most needed it and for many an encouraging conversation.

I thank Ross Kerr, to whom I owe so much, for believing in me and my potential.

I thank my parents for setting me up to succeed and my sister Chelsea and Sasha for their unconditional love.

Abstract

The prevailing drive of modern seismology is to improve our knowledge of the Earth's structure, composition, and dynamics through an analysis of seismic waveforms. With increasing computing power, number and quality of seismic stations, and length of data records, the resolution and spatial coverage of current Earth models has improved substantially over the past few decades. Yet many limitations remain. The advent of ambient noise seismology has provided the solution to many issues, such as the irregular distribution of earthquakes, biases from structures outside the model region, earthquake location errors, and lack of near-surface resolution. Despite improvements to data quality and quantity and the introduction of unconventional datasets such as ambient seismic noise, a persisting shortcoming of many tomographic inversions is ad-hoc error estimation, parameterization, and regularization, which prevent a meaningful portrayal of model complexity and uncertainty. With the rapid increase in computing power, non-linear techniques based on densely sampling favorable regions of model space are now becoming tractable for real-world tomographic problems and directly address these shortcomings. One such recently introduced and promising method is transdimensional and hierarchical Bayesian inference. This alternate approach allows model parameterization and resolution to be driven by the data.

This thesis presents a collection of seismic inverse problems using real world datasets, some of which are tackled using fully non-linear Bayesian statistics. The benefits of a probabilistic approach are demonstrated for datasets targeting the uppermost crust down to the core through the development of novel methods of inversion and uncertainty quantification. To begin, an unconventional methodology for studying earthquake focal mechanisms in intraplate settings is presented through the inversion of ambient noise, receiver functions, and dispersion curves. The ambient seismic noise imaging approach of this study is subsequently applied to Tasmania - to which it is highly suited - and the resulting group and phase velocity maps help decipher Tasmania's enigmatic tectonic history. The same ambient noise dataset is further manipulated to yield a 3D shear velocity model of the region using a two-step transdimensional, hierarchical ensemble inference approach. Two prominent low-velocity anomalies offer insight into the Paleozoic evolution of the east Gondwana margin and support a connection between Tasmania and mainland Australia since the Cambrian. This approach is also applied to a larger dataset encompassing much of mainland southeast Australia.

The Bayesian approach is also applied to a global dataset of differential body wave travel times in an effort to reveal P-wave velocity heterogeneity in the lowermost mantle. Another deep Earth application is demonstrated through an inversion for the time-

dependent differential rotation of the inner core with respect to the mantle using careful measurements of earthquake doublets. The transdimensional nature of the inversion problem means that the data drive the number of free parameters constraining the differential rotation pattern, which exhibits much more complexity than the simple linear trend long-promoted by previous studies. The contents of this thesis help augment the diverse and wide-reaching applications for Bayesian statistics, which will continue to improve with future increases in computational power.

Contents

Acknowledgements	v
Abstract	vii
1 Introduction	1
1.1 The non-linear inverse problem	2
1.2 Bayesian inference	3
1.3 Ambient seismic noise tomography	7
1.3.1 Global travel time tomography	10
1.4 Contents of the thesis	11
1.4.1 Seismic source parameter inversion using a composite model of the upper lithosphere	11
1.4.2 Ambient noise tomography of Tasmania	12
1.4.3 3D shear velocity model from ambient seismic noise	13
1.4.4 Imaging the crustal structure of SE Australia	13
1.4.5 A probabilistic approach to imaging the lowermost mantle	14
1.4.6 The differential rotation of the Earth's inner core	17
1.5 Publication schedule	17
2 Full waveform moment tensor inversion in a low seismicity region using multiple teleseismic datasets and ambient noise	21
2.1 Foreword	21
2.2 Abstract	21
2.3 Introduction	22
2.3.1 Motivation	22
2.3.2 A two-step approach	24
2.4 Tectonic setting	25
2.5 Data and methods	26
2.5.1 Receiver function analysis	27
2.5.2 Surface wave dispersion curves	30
2.5.3 Joint inversion of teleseismic and ambient noise data	33
2.6 Moment tensor inversion of the Shark Bay event	35
2.6.1 Method	38
2.6.2 Results	38
2.7 Discussion	42

2.8	Conclusions	44
3	High-frequency ambient noise tomography of southeast Australia: New constraints on Tasmania's tectonic past	47
3.1	Foreword	47
3.2	Abstract	47
3.3	Introduction	48
3.4	Data and method	50
3.5	Results	52
3.6	Discussion	53
3.7	Conclusions	56
4	Transdimensional inversion of ambient seismic noise for 3D shear velocity structure of the Tasmanian crust	59
4.1	Foreword	59
4.2	Abstract	59
4.3	Introduction	60
4.4	Phase velocity maps	63
4.4.1	Data	63
4.4.2	Inversion method	64
4.4.3	Results	68
4.5	Inversion of dispersion curves	72
4.5.1	Data	72
4.5.2	Inversion method	72
4.5.3	Results	74
4.5.4	3D crustal model of Tasmania	78
4.6	Conclusions	82
5	Crustal structure of the east Gondwana margin in southeast Australia revealed by transdimensional ambient seismic noise tomography	85
5.1	Foreword	85
5.2	Abstract	85
5.3	Introduction	86
5.4	Data and method	88
5.5	Results and discussion	89
5.6	Conclusions	93
6	Global P-wave tomography of Earth's lowermost mantle from partition modeling	95
6.1	Foreword	95
6.2	Abstract	96
6.3	Introduction	96

6.3.1	Advances in data quality	97
6.3.2	Advances in inverse methods	98
6.4	Data	100
6.4.1	PKPab-df dataset	101
6.4.2	PKPbc-df dataset	104
6.4.3	PcP-P dataset	105
6.5	Inversion method	105
6.5.1	Transdimensional Bayes	106
6.5.2	Hierarchical Bayes	107
6.5.3	Model parameterization	109
6.5.4	Misfit evaluation	111
6.5.5	Sampling of the model space	112
6.5.6	Measurement corrections	114
6.6	Results	115
6.6.1	Resolution tests	115
6.6.2	Models using different data subsets	118
6.6.3	Final P-wave velocity model	123
6.7	Discussion	123
6.8	Conclusions	127
6.9	Acknowledgments	129
A	The shuffling rotation of the Earth's inner core revealed by earthquake doublets	131
A.1	Foreward	131
A.2	Abstract	131
A.3	Introduction	132
A.4	Earthquake doublets	136
A.5	PKPdf differential travel times measurements	137
A.6	Regression problem	148
A.6.1	Linear fitting	148
A.6.2	Model parameterization	148
A.7	Variable rates of inner-core rotation	150
A.8	Reconciling rotation from body waves and normal modes	152
A.9	Geodynamical implications	154
B	Chapter 2 supplementary information	157
C	Chapter 3 supplementary information	163
D	Chapter 4 supplementary information	167

E Chapter 5 supplementary information	171
E.1 Data analysis and inversion scheme	171
E.2 Final 3D shear wave velocity model	174
F Chapter 6 supplementary information	179
Bibliography	181

Introduction

Seismology is the tool of choice for studying the Earth's interior, as only a small fraction of the planet can be explored directly. Motivation for studying the 3D structure of the planet includes understanding its geodynamical processes, tectonic history, natural resource distribution, and seismic hazard. Models of crustal structure are in many cases at the refinement stage, as a large variety of seismic methods have developed to map the distribution of various geophysical properties at these shallower depths. Much of the deeper Earth structure remains an enigma, however, as techniques for imaging at great depth are more limited and dependent on an unrealistically dense and even spatial distribution of earthquakes and seismic stations. The advent of digital seismology enabled a preliminary sweep through the Earth's interior (e.g. Dziewonski et al. (1977)), and the gradual expansion of the global deployment of highly sensitive seismometers has since significantly improved upon those early pictures. Maps of Earth structure are not only improving in resolution and spatial extent, but also in reliability, as inversion methods are being continually upgraded and seismological theory steadily updated. Nonetheless, many challenges still remain, and there is great room for improvement in the portrayal of global Earth structure. One likely unavoidable difficulty is the irregular distribution of earthquakes and seismic stations. Recent work in ambient seismic noise tomography and the joint inversion of multiple datasets offers mitigations to this obstacle. This thesis will provide several examples of these types of inversions. Chapter 2 demonstrates the development of a composite crustal model in a region of very little seismicity and limited station coverage through the joint inversion of several different seismic datasets. In chapters 3, 4, and 5 we show how high resolution 3D images of the crust can be derived from ambient seismic noise, thus avoiding the need for earthquakes. Here we apply a novel inverse technique based on Markov chain Monte Carlo sampling within a Bayesian framework which allows the measurements to drive the handling of data noise and model parameterization. We also apply this probabilistic approach at a global scale, thereby tackling the problem of uneven raypath sampling and producing a model of P-wave velocity heterogeneity in the lowermost mantle (Chapter 6). Finally, we provide some insight into the dynamics of the deepest part of the planet, the inner core, through the use of Bayesian analysis (Appendix A).

1.1 The non-linear inverse problem

Solving an inverse problem is equivalent to reversing, or “inverting”, the forward problem of calculating data predictions based on known model parameters. These calculations are based on a very particular relationship G between the data \mathbf{d} and the model \mathbf{m} such that $\mathbf{d} = G(\mathbf{m})$. In the case of geophysical inversion, the forward operator G is generally known, or at least approximated, the model \mathbf{m} represents a particular set of physical properties of the Earth, and the data \mathbf{d} are a set of measurements. Since most geophysical inverse problems are underdetermined, these measurements are rarely adequate to uniquely constrain the solution. Moreover, for seismic travel-time tomography, the problem is non-linear since the traveltime t of the wavefront along path L depends on the seismic velocity structure $v(x)$ through which it travels:

$$t = \int_{L(v)} \frac{1}{v(x)} dl. \quad (1.1)$$

Given the challenge presented by this non-linearity, seismic tomography problems were originally linearized about a reference model, thereby avoiding the issue of ray path updates. This can be a reasonably accurate tactic if the reference model is known to be very similar to the actual model and the ray paths are not significantly effected by model perturbations. Linear tomography is computationally feasible for even the largest of datasets given that the inverse problem must only be solved once. For example, Inoue et al. (1990), van der Hilst et al. (1997), Bijwaard et al. (1998), Zhao (2004), Li et al. (2008), and Ritsema et al. (2011) have performed linear inversion of millions of travel time measurements to produce global-scale velocity models.

However, in cases of extreme velocity perturbations, especially in near-surface, high-frequency applications, accounting for bending rays is critical. In such a situation, the additional computational cost of an iterative, non-linear approach becomes justified. Although, the dependence on velocity structure of the ray path is still ignored at the time of inversion, the problem is treated non-linearly by iteratively re-tracing the ray paths according to the velocity corrections of the current model. Smoothing and damping regularization is applied to account for the under-determined nature of the inverse problem. Such an approach is demonstrated in Chapters 2 and 3 of this thesis where we use the iterative non-linear inversion approach of Rawlinson and Sambridge (2004a,b) to perform a tomographic inversion in Western Australia and Tasmania. This fast-marching surface wave inversion scheme uses an eikonal solver to predict traveltimes and a subspace scheme to solve the inverse problem.

Whether linear or iteratively non-linear, an inverse approach that seeks to minimize some cost function makes the questionable assumption that a better fit to the data yields a better model. In the case of noisy data, however, the model of minimum data variance is likely unjustified and meaninglessly complex. Regularization such as smoothing (discourages model roughness) and damping (discourages model

amplitude) can moderate complexity, but the applied strength of these procedures is arbitrary. Moreover, the uniform spatial application of regularization is unrealistic given the uneven distribution of data information and uncertainty.

Another important consideration when assessing results is the dependence of the final model on the initial model. In order to solve the inverse problem by minimizing the objective function, its gradient is calculated and used to locate a local minimum of the objective function. Unfortunately, there is no guarantee that this local minimum is also the global minimum. Furthermore, model space is not well explored and the final model will depend heavily on the initial model. In regions for which there is little a priori velocity structure information, such as the heterogeneous upper crust or the lowermost mantle, a linearized optimization approach is unlikely to produce a reliable portrayal of Earth structure.

Also of great influence on the final model is the model parameterization. Even if complete exploration of the model space was assured, the final model will exhibit features inherited by the choice of parameterization rather than required by the data, whether it be blocks (e.g. Tkalčić et al. (2002), Vasco et al. (2006), Houser et al. (2008), Soldati et al. (2012)), spherical harmonic expansions (e.g. Su et al. (1994), Antolik et al. (2003), Tanaka (2010), Ritsema et al. (2011)), or grids (e.g. Rawlinson and Sambridge (2004b,a)). Discontinuities or smoothness inherent to the base parameterization will leave their imprint on the final model.

Given the many sources of error beyond data noise, a reliable measure of model uncertainty seems fitting, if not required. Unfortunately, linear or iterative non-linear techniques do not generate uncertainty estimates automatically and most attempts to do so are ad-hoc. Fortunately, as computing power increases, fully non-linear inversion approaches are being introduced that may solve the drawbacks of linear and iterative non-linear inversion schemes while providing much-needed uncertainty estimates.

1.2 Bayesian inference

This thesis presents a series of inversion techniques which for the most part bypasses the setbacks of linear and iterative non-linear schemes regarding data noise considerations, dependence on initial models, arbitrary parameterization, and uncertainty estimation. The approach applies Bayesian statistics to a Monte Carlo Markov chain search of parameter space. This is a probabilistic approach in which the current model is assigned a probability based on the data and on prior information about the known range of acceptable models. Based on Bayes' Theorem (Bayes, 1763), a mathematical statement of Bayesian theory can be summarized as follows:

$$p(\mathbf{m} \mid \mathbf{d}_{obs}) \propto p(\mathbf{d}_{obs} \mid \mathbf{m})p(\mathbf{m}), \quad (1.2)$$

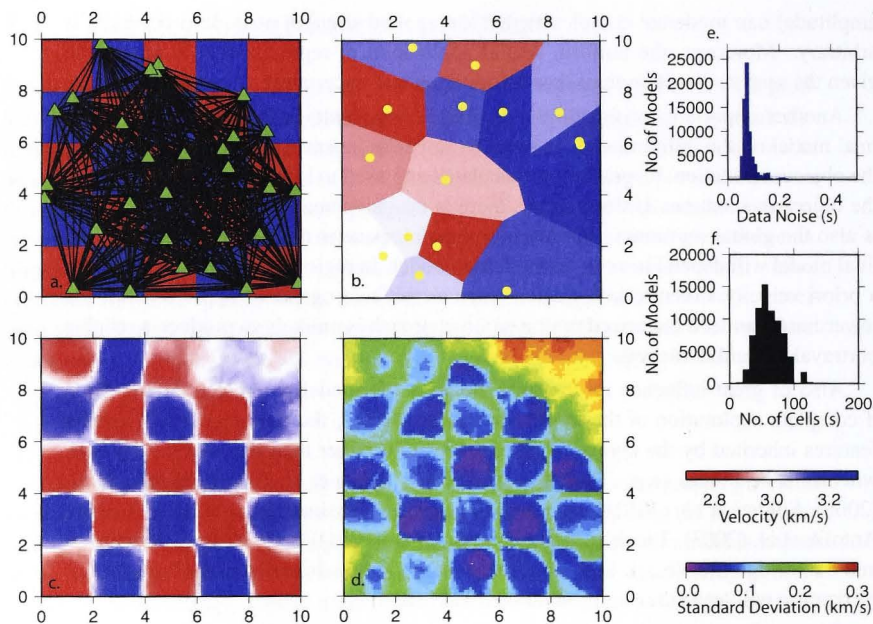


Figure 1.1: Synthetic tomographic inverse problem. Noise with a standard deviation of 0.1 s has been added to the synthetic travel times. (a.) Actual velocity model. Alternating squares are of ± 0.2 km/s. Receivers are shown by green triangles. Raypaths are shown by black lines. (b.) Example Voronoi cell model. Cell centers are marked by yellow circles. (c.) Final point by point spatial average of the velocity model ensemble. (d.) Final point by point standard deviation of the velocity model ensemble. (e.) Posterior distribution of data noise (f.) Posterior distribution of the number of cells.

where $p(\mathbf{m} \mid \mathbf{d}_{obs})$ is the probability distribution function of the unknown model parameter \mathbf{m} given the data \mathbf{d} . The term $p(\mathbf{d}_{obs} \mid \mathbf{m})$ is the likelihood function, which yields the probability of observing data \mathbf{d} given model \mathbf{m} . Any prior information about model \mathbf{m} is represented by the a priori probability distribution $p(\mathbf{m})$.

After a large number of models are sampled via a Markov process, the resulting posterior probability density function becomes the solution to the inverse problem (Figure 1.1). This is very different to a linear or iterative non-linear optimization approach in that instead of yielding a single value for each unknown model parameter, a complete distribution of values is produced. This allows more complete analysis and understanding of the solution. While typically either the mean, median, maximum, or standard deviation of the parameter distributions are extracted for interpretation, such calculations merely offer a very concise summary of the final model.

The Bayesian inversion methods employed in this work are both transdimensional and hierarchical. The term “transdimensional” refers to the fact that the number of unknowns is treated as a free parameter in the inversion. This means that as the Markov chain progresses through parameter space, the number of unknowns (and therefore the parameterization) is allowed to change. In fact, Monte Carlo sampling is the only way to solve this inverse problem, as the transdimensionality makes the forward operator G (see equation A.1) highly non-linear. The evolution of the model parameterization will be driven by the content and quality of the data (Bodin et al., 2012a) and relatively loose prior assumptions represented by posterior probability distributions on each parameter. Additional unknowns, or model parameters, resulting in increased complexity of the final model, will only be added if justified by the data noise level, as the “natural parsimony” of Bayesian inference discourages high dimensional models. Given the option of two models that provide comparable fits to the data, the simpler of the two will be naturally preferred (Malinverno, 2002). The key to allowing a transdimensional approach to the inversion is the method of parameterization. For a tomographic inversion, an efficient and flexible way to describe a velocity field is as a mosaic of Voronoi cells (Voronoi, 1908; Okabe et al., 1992) based on the nucleus of each cell (Figure 1.1b). Each cell comprises all points that are closer to its nucleus than any other. Therefore, cell boundaries form perpendicular bisectors between nuclei, and polygons of a variable surface area and number of sides are allowed.

As stated previously, the number of free parameters, or Voronoi cells, is driven by the data. Very noisy data will not merit as many cells as high quality data. This means that the assessment of the data noise content is crucial to explaining the data with a model that is sufficiently complex, but not too complex. The most judicious method of properly assessing the noise is to make the inversion hierarchical and leave the noise as an unknown hyper-parameter. In a hierarchical inversion, there are two levels of inference. The first describes the physical properties of the Earth, for example the velocity and location defining each Voronoi cell. Above that are the hyper-parameters, such as data noise. These values regulate the values in the lower level. The posterior probability distributions of the physical parameters are conditional upon those of the hyper-parameters (Bodin et al., 2012a).

Although Bayes theorem dates back to the eighteenth century, it is only relatively recently that it has been applied to tomography problems. The transdimensional and hierarchical ensemble inference approach of this thesis is the product of gradual progress in seismic inversion. Devised in the 1940s, the Markov chain Monte Carlo sampling method has been more recently adopted by the geosciences to directly generate posterior probability distributions as a means of solving inverse problems (see Mosegaard and Tarantola (1995), Sambridge and Mosegaard (2002), Gallagher et al. (2009) for reviews). A Monte Carlo Markov chain involves a random walk through parameter space that samples a variety of unique models. At each stop along the way, the ability of the current model to fit the data is calculated. The level of data fit gov-

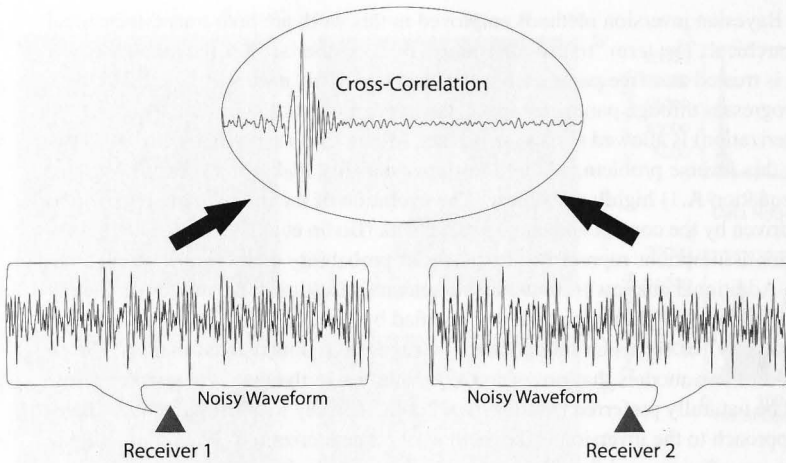


Figure 1.2: Cartoon illustrating the retrieval of signal from the cross-correlation of ambient seismic noise.

erns whether the current model is accepted or rejected. As the number of sample steps increases, the sampling pattern will converge toward the posterior probability distribution of the solution model (Tierney, 1994).

Very often in geophysical inverse problems, the required number of model parameters is not known. For this reason transdimensional Markov chains (Sisson, 2005; Sambridge et al., 2006) have become a preferred route to solving tomography problems. Here we use the reversible jump algorithm of Green (1995, 2003) to handle changes of dimension. There have been many previous applications of the reversible jump algorithm to geoscience problems, for examples see Malinverno and Leaney (2000), Gallagher et al. (2009), Bodin and Sambridge (2009), Piana Agostinetti and Malinverno (2010), Bodin et al. (2012b), Sambridge et al. (2013). First applied to geophysical datasets by Sambridge et al. (1995), Voronoi cells have consistently been the parameterization of choice for transdimensional Bayesian inference approaches used to recover multi-dimensional models.

In addition to uncertain model parameterization, data noise is also often a unknown in an inversion. Given that data noise is critical to determining model resolution, an enhanced form of Bayesian inference known as Hierarchical Bayes (Gelman et al., 1995) has been developed. Malinverno and Briggs (2004) were the first to exploit this modified version for a geophysical application. They treated the variance in the observed data as an unknown in the inversion, so it too was assigned prior bounds and was interpreted in terms of a posterior probability distribution. This thesis expands

the current range of applications for both hierarchical and transdimensional Bayesian ensemble inference and argues for its advantages over linear and iterative non-linear inversion techniques.

1.3 Ambient seismic noise tomography

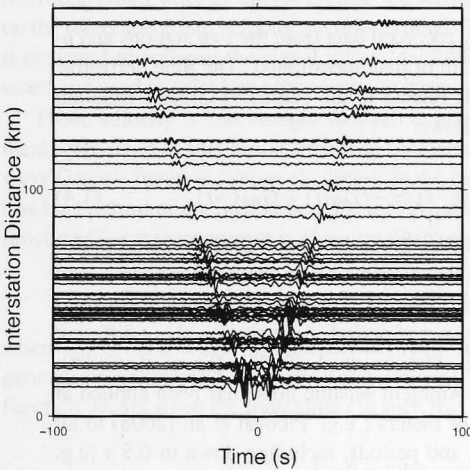


Figure 1.3: Example of cross-correlation functions associated with a particular station and every other station in an array. Waveforms are sorted according to the epicentral distance between the two stations.

Ambient seismic noise tomography is a rapidly expanding topic in geophysical inverse problems. This relatively new method is based on the fact that the cross-correlation of ambient noise recorded at two different simultaneously recording seismic stations estimates the surface wave Green's function corresponding to Earth's structure between the two stations (Figures 1.2, 1.3) (Lobkis and Weaver, 2001; Snieder, 2004; Shapiro and Campillo, 2004). Usually, fundamental modes of surface waves are extracted from the ambient noise because they dominate the Green's function between two receivers located at the surface (Campillo, 2006). This is in accordance with the fact that the majority of

ambient seismic noise is generated by sources located at the surface, such as oceanic microseisms and atmospheric disturbances (Friedrich et al., 1998; Tanimoto, 1999; Rhie and Romanowicz, 2004). The frequency spectrum of the noise defines the frequency bandwidth over which an impulse response can be retrieved (Roux et al., 2005b). When receivers are far apart, the coherent noise must have sufficient amplitude to propagate to both receivers despite geometrical spreading and attenuation. Therefore, slowly-attenuating surface waves tend to dominate the impulse response obtained from the correlation of seismic noise. However, there have been a few more recent studies that recover the body wave part of the Green's function (e.g. Roux et al. (2005a), Ryberg (2011), Poli et al. (2012)). Theoretical studies by Wapenaar (2004, 2006) indicate that the retrieval of body wave Green's functions at the surface requires a distribution of noise sources in depth. Although this could come from local an-

thropogenic sources, most likely this high frequency noise is a result of surface wave energy being converted into body waves due to heterogeneities and scatterers at depth (Roux et al., 2005b).

The ambient noise cross correlation function $C_{AB}(t)$ associated with two simultaneously recording stations A and B is given by

$$C_{AB}(t) \approx \int_0^{t_c} v_A(\tau)v_B(t+\tau)d\tau, \quad (1.3)$$

where $v_A(t)$ and $v_B(t)$ are the continuously recorded data from the two stations and t_c is the total cross-correlation time (i.e. length of data recordings). The time derivative of this cross correlation function $C_{AB}(t)$ is related to the empirical Green's function $\check{G}(t)$ and real Green's function $G(t)$ as follows:

$$\frac{dC_{AB}(t)}{dt} = -\check{G}_{AB}(t) + \check{G}_{BA}(-t) \approx -G_{AB}(t) + G_{BA}(-t). \quad (1.4)$$

The empirical Green's function differs slightly from the actual Green's function due to unknown effects of anelasticity, irregular distribution of the ambient noise, and spectral properties of the noise (Roux et al., 2005b). The Green's function is dispersive, which means that by filtering over a range of periods, information about different depths of the Earth can be retrieved (e.g. Shapiro et al. (2005); Lin et al. (2008); Bensen et al. (2008); Yang et al. (2010)). Ambient seismic noise has been applied at a wide range of spatial scales, such tens of meters (e.g. Picozzi et al. (2008)) to all of Australia (Saygin and Kennett, 2012), and periods, including down to 0.5 s (e.g. Huang et al. (2010)) and up to 80 s (e.g. Stehly et al. (2009)).

The advent of ambient noise tomography marks an opportunity to image regions previously left poorly explored due to the limitations of earthquake-based tomography. An uneven distribution of earthquakes around the world means that seismic surface waves only sample certain preferential azimuths and regions. Moreover, in aseismic regions (for example, western Australia - see Chapter 2) surface wave dispersion information can only be measured using distant earthquakes. These teleseismic velocity measurements are usually restricted to periods of ~ 20 s or greater due to attenuation and scattering along ray paths. This is a severe limitation, as short-period waves are critical to constraining fine-scale structure. Another difficulty with earthquake tomography is that source information is required, such as earthquake hypocentral locations and sometimes moment tensors, which are often very difficult to obtain, particularly for small events. Ambient noise tomography bypasses all of these drawbacks and allows unprecedented imaging of the Earth's crust.

Most previous ambient noise tomography studies focus on group velocity measurements (e.g. Villaseñor et al. (2007), Yang et al. (2007), Lin et al. (2007), Arroucau et al. (2010), Stankiewicz et al. (2010)) because of the relative ease of measuring group velocities compared to phase velocities. The majority of these group velocity studies,

including the ones presented in Chapters 2 and 3 of this thesis, are based on a two-step frequency time analysis (FTAN) procedure (e.g. Dziewonski et al. (1969), Levshin et al. (1972), Levshin and Ritzwoller (2001), Bensen et al. (2007)). The first step produces a 2-D image of signal power as a function of time and the central frequency of the bandpass filter. The automatic procedure tracks the local power maximum along the frequency axis for the desired range of central frequencies. The group arrival times of the maximum amplitude as a function of central frequency are used to calculate a reference group velocity curve. During the second step, a phase-matched filter based on the reference group velocity curve is applied. This phase-matched filtering process is designed to collapse the signal into a ‘delta-like’ arrival. The arrival time is measured and used to calculate group velocity based on the known interstation distance.

Phase velocity is less straight forward to estimate. The phase velocity measurements presented in this thesis are based on the far-field representation of the surface wave Green’s function (Yao et al., 2006). In the far field (i.e. when the wavelength λ is less than a third of the interstation distance Δ), the time harmonic wave of the Green’s function G_{AB} at frequency ω is given by (Dahlen and Tromp, 1998)

$$\text{Re}\{G_{AB}(\omega)\exp(-i\omega t)\} \approx (8\pi kS)^{-1/2} \cos(k_{AB}\Delta - \omega t + \frac{\pi}{4}), \quad (1.5)$$

where k_{AB} is the average wavenumber between ‘source’ A and receiver B, and S is the geometrical spreading for surface waves. A peak in the harmonic wave of the Green’s function occurs when the traveltime t is such that

$$k_{AB}\Delta - \omega t + \frac{\pi}{4} = 0. \quad (1.6)$$

In this case, the average phase velocity at frequency ω is given by

$$c_{AB}(T) = \frac{\Delta}{t - T/8}, \quad (1.7)$$

with T denoting the corresponding central period. We first produce a time-period image where each column of the image represents an amplitude normalized empirical Green’s function filtered around central period T . Using the simple relationship in equation 1.7, we transform the image to a velocity-period diagram from which a continuous phase velocity curve can be automatically extracted. Unlike when measuring group velocities, special care must be taken to properly assess the 2π phase ambiguity and select the curve corresponding to the fundamental mode.

Once group and/or phase velocities are calculated, the next step in a comprehensive ambient noise tomography study is to produce a 3D shear velocity model (e.g. Yang et al. (2008a,b), Yao et al. (2008), Stehly et al. (2009), Bensen et al. (2009), Behr et al. (2011)). First, group and/or phase velocity maps are produced from the dispersion curves extracted from the cross correlation of ambient seismic noise as outlined above. Traditionally this is a linear or iterative non-linear procedure that seeks to minimize

some cost function and involves a subjective application of smoothing and damping. For this reason, the application of a fully non-linear, Bayesian technique as in Chapter 4 of this thesis is an important step to conserving data information and avoiding arbitrary smoothing and damping regularization. Second, the 2D maps are sampled over a range of periods at regular intervals in latitude and longitude to produce a new collection of dispersion curves. The spatial variation of uncertainty in the 2D maps is traditionally impossible to determine. However, an ensemble inference approach provides an inherent estimate of model uncertainty through the assessment of the standard deviation of the collection of 2D models at each grid point. Each curve is inverted for a 1D shear velocity model, which traditionally requires arbitrary decisions about model parameterization. As discussed earlier, the transdimensional and Voronoi cell based Bayesian inversion scheme presented here instead lets the data drive the model parameterization. Finally, the 1D models are combined to produce a pseudo-3D shear velocity model of the region. When time and computational resources permit, implementing a hierarchical and transdimensional Bayesian inversion approach will greatly improve the reliability of results. The research in this thesis confirms this statement for a variety of datasets.

1.3.1 Global travel time tomography

One of the ways of imaging the Earth's deepest structure is through the use of P- and S-wave arrival times of mantle and core sensitive seismic phases. These observed arrival times of seismic waves are compared to theoretical times predicted by a reference Earth model to reveal variations within the Earth with respect to the reference model. The travel time residual δt is denoted by:

$$\delta t = t_{obs} - t_{pred}, \quad (1.8)$$

where t_{obs} is the observed and measured travel time and t_{pred} is the predicted travel time according to an Earth reference model. There will be a certain amount of error associated with each measurement, related either to reading error, station elevation, instrument response, and/or origin time and location approximations. Corrections can be made for the Earth's ellipticity (e.g. Kennett and Gudmundsson (1996)). The deviations in arrival times from the reference Earth model are often dominated by effects of near surface crustal heterogeneity and earthquake mislocation. For this reason, using differential travel times can provide a more accurate reading of velocity perturbations at depth. In this case, the travel time residuals of two different seismic phases, recorded on the same instrument and originating from the same source are compared. The differential travel time residual is given as:

$$\delta t^{A-B} = (t_{obs}^A - t_{pred}^A) - (t_{obs}^B - t_{pred}^B), \quad (1.9)$$

where A denotes one phase and B denotes another different seismic phase. This will remove the effects of source mislocation and station elevation. If the ray paths of the two phases are sufficiently close within the crust, the effect of strong heterogeneity near the surface will also be largely avoided.

The aim of the last chapter of this thesis is to establish an improved model of compressional velocity structure within the lowermost mantle by using a probabilistic inversion approach and a high quality differential travel time data set. This research is performed with confidence that improved tomography models of deep Earth structure will provide further insight into geodynamical processes and allow for better travel time prediction and therefore more accurate event locations.

1.4 Contents of the thesis

This thesis is structured into six principal sections of research and provides a progression of tomography problems where the inverse approach in each subsequent chapter is in general an improvement upon the one before. As the inversion approaches become more sophisticated (and time-consuming!) we also incorporate increasingly larger datasets - on a local, then regional, and finally a global scale. In most cases, the dataset and inversion methodology used is different for each section. For this reason, an introduction to the problem, tectonic region, data, and methods pertinent to the section is given in each chapter rather than presenting them iteratively here. The content of each chapter has been previously published as a peer-reviewed paper in an internationally recognized journal as outlined at the end of this chapter. Additional figures not included in the papers, but that provide additional insight into the research projects, are provided in Appendices B-F at the end of this thesis.

1.4.1 Seismic source parameter inversion using a composite model of the upper lithosphere

The first research project of this thesis targets western Australia (WA) (Chapter 2), for which we produce a composite shear wave velocity model of the upper lithosphere. There have been relatively few studies of the region, given the limited number of stations and earthquakes in the area, so our work marks a significant improvement to existing velocity models of WA crustal structure. Our results agree well with previous work on the region and greatly improve upon existing constraints on Moho depth. Our composite model suggests a sharp and intermediate-depth Moho beneath the Pilbara and Yilgarn cratons and a broader, deeper transition beneath the Capricorn Orogen. This is the first time that a shear wave velocity model has been provided for coastal stations, providing valuable information about the structure of the Pinjarra Orogen. Importantly, this model enables a full-waveform inversion for the seismic moment

tensor of the 2007 Shark Bay, WA, earthquake. The solution is obliquely normal and is interestingly orthogonal to the generally accepted pressure axis of the Shark Bay region. This inconsistency indicates that the focal mechanism was a product of differently orientated pre-existing faults and rock defects in the area.

With data from only 21 seismic stations we develop a new methodology for imaging aseismic regions with limited station coverage. The comparatively narrow window for observation forced us to be resourceful; we produced a composite model of the WA crust using a joint inversion of ambient noise, two-station method dispersion measurements, and receiver functions. We also used forward modeling of the waveforms to confirm the reliability of our solution model. The methodology is especially pertinent to studies of earthquake focal mechanisms in intraplate regions where dense seismic arrays have not been deployed. It is in these areas that in the unlikely event of an earthquake, a detailed analysis of its focal mechanism can greatly improve the understanding of the tectonics of the region. We also importantly demonstrate that first motion analyses do not always accurately represent the rupture properties of the source as obtained through a full waveform inversion. A key outcome of this study, however, is that in order to retrieve a reliable focal mechanism solution from such an inversion, an accurate velocity model is required.

1.4.2 Ambient noise tomography of Tasmania

We further exploit the unique potential of ambient noise tomography to image the Earth's crust in the absence of earthquakes by applying the method to southeast Australia. In particular, the island of Tasmania makes an ideal target region, as the surrounding ocean provides a consistent, strong source of ambient noise, and the station coverage is superb. We improved upon the method by producing phase velocity maps, which present more challenges than group velocity maps. We used a frequency-time analysis procedure on approximately nine months of vertical component, short period data, and the resulting group and phase velocity images for periods between 1 and 12 s are of unprecedented resolution. This marks an important step forward in ambient noise tomography, as typically, ambient noise studies have a lower period limit of around 5 s. Phase velocity dispersion curves were calculated using the far-field approximation and image transformation technique discussed earlier. The maps (obtained from an iterative, non-linear tomographic inversion scheme) reinforce results from previous wide-angle tomography and surface heat flow studies and clearly discriminate between regions of hard rock and sediment. One of the prominent features of the maps is a pronounced low velocity lineation that coincides with the Tamar conductivity anomaly, a region of elevated conductivity and heat flow, which may reflect the presence of a lithospheric boundary. We suggest that this zone is a marker of a broad and heavily deformed transition zone resulting from the accretion of oceanic material against a more rigid continental lithosphere.

1.4.3 3D shear velocity model from ambient seismic noise

This next section presents an improved approach to analyzing the Tasmanian seismic ambient noise data set. A shortcoming of the tomographic inversions of the previous chapter is that they require ad-hoc error estimation and arbitrary parameterization, smoothing, and damping, thereby making model complexity and uncertainty difficult to meaningfully quantify. The transdimensional and hierarchical Bayesian analysis within this chapter, on the other hand, allows the model parameterization and resolution to be driven by the data. This work presents a novel method of uncertainty analysis for geophysical inverse problems. The noise level of the data is inferred from the data itself, for a principal advantage of the hierarchical approach is that noise is treated as an unknown in the problem. We preserve uncertainty information from each step and use it to further constrain the next step in the inversion. In this sense, we let the input data, along with its quantity and quality, decide the parameterization and appropriate complexity of the final model.

Taking the analysis of the Tasmanian ambient noise dataset a step further, we then present a pseudo-3D shear wave velocity model of the region. We invert phase velocity maps for shear velocity and importantly, also provide a complementary map of model uncertainty. Our model images down to 15 km depth and exposes two fundamental low velocity zones. The first runs along the Tamar River, as in the dispersion maps of our previous study (Chapter 3). Upon taking vertical cross sections through the 3D model it becomes evident that this anomaly is east-dipping. To the west, beneath the Dundas Trough, lies a second eastward-dipping low velocity zone. The geometry of these features suggests ties with the deformation and shortening event of the Tyennan Orogeny and implies a connection between Tasmania and the mainland since the Cambrian. The resulting high resolution 3D shear velocity model has strong geophysical implications for the current debate concerning the tectonic history of the Tasmanian lithosphere.

1.4.4 Imaging the crustal structure of SE Australia

We then apply our 3D shear velocity modeling approach to mainland southeast Australia using data from the WOMBAT rolling seismic array (Chapter 5). The resulting shear velocity model spans SE Australia from the surface down to 30 km depth and is the first of its kind for the region. The 3D velocity variations help elucidate the geometry and position of key crustal features related to the transition from Paleozoic eastern Australia to Precambrian central and western Australia. Of particular note is the prominent high-velocity and crustal-scale feature along the Torrens Hinge Zone, which points to a vast zone of Paleozoic crustal extension.

Again, our hierarchical and transdimensional Bayesian inversion scheme is applied in two steps: (1) the inversion for phase velocity maps and (2) the inversion for 1D shear velocity models. In both cases, the number and distribution of model pa-

parameters are implicitly controlled by the data, and the standard deviation of the data noise is left as an unknown. Model complexity is intricately linked to the estimated noise in the measurements rather than arbitrary smoothing regularization and model parameterization, as is the case for many traditional inversion techniques. In this section, we furthermore show how multiple, asynchronously running arrays can be used in combination to produce a single cohesive model. Because of the unique ability of an ensemble inference approach to deal with an uneven spatial distribution of data, this aggregation does not result in artifacts such as unjustified structure between arrays. Our two-step Bayesian inverse approach is widely relevant, as it is applicable to any seismic array for which more traditional ambient noise tomography has been deemed viable.

1.4.5 A probabilistic approach to imaging the lowermost mantle

Moving to a global scale, we extend Bayesian tomography to the Earth's lowermost mantle (Chapter 6). For the first time, a transdimensional and hierarchical partition modelling approach is applied to the deep Earth at a global scale. We provide a unique picture of lowermost mantle P-wave velocity heterogeneity and reveal that the strength of the velocity perturbations is approximately three times larger than previous estimates. Our results reveal velocity heterogeneities on a variety of scales, thus providing an important link between the very short-scale imaging achieved through scattering experiments and the long wave-length maps resulting from more traditional tomographic approaches. Our model also provides further constraints on the size and location of key velocity anomalies, such as the southern Africa and southwest Pacific low velocity zones. The additional raypath coverage provided by the study also helps to image areas of more limited exploration, such as northern Africa, Australia, and the north Atlantic. The characteristic amplitude of heterogeneity revealed by this study will help to significantly refine allowable models of lowermost mantle heterogeneity.

Our application of Bayesian methods to the lowermost mantle marks a significant advance in global imaging, as it overcomes two major shortcomings of traditional, linearized global inversion styles. The first issue we resolve is error estimation. Usually ad-hoc techniques are employed to quantify error, necessitating arbitrary smoothing and damping regularization. We instead treat data uncertainty as an unknown parameter in the inversion and let the complexity and strength of the model perturbations depend upon the data quality and quantity. The second issue is arbitrary model parameterization, which typically for global-scale models involves either blocks or spherical harmonic expansions. Either way, full utilization of the irregular information content in the data is prevented. We overcome this limitation by partitioning the model into a mosaic of ever-changing Voronoi polygons. The size, location, and number of these polygons evolve during the inversion and after many iterations, an ensemble of uniquely parameterized models is used to produce a final, preferred, average model.

This method precludes smoothing or damping and produces a model capable of expressing both velocity gradients and sharp discontinuities.

There are many avenues for progressing our global-scale inversions for P-wave velocity structure in the lowermost mantle. Those which would yield the greatest improvement to data fit are likely improving how we parameterize the model, jointly accounting for core mantle boundary topography and P-wave velocity structure, and an inversion for whole mantle structure. We make several approximations when parameterizing the model. The first is that we represent the lowermost mantle with a single layer of uniform thickness. We predict data fit could be greatly improved by allowing for multiple layers. The results of preliminary experiments involving two equal thickness layers are promising. Although currently computationally cost-prohibitive, one would ideally leave the number and thickness of these layers as free parameters in the inversion. By enabling the existence of thin layers we might hope to image ultra low velocity zones, whose thickness is on the order of tens of kilometers (Wen and Helmberger, 1998; Garnero et al., 1998). Additionally it would be revealing to allow these thicknesses to vary spatially.

A relatively minor, but nonetheless important improvement would be the utilization of a spherical distribution of Voronoi cells. This would decrease computation time by approximately half, as duplicating and "wrapping" the data around longitudinally would no longer be required in order to ensure the model is continuous around the globe. Moreover, the model would exhibit realistic and self-consistent behaviour at the poles. Although 2D Voronoi cells can change size to adapt to changing raypath density, a spherical grid would provide a more straightforward way of ensuring an accurate level of complexity in less-sampled regions such as the poles. Currently these areas are artificially stretched to fit a 2D rectangular grid, and so overly complex structures may result.

Yet another amendment to the forward modeling procedure would be a continuous, or even occasional, update of raypath geometries. Again, this is currently computationally cost-prohibitive. Although this modification would not likely create a dramatic change to the final model, areas of strong velocity variations would be better imaged once bending rays can be accounted for.

A further improvement involves accounting for the possible effects of topography on the traveltime residuals, which will involve a joint inversion for topography and velocity. This inclusion will likely decrease the data variance and increase the reliability of our velocity model. Topography becomes especially important when considering PcP raypaths, so accounting for core mantle boundary depth changes may greatly reduce the discrepancy between the PcP and PKP datasets.

The joint inversion for topography and velocity structure is relatively computationally inexpensive if we approximate that the change in travel time δt due to raising or lowering a discontinuity in velocity v by an amount δr is (Dziewonski and Gilbert, 1976)

$$\delta t = -(\delta r/r)[(\eta_+^2 - p^2)^{1/2} - (\eta_-^2 - p^2)^{1/2}] \quad (1.10)$$

for a transmitted ray (for example PKPab, PKPbc, or PKPdf) and

$$\delta t = \mp 2 \frac{\delta r}{r_{core}} (\eta_{\pm}^2 - p^2)^{1/2}, \quad (1.11)$$

for a reflected ray, where $\eta_{\pm} = r_{core}/v_{\pm}$, p is the slowness value, r_{core} is the radius of the core, and subscripts + and - denote values above and below the core mantle boundary respectively. Since there is only one value (δt) to calculate per raypath and only one coordinate pair with which to associate it (point of reflection off or transmission through the core mantle boundary), inverting for topography is computationally much cheaper than inverting for velocity structure, which requires the maintenance of knowledge about the entire raypath.

Based on previous work, we expect topography amplitudes of up to ± 6 km (e.g. Morelli and Dziewonski (1987); Rodgers and Wahr (1993); Obayashi and Fukao (1997); Earle and Shearer (1997); Boschi and Dziewonski (2000), although more recent work has suggested a more limited range of ± 2.5 km (Sze and van der Hilst, 2003; Koper et al., 2003; Tanaka, 2010; Koelemeijer et al., 2012). Therefore, we have performed preliminary joint inversions for topography and velocity with a prior bound of ± 10 km in topography amplitude. When inverting for topography only, the noise in the PcP-P dataset actually becomes the lowest compared to that of the PKPab-df and PKPbc-df datasets. This makes sense, for the PcP raypaths are most sensitive to topography. Another raypath that is highly sensitive to topography (due to reflection off the core mantle boundary) is P4KP. Therefore, when inverting for topography it would be prudent to include the high quality P4KP-PcP differential traveltime dataset of Tanaka (2010).

In Chapter 6 we correct for mantle structure using the model of Della Mora et al. (2011). Although we find this model adequate for our purposes, the lack of resolution in the lower mantle layers and the use of less reliable ISC data call to question its reliability. Of arguably greater concern is their use of smoothing and damping regularization. This arbitrary manipulation of results has the potential to underestimate perturbation amplitudes and smooth discontinuities. A superior approach would be to simultaneously invert for whole mantle structure using N layers, where N is left as a free parameter. This would require a great increase in computational power as well as an expansion of the dataset. A possibility would be to include absolute travel times of P, PP, and PcP phases; however, this could lead to traveltime contamination by crustal structure. Nonetheless, given the rate of advances in technology, it should not be far-fetched to assume that a new Earth reference model will some day be derived from a purely probabilistic approach.

1.4.6 The differential rotation of the Earth's inner core

Although the primary goal of this thesis is to highlight the benefits of using a Bayesian approach to tomography problems, we also include an example in the Appendix where probabilistic techniques are used to explore the differential rotation of the Earth's inner core. The rate at which the inner core rotates with respect to the rest of the mantle remains highly controversial despite many efforts to unravel the rotational dynamics of the innermost Earth. Repeating earthquakes, or earthquake doublets, have been used for over a decade now (starting with Poupinet et al. (2000)) to argue with regards to the differential rotation of the inner core. We assess PKP arrival times coming from previously and newly observed earthquake doublets using three independent measurement techniques. With this expanded dataset and a probabilistic approach, we challenge the previously held assumption of a constant inner core rotation rate. The rotation pattern instead appears more complex, undergoing periods of both prograde and retrograde motion. Our preferred model includes decadal fluctuations in inner core rotation superimposed upon an average prograde rotation with respect to the rest of the mantle. We allow the data to drive the parameterization of the rotation pattern by using a transdimensional Bayesian inversion scheme.

Transdimensional Bayesian inversion has the ability to allow the data noise to guide the most probable number of free parameters needed to model the data. This advantage is especially evident in our analysis of earthquake doublets with regards to inner core differential rotation. Not only do we add new data to the existing doublet dataset, but we improve upon traditional measurement and inversion techniques. This approach would benefit a variety of different time series analyses where results are heavily dependent on model parameterization.

1.5 Publication schedule

Chapter 2

Young, M.K., H. Tkalčić, N. Rawlinson, and A. M. Reading (2012), Exploiting seismic signal and noise in an intracratonic environment to constrain crustal structure and source parameters of infrequent earthquakes, *Geophysical Journal International*, doi:10.1111/j.1365-246X.2011.05326.x.

Chapter 2 contains the paper published on the Shark Bay earthquake focal mechanism in *Geophysical Journal International* by myself and three coauthors. I was chiefly responsible for the data processing and analysis in this research project and was the principal author of the text and figures of the resulting paper. Dr Hrvoje Tkalčić supervised this project and directed my research. He provided much guidance and advice. Many of the receiver function and moment tensor inversion computer scripts were provided by Hrvoje as well. Although I alone composed the first draft of paper,

Hrvoje was important to the editing of subsequent drafts. Dr Nick Rawlinson guided the ambient noise tomography aspect of the project and also provided excellent suggestions to improving the manuscript. Dr Anya Reading critically contributed to the explanation of the geological setting as well as the interpretation of results. She also led the deployment of the instruments in Western Australia.

Chapter 3

Young, M.K., N. Rawlinson, P. Arroucau, A. M. Reading, and H. Tkalčić (2011), High-frequency ambient noise tomography of southeast Australia: New constraints on Tasmania's tectonic past, *Geophysical Research Letters*, doi:10.1029/2011GL047971.

Chapter 3 contains the paper published in *Geophysical Research Letters* by myself and four coauthors about ambient noise tomography in Tasmania. I performed all of the data measurements and processing and most of the analysis for this research project. I was the principal author of the text and figures of the resulting paper. Dr Nicholas Rawlinson directed the project and authored the Fast Marching Surface Tomography (FMST) software package used to perform the inversion. He was invaluable to trouble shooting problems with the data processing and inversion and contributed significantly to the interpretation of results. His knowledge of southeast Australian tectonics and geology was essential to the Discussion and Conclusions sections of the paper. Nick also reviewed the initial draft and significantly improved the paper. Pierre Arroucau provided many of the ambient noise cross correlation scripts which facilitated the production of the Green's functions estimates. He was also always very quick to respond to my questions with much needed advice and assistance. Hrvoje provided constructive comments to the manuscript and aided the rebuttal of reviews. This research was made possible by Drs Anya Reading, Hrvoje Tkalčić, and Nicholas Rawlinson, as they deployed the instruments.

Chapter 4

Young, M.K., N. Rawlinson, and T. Bodin (2013), Transdimensional inversion of ambient seismic noise for 3D shear velocity structure of the Tasmanian crust, *Geophysics*, 78(3), WB49-WB62.

Chapter 4 contains the paper which represents the culmination of my tomography work in Tasmania. I performed the data processing, measurements, and inversion, produced the figures and wrote the first draft of the paper. Dr Nicholas Rawlinson guided me along the way and provided much needed advice and direction. He also significantly contributed to the interpretation of results and helped prepare the manuscript for submission. Dr Thomas Bodin provided the computer codes on which I based my

Bayesian inversions for phase velocity maps and 1D shear velocity models. He also edited the text and helped respond to comments by the reviewers. The Bayesian inversion techniques of this paper are based upon the content of Thomas's thesis and related papers.

Chapter 5

Young, M.K., R.A. Cayley, M.A. McLean, N. Rawlinson, P. Arroucau, and M. Salmon (2013), Crustal structure of the east Gondwana margin in southeast Australia revealed by transdimensional ambient seismic noise tomography, *Geophysical Research Letters*, 40, 42664271, doi:10.1002/grl.50878.

Chapter 5 contains the paper published in *Geophysical Research Letters* on ambient noise tomography in southeast Australia. As the lead author, I performed all the data processing and inversions. I wrote the first draft of the paper; although, Ross Cayley contributed substantially to the interpretation of results. He edited the first draft and guided the direction of our Discussion and Conclusions for the paper. Mark Mclean helped with the interpretation of results and aided our analysis through the manipulation of the GOCAD 3D modelling software suite. He also created the figures for the paper. Dr Nick Rawlinson guided my work and also helped to edit text. Thanks are due to Drs Pierre Arroucau and Michelle Salmon for the deployment and maintenance of instruments.

Chapter 6

Young, M.K., H. Tkalčić, T. Bodin, and M. Sambridge (2013), Global P-wave tomography of Earth's lowermost mantle from partition modeling, *Journal of Geophysical Research*, 118, 5467-5486.

Chapter 6 contains my work on the lowermost mantle, which is soon to be published in the *Journal of Geophysical Research*. I performed a significant portion of the differential travel time measurements, all of the processing and inversion and much of the analysis. Dr Hrvoje Tkalčić also contributed to the production of the travel time dataset. He guided my work and provided advice and suggestions all along the way. Although I wrote the first draft of the paper, he edited the text and helped prepare it for submission. Hrvoje was also important to the interpretation of results. Thomas Bodin and Malcolm Sambridge provided the framework for the Bayesian inversion approach and also helped to edit the manuscript.

Appendix

Tkalčić, H., M.K. Young, T. Bodin, S. Ngo, and M. Sambridge (2013), The Shuffling Rotation of the Earth's Inner Core Revealed by Earthquake Doublets, *Nature Geoscience*, 6, 497-502, doi:10.1038/ngeo1813.

The paper published in *Nature Geoscience* on the differential rotation of the inner core comprises the appendix of this thesis. As second author, I performed data processing and measurements. I also provided some of the figures for the paper and contributed significantly to the editing of text. Hrvoje Tkalčić led the work, directed the interpretation of results, and composed the first draft of the manuscript. Thomas Bodin performed the Bayesian inversion of the travel time measurements and synthetic tests. Silvie Ngo discovered the new doublets. Malcolm Sambridge helped develop the methodology for the inverse approach. All authors helped edit the manuscript.

Full waveform moment tensor inversion in a low seismicity region using multiple teleseismic datasets and ambient noise

2.1 Foreword

The first section of this thesis explores a medley of different seismological techniques which provide a basic introduction to several types of iterative non-linear geophysical inversion. The end goal is to perform a full waveform inversion for the source mechanism of the 2007 Shark Bay earthquake in Western Australia. But such an inversion requires a basic knowledge of the lithospheric structure of the region. Given the relatively limited station coverage and paucity of local earthquakes, some resourcefulness is required to produce a composite 3D shear velocity model of the area. A combination of seismic signals and noise is exploited, facilitating a new interpretation of the Shark Bay earthquake. This work was published in *Geophysical Journal International*:

Young, M. K., Tkalčić, H., Rawlinson, N. and Reading, A. M. (2012), Exploiting seismic signal and noise in an intracratonic environment to constrain crustal structure and source parameters of infrequent earthquakes. *Geophysical Journal International*, 188: 1303-1321, doi: 10.1111/j.1365-246X.2011.05326.x

2.2 Abstract

In many regions of the world characterised by a relatively low rate of seismicity, the determination of local and regional seismic source parameters is often restricted to an analysis of the first onsets of P-waves (or first motion analysis) due to incomplete information about Earth structure and the small size of the events. When rare large earthquakes occur in these regions, their waveforms can be used to model Earth structure. This, however, makes the nature of the earthquake source determination problem

circular, as source information is mapped as structure. Presented here is one possible remedy to this situation, where through a two-step approach we first constrain Earth structure using data independent of the earthquake of interest. In this study, we focus on a region in Western Australia with low seismicity and minimal instrument coverage and use the CAPRA/LP temporary deployment to demonstrate that reliable structural models of the upper lithosphere can be obtained from an independent collection of teleseismic and ambient noise datasets. Apart from teleseismic receiver functions, we obtain group velocities from the cross-correlation of ambient noise and phase velocities from the traditional two-station method using carefully selected teleseismic earthquakes and station pairs. Crustal models are then developed through the joint inversion of dispersion data and receiver functions, and structural Green's functions are computed from a layered composite model. In the second step of this comprehensive approach, we apply a full waveform inversion (three-component body and surface waves) to the 2007 $M_L=5.3$ Shark Bay, Western Australia, earthquake to estimate its source parameters (seismic moment, focal mechanism, and depth). We suggest that the full waveform inversion analysis provides constraints on the orientation of fault planes superior to a first motion interpretation.

2.3 Introduction

2.3.1 Motivation

On February 15th, 2007, Western Australia (WA) experienced a rare magnitude 5.3, earthquake approximately 18 km beneath Shark Bay (Figure 2.1a, b). Its location (-25.97° N, 113.28° E, 18 km depth) and size ($M_L=5.3$) were determined by Geoscience Australia (GA), which uses a network of permanent broadband seismometers operating in real-time (www.ga.gov.au). Although Australia is generally seismically quiet, one magnitude 6.0 event occurs approximately every five years (McCue, 1990). Careful analysis of these anomalous events is necessary to establish a model for describing the causes, character, and frequency of intraplate earthquakes (Stein, 2007) as well as the state of the regional stress-field (Clark and Leonard, 2003).

In order to invert a seismic waveform for source properties, the structure of the Earth between the source and receiver must be understood (Aki and Richards, 2002). Unfortunately, mapping the Earth's crust is not an easy task in a seismically inactive region sparsely covered by recording stations. Under these circumstances, simpler and structure-independent methods of determining seismic moment tensors are often employed. The most straightforward approach is to evaluate the polarity of P-wave first motions recorded by seismic stations that provide adequate azimuthal coverage of the source. S- and P-wave amplitude ratios have also been utilised with success to constrain focal mechanisms (Julian and Foulger, 1996; Julian et al., 1997; Hardebeck and Shearer, 2003). The solutions, however, depend on the clarity of phase arrivals and

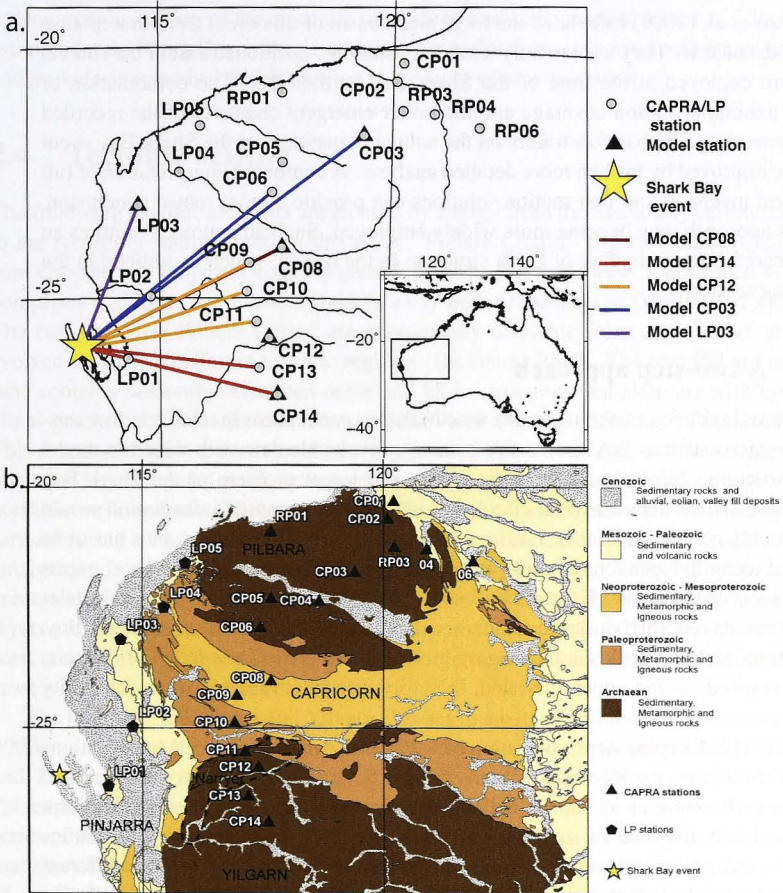


Figure 2.1: (a) Location of all CAPRA/LP stations used in this study along with the epicentre of the February 2007 Shark Bay event (marked by the yellow star). “Model stations” refer to stations for which a 1-D Earth model of the crust and upper lithosphere is created using a joint inversion of receiver functions and dispersion information. Stations with names beginning with “CP” and “RP” are part of the CAPRA array deployed by the Australian National University. Stations with names beginning with “LP” were deployed by the University of Western Australia. Coloured lines between source and receiver indicate the model used for each station. (b) Tectonic elements of Western Australia.

the position of stations with relation to epicentral distance and azimuthal distribution.

Revels et al. (2009) calculated the focal mechanism of this event from first motion P-wave data alone. They used mainly temporary stations, positioned east of the source, that were deployed at the time of the Shark Bay earthquake. The combination of limited azimuthal station coverage and the rather emergent character of the recorded waveforms suggests that constraints on the source parameters of the Shark Bay event could be improved by further, more detailed analysis. A combined interpretation of full waveform inversion and first motion solutions can provide a more robust conclusion, and this approach may become more widely employed. Such an approach requires an initial, careful determination of Earth structure in the region, which is outlined in the following section.

2.3.2 A two-step approach

When rare significant earthquakes like the Shark Bay event occur in relatively low seismicity regions such as WA, their waveforms are invaluable data with which to model Earth structure. Such modelling would make our target problem of the Shark Bay earthquake source determination circular in nature, as the source information would be inevitably coupled with final Earth structure models. Earth structure thus has to be retrieved using independent datasets, in this case, limited to either small local events weakly recorded at several GA stations located far from Shark Bay, or, preferably, teleseismic events recorded during a temporary deployment located closer to Shark Bay. In addition, ambient noise Earth imaging techniques improve knowledge of the seismic wavespeeds in the upper crust and, therefore, can be invaluable when seismicity is sparse.

The CAPRA deployment, consisting of ~ 20 three-component broad-band stations installed in WA by the Research School of Earth Sciences at the Australian National University (Reading et al., 2012) in WA, was operational at the time of the Shark Bay event with the goal of studying deep structure. The presence of these stations enables us to produce a working composite model of WA that reflects the different Moho character and seismic velocities of each geological region.

The ancient West Australia Craton was assembled as a result of the collision of the Archaean Pilbara and Yilgarn cratons. They were joined along the Capricorn Orogen with the Pinjarra Orogen bounding them to the west (Fitzsimons, 2003). Forward modelling is used to create initial crustal models that are fed into a linearised joint inversion of teleseismic receiver functions and group and phase dispersion information calculated using a combination of teleseismic signals and ambient noise data.

The procedure presented here is naturally divided into two steps: in the first step, we determine Earth structure within the region spanned by the source and receiver array using a multiplicity of methods, and in the second step, we use this information to invert for the seismic moment tensor of the Shark Bay earthquake. We are able

to invert the long period waveforms (15-35 s) recorded at CAPRA/LP stations within approximately 750 km of the epicentre to produce a seismic moment tensor and depth estimate for the Shark Bay event. In addition, we perform our own first motion analysis and provide an appraisal of this method in the light of previous work.

2.4 Tectonic setting

The following tectonic elements are crossed by energy from the Shark Bay earthquake to the recording stations used in this study: Pilbara Craton, Yilgarn Craton, Capricorn Orogen, and Pinjarra Orogen (Figure 2.1b). The Pilbara Craton in northwest WA comprises a granite-greenstone terrain of early-mid Archaean age (Wellman, 2000). The east and west Pilbara Craton are geologically disparate from one another and evolved under two different tectonic regimes (Hickman, 2004). The east Pilbara terrane contains randomly-orientated dome and basin structures that alternate with synclinal greenstone (volcano-sedimentary rocks) belts (Van Kranendonk et al., 2007). This dome and basin pattern is absent in the west Pilbara terrane, which is instead dominated by elongated granitoid complexes, greenstone belts, and numerous east and northeast striking faults (Hickman, 2004). The Yilgarn Craton, in southwest Australia, formed during a Proterozoic episode of increased tectonic activity that resulted in the amalgamation of various continental fragments (Cassidy et al., 2006). Granite and greenstones form the majority of the upper crust, and deeper Late Archaean crustal layers are exposed in the northwest and southwest (Ivanic et al., 2010). At the northwest corner of the Yilgarn Craton lies the Narryer terrane, which contains the oldest crust in Australia (Spaggiari et al., 2008).

The joining of the Pilbara and Yilgarn Cratons in the Palaeoproterozoic produced the 300 km wide, heavily deformed, tectonic belt known as the Capricorn Orogen (Tyler and Thorne, 1990; Betts et al., 2002; Sheppard et al., 2010). The orogen contains Palaeoproterozoic plutonic igneous rocks, medium- to high-grade metamorphic rocks, a series of volcano-sedimentary and sedimentary basins, and is rimmed by the deformed margins of the Pilbara and Yilgarn cratons (Cawood and Tyler, 2004). To the west of the Darling Fault, lies the Neoproterozoic Pinjarra Orogen, which is the resulting passive margin that formed when Australia separated from India (Myers et al., 1996). The rift valley is concealed by 10-15 km of sedimentary rocks, and so little of its Precambrian geological history is known. Some evidence is, however, provided by three main sources of exposed Precambrian rocks in the Leeuwin, Mullingarra, and Northampton complexes (Myers, 1993).

Previous seismic studies in this part of WA have utilised receiver function, reflection and refraction data. Drummond (1988) used reflection and refractions studies to characterize the Pilbara and Yilgarn Cratons as having a two-layered crust with a broad transition between these layers occurring between 10 and 15 km depth. He estimated the Moho to lie between 28 and 35 km depth. Clitheroe et al. (2000) inverted receiver

functions for shear velocity profiles beneath 65 broad-band stations across Australia and combined the results with 51 independent estimates of crustal thickness from refraction and reflection profiles to produce a Moho map of the continent. He found the crust to be thin and the Moho transition to be sharp beneath the Archaean cratons. A few years later, Collins et al. (2003) confirmed the results of Clitheroe et al. (2000) using additional data newly acquired from refraction and reflection profiles. Using mostly temporary seismic stations, Reading and Kennett (2003) completed a receiver function analysis of the Pilbara Craton, Capricorn Orogen, and northern Yilgarn Craton. They characterised the Pilbara Craton as having a sharp, shallow (~ 30 km) Moho, the Yilgarn as having a sharp, yet deeper (~ 40 km) Moho, and were barely able to discern the Moho beneath the Capricorn Orogen. Reading et al. (2012) provide a more comprehensive analysis of the Moho character of the region using receiver functions from the CAPRA deployment. In general, they found a deeper Moho transition (36–44 km depth) beneath the Capricorn Orogen; a sharper, less deep (~ 35 km) Moho in the north Yilgarn Craton, except for the Narryer terrane, which exhibits an abnormally shallow discontinuity at 29 km; and a shallower (29–34 km) more pronounced discontinuity beneath the Pilbara Craton.

We will use data from stations CP08, CP09, CP10, and CP11 to constrain the structure within the Capricorn Orogen; stations CP14 and CP13 for the Yilgarn Craton, with CP12 on the Narryer Terrane; and stations CP02, CP03, CP05, CP06, RP01, RP03, and RP04 for the Pilbara Craton (Figure 2.1b). There have been no previous receiver function analyses of the Pinjarra Orogen, but we expect to find a thinner crust (Collins et al., 2003; Clitheroe et al., 2000) relative to the cratons and a thin surface layer of sediments using stations LP01, LP02, LP03, LP04, and LP05 (Figure 2.1 b).

2.5 Data and methods

In this study, we use data recorded at a total of 17 CAPRA seismic stations. There were two main transects recording between June 2006 and June 2007: one running roughly north-south (CP stations in Figure 2.1a, b), and another running west-east along the Telfer Road (RP stations in Figure 2.1a, b). Data from five stations operated by the University of Western Australia were also incorporated (LP stations in Figure 2.1a, b). This transect ran along the northwestern margin of WA between October 2005 and April 2007. The CP and RP stations comprised EarthData recorders and Guralp CMG-3ESP sensors (with the exception of CP13 where a Streckeissen STS-2 was deployed) while the LP stations comprised Reftek recorders and CMG-40T sensors. Five representative models produced for the region are entitled CP14, CP12, CP08, CP03, and LP03 (Figure 2.1a). These models together represent a composite model that is used to produce synthetic waveforms for the seismic moment tensor inversion. In the following sections, we will describe three methods that were applied to the CAPRA/LP data to obtain this composite 1D model of the Earth. In the last part of each

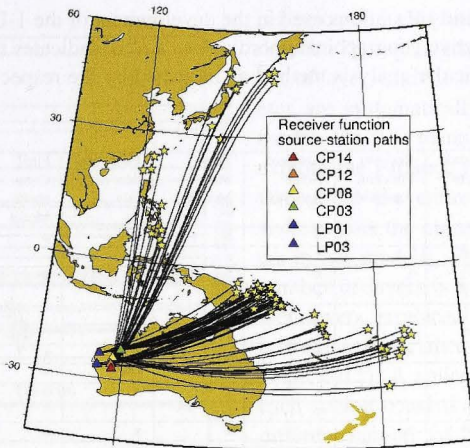


Figure 2.2: Map showing all source-receiver pairs used in the receiver function analysis. Sources are marked by yellow stars and stations by colored triangles.

of the following subsections, we state the results of the structure determination (step 1), which are subsequently used in the complete waveform inversion for an improved focal mechanism (step 2).

2.5.1 Receiver function analysis

Receiver function analysis is a popular method for determining a shear-wave model of the lithosphere beneath a station. By deconvolving the vertical with the radial response of a plane-layered structure, the shear-wave response of the crust and upper mantle can be extracted to produce a time series called a receiver function (RF) (Langston, 1979). RFs are particularly sensitive to pronounced gradients in elastic properties as a function of depth and are critical to determining the depth of the Moho.

In this study, RFs are calculated from teleseismic events using a relatively conservative threshold on earthquake magnitudes of 5.0 or greater. The events, mainly from surrounding subduction zones of Indonesia, Japan, and Tonga-Fiji (Figure 2.2), are pre-processed and only coherent waveforms are selected for further analysis. The waveforms are iteratively deconvolved in the time domain according to Ligorria and Ammon (1999) using a 2.5 Gaussian filter. The resulting RFs are subsequently band-pass filtered to decrease the noise and improve coherency using an optimised filter width: band-pass between 0.75 Hz and 2.0 Hz for stations CP14 and CP12, bandpass

Table 2.1: All CAPRA and LP stations used in the development of the 1-D composite model along with respective geographical coordinates. An “x” indicates that that station was used for a particular analysis method as indicated by the respective column headings.

Station Name	Latitude (degrees)	Longitude (degrees)	Receiver Function Analysis	Ambient Noise Analysis	Two-Station Method	First Motion Analysis	Final Composite Model	Moment Tensor Inversion
CP14	-26.93	117.60	x	x	x	x	x	x
CP13	-26.39	117.18		x		x		x
CP12	-25.79	117.40	x	x		x	x	
CP11	-25.47	117.12		x		x		x
CP10	-24.86	116.91		x		x		x
CP09	-24.29	116.96		x		x		x
CP08	-23.99	117.67	x	x	x	x	x	x
CP06	-22.88	117.44		x				x
CP05	-22.28	117.67		x		x		
CP04	-22.33	118.67		x				
CP03	-21.73	119.40	x	x	x	x	x	x
CP02	-20.63	120.08		x		x		
CP01	-20.26	120.21		x		x		
RP01	-20.89	117.64		x		x		
RP03	-21.22	120.22		x		x		
RP04	-21.27	120.89		x		x		
RP06	-21.51	121.85		x		x		
LP01	-26.21	114.29	x	x	x			
LP02	-24.96	114.80		x				
LP03	-23.15	114.55	x	x	x	x	x	x
LP04	-22.49	115.45		x		x		
LP05	-21.56	115.89		x		x		

between 1.0 Hz and 2.5 Hz for stations CP08 and CP03, and a high-pass with a corner frequency of 0.4 Hz for stations LP01 and LP03. RFs for a back-azimuth range of approximately 20° are selected and stacked for each station to create an average RF which is used in the linearised inversion.

The first step in inverting RFs for a 1-D model is to produce a reasonable initial model, as the final solution will not be allowed to differ greatly from the initial model. We utilize a priori information from previous studies (Reading and Kennett, 2003) in our forward modelling approach using the RF forward modelling software IRFFM (Tkalčić et al., 2011). This interactive tool allows manual manipulation of thicknesses, velocities, and v_p/v_s ratios for a 1-D Earth model. A simple model with two crustal layers is created to represent the Earth’s structure beneath each of the following six stations: CP14, CP12, CP08, CP03, LP03, and LP01 (Table 2.1). These become the initial models in a linearised inversion (Julia et al., 2000) that allows easy manipulation of the smoothness parameter. We find an inverted shear velocity model that produces synthetic RFs with a high variance reduction by taking the initial model and iteratively perturbing each layer. Increasing the number of layers in a model improves the fit between the observed and synthetic RF at the expense of over-parameterising the model space. Likewise, increasing the smoothness parameter makes a model more

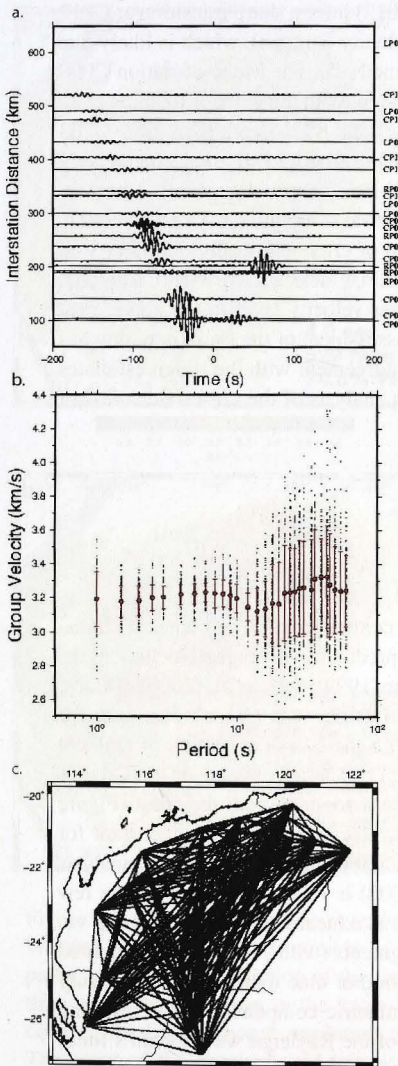


Figure 2.3: (a) All ambient noise cross-correlograms associated with station CP04. (b) Average group velocity curve with error bars showing one standard deviation; (c) All possible ray paths between the CAPRA/LP array station pairs.

realistic at the expense of decreasing the data fit. Through a grid-search, the number of layers and the smoothness parameter are systematically varied for each model. In this manner we are able to explore the variance reduction achieved throughout the entire parameter space and estimate the optimal number of layers in our models. For each model, the number of layers is increased until further layers produce no significant improvement in variance reduction (Tkalčić et al., 2011). A collection of models for each station consists of versions with a different number of layers, smoothness parameter, and iteration number, all of which are empirically determined. The preferred model is an average over a limited range of these models. For example, the final CP14 model is averaged over versions having 7, 9, or 11 crustal layers, smoothnesses of 0.2 or 0.3, and iterations between 10 and 40. Though the resulting final averaged model does not have the overall best fit, it provides a more probable representation of the Earth's structure beneath a given station.

Fig. 6a provides the final model as inverted from the RF data for CP14 (light blue dashed line). Located near the northern rim of the Yilgarn Craton, the interpreted Moho depth of CP14 is approximately 34 km, which is in good agreement with previous RF studies (Clitheroe et al., 2000; Collins et al., 2003; Reading and Kennett, 2003; Reading et al., 2012). The RFs of CP12 in general have an ill-defined and inconsistent peak around 3.5 s, yielding less obvious information about the character of the Moho, but the beginning of a broad

transition is seen at about 28 km. Reading et al. (2012) infer a sharp transition at CP12 at this depth (although not a very large seismic velocity contrast), which is likely due to the slight difference between the two inversion methods. The Moho of station CP08 appears to begin at around 30 km depth, and, consistent with the work of Reading et al. (2012), there is an upper crustal discontinuity at around 8 km depth (Fig. 6b). CP03 has a distinct Moho transition around 28 km. The RFs of both LP01 and LP03 are very noisy, and thus the majority of them are discarded from the final stacking. Nonetheless, the average RF for LP03 does show a strong arrival at around 4 s. Upon inversion, a strong low velocity zone in the uppermost 4 km of crust - probably due to coastal sediments - and a Moho transition at 31 km result. LP01 lacks a sharp Moho; a gradual transition begins at about 27 km depth, and a lower velocity layer in the upper crust is present as with LP03. Although a detailed RF assessment of the Pinjarra region has not yet been completed, these values are in good agreement with the rough estimates for the region given by Collins et al. (2003) in his analysis of the crustal thickness of Australia.

2.5.2 Surface wave dispersion curves

Although RFs provide good estimates of velocity contrasts, when combined with dispersion data, they more accurately and uniquely predict the average velocities in the crust (e.g. Ozalaybey et al. (1997); Du and Foulger (1999); Julia et al. (2000); Tkalčić et al. (2006, 2012)). In this study, we calculate Rayleigh wave Green's functions for the Earth between all possible station pairs through the cross-correlation of ambient noise recorded by the CAPRA/LP array (Table 2.1). The asymmetry of the Green's functions is most likely due to the increased noise associated with the coast (Figure 2.3). The Green's functions reveal short-period velocity information important for resolving crustal and upper mantle structure. An automated frequency-time analysis (FTAN) procedure according to Bensen et al. (2008) is followed along with the few modifications described by Arroucau et al. (2010) as a means of measuring group velocities. Cross-correlations of 40-minute noise segments (with 75% overlap) recorded by all possible station pairs are stacked over a period of nine months starting on July 1, 2006. The negative time derivative of the symmetric component of the resulting average cross-correlograms provides an estimate of the Rayleigh wave Green's functions between each station pair within a frequency-dependent amplitude factor (Lobkis and Weaver, 2001), which does not affect the dispersion measurements. Using an automated phase-matched filtering technique described in depth by Levshin and Ritzwoller (2001), group velocities are extracted for periods between 1 and 60 s (Figure 2.3). Assuming the phase shift resulting from the differentiation minimally affects the group velocity signals (Yao et al., 2006), the average of the measurements from

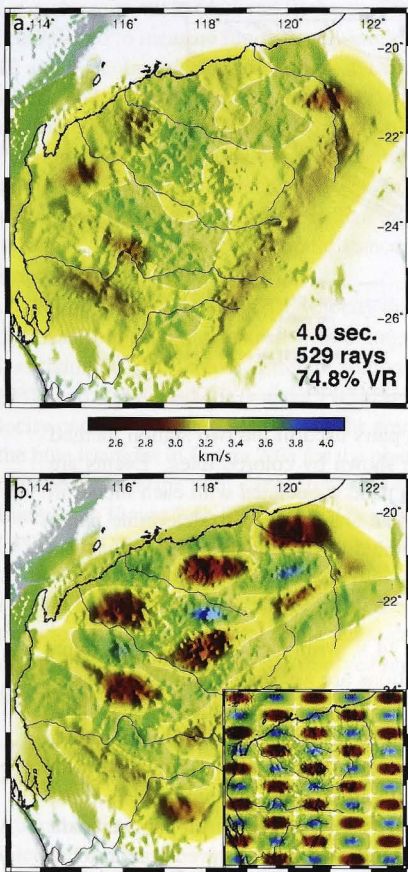


Figure 2.4: (a) 4.0 s group velocity map of Western Australia. Period, number of ray paths, and variance reduction of the travel time residuals are shown in the lower left corner. (b) Checkerboard resolution test. The input of the checkerboard tests is an alternating pattern of positive and negative velocity squares with a maximum perturbation of 0.8 km/s.

the differentiated and un-differentiated cross-correlograms is used as long as the two measurements do not vary from each other by more than 3.0%. This promotes the selection of only high quality data (Arroucau et al., 2010). In another effort to preserve only the reliable waveforms, a signal to noise ratio (SNR) greater than 3 and an interstation spacing of at least 3 wavelengths is made a requirement (Bensen et al., 2008).

Group velocity curves are calculated from the Green's function corresponding to a given model station (CP14, CP12, CP08, CP03, or LP03) and LP01, whose location approximates that of the earthquake. In this manner, we are able to obtain a dispersion curve that represents the average structure between source and receiver (the pink dotted line in the bottom right portion of Figure 2.6a, b). The Green's functions associated with the pairs CP12 and LP01, and LP03 and LP01, have poor SNRs. We thus employ a different method that aims to extract the average dispersion curve representing the Earth directly beneath the station. A fast marching surface wave tomographic inversion scheme (Rawlinson and Sambridge, 2004a,b) is used to estimate velocity variations for different periods (Figure 2.4a). This iterative, nonlinear approach uses cubic B-splines to describe the velocity continuum and provides stable, robust solutions even in heterogeneous media. Significant improvement in traveltme residual misfit is seen for

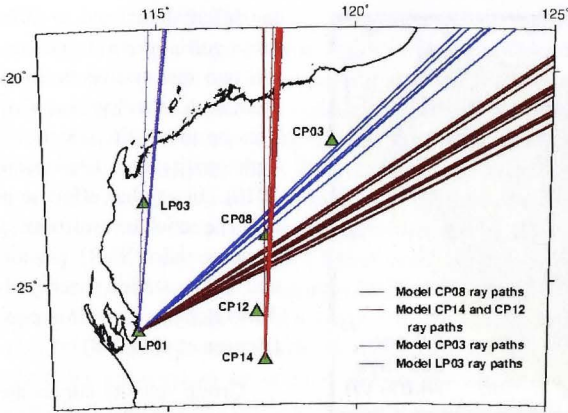


Figure 2.5: Great circle paths for station-event pairs used in the two station method of phase velocity dispersion curve retrieval are shown by colored lines. Events are from Japan, Tonga-Fiji, and Indonesia. The ray paths associated with each model in the legend refer to the teleseismic waveforms that are analysed to determine phase velocity curves for the 1-D Earth model(s) associated with the mentioned stations.

maps associated with periods between 1.5 and 14 s, with variance reductions ranging from 41 to 77%. The lower variance reductions are associated with the longest- and shortest-period (> 9 s and < 2 s) solutions, which is when there is a gradual degradation of dispersion measurements. Synthetic “checkerboard” resolution tests are performed in order to access the resolving power of the data. Gaussian noise with a standard deviation of 0.15 s is added to the synthetic data to simulate the noise content of the observed traveltimes. Figure 2.4b displays the results of a checkerboard resolution test for a period of 4 s. A sampling of the maps at a given station location for each period enables the interpolation of a dispersion curve for the lithosphere beneath that station.

The general pattern of lower velocities in the coastal regions of Western Australia can likely be attributed to a layer of surface sediments. The work of Abdulah (2007) provides a 3-D P-wave velocity perturbation map of northwest Australia derived from traveltimes of both local and teleseismic events. The relative velocity patterns evaluated at 35 km depth largely agree with our longer period maps (~ 30 s period), which roughly sample the same depth. The north Pinjarra Orogen and the Glenburg terrane (west of the Capricorn Orogen) (Figure 2.1b) demonstrate significantly lower velocities, which corresponds to the generally younger geological structures of WA.

Phase velocity information provides a much better constraint on average shear velocity than just group velocity alone, as multiple phase velocity curves are possible

for each group curve (Aki and Richards, 2002). Consequently, the two-station method is employed to measure fundamental-mode Rayleigh phase dispersion curves between 10 and 60 s. In order to safely assume that the influence of the structure between the source and nearest station is negligible, the two stations must be on approximately the same great circle path with the source (Knopoff et al., 1966). We require that the azimuthal difference between the earthquake to the two different stations and the azimuthal difference between the earthquake and the nearest station, and the nearest station to the farther station be less than 2.0° . To promote reliability in measurements at longer periods, the inter-station distance is required to be at least half of the wavelength (Yao et al., 2006).

We obtain 29 reliable phase velocity dispersion curves from earthquakes from Indonesia, Tonga-Fiji, and Japan with a magnitude between 5.0 and 7.0 and a depth of less than 100 km for four different station pairs: LP01 and LP03; CP08 and CP14; LP01 and CP08; and LP01 and CP03 (Figure 2.5; Table 2.1). An average phase velocity curve is obtained for each of the four sets. The models for stations CP14 (see the blue triangles in Figure 2.6a for the phase dispersion curve) and CP12 incorporate the curves from the path connecting CP14 and CP08; the CP08 model (see the blue triangles in Figure 2.6b for the phase dispersion curve) use those connecting LP01 and CP08; the CP03 model those connecting LP01 and CP03, and the LP03 model those connecting LP01 and LP03 stations. Although a phase velocity analysis using ambient seismic noise was attempted, the 2π phase ambiguity factor prevents confident identification of the fundamental mode phase curves. Such analysis would require the use of a global 3-D model or local, observed phase velocity maps to roughly predict phase speeds (Bensen et al., 2008).

2.5.3 Joint inversion of teleseismic and ambient noise data

After the average phase and group velocity dispersion curves are compiled for each intended model station, a joint inversion of RF and dispersion data is performed (Figure 2.6a, b). The first step involves using the interactive, forward modelling software for joint modelling of RFs and surface wave dispersion curves IRFFM2 (Tkalčić et al., 2012) to create a reasonable initial model. The average model from the RF inversion is altered manually until the synthetic RF better fits the dispersion data. Then we invert the fundamental-mode group and phase velocities simultaneously with the radial RFs for a shear-wave velocity profile beneath each station (Figure 2.6a, b) (Herrmann, 2004). Our approach is similar to that of Julia et al. (2000, 2003). A fixed bottom layer below 47 km, which approximates the lower limit of the RF and dispersion curve sampling depth, is used to focus the inversion sensitivity on the uppermost lithosphere. A time window of -5 to 15 s is used to invert the RFs to concentrate the inversion on the Moho character. Differential smoothing is applied while an influence parameter controls the relative weight between the dispersion curve and the RF data. We then

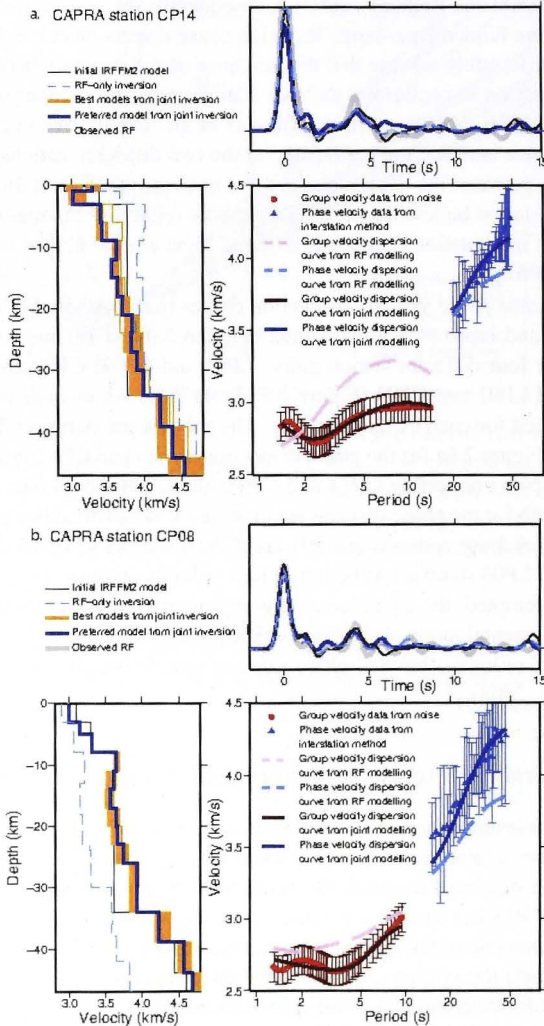


Figure 2.6: 1-D shear wave velocity models for (a) station CP14 and (b) station CP08 are shown in the lower left. An ensemble of best models (yellow) comprise 279 individual models, which include 3 weight values, 3 damping values, and 31 iterations. Error bars for the dispersion curves show one standard deviation of the velocities (see bottom right).

run a series of inversions, each with an influence parameter ranging between 0.0 and 1.0 (where 0.0 indicates only an inversion of RF data, and 1.0 only inverts dispersion data). We choose the models resulting from the weight value that best balances the individual fits of the dispersion and RF data. Successive inversions converge after about five iterations; however, the final model is created by the average of iterations 20 through 40, in which range no discernible improvement in variance reduction is seen.

Our final jointly-inverted models agree well with previous studies and, moreover, provide further constraints on the upper lithosphere of WA. The general pattern of a deeper Moho depth in the Capricorn Orogen and more shallow crust under the cratons is consistent with the work of Reading et al. (2012). Upon jointly inverting for the Capricorn Orogen structure associated with station CP08, the Moho depth estimate increases from 30 km (resulting from the RF analysis) to 34km (the dashed light blue line and solid blue line of Figure 2.6b), which agrees more closely with Reading et al. (2012) who estimated the Moho to be at 36 km depth. This change arises due to a trade-off between the absolute velocity and the thickness of the crust when only information from RFs is available. Due to the fact that long period phase velocity dispersion data brings additional information about the absolute velocity of the lower crust (faster in this case; Figure 2.6b), the crustal thickness increases to accommodate the faster propagation of shear waves through the crust.

While no previous studies have performed a high-resolution group or phase velocity analysis of WA, Saygin and Kennett (2010) completed a set of continental-scale group velocity maps using ambient noise for periods between 5 and 12.5 s. Our results are in rough agreement in that upper crust group velocities range from 2.8 to 3.4 km/s. We improve the constraints by increasing resolution and including phase velocity information derived from the two-station method. For the first time, RFs are analysed for the Pinjarra Orogen. Although the data are very noisy for these coastal stations, we are able to obtain a rough estimate of crustal structure and Moho character for the area.

2.6 Moment tensor inversion of the Shark Bay event

Equipped with a collection of upper lithosphere models of WA, we are now ready to perform a full waveform inversion for source properties of regional earthquake recordings. After first using the Earth reference model ak135 (Kennett et al., 1995), we will then use our own models to produce synthetic Green's functions and compare them with the filtered observed waveforms. It is assumed that the Green's functions resulting from our composite model represent the average structure between the source and each station. To represent Earth structure associated with stations CP14 and CP13, we use the model CP14; for stations CP12, CP11, CP10, and CP09 we use the model CP12; for stations CP03, CP05, CP06 we use the CP03 model; and stations LP03 and CP08 each have their own model.

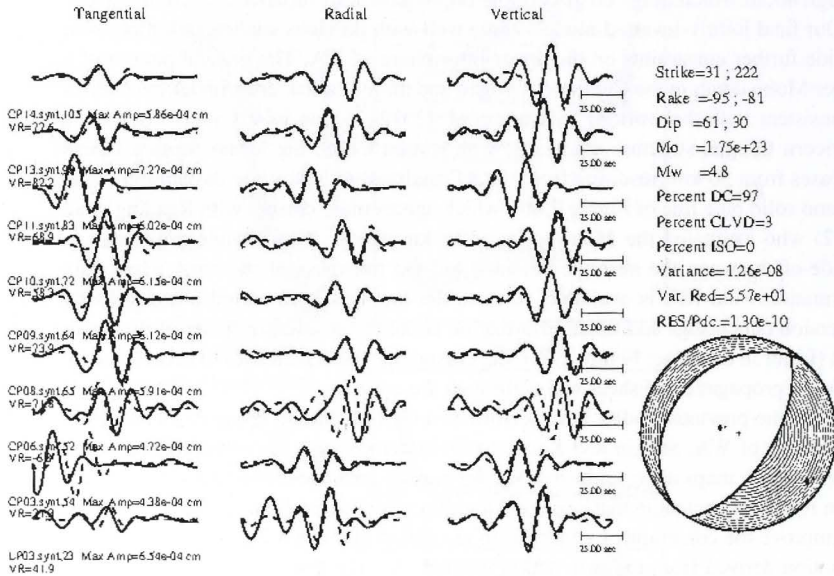


Figure 2.7: Results of moment tensor inversion for the case in which a single 1-D model (model CP14) is used to produce structural Green's functions for nine selected stations. The solid lines show the observed waveforms filtered between 15 and 35 s, whilst the dashed lines are the synthetic waveforms filtered in the same way. The three different components of the seismograms are shown from left to right: tangential, radial, and vertical. The lower-hemisphere projection of the P-wave radiation pattern is shown in the lower right along with the pressure (P) and tension (T) axis. The strike, rake, and dip of the two nodal planes along with the scalar seismic moment, moment magnitude, percent double couple (DC), compensated linear vector dipole (CLVD), and isotropic (ISO) of the best solution are listed on the right.

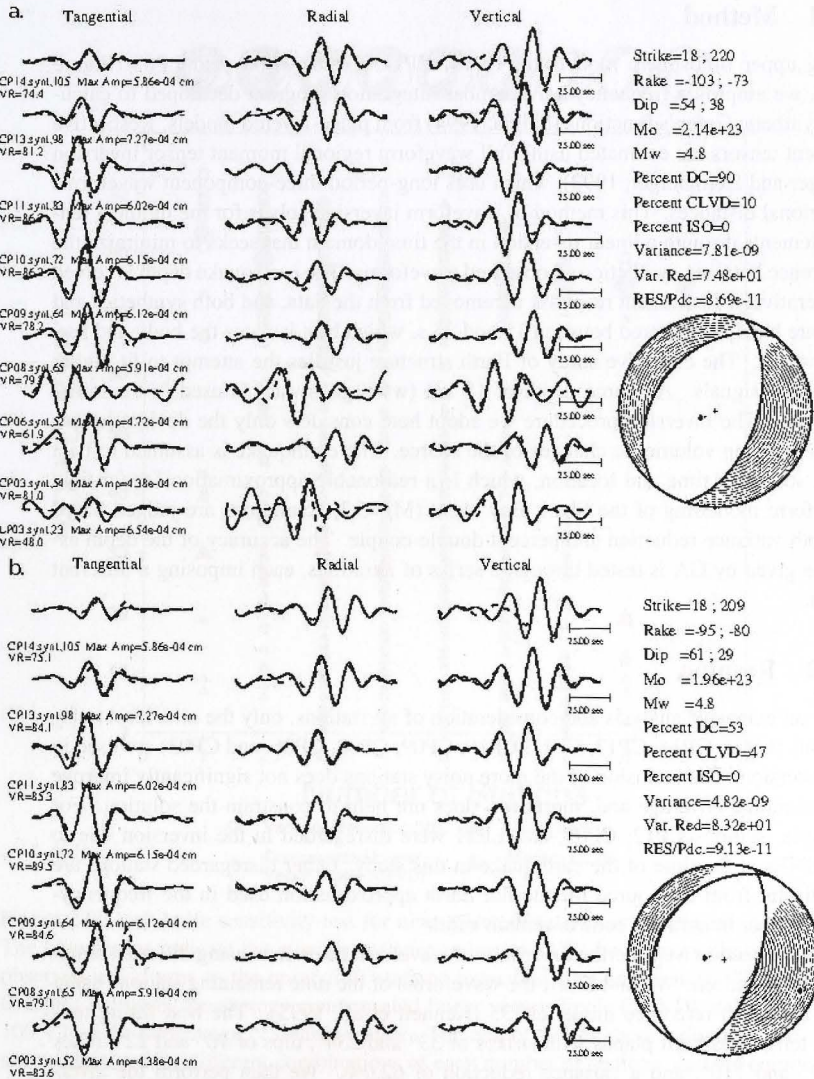


Figure 2.8: Results of moment tensor inversion for the case in which a composite 1-D model is used to produce structural Green's functions for the total of nine and (b) seven stations. For the explanation of waveforms, focal mechanism plot and the legend, see captions of Figure 2.7.

2.6.1 Method

Using upper lithosphere models for CP14, CP12, CP08, CP03, and LP03 (Figure 2.1a), we employ a frequency-wavenumber integration program developed to calculate synthetic Green's functions (Saikia, 1994) from plane-layered models. Respective moment tensors are estimated using full waveform regional moment tensor inversion (Dreger and Helmberger, 1993), which uses long-period three-component waveforms at regional distances. This method of waveform inversion solves for the moment tensor elements through a linear inversion in the time-domain that seeks to minimize the difference between synthetic and observed waveforms. The earthquake depth is solved for iteratively. Instrument response is removed from the data, and both synthetics and data are bandpass-filtered between 15 and 35 s, which best isolates the body and surface waves. The extensive study of Earth structure justifies the attempt to fit higher frequency signals. A source depth of 18 km (www.ga.gov.au) is used in the initial inversion. The inversion procedure we adopt here considers only the deviatoric tensor, neglecting volumetric changes of the source. The earthquake is assumed to be a point source in time and location, which is a reasonable approximation for far-field waveform modelling of the Shark Bay event ($M_L=5.3$). Solutions are judged based on both variance reduction and percent double-couple. The accuracy of the depth estimate given by GA is tested through a series of iterations, each imposing a different depth.

2.6.2 Results

After an extensive analysis and consideration of all stations, only the nine least noisy stations (LP03, CP14, CP13, CP11, CP10, CP09, CP08, CP06, and CP03) are used in the inversion. The inclusion of the more noisy stations does not significantly improve the azimuthal coverage and, moreover, does not help to constrain the solution. For example, stations CP12, CP05, and LP01 were disregarded in the inversion due to low SNRs at the time of the earthquake in this study. Other disregarded stations are too distant from the source for the flat Earth approximation used in the frequency-wavenumber integration code to remain valid.

In this section we describe the results of waveform inversions using different structure combinations. We first invert the waveforms of the nine remaining stations using only the Earth reference model ak135 (Kennett et al., 1995). The best fitting moment tensor has fault planes with strikes of 33° and 234° , dips of 70° and 22° , rakes of 82° and 110° , and a variance reduction of 62.0%. We then perform the inversion using only the model CP14, which is a robust model and a good approximation for much of the region (Figure 2.6a). The best fitting moment tensor has fault planes with strikes of 31° and 222° , dips of 61° and 30° , and rakes of -95° and -81° ; the variance reduction is only 57.8% (Figure 2.7). Previous experience in inverting waveforms for the seismic moment tensor in a complex tectonic setting suggest that

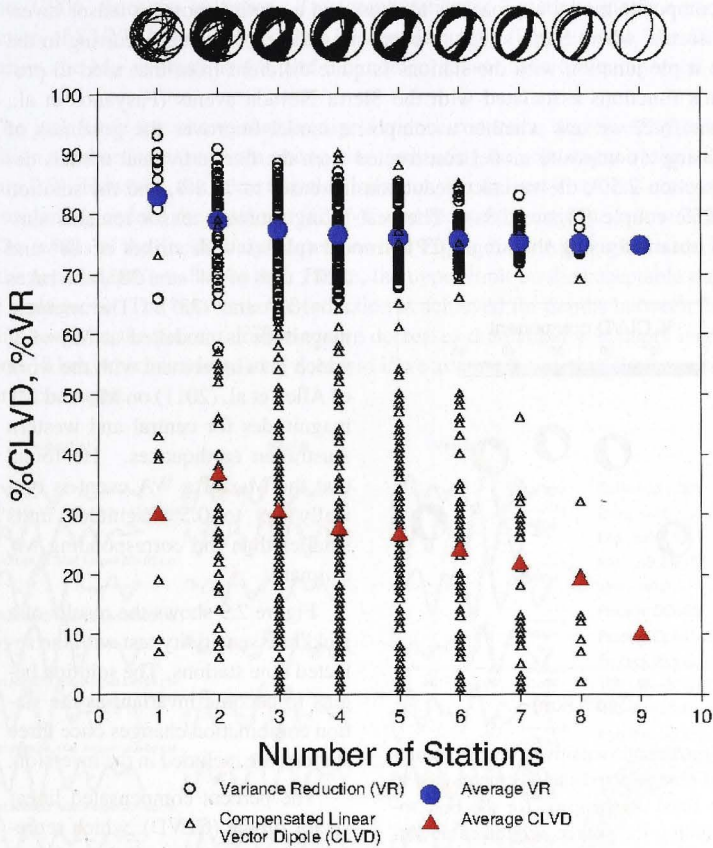


Figure 2.9: Jack knife sensitivity test for nine selected stations as mentioned in text. The blue circles indicate the average variance reduction (VR) between synthetic and observed waveforms as the number of stations increases from one to nine. The red triangles represent the average compensated linear vector dipole (CLVD), defined as 100% less the percentage of double couple. The empty circles show individual variance reductions for different combinations of each number of stations, and the empty triangles show the corresponding %CLVDs. The resulting focal mechanism solutions for each number of stations are superimposed upon each other and displayed at the top of the figure.

it is possible to improve the overall fit by using a composite model (Tkalčić et al., 2009). A composite model approach is also used in a routine moment tensor inversion in California, where Earth structure connecting the earthquakes occurring in the Mendocino triple-junction with the stations is quite different from that used to produce Green's functions associated with the Sierra Nevada events (Pasyanos et al., 1996). Therefore, we test whether a composite model improves the goodness of fit. When using a composite model constructed from the five individual models described in section 2.5.3, the variance reduction increases to 74.8%, and the solution is 90% double couple (Figure 2.8a). The best fitting moment tensor remains similar to that obtained using the single CP14 model (planes with strikes of 18° and 220° , dips of 54° and 38° , and rakes of -103° and -73°). The moment magnitude is modelled at $M_W=4.8$;

which is in agreement with the work of Allen et al. (2011) on M_W and M_L magnitudes for central and western Australian earthquakes. He found that the M_W of a WA event is typically 0.3 to 0.5 magnitude units smaller than the corresponding M_L estimate.

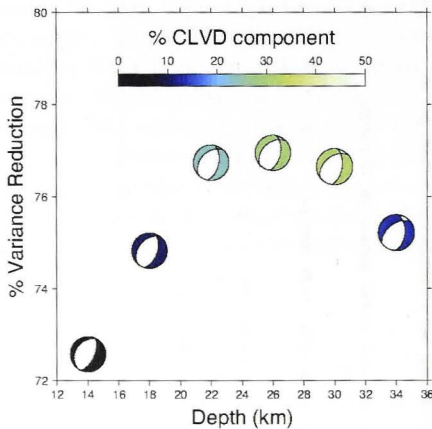


Figure 2.10: A depth-sensitivity test for a combination of nine selected stations mentioned in text. The focal mechanisms for the best solution assuming the source originated at various depths (14, 18, 22, 26, 30, and 34 km) are shown. The quadrants associated with the tension-axes are colored according to the percent of compensated linear vector dipole (CLVD), defined as 100% less the percentage of double couple. The initial estimate as quoted by GA is 18 km.

Figure 2.9 shows the results of a jackknife sensitivity test with the selected nine stations. The solution begins to become invariant as the station combination changes once three stations are included in the inversion.

The percent compensated linear vector dipole (CLVD), which represents the percentage of the solution that is non-double-couple, decreases with increasing number of stations as the solution becomes increasingly well constrained. LP03 has the poorest signal to noise ratio of the chosen nine stations, but we experiment with including this station in the inversion as it significantly improves azimuthal coverage. If we remove LP03 from the inversion, the moment tensor changes only very slightly, and the variance reduction increases to 79.3%; however, the percent double couple drops to 68%, which could be a result of spurious effects caused by insufficient azimuthal coverage (e.g. Šílený et al.

inversion as it significantly improves azimuthal coverage. If we remove LP03 from the inversion, the moment tensor changes only very slightly, and the variance reduction increases to 79.3%; however, the percent double couple drops to 68%, which could be a result of spurious effects caused by insufficient azimuthal coverage (e.g. Šílený et al.

(1996)). We can improve the variance reduction further by excluding another noisy station, CP06, from the inversion. This combination of 7 stations yields a variance reduction of 83.2%, but contains only 53% double couple (Figure 2.8b). For all three scenarios, the M_W estimate is 4.8, and the moment tensor is an oblique normal thrust fault.

The jack knife test shows that average variance reduction decreases by only 9% as station number increases from one to nine, indicating the robustness of the solution (Figure 2.9). However, the same test also indicates that at least 8 stations are required to considerably reduce the scatter in %CLVD and reduce the estimate below 20%.

The results of the depth analysis are shown in Figure 2.10. Although it is not likely that the actual depth was lower than 18 km, the upper limit on the acceptable range is more ambiguous. The best variance reduction is achieved for depths between 22 and 30 km; however, the percent double couple decreases dramatically as depth increases beyond 18 km, which is a less likely scenario if we assume the earthquake has a simple tectonic character.

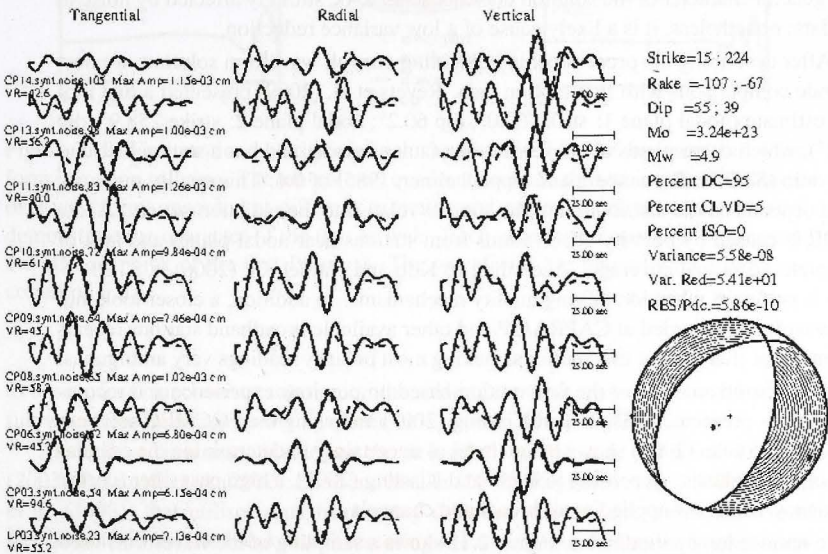


Figure 2.11: Results of moment tensor inversion using the synthetic data generated with the composite model and added noise with a rms of 150% the peak amplitude of the signal. For the explanation of waveforms, focal mechanism plot and the legend, see captions of Figure 2.7.

2.7 Discussion

A set of sensitivity tests were performed to assess the reliability of the inversion method. Synthetic waveforms are generated utilizing the E3D finite difference method (Larsen and Schultz, 1992) using our preferred orientation of nodal planes (Figure 2.8a) (strike 18° , dip 54° , and rake -103°) as well as a M_W of 5.0. The synthetics are processed in the same manner as the observed data. Using the same crustal model and hypocentre location, Green's functions are created and compared to the synthetics. As expected, we recover the same moment tensor with 100% variance reduction when using the nine station locations used in the actual inversion of the Shark Bay event.

To assess the effect of noise on the solution, white noise with a root mean square of 150% of the peak amplitude of the signal is added to the synthetic data. Again the inversion is performed on the synthetic data. The strike, dip, and rake vary by at most 4° from the situation without noise. The estimated magnitude is 4.9, the percent double-couple is 95%, and the variance reduction decreases to 54.1% (Figure 2.11). The general character of the solution does not seem to be strongly affected by noise in the data; nonetheless, it is a likely cause of a low variance reduction.

After describing the process behind obtaining our full waveform solution, we now provide comparisons with first motion data. Revets et al. (2009) presented a first motion estimate (nodal plane 1: strike 60.0° , dip 60.2° ; nodal plane 2: strike 258.9° , dip 31.2°), which corresponds to a reverse thrust fault scenario, and has a station distribution ratio (STDR) (Reasenber and Oppenheimer, 1985) of 0.6. This quality measurement depends on the distribution of the stations relative to the radiation pattern. A low STDR is caused by polarity observations from stations near nodal planes and lack of complete azimuthal coverage. According to Kilb and Hardebeck (2006), a STDR > 0.65 is preferred when identifying quality mechanisms. In addition, a closer look into the waveforms recorded at CAPRA/LP and other available broadband stations reveals an emergent character of first motions, making most polarity readings very ambiguous.

A bootstrap analysis of the first motion based on previous experience and recommendations presented in Diehl and Kissling (2007) and using the FOCMEC software package of Snoke (2003) shows a high level of uncertainty in determining the orientation of nodal planes. According to Diehl and Kissling (2007), a high pass filter (corner frequency 1.0 Hz) is applied to all broadband channels

to remove long period noise. Figure 2.12 shows a sampling of the waveforms used in the first motion analysis superimposed on our preferred solution from the full waveform moment tensor inversion. Table 2.1 and A.2 list all stations used. For the majority of selected recordings it is very difficult to identify a first arrival and, moreover, determine its polarity. Our conclusion is that the first motion solution is not robust and cannot diminish the waveform solution on the basis that they do not agree entirely. We believe that this is the indication that the Shark Bay event is more complex than previously understood from the first motion solution. We therefore find it preferable

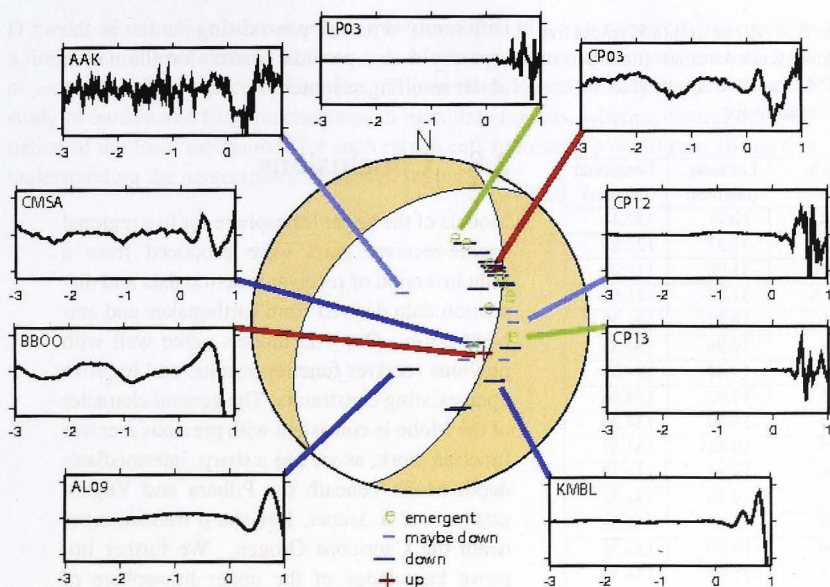


Figure 2.12: First motion polarity readings superimposed on the preferred full waveform inversion solution. The tan-colored quadrants contain the tension axes. A sample of 9 waveforms recorded at different azimuths and epicentral distance are shown to demonstrate the character of the first arrivals. Each waveform is cut to 3 s before and 1 s after our pick of the first P arrival. The waveforms are filtered with a high pass corner of 1 Hz.

to base a focal mechanism solution on the seismic moment tensor obtained from the full waveform inversion as we have been able to do in this detailed analysis.

There have been many studies on the stress field of WA (e.g. Clark and Leonard (2003); Reynolds et al. (2002); Zhao and Muller (2003); Reynolds et al. (2003); Coblentz et al. (1998)) that utilised data from many different sources, i.e. earthquake focal mechanisms, borehole breakouts, overcoring measurements, hydraulic fracture measurements, geological indicators, and drilling-induced tensile fractures. There is general agreement that the pressure axis in the Shark Bay, WA region, runs approximately east-west. Although the pressure axis of our preferred solution (Figure 2.8a) is orthogonal to that, orientated approximately southwest of vertical, the plausibility of our solution is not diminished. The work of Kagan (1992) has shown that earthquakes in tectonic blocks often weakly depend on the current deformation and tectonic stresses, and are instead more heavily dependent on known and hidden defects in the rock medium.

Table 2.2: All stations (and respective geographical coordinates) not part of CAPRA or LP arrays used in the first motion analysis.

Station Name	Latitude (degrees)	Longitude (degrees)
KAKA	-12.71	132.44
KMBL	-31.37	121.88
MUN	-31.98	116.21
STKA	-31.88	141.60
WB0	-19.77	134.39
WB1	-19.96	134.35
WB2	-19.94	134.35
WB3	-19.92	134.36
WB4	-19.90	134.36
WB5	-19.88	134.37
WB6	-19.85	134.37
WB7	-19.84	134.38
WB8	-19.81	134.38
WB9	-19.79	134.38
WC1	-19.92	134.34
WC2	-19.93	134.37
WC3	-19.96	134.37
WC4	-19.96	134.34
WR0	-19.96	134.54
WR1	-19.94	134.34
WR2	-19.95	134.36
WR3	-19.95	134.39
WR4	-19.95	134.41
WR5	-19.95	134.43
WR6	-19.95	134.45
WR7	-19.96	134.48
WR8	-19.96	134.50
WR9	-19.96	134.51
MBWA	-21.16	119.73
NWAO	-32.93	117.24
AL09	-74.30	66.79
S2B5	-33.39	143.48
S2B8	-33.49	145.07
stc1	-42.15	146.47
BBOO	-32.81	136.06
CMSA	-31.54	145.69
FITZ	-18.10	125.64
FORT	-30.78	128.06
AAK	42.63	74.49
EKS2	42.66	73.78

Differently-oriented pre-existing faults in the area could also provide controls on the nature of the resulting seismicity.

2.8 Conclusions

Models of the upper lithosphere for five regional source-receiver pairs were produced from a joint inversion of receiver function data and dispersion data derived from earthquakes and ambient noise. Our 1-D models agree well with previous receiver function results, and improve upon existing constraints. The general character of the Moho is consistent with previous receiver function work, as we see a sharp, intermediate-depth Moho beneath the Pilbara and Yilgarn cratons and a deeper, less-sharp transition beneath the Capricorn Orogen. We further improve knowledge of the upper lithosphere of Western Australia by combining dispersion with receiver function data and by providing a shear velocity model for coastal stations. We show that a composite model enables a more robust inversion of 3-component full waveforms for the seismic moment tensor than a simple 1-D model. In particular, we calculate the moment tensor and depth of the 2007 Shark Bay, Western Australia, earthquake, and obtain a robust oblique normal solution of strike 18° , dip 54° , and rake -103° . The pressure axis of this solution is orthogonal to the generally accepted pressure axis of the Shark Bay region, indicating that the focal mechanism was influenced by differently oriented pre-existing faults and rock defects in the area. Despite this, we find that our full waveform solution, which incorporates our composite crustal structure model, improves on the determination of the focal mechanism of the Shark Bay event from first motion analysis alone.

This study demonstrates how a composite 1-

D model of the upper lithosphere may be developed in a low seismicity region with a limited number of seismic stations and its subsequent use can improve the analysis of an earthquake's source mechanism. The methodology is widely applicable to the study of earthquake focal mechanisms in intraplate regions, where a careful determination of the focal mechanism for such rare events represents a significant advance in understanding the neotectonics of a given region.

3.1 Foreword

The vibrant seismic zone transgressing northwards through Tasmania, southwards through the rugged terrain of the United Kingdom and beyond, has been a source of interest and concern in order to explore the potential of the isolated region. The study of a low seismicity region, namely Tasmania, where the occurrence of major earthquakes is rare, is a source of interest and concern because of the potential for a major earthquake in the same tectonic region. This paper presents a preliminary study of the seismicity of Tasmania in order to map its location in regard to the rest of the world. This work is a preliminary study of the seismicity of Tasmania.

Young, M. R., A. Campbell, P. Armstrong, A. J. H. Hearn, and J. H. Woodsworth. 1990. High-frequency seismicity in the northwestern region of Tasmania. *Journal of Geological Research*, *17*, 1: 101-110.

3.2 Abstract

The island of Tasmania, which lies in the southern tip of Australia, is a tectonically isolated and tectonically inactive island. The seismicity of the island is a source of interest and concern in order to explore the potential of the isolated region. The study of a low seismicity region, namely Tasmania, where the occurrence of major earthquakes is rare, is a source of interest and concern because of the potential for a major earthquake in the same tectonic region. This paper presents a preliminary study of the seismicity of Tasmania in order to map its location in regard to the rest of the world. This work is a preliminary study of the seismicity of Tasmania.

High-frequency ambient noise tomography of southeast Australia: New constraints on Tasmania's tectonic past

3.1 Foreword

The ambient seismic noise tomography results in Western Australia were very promising despite the limited number of stations and uneven source of ambient noise. In order to explore the potential of the method further, we sought a more suitable locale, namely Tasmania, where the surrounding ocean provides a strong and consistent source of ambient noise and a dense seismic array provides excellent coverage. We use the same iterative non-linear inversion approach but now also invert for phase velocity maps in addition to group velocity. This work was published in *Geophysical Research Letters*:

Young, M. K., N. Rawlinson, P. Arroucau, A. M. Reading, and H. Tkalčić (2011), High-frequency ambient noise tomography of southeast Australia: New constraints on Tasmania's tectonic past, *Geophysical Research Letters*, 38, L13313, doi:10.1029/2011GL047971

3.2 Abstract

The island of Tasmania, which lies at the southeast tip of Australia, is an ideal natural laboratory for ambient noise tomography, as the surrounding oceans provide an energetic and relatively even distribution of noise sources. We extract Rayleigh wave dispersion curves from the continuous records of 104 stations that form two adjacent seismic arrays with ~ 15 km station separation. Unlike most passive experiments of this type, which observe very little coherent noise below a 5 s period, we clearly detect energy at periods as short as 1 s, thanks largely to the close proximity of oceanic

microseisms on all sides. The main structural elements of the eastern and northern Tasmanian crust are revealed by inverting the dispersion curves (between 1 and 12 s period) for both group and phase velocity maps using an iterative, non-linear tomography scheme. Of particular significance is a pronounced band of low velocity, observed across all periods, that underlies the Tamar River Valley and continues south until dissipating in southeast Tasmania. Together with evidence from combined active source and teleseismic tomography and heat flow data, we interpret this region as a diffuse zone of strong deformation associated with the mid-Paleozoic accretion of oceanic crust along the eastern margin of Proterozoic Tasmania. In the northwest, a narrower low-velocity anomaly is seen in the vicinity of the Arthur Lineament, which may be attributed to local sediments and strong deformation and folding associated with the final phases of the Tyennan Orogeny.

3.3 Introduction

The island of Tasmania comprises the southern limit of the Tasman Orogen, or “Tasmanides” of eastern Australia, which formed largely as a result of subduction-accretion along the proto-Pacific margin of east Gondwana throughout the Paleozoic (Glen, 2005). Tasmania may be divided into two basement geology domains: the Western Tasmanian Terrane (WTT) and the Eastern Tasmanian Terrane (ETT) (Figure 3.1a) (Williams, 1989). WTT has large areas of exposed Proterozoic basement which contrast with the Phanerozoic rocks of the adjacent mainland Lachlan Fold Belt (Reed, 2001). ETT, however, exhibits no evidence of Proterozoic outcrop and is predominantly Paleozoic in origin (Reed, 2001). Much of the boundary between WTT and ETT underlies cover rocks, making Tasmania difficult to position in plate tectonic reconstructions, e.g. (Greene, 2010).

In an attempt to elucidate the lithosphere beneath southeast Australia, including Tasmania, a transportable passive seismic array experiment known as WOMBAT commenced in 1998 (Rawlinson et al., 2010b). After 13 consecutive subarray deployments, over 550 stations have been installed to date. In northern Tasmania, 3-D teleseismic tomography (Rawlinson et al., 2006) has revealed a pronounced low velocity anomaly in the lower crust and lithospheric mantle near the transition between the ETT and WTT. In a subsequent study that involved the joint inversion of wide-angle (refraction and reflection) and teleseismic data (Rawlinson et al., 2010b), the presence of this anomaly was confirmed.

Magnetotelluric and magnetovariational studies (Parkinson et al., 1988) have revealed a major conductivity anomaly in northeast Tasmania, directly in line with the Tamar River, which has since become known as the Tamar Conductivity Anomaly. The top of the anomaly was estimated to lie between 1.5 and 5 km depth. In 2007, KUTh Energy Ltd. [www.kuthenergy.com] performed an extensive heat flow survey in east Tasmania using a grid of shallow (~300 m) drill holes spaced every 20 km in

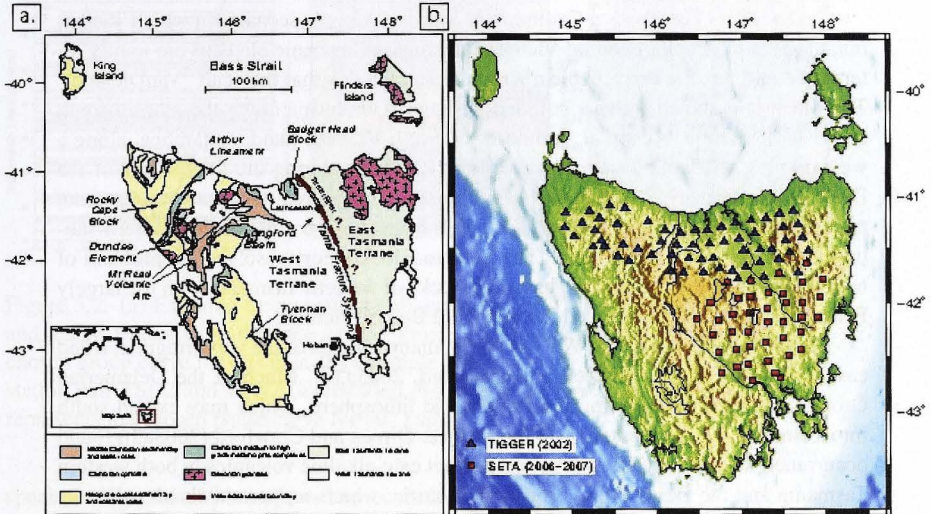


Figure 3.1: (a) Map showing the summary basement geological units of Tasmania (based on Spaggiari et al. (2003)). Only the northern portion of the boundary between the WTT and the ETT is exposed at the surface. The approximate location of the terrane boundary under cover is indicated by a dotted line. (b) Map of WOMBAT subarrays TIGGER and SETA used in this study.

which a significant heat flow anomaly ($> 90 \text{ mWm}^{-2}$) was discovered in a $\sim 4,000 \text{ km}^2$ region of the southern Tamar Valley.

One area of particular controversy in Tasmanian tectonics is the nature of the boundary between WTT and ETT. The limited surface exposure indicates that there is a broad and complex area of deformation between the distinctive surface expressions of the WTT and ETT (Reed, 2001), but evidence of a definite boundary remains elusive. More than two decades ago it was postulated that the Tamar River marks the approximate location of a crustal-scale suture zone (Williams, 1989) - sometimes referred to as the Tamar Fracture System (TFS) - between ETT and WTT. This idea has since been questioned (Leaman, 1994; Reed et al., 2002; Rawlinson et al., 2010b), and the observed changes in stratigraphy that gave rise to the original hypothesis are now interpreted as being related to thin-skinned (near-surface) tectonic processes (Leaman et al., 1994). The region in the neighbourhood of the Tamar River has been explored using teleseismic tomography (Rawlinson et al., 2006), refraction and wide-angle reflection experiments (Rawlinson and Urvoy, 2006; Rawlinson et al., 2010b), and potential field data (Leaman, 1994), but none evince a significant, crustal-scale contrast along the Tamar River Valley.

Cayley (2011) proposes a Cambrian to Silurian tectonic scenario in which Tasmania, the Selwyn block of central Victoria, and adjacent oceanic plateaus are jointly interpreted as an exotic Proterozoic microcontinental block that they call "VanDieland." The block is assumed to have collided with east Gondwana along the margin south of western Victoria, Australia, and north of North Victoria Land, Antarctica, along a west-dipping subduction system in the Late Cambrian during the final stages of the Delamerian Orogeny. VanDieland was ultimately transferred northeast to its present position with the Selwyn block embedded into the eastern edge of the western subprovince of the Lachlan Orogen. The Selwyn Block theory resolves the problem of how to reconcile the Proterozoic basement rocks of western Tasmania with the largely Paleozoic, oceanic crust derived Lachlan Fold Belt of Victoria.

Another possibility is that WTT is one of many salients of the very irregular, rifted east Gondwana margin (Direen and Crawford, 2003a,b). Much of the Delamerian Orogen is underlain by deformed Proterozoic lithosphere, which may extend south into Tasmania, where it outcrops at the surface. Direen and Crawford (2003a,b) found occurrences of rare boninitic rocks and distinct calc-alkaline volcanics in both western Tasmania and the Delamerian Orogen in Victoria, which supports their idea that the Tyennan Orogen of western Tasmania and the Delamerian Orogen are related to the same tectonic event. In this case, the eastern edge of WTT acted as an indenter to the oceanic crust when this margin collided with an intraoceanic arc during the Middle Cambrian (Direen and Crawford, 2003a,b). ETT subsequently resulted from accretion of oceanic crust along Tasmania's eastern margin from the Silurian through Early Devonian (Reed, 2001).

In this study, we image the crust of Tasmania using ambient seismic noise tomography applied to continuous data records extracted from the WOMBAT subarrays TIGGER and SETA. Thanks to the high station density of these arrays and prolific ocean noise from all sides (Yang and Ritzwoller, 2008), this is the first time that high-resolution group and phase velocity maps have been produced for Tasmania. The results from this study complement those from recent seismic and heat flow studies and lead to a substantially better understanding of the tectonic evolution of this enigmatic region of the Australian continent.

3.4 Data and method

The data for this study comes from two subarrays of the WOMBAT transportable seismic array project, which has occupied much of southeast Australia over the past 12 years. The 64 short-period stations of the TIGGER array were deployed in March 2002 and span northern Tasmania, while the 40-station SETA array was installed four years later immediately south of TIGGER on the central east part of the island (Figure 3.1b). We use a total of approximately seven months of data from each of the two arrays to perform ambient seismic noise tomography of the region. The average station

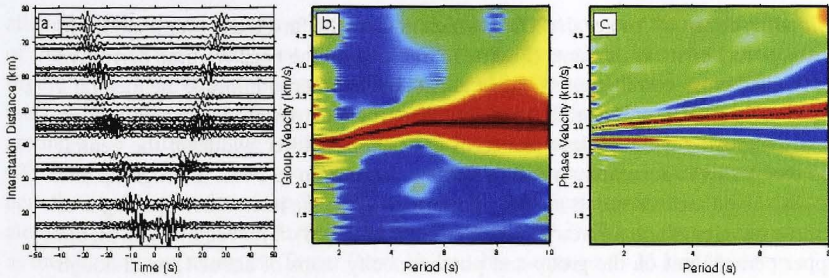


Figure 3.2: (a) Example frequency-time diagram for the TIGGER station pair TSA4 and TSQ3 (interstation distance of 234 km). The dotted black line represents the chosen group curve for this pair. (b) Example phase velocity dispersion image for the station pair TSD2 and TSH2 (interstation distance of 63 km). The dotted black line represents the chosen phase curve for this pair.

spacing of less than 20 km allows unprecedented resolution of the crust.

The ambient noise cross-correlation procedure we employ is similar to that described in depth by Bensen et al. (2008). To produce the highest-quality Green's functions, the noise recordings are divided up into 40 minute segments with 75% overlap. Segments that contain anomalously large amplitudes, either from instrument error or earthquake signals, are removed prior to applying a bandpass-filter between 0.01 and 2.0 Hz. Vertical-component data is cross-correlated and stacked for all simultaneously recording station pairs (Curtis et al., 2006), resulting in 2038 cross-correlograms for TIGGER and 779 for SETA. A phase-matched filtering process described by Levshin and Ritzwoller (2001) enables the utilization of cross-correlograms with a signal-to-noise ratio (SNR) as low as 3 (Arroucau et al., 2010), although the average SNR is 49.3 for SETA and 34.3 for TIGGER.

Shapiro and Campillo (2004) showed that the long-term cross-correlation of ambient seismic noise produces an estimate of the surface-wave Green's function (noise cross-correlation function, or NCF) between two seismograph stations. The negative time derivative of the NCF, known as the empirical Green's function (EGF), is equivalent to the Green's function for the path between the two corresponding stations within a frequency-dependent amplitude factor (assuming there is a random, isotropic ambient noise field) (Snieder, 2004). We perform group velocity dispersion measurements using the frequency-time analysis (FTAN) method presented by Levshin et al. (1972) and selection criteria described by Arroucau et al. (2010) on the symmetric component (average of the causal and acausal signals) of the EGF (Figure 3.2a). The dispersion-curve-picking process is automated using a multiple filter technique described by Dziewonski et al. (1969) to reduce processing time.

Phase velocities are measured using a modified version of the image transformation

technique described by Yao et al. (2006), which invokes the far-field approximation. In this case, we make measurements (Figure 3.2b) based on the negative time derivative of the stacked cross-correlograms (Yao et al., 2006). In order to improve the method's ability to yield results for higher frequencies, we introduce a period-dependent filtering process. Imposing a linear-dependence of the bandpass-filter width on the central period enables us to accurately measure phase velocities up to 1 Hz. Both group and phase dispersion measurements are only performed when the interstation spacing is at least three wavelengths at a given period (Bensen et al., 2008). This requirement places an upper period limit on the group and phase velocity maps of about 12 s, although individual dispersion curves range up to 25 s.

After making the group and phase velocity measurements, a tomographic inversion, e.g. (Stankiewicz et al., 2010), is performed for periods between 1 and 12 s. Fundamental mode Rayleigh wave group and phase velocity variations are mapped on a regular grid of 3,600 nodes using an iterative, non-linear tomographic inversion scheme (Rawlinson et al., 2008) which uses an eikonal solver to predict traveltimes and a subspace scheme to solve the inverse problem. Both damping and smoothing regularization are applied to prevent convergence towards a solution that has unnecessarily large amplitude perturbations and model roughness. Significant improvement in residual misfit is seen for periods between 1 and 12 s, with variance reductions ranging from 24 to 88%. The lower variance reductions are associated with the longest-period (> 9 s) solutions, where there is a gradual degradation of dispersion measurements as the far-field approximation becomes less accurate. Synthetic "checkerboard" resolution tests (Rawlinson et al., 2006) are performed in order to analyze the resolving power of the data. Gaussian noise with a standard deviation of 0.25 s is added to the synthetic data to simulate the noise content of the observed traveltimes.

3.5 Results

Most ambient noise studies are restricted to a lower period limit of 5 to 10 s (Yao et al., 2006; Villaseñor et al., 2007; Bensen et al., 2008; Yang et al., 2007). Moreover, studies that are able to observe coherent energy at 1 s period often lose resolution above 3 s (Huang et al., 2010) due to the reduced spatial extent of their arrays. We, however, have produced group and phase velocity maps for periods between 1 and 12 s using 90% of the SETA dispersion curve measurements and 93% of those from TIGGER. In general, there is a strong correlation between the group and phase velocity variations across north and central east Tasmania. The average group and phase velocity sampling depth increases with period, with the phase velocities sampling slightly deeper than the group velocities at a given period. For typical continental crust, 1 s period surface waves are most sensitive to structure in the upper 1-2 km, whereas 12 s period surface waves are most sensitive to structure at depths between 10-15 km (Saygin and Kennett, 2010).

The most obvious characteristic of the new maps produced in this work, visible at

all well-resolved periods, is a pronounced low-velocity zone within the neighborhood of the Tamar River Valley that continues southwards through both arrays (line A in Figure 3.3). This feature is consistently broad (~ 50 km) and follows a curved path that can be tracked southeast from Tasmania's north coast before bending southward at around 42° S. Although the southern limit of the velocity images occur at around 42.5 - 43° S the low-velocity zone becomes more patchy in this area and possibly terminates near the southern border of the SETA array. We also find significantly lower velocities along the Arthur Lineament to the west (line B in Figure 3.3). While not as consistent as the velocity low along the Tamar River Valley, this narrower (~ 25 km) lineation of decreased velocities is manifest at all periods.

Phase velocities are more difficult to measure accurately compared to group velocities and hence require much higher quality data. In this study, phase velocity maps were produced using 80% of the SETA dispersion measurements and 97% of the TIGGER dispersion measurements for periods between 1 and 12 s. Features denoted by lines A and B in Figure 3.3 remain present as in the group velocity maps and are slightly wider in some areas, which may be attributed in part to the differences between the group and phase velocity sensitivity kernels. Checkerboard resolution tests reveal similar resolution quality as for the group velocity analysis, but due to a slightly higher smoothing factor, the amplitude of the phase velocity anomalies are marginally lower.

3.6 Discussion

The low-velocity anomaly that runs approximately parallel to the Tamar River is present in both the group and phase velocity maps at all periods (Figure 3.3), suggesting that there is a strong change in crustal properties that extends at least 15 km beneath the surface. This low-velocity region has a width of approximately 50 km and is as much as ~ 0.5 km/s slower than the surrounding areas. Since the shape and lateral extent of this anomaly bears some similarity to the surface expression of broad-scale surface geomorphological features in Tasmania, we have given considerable thought to the possible influence of surface features on deeper-seated anomalies. While the low velocities at shorter periods in the northern half of the anomaly are in part due to a localised region of Cretaceous-Holocene sedimentary rocks in the Longford Basin of north Tasmania (Direen and Leaman, 1997), the pattern observed at longer periods cannot be explained by this 800 m (maximum) surface layer of sediments. The low-velocity feature is also seen down to approximately 130 km by wide-angle reflection and refraction studies (Rawlinson et al., 2001) which barely sample the upper crust. The decrease in average wavespeed that we detect is also consistent with elevated conductivity and heat flow levels that have been observed in the area [Parkinson et al., 1988, www.kuthenergy.com]. The new ambient seismic noise work presented here greatly improves the resolution of velocity variations in the Tasmanian crust. We

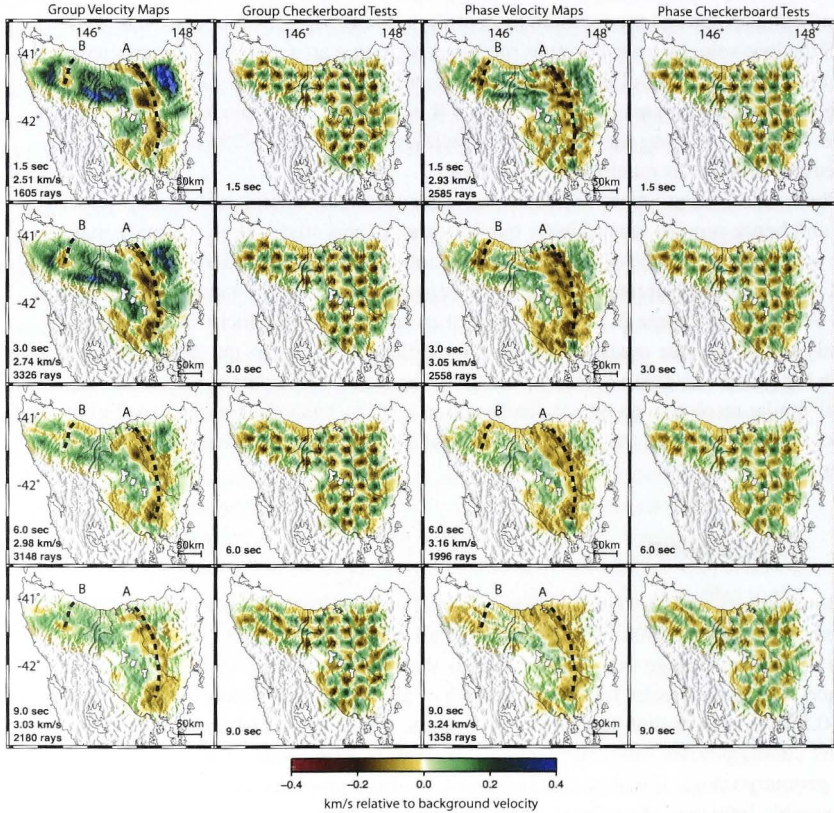


Figure 3.3: Group velocity and phase velocity maps and their corresponding checkerboard resolution tests for periods of 1.5 (top), 3.0, 6.0, and 9.0 (bottom) s. Period, background velocity, and number of ray paths are shown in the lower left corner of each panel. The input of the checkerboard tests is an alternating pattern of positive and negative velocity squares with a maximum perturbation of 0.4 km/sec. Solid black lines labeled "A" = terrane boundary zone anomaly, "B" = Arthur Lineament anomaly.

have better delineated the zones of anomalous seismic velocity and tightened depth constraints.

Although a definite change in crustal properties is present in the vicinity of the Tamar River, the breadth of the low-velocity anomaly seen in the group and phase velocity maps precludes the presence of a lithospheric boundary resulting from the juxtaposition of two separate crustal elements. We prefer the thin-skinned scenario as previously suggested by seismic reflection (Drummond et al., 2003), teleseismic (Rawlinson et al., 2010b), and potential field data (Leaman, 1994). A possible explanation for the unique crustal qualities of the Tamar Valley area is that the confluence of WTT and ETT once represented a passive margin between oceanic crust in the east and Proterozoic continental crust in the west (Reed, 2001).

According to Reed (2001), ETT was deformed and thickened during a pre-Tabberabberan event that correlates with the Benambran deformation of the Australian mainland. In this scenario, the joining of WTT and ETT corresponds to the boundary area between continental and oceanic basement, which is characterized by heavy deformation, shortening, and east-facing recumbent folds and thrusts. This explains the breadth (~50 km) of the low-velocity anomaly seen in our images. Reed (2001) places the paleo-continent ocean boundary west of the Tamar River (corresponding to the left edge of our low-velocity zone) and assumes it continues north beneath the waters of Bass Strait and evolves into the Governor Fault in southeast Australia. Reed (2001) concludes that the boundary between ETT and WTT is equivalent to the separation of the Tabberabbera and Melbourne Zones in Victoria. In this case, we would expect to see a continuation of the low-velocity anomaly through Bass Strait and into Victoria. However, to date, there have been no concurrently running arrays in Tasmania and the adjacent mainland to facilitate ambient noise imaging beneath Bass Strait. In Victoria, recent hot-spot volcanism may have influenced ambient noise group velocity maps (Arroucau et al., 2010), but no analogous low-velocity zone is seen continuing through the mainland. This incongruity may suggest that some components of the Paleozoic tectonic regimes that operated in Victoria and Tasmania are not comparable.

Cayley et al. (2002) and Cayley (2011) argue that the rigid basement block of central Victoria (the Selwyn Block) is the northward extension of the Tasmanian Proterozoic-Early Paleozoic crust, which sits unconformably beneath sedimentary rocks of the Melbourne Zone. They interpret the TFS as being a near-surface feature defined by a change in stratigraphy that terminates or merges with other faults in the eastern part of the Selwyn Block beneath Bass Strait. Heavy deformation and crustal-shortening in the Tamar River Valley area can be attributed to collision with the oceanic crust to the east. In this case, a wide area of deformation would result, which is reflected in our tomographic images (line A in Figure 3.3).

A competing hypothesis is that WTT is a salient of the eastern margin of Gondwana (Direen and Crawford, 2003a,b). The Proterozoic material underlying the Delamerian Orogen of Victoria is proposed to extend down through Bass Strait and into Tasmania.

Western Tasmania shares many geological and petrological-geochemical similarities with western Victoria, such as a late Neoproterozoic-Cambrian continental margin sequence of sediments and rift-related basalts (Direen and Crawford, 2003a). Furthermore, recent teleseismic tomography of mainland southeast Australia (Rawlinson et al., 2011) shows that the Delamerian Orogen extends eastward beneath the surface outcrop of the Lachlan Orogen, thereby increasing the likelihood that WTT is simply a part of Pre-Cambrian Australia. If WTT is assumed to have been a pronounced projection out from east Gondwana, then strong and concentrated deformation would be expected when the exposed margin of WTT collided with oceanic crust during the Middle Cambrian. The resulting intense deformation would be local to WTT, and perhaps this explains the absence of an equivalent low-velocity zone on the mainland.

Another prominent and consistent feature of the models is the low-velocity anomaly beneath the Arthur Lineament, a sheared belt of magnetic metamorphic rocks that separates the Rocky Cape Element from the Dundas Element (Figure 3.1a). Our maps indicate that this transition is heavily deformed and extends at least 8 km beneath the surface. Beyond approximately 9 s period, the anomaly becomes less defined and more dispersed. Refraction and wide-angle reflection studies (Rawlinson et al., 2001) indicate a sharp change in crustal thickness along this margin and conclude that the Arthur Lineament is associated with a deeper structure extending beneath the Moho. The Arthur Lineament was formed during the early stages of the Tyennan Orogeny (Turner et al., 1998), and subsequent deformation during the Tabberabberan Orogeny resulted in further faulting, folding, and granitoid intrusion (Williams, 1989). The zone is highly magnetic, and the lower velocities may reflect the fact that it consists mainly of metasedimentary rocks (Seymour et al., 2007).

3.7 Conclusions

In this study we obtain exceptionally high resolution Rayleigh wave fundamental mode group and phase velocity maps for periods between 1 and 12 s, thereby demonstrating that with dense seismic arrays and close proximity to random oceanic microseisms, high-resolution tomography at high frequencies is possible with ambient noise methods. The resulting tomographic images of the crust across a wide range of periods reveal a ~50 km wide, southeast-trending, low-velocity lineation within the vicinity of the Tamar River. The anomaly arcs southward and dissipates, possibly terminating, near the southern limit of the resolved area. We interpret the low-velocity zone as the mid-upper crustal expression of a broad and heavily deformed transition zone. This deformation can be attributed to the localized shortening, thickening and accretion of oceanic crust along the passive margin of WTT that occurred during the mid-Paleozoic. The wide zone of anomalously low velocities revealed by our maps is consistent with two plate tectonic theories that attempt to explain the lithospheric evolution of the region: (1) WTT can be interpreted to be part of an exotic microcontinent, inherited from

the break-up of Rhodinia, that was embedded into the eastern margin of Gondwana; or (2) WTT is a salient of the eastern margin of Gondwana, and represents the southern extension of the Delamerian Orogen. In either case, it is plausible for the western margin of ETT to be represented by a broad region of strong deformation and faulting (and hence low velocity) due to the accretion of oceanic material against more rigid continental lithosphere.

4.1 Foreword

This new chapter presents an improvement to the algorithms used for the velocity chapter. We now use a fully new linearised iterative approach to the inversion of group and phase velocity maps in Tasmania. We integrate the results of this iterative non-linear technique with the new Bayesian methods of this study and provide a marked improvement over what using a traditional method and its associated uncertainties. We continue this further through the use of synthetic ω_k to test the algorithm through many advantages of the high-speed ω_k and the various ways to extract the information from a pseudo 3D shear velocity model, together with a Bayesian approach, where the results are more performing, more robust, and more accurate. This is a great step forward in the field of inverse problem of a fully non-linear, probabilistic, ω_k and ω_p tomography in the geosphere.

Young, M., Riviere, N., Liu, J., 2024. A new Bayesian approach to the inverse problem of a fully non-linear, probabilistic, ω_k and ω_p tomography in the geosphere. *Journal of Geophysical Research*, *129*, e2023JB022150. doi: 10.1029/2023JB022150.

4.2 Abstract

Modern seismic wave tomography has proved to be a valuable tool for studying the Earth's interior. However, conventional tomography is limited in its ability to provide a quantitative estimate of seismic velocity variations and to account for heterogeneous data coverage. In response to these challenges, we develop a new stage hierarchical, transdimensional, Bayesian method for velocity inversion.

Transdimensional inversion of ambient seismic noise for 3D shear velocity structure of the Tasmanian crust

4.1 Foreword

This next chapter presents an improvement to the inversion method used in the previous chapter. We now use a fully non-linear probabilistic approach to inverting for group and phase velocity maps in Tasmania. We juxtapose the results of an iterative non-linear technique with the new Bayesian results of this study and show the marked improvements seen when using a transdimensional and hierarchical approach. We confirm this further through the use of synthetic tests. In an effort to take maximum advantage of the high-quality ambient seismic noise dataset, we next invert for a pseudo 3D shear velocity model, again using a Bayesian inversion scheme. With regards to performing tomographic inversion, this paper provides multiple lines of evidence in favor of a fully non-linear, probabilistic approach. This work was published in *Geophysics*:

Young, M., Rawlinson, N., and Bodin, T. (2013). Transdimensional inversion of ambient seismic noise for 3D shear velocity structure of the Tasmanian crust. *Geophysics*, 78(3), WB49-WB62, doi: 10.1190/geo2012-0356.1

4.2 Abstract

Ambient seismic noise tomography has proven to be a valuable tool for imaging 3D crustal shear velocity using surface waves; however, conventional two-stage inversion schemes are severely limited in their ability to properly quantify solution uncertainty and account for inhomogeneous data coverage. In response to these challenges, we develop a two-stage hierarchical, transdimensional, Bayesian scheme for inverting sur-

face wave dispersion information for 3D shear velocity structure and apply it to ambient seismic noise data recorded in Tasmania, southeast Australia. The key advantages of our Bayesian approach are that the number and distribution of model parameters are implicitly controlled by the data and that the standard deviation of the data noise is treated as an unknown in the inversion. Furthermore, the use of Bayesian inference - which combines prior model information and observed data to quantify the a posteriori probability distribution - means that model uncertainty information can be correctly propagated from the dispersion curves to the phase velocity maps and finally onwards to the 1D shear models that are combined to form a composite 3D image. We successfully apply the new method to ambient noise dispersion data (1-12 s period) from Tasmania. The results reveal an east-dipping anomalously low shear velocity zone that extends to at least 15 km depth and can be related to the accretion of oceanic crust onto the eastern margin of Proterozoic Tasmania during the mid-Paleozoic.

4.3 Introduction

Various methods for retrieving crustal shear wave velocity structure from passive seismic data have been developed over the past half century. These include receiver function analysis (Langston, 1979; Clitheroe et al., 2001; Xu et al., 2007), surface wave dispersion measurement (Dorman and Ewing, 1962; Villaseñor et al., 2001; Mitra et al., 2011), and local earthquake tomography (Walck and Clayton, 1987; Thurber, 1992; Kissling, 1998; Eberhart-Phillips and Reyners, 1999; Wang et al., 2003; Yolsal-Çevikbilen et al., 2012). Each has its own limitations, with common shortcomings including a lack of near-surface resolution, ad hoc model parameterization, weak uncertainty estimates, dependence on an irregular distribution of earthquake sources, biases from structures outside the model region, earthquake location errors, and bandwidth limitations. The introduction of ambient seismic noise analysis (Shapiro et al., 2005; Lin et al., 2007; Yang et al., 2007; Bensen et al., 2009; Behr et al., 2010) has resolved some of these issues, as earthquakes are no longer a required component. With spatial resolution dictated largely by array geometry and the frequency content of the ambient noise, densely spaced arrays have the potential to image fine scale structures in the crust (Young et al., 2011), albeit at the expense of decreased depth penetration, which shallows as interstation distance decreases. Other issues, such as the choice of model parameterization and noise level estimation, remain regardless of the data set. Uncertainty information obtained from ambient noise analysis is difficult to obtain, and thus error assessment is far from a standardized procedure (Shapiro and Ritzwoller, 2002; Bensen et al., 2009; Yao and Van der Hilst, 2009; Weaver et al., 2011). New methods that allow the data to play a more dominant role in the reconstruction process will be invaluable in tackling these limitations.

The Hierarchical Bayes procedure (Box and Tiao, 1973; Bernardo and Smith, 1994) is a robust technique which is insensitive to variations in parameter settings

such as the allowed number of cells, total number of iterations, or the initial model. Model parameters, including the level of data noise, are represented by a probability distribution function that depends both on known prior information and information provided by the data. Explicit regularization of these model parameters is not required, thereby avoiding arbitrary decisions about the number of model unknowns or the quantification of data error. The hierarchical nature of the method means that the noise in the data is left as an unknown, making the required complexity of the solution inferred from the data itself (Bodin et al., 2012a). Moreover, uncertainty estimates obtained from each stage of our inversion procedure are preserved and utilized in the following step, eliminating the need for the imprecise or ad hoc proxies for error used in more traditional, linear tomographic inversions, such as jack-knife tests, posterior covariance (Rawlinson et al., 2010a), signal to noise ratios (Bensen et al., 2007), etc. Bayesian analysis has been applied to a variety of seismological problems, including tomography (Zollo et al., 2002; Bodin and Sambridge, 2009; Khan et al., 2011; Bodin et al., 2012a), receiver function inversion (Piana Agostinetti and Malinverno, 2010; Bodin et al., 2012b), and seismic source parameter estimation (Myers et al., 2007; Arnold and Townend, 2007; Monelli and Mai, 2008; Walsh et al., 2009).

Conventional approaches to obtaining a 3D shear velocity model from ambient seismic noise data follow a basic procedure similar to our own (Yang et al., 2008a,b; Yao et al., 2008; Stehly et al., 2009; Bensen et al., 2009; Behr et al., 2011). First, group or phase velocity maps are produced from dispersion curves extracted from the crosscorrelation of ambient seismic noise. Generally this is a linearized procedure that seeks to minimize some cost function and involves a subjective application of smoothing and damping, during which valuable information can be lost. We choose to instead use a fully non-linear, Bayesian technique that produces a final model from the average of a large ensemble of models, thus avoiding the need for arbitrary smoothing or damping. The model space is partitioned by non-overlapping, Voronoi polygons of variable number, shape, and velocity, where the uneven spatial distribution of data is managed by relative cell size. Second, the 2D maps are sampled over a range of periods at regular intervals in latitude and longitude to produce a collection of dispersion curves. The spatial variation of uncertainty in the 2D maps is traditionally difficult to determine, and in cases where the dispersion curves are assigned uncertainty estimates, they are often obtained via ad hoc means, such as assessing results from the application of a range of regularization parameters (Bensen et al., 2009) or introducing an arbitrary proportionality constant to relate uncertainty to velocity (Yao et al., 2008).

Our approach provides an inherent estimate of model uncertainty through the assessment of the standard deviation of the ensemble of 2D models at each grid point. Each curve is then inverted for a 1D shear velocity model. Even methods that employ other non-linear inversion techniques, such as non-transdimensional Markov Chain Monte Carlo sampling or the Neighborhood Algorithm (NA) (Sambridge, 1999), are limited in that they use dispersion data without accurate uncertainty estimates (Yang

et al., 2008a; Yao et al., 2008; Stehly et al., 2009; Bensen et al., 2009; Behr et al., 2010). Furthermore, model space is often not fully explored, and there is moderate dependence of the final model on the initial model. On the other hand, a Bayesian inversion allows a more complete sampling of model space and produces results that are independent of the initial, random model. Conventional methods also require arbitrary decisions about model parameterization. The number of crustal layers is generally limited to three, and layer thickness is either fixed or limited in its ability to vary (Yang et al., 2008a,b; Yao et al., 2008; Stehly et al., 2009; Bensen et al., 2009). Moreover, the determination of the final, "preferred" model is often subjective in that a mean curve is produced from a selection of "best" models based on arbitrary acceptance criteria (Yang et al., 2008a,b; Stehly et al., 2009; Bensen et al., 2009). We instead produce expected models from the averaging of the complete ensemble of independent and uniquely parameterized models representing the posterior probability distribution functions of velocity at each depth. Finally, the 1D models are combined to produce a pseudo-3D shear velocity model of the region. The relative superiority of our method lies in the inversion approach and uncertainty analysis.

In this study we show that our Bayesian inversion technique can be successfully applied to ambient seismic noise data to yield a 3D shear velocity model complete with uncertainty estimates. Our target region is the southeast Australian island of Tasmania, where strong ambient noise signals are generated by the surrounding ocean. Due to a number of factors, including widespread cover of Jurassic dolerites and younger sediments, which mask vast tracts of underlying basement, many aspects of Tasmanian tectonics remain contentious. Most notably, there exist a number of theories for the evolution of the Tasmanian lithosphere during the Paleozoic, and its tectonic relationship to mainland Australia remains enigmatic (Reed et al., 2002; Foster et al., 2005; Berry et al., 2008; Gibson et al., 2010; Cayley, 2011). For instance, a first-order feature of Tasmanian geology is that the western part of the island (West Tasmania Terrane or WTT) is dominated by outcrop of Proterozoic origin, whereas the eastern part of the island (East Tasmania Terrane or ETT) has only Phanerozoic outcrop. The so-called Tamar Fracture System (TFS) has traditionally been used to mark the boundary between the two terranes. This stark contrast between geologic regimes was originally attributed to a major crustal fracture system (Williams, 1989), but recent evidence increasingly points to the TFS as being a thin-skinned feature (Leaman, 1994; Rawlinson and Urvoy, 2006; Rawlinson et al., 2010b; Young et al., 2011). However, this is the first time that a high-resolution shear velocity model of the upper crust has been produced, and our results have widespread implications for the tectonic relationship between ETT and WTT.

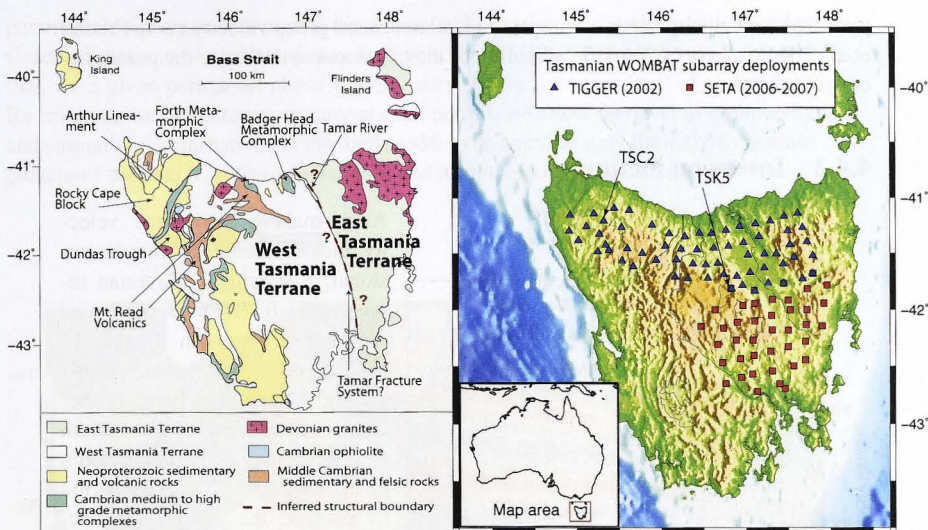


Figure 4.1: (left) Map of basic geological provinces of Tasmania. Major structural features discussed in text are identified. (right) Map of WOMBAT subarrays TIGGER and SETA used in this study.

4.4 Phase velocity maps

4.4.1 Data

The data for this study come from two subarrays of the WOMBAT transportable seismic array project (Rawlinson et al., 2011). The 64 short-period stations (1 s corner period) of the TIGGER array were deployed in March 2002 and span northern Tasmania, while the 40-station SETA array (also 1 s corner period) was installed four years later immediately south of TIGGER on the central east part of the island (Figure 4.1). We use approximately seven months of data from each array to perform ambient seismic noise tomography of the region.

The ambient noise crosscorrelation procedure we employ is similar to that of Bensen et al. (2008). To produce the highest-quality Green's functions, the noise recordings are divided into 40 minute segments with 75% overlap (Seats et al., 2012). Vertical-component data is crosscorrelated and stacked for all simultaneously recording station pairs. Phase velocities are measured (Figure 4.2) using a modified version of the image transformation technique developed by Yao et al. (2006). In order to accurately measure phase velocities up to 1 Hz, we employ a linear-dependence of the band-pass filter width on the central period as introduced by Young et al. (2011). Each

picked phase velocity curve is compared to its associated group velocity curve (Young et al., 2011) to help confirm the reliability of the curve and to minimize the possibility of cycle skipping.

4.4.2 Inversion method

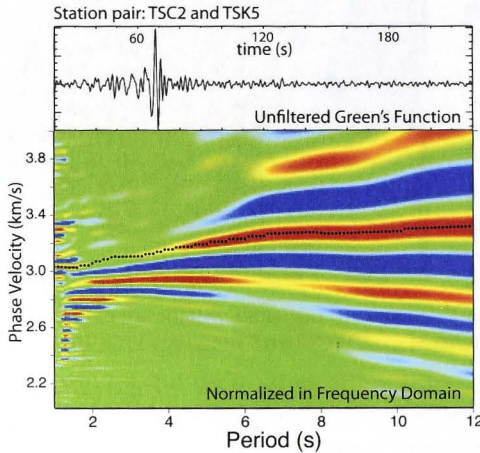


Figure 4.2: (top) The raw, symmetric component crosscorrelation function corresponding to the TIGGER station pair TSC2 and TSK5 (interstation distance of 143 km) (Figure 4.1). (bottom) Corresponding phase velocity dispersion curve that has been normalized in the frequency domain. The dotted black line represents the picked dispersion curve that is dependent on the Earth structure between this pair.

After making the phase velocity measurements, a transdimensional, hierarchical, Bayesian tomographic inversion is performed for periods between 1 and 12 s. A brief description of the method is provided here; further details can be obtained from Bodin and Sambridge (2009) and Bodin et al. (2012a). For each period of interest, the 2D phase velocity field is described by a mosaic of Voronoi cells of variable size, position, and shape (Figure 4.3). The method is “transdimensional” in that the number of cells is allowed to vary throughout the course of the inversion and “hierarchical” in that it has two levels of inference. At the higher level are “hyper-parameters” such as the noise variances of the data. Here data “noise” refers to whatever our model cannot explain (Scales and Snieder, 1998; Bodin et al., 2012a), which can be attributed to measurement errors, shortcomings of the forward model, and mathematical or theoretical approximations.

At the lower level are the physical parameters that represent Earth properties, e.g. seismic velocities. Information on physical parameters at the lower level is conditional on the values of hyper-parameters selected at the upper level. A posterior probability distribution is defined for both hyper-parameters (e.g. data noise variances) and Earth parameters (e.g. Voronoi cell location, Voronoi cell velocity, and total number of cells). One free parameter (hyper-

parameter) is assigned to model the noise in the travel time measurements of the Green's functions when filtered at central periods of 1-12 s. We make the assumption that, for a given period, all phase velocity curves have the same level of uncertainty. By inverting for the data uncertainty at each period, we allow the level of complexity and strength of perturbations in the final model to be appropriately limited by the noise content of the data (e.g. Piana Agostinetti and Malinverno (2010)).

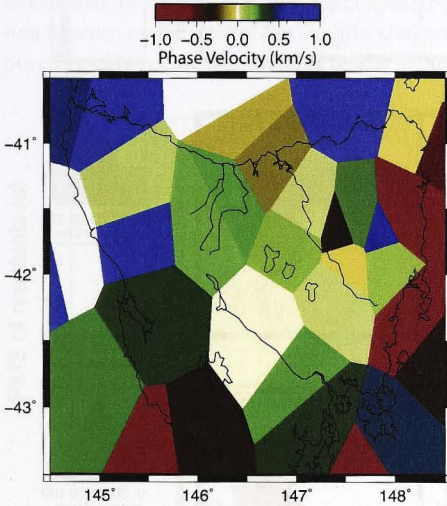


Figure 4.3: Example of a Voronoi cell model, which consists of an irregular, interlocking set of polygons that partition the plane. Each Voronoi cell encompasses all points of the 2D space that are closer to its center than to any other Voronoi cell center.

uniform prior distribution between a minimum and maximum value. This prior phase velocity distribution is 2.4 km/s wide and is centered on the average velocity observed for that period. These bounds are wide enough such that the final recovered model is not hampered by the upper and lower limits. We solve the forward problem with a grid-based eikonal solver (Rawlinson and Sambridge, 2004b).

To generate the posterior probability distribution for each model parameter we use a generalized version of Markov chain Monte Carlo (MCMC) sampling called Reversible Jump MCMC (rj-MCMC) (Green, 1995, 2003). rj-MCMC is an iterative method of sampling the allowed parameter space. The initial model is randomly gen-

We can extract meaningful quantities from the posterior probability distributions such as the mean, median, or maximum. Based on Bayes' theorem (Bayes, 1763), we express the posterior distribution as in Equation A.1 :

$$p(\mathbf{m} \mid \mathbf{d}_{obs}) \propto p(\mathbf{d}_{obs} \mid \mathbf{m})p(\mathbf{m}) \quad (4.1)$$

where $p(\mathbf{m} \mid \mathbf{d}_{obs})$ is the probability distribution function of the unknown model parameter \mathbf{m} given the data, \mathbf{d} . The factor $p(\mathbf{d}_{obs} \mid \mathbf{m})$ is the likelihood function, which yields the probability of observing data d given model m . The likelihood function $p(\mathbf{d}_{obs} \mid \mathbf{m})$ depends on the misfit between the observed data and the synthetic traveltimes computed for a given model and also on the estimated variance of the data noise. Our prior information about model \mathbf{m} is represented by the a priori probability distribution $p(\mathbf{m})$. In this study we use a

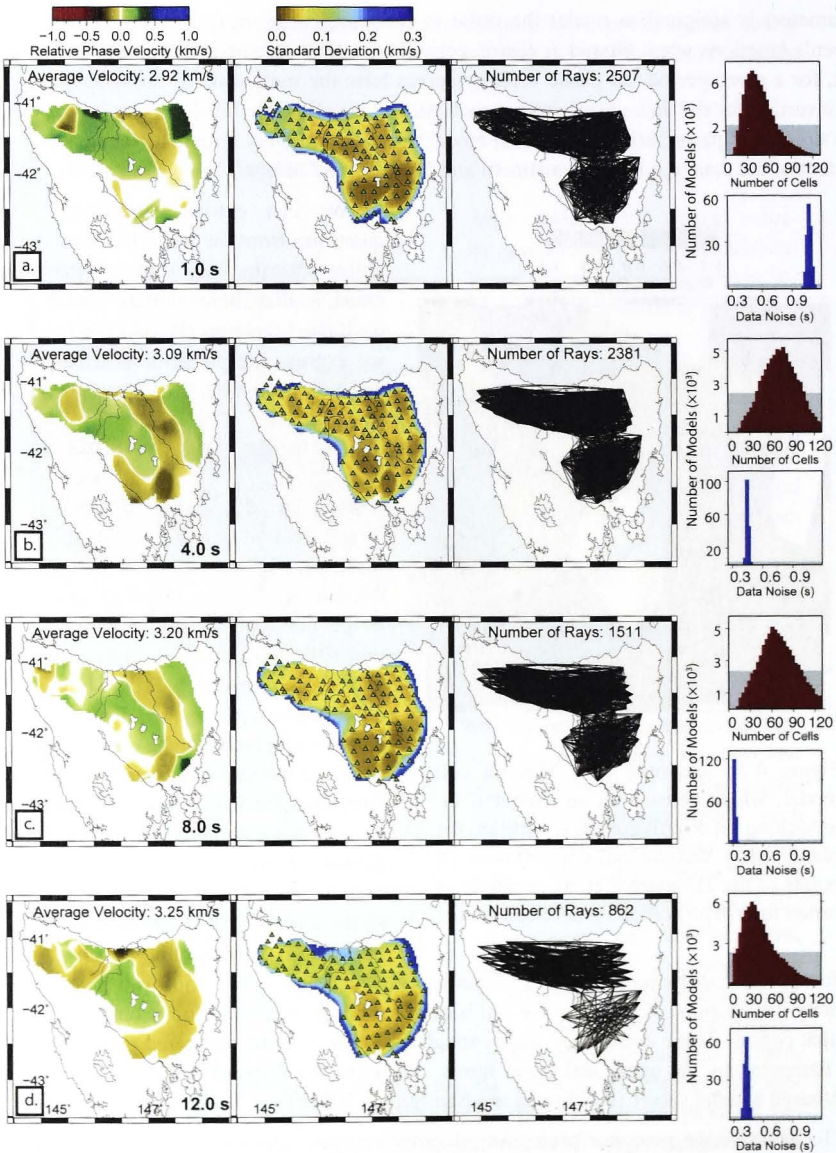


Figure 4.4: Phase velocity maps for periods of (a.) 1.0, (b.) 4.0, (c.) 8.0, and (d.) 12.0 s (left) with corresponding standard deviation and ray path coverage plots. Phase velocities are relative to the “Average Velocity” given at the top of each map. Phase velocity and standard deviation maps are trimmed according to the contour line when standard deviation is equal to 0.3 km/s. Posterior probability distribution histograms for the number of cells (red columns) and data noise (blue columns) are also shown (right). The prior distributions are indicated by shaded gray rectangles.

erated, and subsequent iterations in the random sequence are based on a proposal probability distribution (refer to Bodin et al. (2012b) for a more complete description). After a large number of “burn-in” iterations, the *rj*-MCMC sampler converges to a stable configuration according to the posterior distribution (Green, 1995, 2003). At each iteration, a proposed model is created from a random perturbation of the current model. This proposal is then either accepted or rejected. Proposed models that fit the data better than the original model are always accepted. Proposed models that fit the data worse than the original can also be accepted, but only a fraction of the time. This fraction depends on the ratio of the likelihood of producing the observed data with the proposed model over the likelihood of producing the observed data with the current model.

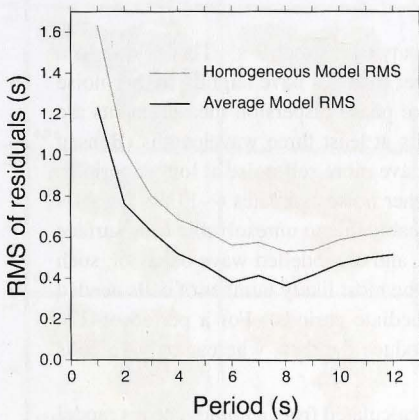


Figure 4.5: Graph of the rms (root mean square) of the residuals versus period for the transdimensional inversion for phase velocity. The Homogeneous Model RMS values are calculated from a homogeneous model with a velocity equal to the average velocity at that period. The Average Model RMS values are calculated from the final average model of the Bayesian tomographic inversion.

The first portion of burn-in iterations is omitted from the final ensemble of models, as the sampling has not yet become stable nor representative of the true posterior probability distribution. We take the average of this ensemble of models to produce our final, preferred model. Since the Voronoi cells can occupy an infinite range of configurations, taking the average of a large number (on the order of 10^5 models for 160 independently run Markov chains) of post-burn-in models creates a continuous final model. This average model contains more detail than any one individual model but none of the artificial discontinuities inherent to the base parametrization. There is no need to apply smoothing or damping procedures, for the perceived model complexity and smoothness is innate to the averaged solution. Although it may seem like an overly complex model would result in order to maximize

data variance reduction, the parsimonious nature of the Bayesian approach promotes the preservation of the simplest models that fit the data, thus preventing unjustified model complexity (Bodin et al., 2012a).

4.4.3 Results

Thanks to the close spacing of the TIGGER and SETA arrays (with interstation distances of approximately 15 km), we have produced phase velocity maps for periods between 1 and 12 s (Figure 4.4). Model parameter convergence is achieved for all periods after 50,000 iterations. Every 50th model of the subsequent 120,000 iterations is used to create the final average model. Simultaneous yet independent sampling of model space was facilitated through the parallel use of 160 CPU cores for 4 hours (640 CPU hours). The standard deviation of the phase velocity at each grid node is extracted from the ensemble of phase velocity maps and provides a good estimate of the spatial variation in uncertainty for each map (Figure 4.4). This information is later used in the inversion for shear velocity.

Model complexity is greatest for periods between 3 and 9 s. This is due to a combination of factors. Maps for periods longer than 9 s have slightly higher noise estimates and increasingly fewer raypaths, since phase dispersion measurements are only performed when the interstation spacing is at least three wavelengths (Bensen et al., 2008), and the short period stations will have more self noise at longer periods. Maps for periods shorter than 3 s also have higher noise estimates (~ 1.05 s for a 1 s period vs. ~ 0.31 s for a 8 s period). This is probably due to unresolvable near-surface effects, like topography and shallow sediments, and unmodelled wave behavior, such as scattering and multi-pathing. Consequently, the most likely number of cells needed to represent the data is greatest for the intermediate periods. For a period of 7 s, approximately 90 cells are needed to best reproduce the data, whereas only 25 cells are needed for the 12 s period data.

The rms (root mean square) of the residuals calculated from a homogeneous model of phase velocity equal to the average phase velocity at a given period are plotted along with the rms values resulting from the final average model (Figure 4.4, left) in Figure 4.5. The estimated noise in the data prevents further reduction of the rms values. Unlike traditional linear inversions which seek to produce a single model that minimizes the variance of the data, the Bayesian method produces an ensemble of solutions whose complexity is reflected by the interpreted noise in the data. The data uncertainty determines how accurately the measurements should be fit. Consequently, one should not view Figure 4.5 in quite the same way as would be done for a linearized inversion, as data noise and unmodelled effects are also accounted for. Furthermore, the average model is only one measure of the ensemble of solutions, and it would be possible to select individual models that have smaller rms residuals (e.g. Shapiro et al. (2004); Moschetti et al. (2010); Behr et al. (2010)).

Synthetic resolution tests are performed in order to analyze the resolving power of the data (Figure 4.6a). Noise with a standard deviation equal to the peak of the corresponding posterior probability distribution of noise for the actual data set is added to the synthetics. The standard deviation of the noise added to the 1 s, 4 s, 8 s, and

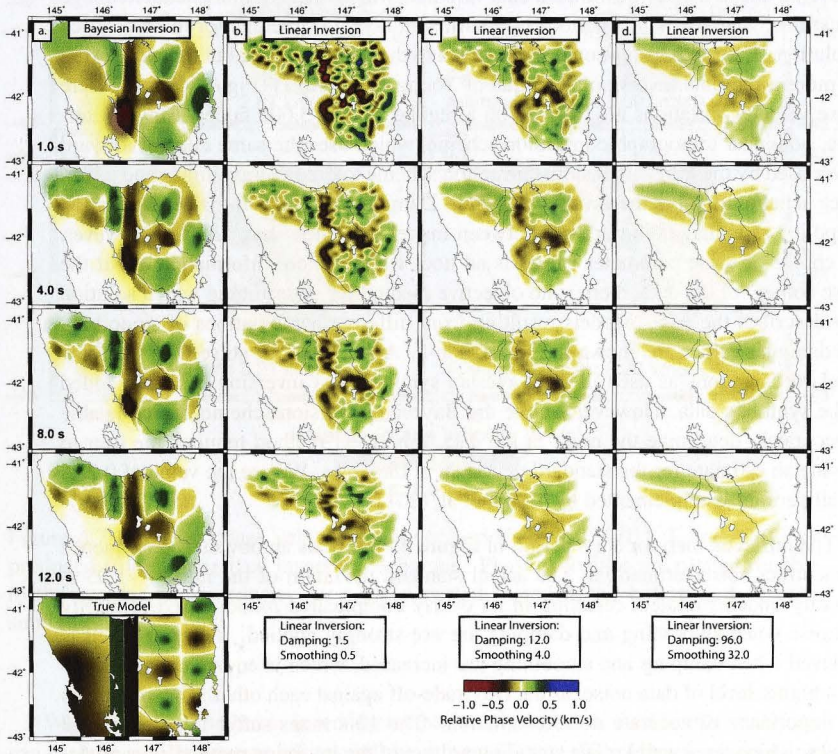


Figure 4.6: Results of the synthetic resolution test for both the Bayesian inversion method (a) and the linearized inversion (b-d). Linear inversion results of applying smoothing and damping parameters of (b) 1.5 and 0.5, (c) 12.0 and 4.0, and (d) 96.0 and 32.0 are shown. The standard deviations of the noise added to all 1 s, 4 s, 8 s, and 12 s data sets are 1.05 s, 0.44 s, 0.31 s, and 0.43 s respectively. The maximum velocity perturbation of the rectangles is ± 0.3 km/s.

12 s data sets is 1.05 s, 0.44 s, 0.31 s, and 0.43 s respectively. The true model has been designed to demonstrate the capability of the method to retrieve velocity discontinuities, smooth velocity transitions, and structures of varying scales. The maximum perturbation of the alternating rectangles is ± 0.3 km/s. The original pattern is best retrieved for periods between 2 and 10 s. For a 1 s period, the pattern is less precisely recovered due to the large estimated data variance, which makes a more detailed image unjustified. Maps of >10 s periods lack sufficient raypath coverage for more detailed resolution. The same resolution test is applied to the data set again, but this time using the more traditional inversion technique of Young et al. (2011) (Figure 4.6b-d). Here phase velocity variations are mapped on a regular grid of 3,600 nodes using an iterative, nonlinear tomographic inversion scheme, which uses the same eikonal forward solver used by the transdimensional inversion scheme to predict traveltimes and a subspace scheme to solve the inverse problem. Damping and smoothing regularization is applied to manage the trade-off between model roughness and data fit. However, the choice of these parameter values is ad hoc; without more information about the noise content of the data, there is no objective method for determining which solution best describes the data. Models resulting from different combinations of smoothing and damping values are shown in Figure 4.6b-d. Again, random noise with the same standard deviations as used in the Bayesian synthetic test inversion has been added to the synthetic data. However, unlike the Bayesian inversion scheme, which is able to accurately determine the noise in the data, this linear method requires the user to provide an estimate for the standard deviation of the noise. We use the value of 0.25 s for all periods as implemented by Young et al. (2011).

The retrieved map for a 1 s period in Figure 4.6b reveals an obvious consequence of incorrect noise estimation. The actual standard deviation of the noise (~ 1.05 s) is vastly underestimated, resulting in an overly complicated model based primarily on noise when smoothing and damping are not strongly applied. A better result is achieved when damping and smoothing are increased, which is equivalent to assuming a higher level of data noise, as the two trade-off against each other. This illustrates the importance of accurate noise estimation. The 12 s maps suffer from elongated streaks, which are a well known smearing artifact of the inversion method's heavy dependence on raypath configuration; this effect is absent from the Bayesian inversion results. Another advantage of the Bayesian inversion method is that it is much more accurately able to recover the strong velocity discontinuity between the two north-south bars of contrasting velocities. This sharp transition can coexist along with smooth variations because the averaging process over a large number of Voronoi models results in a natural smoothing which is spatially variable and determined by the data, whereas the smoothing imposed in a standard tomographic approach is generally global. This method also provides a more reliable estimate of absolute velocities, whereas in the linear inversion results, absolute velocity is heavily dependent on smoothing and damping.

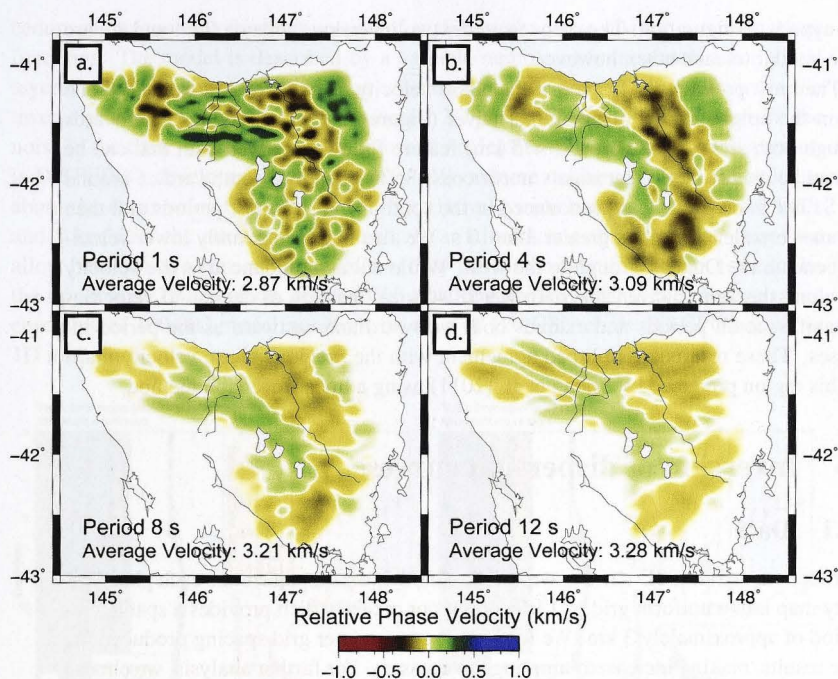


Figure 4.7: Average phase velocity maps for periods of 1.0, 4.0, 8.0, and 12.0 s as produced from a linearized inversion technique. Phase velocities are plotted relative to the average phase velocity for a given period (noted in the bottom left of each subfigure).

When applying the linear inversion method to the real data used in this study, we can assume similar adverse effects will be present (Figure 4.7). Here the smoothing and damping regularization parameters match those of Young et al. (2011) and are uniformly applied to the data, regardless of raypath coverage or relative data uncertainty. Here, while artifacts due to noise may be subdued, actual details in the model may be indiscriminately lost as well. The heterogeneity seen in the map of the 1 s period data (Figure 4.7a) is of much shorter wavelength than that of the corresponding Bayesian inversion result. In the latter case, we know that the noise level of the data cannot support much detail. As in the checkerboard test, the 12 s map (Figure 4.7d) from the linear inversion exhibits elongated, streaky anomalies. For the Bayesian inversion (Figure 4.4), the result of poorer raypath coverage is decreased detail rather than poorly constrained, elongated anomalies, which are almost certainly an artifact of

the raypath configuration. The maps from the two inversion methods for 4 and 8 s are more similar to each other, however.

The most pronounced feature of the phase velocity maps is the low-velocity zone within the neighborhood of the Tamar River (Figure 4.1) that continues southwards through both arrays. This broad (~ 75 km) feature follows a curved path that can be tracked southeast from Tasmania's north coast before bending southward at around 42° S. The anomaly is less pronounced in the south for the shortest periods and then becomes broader at periods greater than 10 s. We also find significantly lower velocities beneath the Dundas Trough to the west. While not as pronounced as the velocity low along the Tamar River, this narrower (~ 40 km) lineation of decreased velocities is manifest at all periods and extends both westward and eastward as the period increases. These results are in broad agreement with the previous phase velocity maps for this region produced by Young et al. (2011) using a linear inversion method.

4.5 Inversion of dispersion curves

4.5.1 Data

In order to constrain a 3D shear wave velocity model, we first discretize each phase velocity map into a uniform grid of 13,685 nodes or pixels, which provides a spatial resolution of approximately 3 km. We found that using a finer grid spacing produced the same results, making increased sampling unnecessary. For further analysis, we choose to only use the 2,952 data points located within the confines of the seismic array. We sample the phase velocity maps at each node of interest and create a corresponding set of phase velocity curves. The curves are already complete with uncertainty information, as we can extract the standard deviation of the posterior probability distribution of the velocity at each pixel of the phase velocity maps. This is a significant step forward, as previous inversion schemes employ improvised methods of estimating the spatial distribution of uncertainty of the phase velocity maps prior to the inversion for shear velocity, e.g. Shapiro and Ritzwoller (2002); Bensen et al. (2009). Pixels for which the velocity varies widely throughout the post-burn-in iterations will have a large standard deviation, and thus a larger uncertainty. An explanation of the inversion of the phase velocity curves for 1D shear velocity models, the merging of the resulting shear velocity models, and the creation of a pseudo-3D representation of the shear velocity structure of Tasmania is provided in the following sections.

4.5.2 Inversion method

Each phase velocity curve is inverted for a 1D shear velocity model using the same hierarchical, transdimensional Bayesian technique as before. Bodin et al. (2012b) provides a more detailed description of the surface wave dispersion curve inversion pro-

cedure in the context of joint inversion of surface wave group dispersion and receiver functions. The model is described by a variable number of homogeneous horizontal layers, and the number, position, and velocity of the layers are all unknowns in the inverse problem. Similar to the inversion for 2D phase velocity, we also invert for the noise in the data. The forward method used to calculate the phase velocity dispersion is DISPERSO, developed by Saito (1988). We assume unobtrusive prior knowledge about the shear velocity model by setting relatively wide bounds of between 2 km/s and 5 km/s for the allowed shear velocity variation during the inversion. Also, we allow between two (the minimum allowed by the method) and 30 layers to describe the uppermost 15 km of the crust. Each resulting shear model is the average of an ensemble of 100,000 model iterations on each of 120 CPU cores (30 CPU hours per 1D inversion).

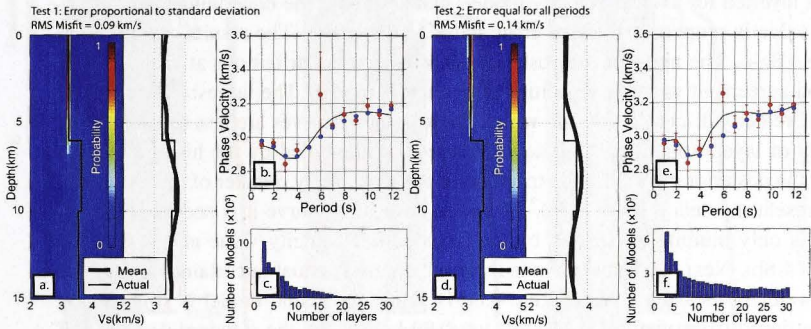


Figure 4.8: Ensemble solutions for crustal shear velocity from two synthetic tests. Test 1 (a-c) treats the noise in the phase velocity measurements as being proportional to the input standard deviations. Test 2 (d-f) treats the noise as being equal for all periods. To the right of each color density plot is the mean of the velocity distribution at each depth. Also shown are the phase velocity curves associated with the best-fitting shear velocity model (black lines) overlaid on the actual phase velocity values of the curve (red dots) (b, e). Standard deviations are shown by red bars, and the original phase curve prior to the addition of random noise is shown by blue dots. (c, f) Histograms representing the accompanying posterior probability distribution functions for the number of layers in the models.

The data noise parameter retrieved from the inversion is represented by λ . Here the uncertainty of each phase velocity value is assumed to be proportional to the standard deviation associated with that value, with the constant of proportionality λ serving as an unknown in the problem. The standard deviation at a particular period for a particular curve is extracted from the posterior velocity distributions resulting from the previous phase velocity inversion step. The noise of each measurement determines

its relative weight in the inversion such that very noisy data (having large standard deviations) do not disproportionately influence the final solution.

4.5.3 Results

We perform a synthetic test to illustrate the benefits of utilizing the standard deviations from the phase velocity maps. An alternative would be to assume all phase velocity values, regardless of period, have the same uncertainty for a given curve. In our synthetic test we assume a known, simple three-layer model of the upper 15 km of crust. We calculate the corresponding phase velocity curve and randomly add noise of up to ± 0.05 km/s to all but one value (associated with the 6 s period). To this remaining value, we add a 0.25 km/s error to mimic the presence of an outlier. The curve is then inverted for a shear velocity model, first assuming the uncertainty of each velocity value is proportional to the error added to the curve. The results are shown in Figure 4.8a-c. The mean of the posterior shear velocity distributions at each depth is in good agreement with the velocities of the actual model. The largest discrepancies arise at velocity discontinuities, to which phase velocity curves are less sensitive. The number of layers (three) is accurately retrieved, as illustrated by the histograms that reflect the posterior probability distribution of the most likely number of layers needed to represent the data (Figure 4.8c). From the best fitting curve it is seen that the solution is only minimally effected by the large outlier velocity value at a 6 s period (Figure 4.8b). Next, the same curve is inverted assuming equal uncertainty among the phase velocity measurements (Figure 4.8d-f). Here the actual model is slightly less well-retrieved (rms misfit of 0.14 km/s vs. 0.09 km/s), and the standard deviation of the posterior shear velocity distributions at each depth is larger (0.58 km/s vs. 0.50 km/s) (Figure 4.8a). Again, the number of layers is accurately recovered, however, this time with slightly less certainty. The best fitting curve is significantly more distorted due to the erroneous phase velocity value at 6 s. The inversion is not able to identify this value as being less reliable than the others.

To demonstrate the advantages of using a Bayesian technique over more traditional methods, we use the same test model to perform a synthetic inversion using the non-Bayesian Neighborhood Algorithm (NA) of Wathelet (2008). This method requires the user to predetermine, in part, the model parameterization. The number of layers is set to three based on results of the Bayesian inversion. Each horizontal layer is described by a constant velocity. The thickness, position, and velocity of each layer is allowed to vary throughout the inversion. Each phase velocity measurement is given equal weight, unlike the Bayesian method which assigns weights based on the relative noise of each measurement. The same depth (0-15 km) and velocity (2-5 km/s) limits apply. A comparison between the two solutions (Figure 4.9a, b) shows that the NA is less capable of retrieving the true model. Most obviously, the mean of the velocity distribution fails to recover the high-velocity zone between 6 and 10 km depth.

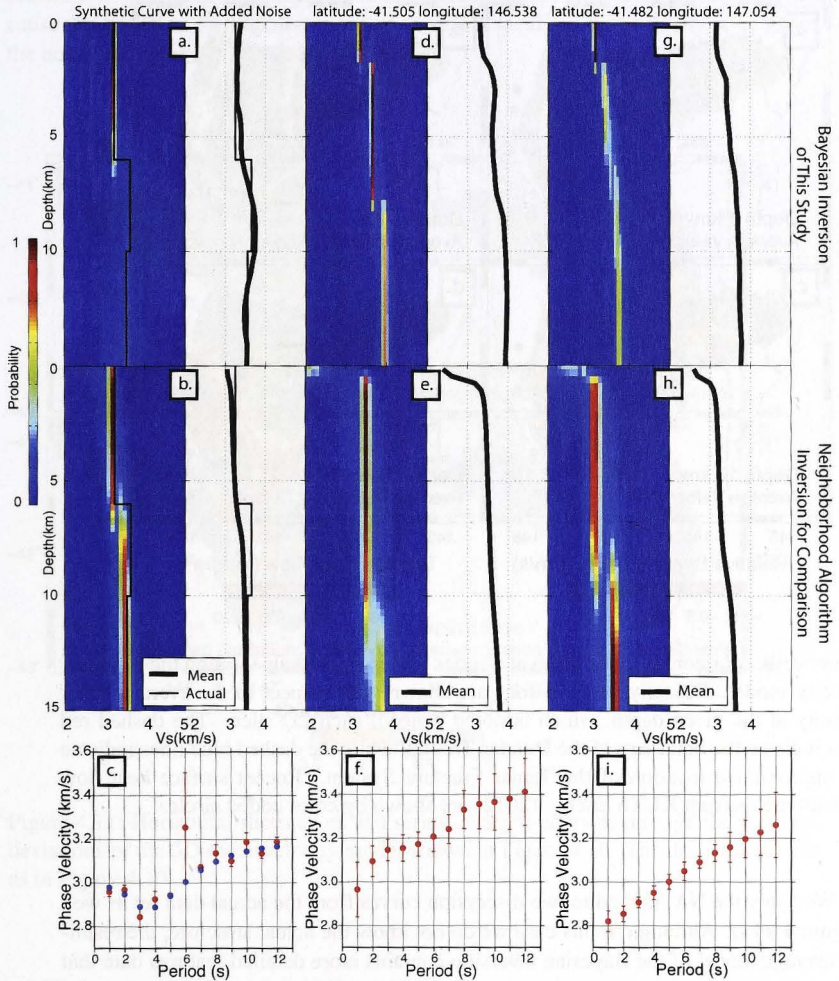


Figure 4.9: Ensemble solutions for crustal shear velocity from the Bayesian methods of this study and the Neighborhood Algorithm for a synthetic case (a, b) and two real data examples (d, e, g, h). To the right of each color density plot is the mean of the velocity distribution at each depth. At bottom are the corresponding phase velocity curves (red dots) and for the synthetic case, the actual curve (blue dots). The amount of noise added to the curves is shown by red error bars.

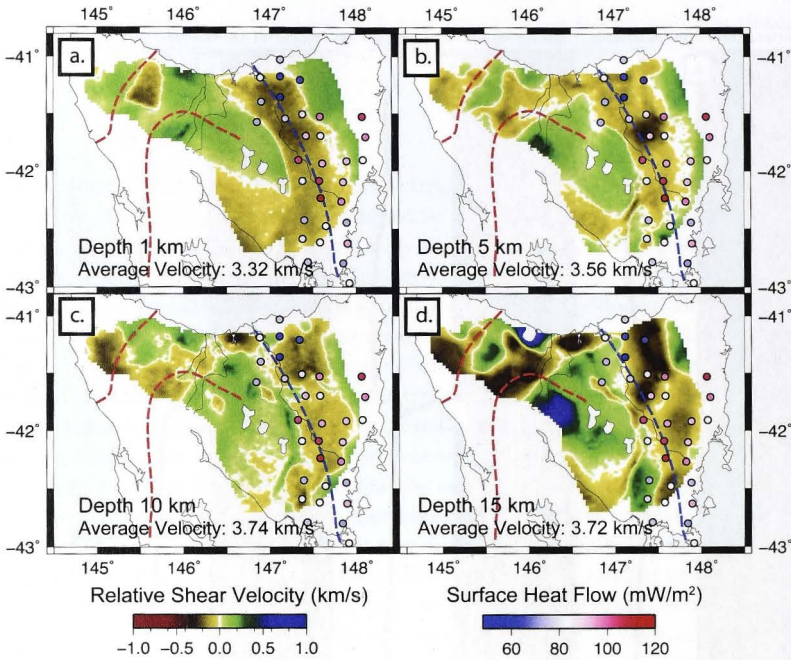


Figure 4.10: Horizontal slices taken at a series of depth intervals through the 3D shear velocity model. Velocity perturbations are shown with respect to the average shear velocity at the given depth, which is noted beneath each 2D slice. The dashed red lines indicate the boundary of the Dundas Trough, while the dashed blue lines indicate the approximate location of the Tamar Fracture System. Recent surface heat flow measurements from KUTh Energy (2012) are shown by color coded circles.

We apply the NA method to two dispersion curves from the actual data set as well (Figure 4.9d-i). Although in this case we do not know the actual structure, the resulting average model of the Bayesian inversion contains more detailed features than that of the NA method (Figure 4.9d, g). This is due to the permitted variation in layer number throughout the inversion. Although there are far fewer models with significantly greater than the average number of layers contributing to the final ensemble, these iterations add valuable information about model complexity. The standard deviations of the mean model are also much smaller for the Bayesian inversion, meaning that the most likely model is retrieved with greater certainty. Of notable difference between the Bayesian and NA results for the two real data applications is that the NA method retrieves a very thin low-velocity layer in the uppermost crust (Figure 4.9e, h). This

feature is not present in the Bayesian inversion results. The reason for this is likely because the Bayesian method does not permit such a localized low-velocity zone given the noise and number of data.

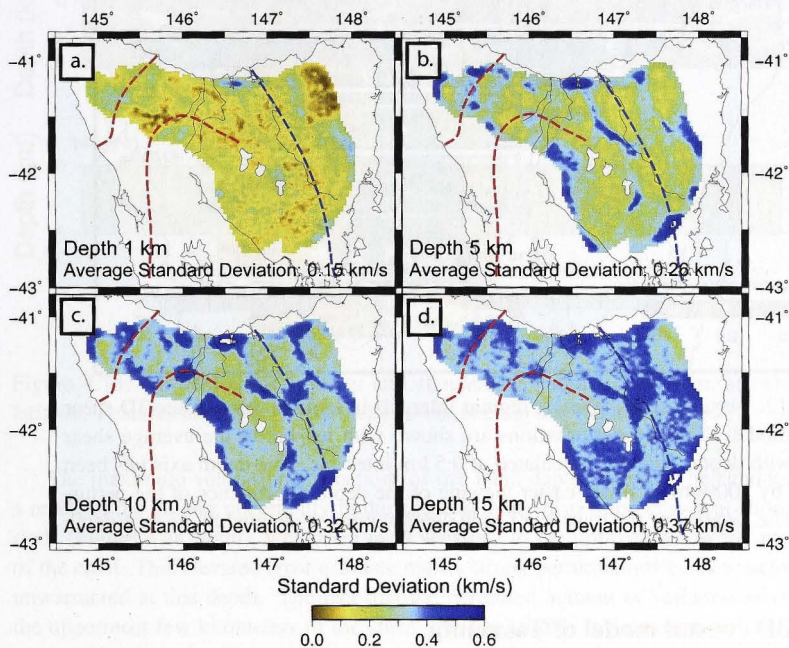


Figure 4.11: Horizontal slices taken at a series of depth intervals through the standard deviations of the 3D shear velocity model shown in Figure 4.10. The dashed lines are as in Figure 4.10.

We have shown that the Bayesian method of surface wave inversion is best at recovering 1D shear velocity profiles from surface wave dispersion data. Since surface wave dispersion is not very sensitive to sharp discontinuities in elastic properties with depth, the degree of vertical smoothing depends on the noise and number of the input data; data of greater number and certainty enable finer vertical resolution of velocity structure. Most of the resulting shear velocity models derived from the Tasmanian data set are relatively simple and are best described by three to six layers (e.g. Figure 4.9d, g).

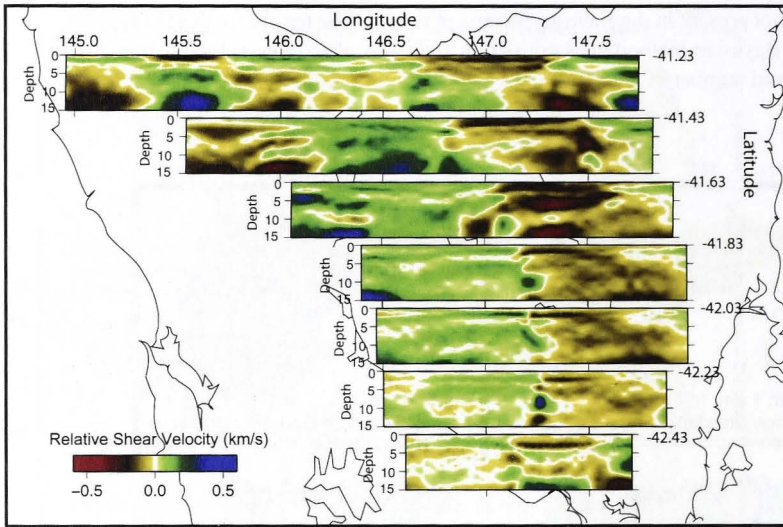


Figure 4.12: Vertical slices taken at regular intervals in latitude through the 3D shear velocity model. Velocity perturbations are shown with respect to the average shear velocity with depth, which is calculated at 0.5 km intervals. The depth axis has been stretched by 100% to facilitate easier viewing of the depth dependence of the perturbations. The location of the transect of each depth section is denoted by its zero depth line.

4.5.4 3D crustal model of Tasmania

At this point in the inversion procedure, we have a discrete, regular sampling of 3D shear velocity space for the uppermost 15 km of the Tasmanian crust. Each point is represented by a shear velocity posterior probability distribution curve rather than a single velocity value. To visualize the results, the average of the posterior probability distribution at a given depth is extracted from each of the 1D shear velocity models. The velocity values are then plotted according to their respective geographic location. In this sense, each shear velocity value extracted from a 1D model represents a single pixel in the image. For purely aesthetic reasons, the resulting grid of velocity pixels is then transformed into a continuous curvature surface using the Generic Mapping Tools (GMT) package of Wessel and Smith (1995) (Figure 4.10) to smooth out the pixelation (3 km resolution) of the image. The same procedure can be applied to 2D slices in longitude and latitude as well. The spatial variation of uncertainty can be assessed by viewing a similar surface of standard deviations. For each pixel, the standard deviation of the shear velocity can be extracted from the representative ensemble of shear models

for a given depth (Figure 4.11).

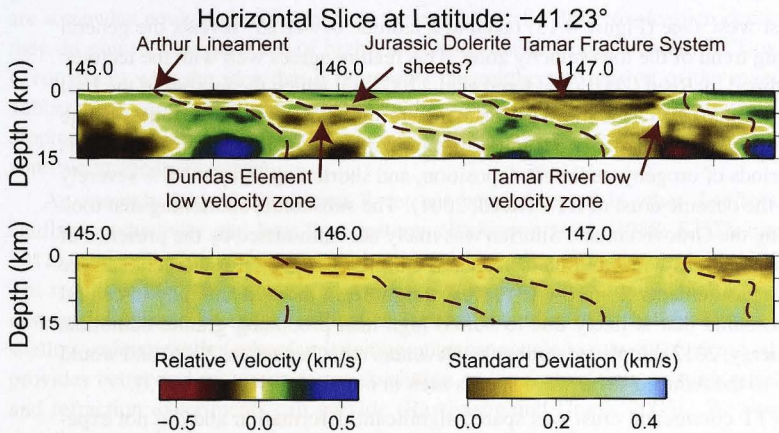


Figure 4.13: Vertical shear velocity and standard deviation slices taken at -41.23° latitude. Features and velocity anomalies mentioned in text are highlighted.

The maximum velocity perturbations of the 1 km depth slice may be subdued as a result of the greater uncertainty in the phase velocity dispersion curves at short periods (Figure 4.4a, right), which are most sensitive to the uppermost few kilometers of the crust. This elevated error estimate makes strong perturbations in shear velocity unwarranted at this depth. The fact that the permitted amount of variation amongst the uppermost few kilometers of the shear velocity models is decreased may also be a contributing factor to the relatively low average standard deviation value for the 1 km depth slice (Figure 4.11a). The average standard deviation increases with depth likely in response to the decreasing sensitivity of phase velocity to shear velocity as depth increases. At shallow depths, a small change in shear velocity produces a large change in phase velocity, yielding greater certainty in the inversion. On the other hand, decreased sensitivity is manifested by increased uncertainty estimates. For a period of 12 s, phase velocity sensitivity to shear velocity starts to drop off sharply at around 15 km depth, depending on the Earth model (Yang et al., 2010). For this reason we choose 15 km as the depth limit of our 3D shear velocity model.

Horizontal and vertical slices (Figures 4.10, 4.12) reveal that as in the phase velocity maps, there is a definite and consistent north-south orientated low-velocity zone. Although the low velocities at the shallowest depths in the northern half of the anomaly are in part due to a patch of sediments in the Longford Basin of north Tasmania (Direen and Leaman, 1997), there appears to be a strong change in crustal properties extending to at least 15 km depth, the limit of our 3D velocity model. The anomaly broadens

to the east while the southern extreme becomes less pronounced and more patchy as depth increases.

An east-west slice (Figure 4.13) taken at a latitude of -41.23° reveals the general east-dipping trend of the low-velocity zone. This feature agrees well with the tectonic model outlined by Reed (2001) and Reed et al. (2002), in which the joining of the East Tasmania Terrane (ETT) and the West Tasmania Terrane (WTT) represents the change from east to west of Paleozoic oceanic to Proterozoic continental basement. In this model, periods of orogeny, sediment deposition, and shortening of up to 90% severely deformed the oceanic crust of ETT (Reed, 2001). The substantial shortening that took place during the Ordovician and Silurian was likely accommodated by the presence of multiple shear zones with fluid inclusions and elevated temperatures. Recent surface heat flow measurements (Figure 4.13) reveal a significant thermal anomaly in central eastern Tasmania that is likely due to buried high-heat-producing granite batholiths (KUTh Energy, 2012) emplaced during the Devonian (McClenaghan, 2006) and would contribute to the reduced shear wave speeds seen in our model (Karato, 1993).

The WTT continental crust was spared significant deformation and did not experience the same shortening event. Reed (2001) places the ETT and WTT boundary between the Tamar River and the Port Sorell embayment to the west. This location agrees well with the western edge of the low-velocity zone along the Tamar River. Moreover, the breadth of the anomaly indicates a zone of deformation much wider than the relatively narrow Tamar Fracture System (TFS) that has been hypothesized to represent the joining of two distinct crustal blocks (Williams, 1989). Our results provide one more piece of evidence that the TFS, which straddles the Tamar River Valley, is merely a thin-skinned feature resulting from a final bout of folding during the Devonian and that ETT and WTT have been passively joined since the Ordovician.

A solid tectonic link between Tasmania and mainland Australia has remained elusive until quite recently, when Dieren and Crawford (2003a) found paired suites of olivine-rich mafic volcanics and boninites in both western Tasmania and the mainland. This discovery added further momentum to the idea that the early Paleozoic Tyennan Orogeny, which shaped western Tasmania, is part of a much larger orogenic cycle that manifested as the Delamerian Orogeny in mainland southeast Australia and the Ross Orogeny in Northern Victoria Land, Antarctica. A connection between eastern Tasmania and the mainland has also been postulated (Talent and Banks, 1967; Powell and Baillie, 1992), with several authors (Foster and Gray, 2000; Reed, 2001; Cayley et al., 2002; Fergusson, 2003) pointing out that the Tabberabbera Zone east of Melbourne experienced Ordovician to Silurian orogenesis and appears to overlie oceanic basement. Reed (2001) has therefore suggested that the boundary between WTT and ETT is a southerly continuation of the boundary between the Melbourne Zone and Tabberabbera Zone represented on the mainland by the Governor Fault. In this scenario, Cayley et al. (2002) and Cayley (2011) see the basement underlying the Melbourne Zone sediments as a northward continuation of Proterozoic western Tasmania, and invoke the

idea of an exotic microcontinent to explain the presence of much older rocks in a region of Victoria characterized by early-mid Paleozoic exposure. Although our results are somewhat equivocal with regard to the existence of a Proterozoic microcontinent, they do point to the presence of highly deformed oceanic crust beneath ETT, which is consistent with the idea that it represents the southern extension of the mainland Tabberabbera Zone. Furthermore, the Governor fault in Victoria is approximately east dipping (Cayley et al., 2002) which agrees with the dip direction of the low-velocity zone we image in Tasmania.

An anomaly beneath the Tamar River has been observed in other data sets, including conductivity and heat flow patterns (Parkinson et al., 1988; KUTh Energy, 2012), and reflection, refraction, and teleseismic studies (Rawlinson et al., 2010b). The results of this study provide conclusive evidence that the anomaly is deep-seated, eastward dipping, and not an artifact of vertical smearing of a shallow feature (e.g. shallow sediments) that teleseismic tomography cannot alone rule out. Our model also provides better and more consistent resolution of the feature than existing reflection and refraction experiments can provide (Rawlinson and Urvoy, 2006). We propose that the low-velocity zone is the result of pronounced deformation associated with the shortening, thickening, and accretion of oceanic crust along the passive margin of Tasmania during the early-mid Paleozoic, coupled with intrusion of heat producing granites in the Devonian. In this case, we would expect the seismic velocity signature to be wide and deep as seen in our 3D model.

Another prominent element of the shear velocity model is the low-velocity anomaly beneath the northwest corner of Tasmania (Figure 4.13). The western edge closely follows the Arthur Lineament, a sheared belt of magnetic metamorphic rocks that separates the Rocky Cape Block from the Dundas Trough (Seymour et al., 2007). This anomaly dips to the east (Figure 4.13) and supports the interpretation that Tasmania was initially drawn into an east-dipping subduction zone in the Middle Cambrian before being obducted westward into an arc-continent collision (Crawford et al., 2003; Gibson et al., 2010; Cayley, 2011).

The strength and eastward trend with depth of the anomaly could therefore be interpreted as the vestige of the initial eastward-dipping phase of subduction during the mid-Cambrian Tyennan Orogeny. The low-velocity zone in our model beneath the Dundas Trough is consistent with a transition that is heavily deformed and composed of mainly sedimentary rock, and since like the Tyennan Orogeny, the coeval Delamerian Orogeny of mainland southeast Australia experienced eastward dipping subduction, generates further evidence in support of the direct connection between Tasmania and the neighboring mainland.

The elongated high-velocity zone identified in Figure 4.13 in the uppermost ~ 3 km of the crust between the two low-velocity anomalies may be a signature of extensive dolerite sheets emplaced during the Jurassic (Brauns et al., 2000). A similar shallow area of elevated velocity to the east is attributable to the Devonian granites

of ETT (Patison et al., 2001). The high resolution potential of our method justifies analysis of model features on the horizontal scale of ~ 10 km. For example, the high-velocity anomaly along the north edge of the TIGGER array at about 146° longitude (Figure 4.10) underlies the Forth metamorphic complex (Figure 4.1), which was formed and exhumed during the Cambrian Delamerian orogeny and contains Proterozoic quartzite, amphibolite, phyllite and schist (Meffre et al., 2000). Interestingly, the Badger Head metamorphic complex (Figure 4.1), which lies about 75 km west of the Forth metamorphic complex, overlies a localized low-velocity zone. The Proterozoic sedimentary rocks of this structurally-complex turbidite package are intensely deformed, highly metamorphosed, and are considered allochthonous (Leaman et al., 1973; Reed et al., 2002). Metamorphic grade for the complex is mostly lower greenschist facies (Reed et al., 2002), while the Forth metamorphic complex experienced higher temperatures and pressures with metamorphism ranging from upper greenschist to upper amphibolite facies (Foster et al., 2005). The difference in shear velocity beneath these two complexes likely arises from compositional and density differences.

4.6 Conclusions

In this paper we present a scheme for producing a 3D shear velocity model from ambient seismic noise dispersion measurements using fully non-linear Bayesian techniques. Model parameters, such as the number of layers, data variance, and model complexity, are left as unknowns in the inversion and are therefore driven by the information content of the data. Using a transdimensional approach, we first calculate 2D phase velocity maps for a range of periods. From these maps, 1D dispersion curves, complete with standard deviations, are produced at a regular grid of points in latitude and longitude. Each curve is independently inverted for a 1D shear velocity model. The 1D models are then joined together to create a pseudo-3D map of the shear velocity structure. Unlike more conventional methods which often employ ad hoc error estimation, we preserve uncertainty information from each step and use it to further constrain the next step in the inversion. Each inversion, whether for 2D phase velocity variations or a 1D shear velocity model, is uniquely parameterized according to the quantity, quality, and distribution of the input data.

We apply our method to data from two adjacent, densely spaced seismic arrays in Tasmania. Phase velocity maps for periods between 1 and 12 s and a 3D shear velocity model down to a depth of 15 km are produced. The resulting tomographic images reveal a ~ 75 km wide, southeast-trending, eastward-dipping, low-velocity lineation within the vicinity of the Tamar River. This feature is likely the result of strong deformation and faulting associated with the Phanerozoic accretion of oceanic material along the more rigid Proterozoic continental Tasmanian lithosphere. To the west, a pronounced low-velocity zone is also present beneath the Dundas Trough of northwest Tasmania. The eastward-dipping geometry of this anomaly suggests an association

with the deformation and shortening of the Tyennan Orogeny and supports a connection between Tasmania and mainland Australia since the Cambrian.

Crustal structure of the east Gondwana margin in southeast Australia revealed by transdimensional ambient seismic noise tomography

5.1 Foreword

This chapter presents the physical and mathematical description of the ambient seismic noise tomography method used in this thesis. The model estimates the geometry and velocity of a spatial structure revealed by the data using a Bayesian method. The model is based on a Bayesian method. This research also shows how data from multiple stations can be combined to improve the resolution of the model. The model is based on a Bayesian approach and is used to estimate the geometry and velocity of a spatial structure. The model is based on a Bayesian approach and is used to estimate the geometry and velocity of a spatial structure. The model is based on a Bayesian approach and is used to estimate the geometry and velocity of a spatial structure. The model is based on a Bayesian approach and is used to estimate the geometry and velocity of a spatial structure.

Yuan, M. F., R. A. Cooper, M. A. McCaus, M. S. Bagshaw, J. P. Clague, and J. V. Salmon (2017). Crustal structure of the east Gondwana margin in southeast Australia revealed by transdimensional ambient seismic noise tomography. *Geophysical Research Letters*, 44, 4266–4277, doi:10.1002/2016GL071472.

5.2 Abstract

Ambient seismic noise data from the ongoing WILDAF (Wildlife and Environmental Monitoring) in southeast Australia, the largest deployment of its kind in the southern hemisphere

Crustal structure of the east Gondwana margin in southeast Australia revealed by transdimensional ambient seismic noise tomography

5.1 Foreword

This chapter presents the application of the Bayesian inversion methods of the previous chapter to a larger mainland southeast Australia dataset. The resulting 3D velocity model establishes the geometry and position of key crustal features related to the transition from Paleozoic eastern Australia to Precambrian central and western Australia. This research also shows how data from multiple, asynchronously running arrays can be combined and used to produce a single model. The Bayesian ensemble inference approach handles uneven data coverage such that this joining does not result in artifacts, such as unjustified structure between arrays. Auxiliary material was published with the manuscript and is included in Appendix E. This work was published in *Geophysical Research Letters*:

Young, M.K., R. A. Cayley, M. A. McLean, N. Rawlinson, P. Arroucau, and M. Salmon (2013), Crustal structure of the east Gondwana margin in southeast Australia revealed by transdimensional ambient seismic noise tomography, *Geophysical Research Letters*, 40, 42664271, doi:10.1002/grl.50878.

5.2 Abstract

Ambient seismic noise data from the ongoing WOMBAT transportable seismic array in southeast Australia, the largest deployment of its kind in the southern hemisphere,

are used to produce a high resolution 3D shear wave velocity model of the region. We apply a two-stage, transdimensional, hierarchical Bayesian inversion approach to recover phase velocity maps at periods of 1-20 s and then invert phase velocity dispersion for 3D shear wave velocity structure to the base of the crust. Data uncertainty is propagated through the sequence of inversions, ensuring that model complexity is justified by the quality and quantity of the measurements. The pattern of 3D velocity variations helps elucidate the geometry and position of key crustal features - such as the Torrens Hinge Zone - associated with the transition from Paleozoic eastern Australia to Precambrian central and western Australia that formed along the proto-Pacific margin of east Gondwana.

5.3 Introduction

The Proterozoic and Archean terranes that now form the western two-thirds of the Australian continent represent an amalgamation of fragments of the former supercontinent Rodinia (Powell et al., 1994). The remaining eastern third of the present-day Australian continent, the region east of the locus of the Neoproterozoic Rodinia breakup, comprises the Tasmanides (Figure 1). This orogen, also known as the Tasman Fold Belt System, formed as a result of accretion along the (then) east Gondwana margin throughout the first half of the Phanerozoic (Glen, 2013).

In southeast Australia the Torrens Hinge Zone (THZ) (Figure 1) is the westernmost surface expression of the Tasman Fold Belt System and separates the Archaen-Mesoproterozoic Gawler Craton from the Neoproterozoic-Paleozoic Delamerian Orogen. The THZ is a north-trending belt of tight folds and meridional faults of Late Cambrian age, imposed on Neoproterozoic-Cambrian, predominantly epicontinental, metasedimentary rocks of the Adelaide Rift Complex (Cawood, 2005). A major crustal-scale feature, the THZ is estimated at between 15 and 60 km wide (Schmidt and Williams, 1995), but its geometry and depth extent are not well understood.

Ambient noise tomography has the potential to increase tomographic resolution for structures such as the THZ, and especially the subsurface orientation of faults, that play a key role in deciphering the tectonic history of a complicated region. This has been demonstrated previously by Arroucau et al. (2010), who produced a model of group velocity for southeast Australia through a linearized inversion of WOMBAT ambient seismic noise data. WOMBAT is the largest transportable seismic array experiment in the southern hemisphere and has resulted in dense passive seismic coverage of Tasmania, Victoria, New South Wales (NSW) and eastern South Australia (SA). This same dataset was later used by Bodin et al. (2012a) to produce a hierarchical Bayesian group velocity model. In this study we substantially augment the dataset and use a novel Bayesian inversion technique to produce the first 3D model of crustal shear velocity structure beneath mainland southeast Australia. Our 3D model is the most detailed map of its kind yet created for southeast Australia, with maximum horizontal

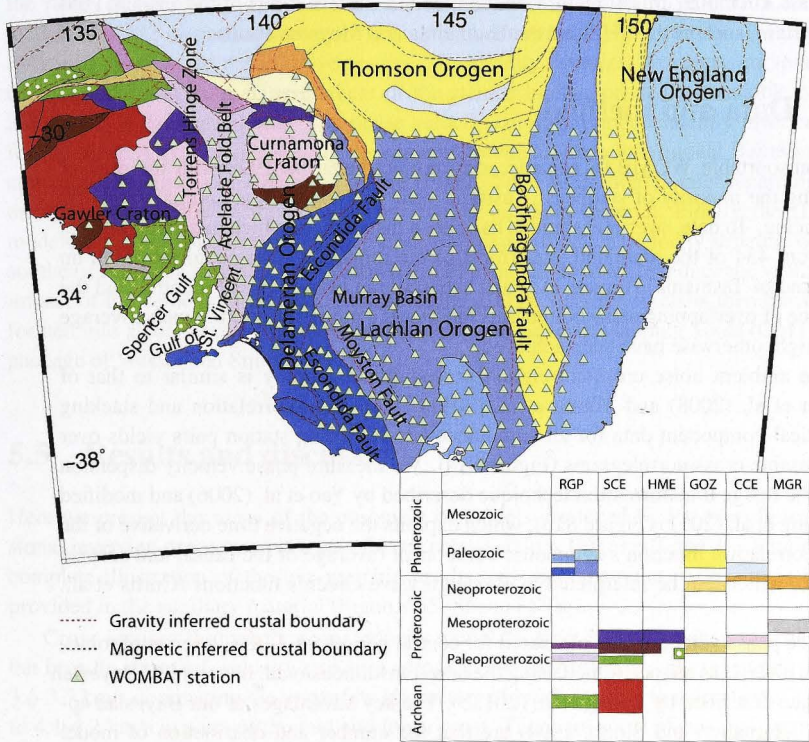


Figure 5.1: The crustal elements of southeast Australia, as inferred from potential field data (based on data contained in Shaw et al., 1996). RGP=relict geophysical pattern; SCE=standard crustal element; HME=highly magnetic element; GOZ=geophysically overprinted zone; CCE=covered crustal element; MGR=sub-element with muted geophysical response (see Shaw et al., 1996, for more details). The location of most geological features discussed in the text, such as the Torrens Hinge Zone, are identified.

and vertical resolution on the order of 20 km and 1 km respectively. Importantly, data noise is treated as an unknown in the inversion, thereby producing maps of a complexity that is justified by the quality and quantity of the data. Our 3D shear velocity model provides important constraints on the position, location, and extent of primary southeast Australian crustal features that define the western limits of the Tasman Fold Belt System, such as the THZ and the Escondida and Moyston Faults.

5.4 Data and method

The transportable WOMBAT seismic array project began in 1998 with the goal of spanning the majority of southeast Australia with seismometers at approximately 50 km spacing. To date, over 600 stations have been installed, of which this study utilizes data from 434 of the mainland sites (most of the remaining sites lie to the south on the island of Tasmania) (Figure 1). Each subarray ran between 6-12 months, and the presence of overlapping array boundaries facilitates a more uniform ray path coverage than might otherwise have been achieved.

The ambient noise cross-correlation procedure we employ is similar to that of Bensen et al. (2008) and Young et al. (2011). The cross-correlation and stacking of vertical-component data for all simultaneously recording station pairs yields over 8,200 usable cross-correlograms (Figure S1a). We measure phase velocity dispersion using the image transformation technique described by Yao et al. (2006) and modified by Young et al. (2011) (Figure S1b), which exploits the negative time derivative of the cross-correlation function's symmetric component (average of the causal and acausal signals), which can be interpreted as Rayleigh wave Green's functions (Curtis et al., 2006).

Once phase velocities are measured for central periods of 1-20 s, a series of tomographic inversions are performed using the new transdimensional, hierarchical Bayesian technique described by Young et al. (2013b). The key advantages of our Bayesian approach (Bernardo and Smith, 1994) are that the number and distribution of model parameters are implicitly controlled by the data and that the standard deviation of the data noise (assumed to have a Gaussian distribution) is treated as an unknown in the inversion. This "noise" includes whatever our model cannot explain (Bodin et al., 2012a), which can be attributed to measurement errors, shortcomings of the forward model, and mathematical or theoretical approximations. As a result, the required complexity of the solution is inferred from the data itself (Bodin et al., 2012a), rather than from ad hoc uncertainty estimation techniques and arbitrary parameterizations so often utilized by more traditional, linearized inversion techniques (see review by Rawlinson et al. (2010a) for more discussion). The recovery of a phase velocity map for a given central period takes approximately 1000 CPU hours. Although this is three to four orders of magnitude greater than the time taken by a more traditional iterative, non-linear approach (Young et al., 2011), the improved quality of the results and provision

of uncertainty estimates fully justify the additional cost (for example, see the synthetic tests of Young et al. (2013b)).

The final phase velocity maps (Figures S2 and S3) represent the average of a large ensemble of models of varying parameterization. The 2D maps are sampled over the range of periods at 20 km intervals in latitude and longitude to produce a collection of 1,572 dispersion curves. This is the maximum sampling density at which finer grid spacing did not improve results. Uncertainty estimates for every curve at each period come from an assessment of the standard deviation of the ensemble of 2D models at each grid point. The phase velocity curves are independently inverted for 1D shear velocity models using the same hierarchical, transdimensional Bayesian approach (Young et al., 2013b) as before (Figure S4). Additional details regarding the application of this method can be found in the auxiliary material. Finally, the 1D models are joined together to create a pseudo-3D map of the shear velocity structure of southeast Australia from the surface down to 30 km depth. In order to reduce the visual impact of the velocity pixelization, the resulting grid of velocity pixels is then transformed into a continuous curvature surface using the Generic Mapping Tools (GMT) package of Wessel and Smith (1995).

5.5 Results and discussion

Here we present the mean of the ensemble of models produced by the transdimensional inversion procedure via a set of three cross-sections (Figures 2 and 3). A more complete illustration of the tomographic results and accompanying uncertainties is provided in the auxiliary material (Figures S5, S6, and S7).

Cross-sections through the shear velocity model (Figures 2 and 3) show a variable, but broadly stratified, velocity structure across southeast Australia, with velocities of 3.6–3.7 km/s dominating the upper few kilometers of crust, grading to velocities of up to 4.1–4.2 km/s in parts of the mid and lower crust. There are some places, for example near the southern edge of the Curnamona Craton near the NSW-SA border, where near-surface regions with lower velocities (red in cross-section of Figure 3) thicken abruptly towards the mid-crust (~10 km depth), to form a block of low velocity material. Presumably this reflects the presence of deeper, steep sided, sediment-filled basin structures. Low shear velocities of likely similar origin also occur in eastern Victoria, coincident with the surface distribution of igneous rocks, including silicic volcanics and carbonates related to the Early Devonian Buchan Rift (VandenBerg et al., 2000).

Because the Torrens Hinge Zone (THZ) marks the eastern edge of the Gawler Craton and the western limit of Tasmanides-related deformation in southeast Australia, distinguishing the subsurface geometry of this boundary is important to understanding the accretion of the Delamerian Orogen to the east. Until now, with few exceptions, the THZ has been studied at the surface, limiting our understanding of this structure at

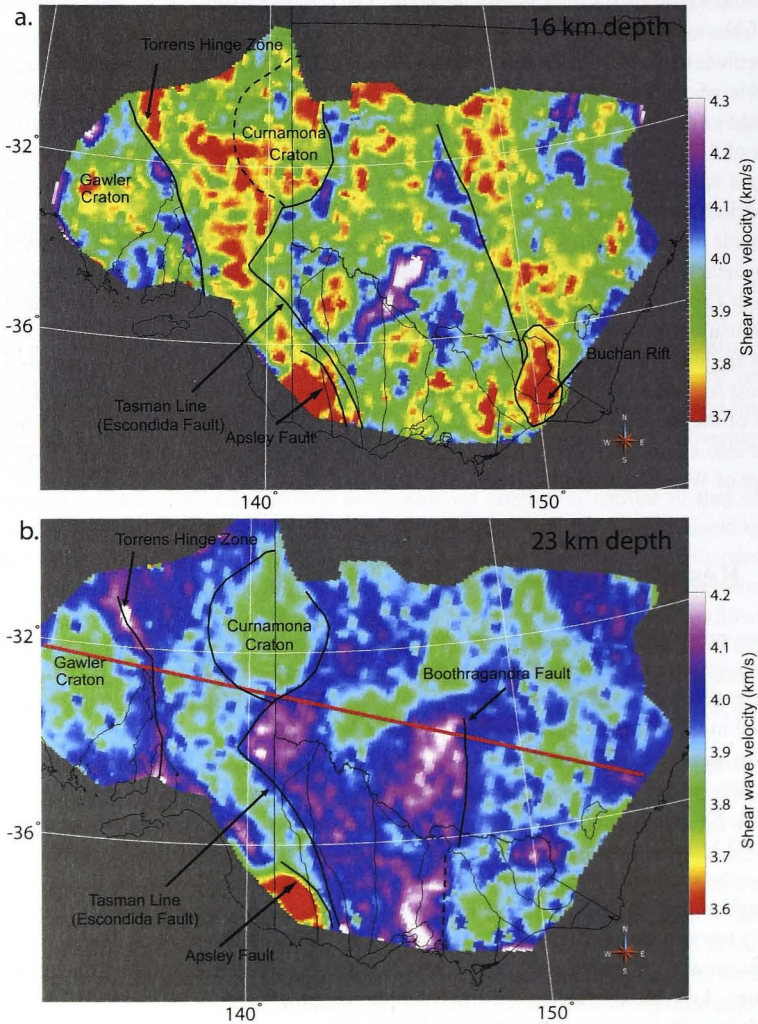


Figure 5.2: Horizontal cross-sections taken at a depth of (a) 16 km and (b) 23 km through the 3D shear wave velocity model. Key features discussed in text are indicated. Location of vertical cross-section in Figure 5.3 given by red line.

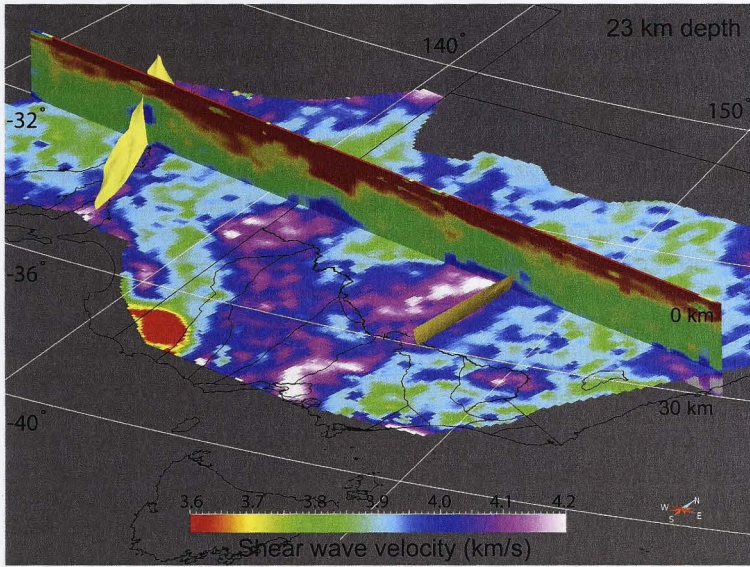


Figure 5.3: Horizontal cross-section taken at a depth of 23 km through the 3D shear wave velocity model and a vertical cross-section. See Figure 5.2 for bird's eye view of cross-section location. Yellow surfaces show inferred Bootheragandra (east) and Torrens Hinge Zone (west) structures.

depth. The new 3D shear velocity model introduces important new data that constrain the geometry and origin of the hinge zone.

The singular most striking feature of the 3D shear velocity model is the subvertical zone of relatively high shear wave velocity in the mid-lower crust (Figure 2) that cleaves from the northwestern edge of the model toward the Gulf of St Vincent (Figure 1) in the southeast, where it is lost at the model's southern margin. This feature coincides with the surface position of the THZ. It is easily identified from surface down to 30 km and dips slightly to the east with a width of ~ 50 km. This subsurface constraint is invaluable, for previous studies at depth were often of limited horizontal extent (e.g. Belperio and Flint (1993)) or lower resolution (e.g. Saygin and Kennett (2012)).

The THZ is a major crustal feature with a variety of interpretations. The slight eastward dip seen in our model accommodates several theories. Clarke and Powell (1989) interpreted the THZ as a thrust fault boundary, with the Tasman Fold Belt to the east pushing and buckling over the undeformed Gawler Craton to the west. Such an interpretation would likely require the THZ to dip to the east. Preiss (2000) advocates discrete episodes of rifting characterized by crustal extension and basin formation.

He suggests normal faults along this zone produced a series of half-grabens stepping down into the basin center. If this is the case, faulting would have occurred nearly subvertically, compatible with the very steep east dips indicated in our model. Belperio and Flint (1993) present yet another picture in which the THZ is portrayed as a zone of faulting and monoclinical flexuring that is bounded on the west by the Cygnet-Snelling Fault, which dips slightly to the east. The new shear velocity model makes it clear that the THZ is a linear, steep-sided, crustal-scale structure in marked contrast to the younger and shallower intracratonic rifts and basins that scatter across the surface of the Tasmanides farther east. Below ~ 8 km depth shear velocities within the THZ are markedly higher than in the flanking Mesoproterozoic Gawler and Curnamona cratons.

Because of its position, steep overall geometry, and deeply-penetrating shear velocity structure, we concur with authors who favour an extensional origin for the THZ. Its formation in the Neoproterozoic presumably related to protracted whole-of-crust rifting at the onset of the Rodinia breakup. The THZ extends the full depth of the shear velocity model and therefore represents a major failed branch of this rift event. Although dominated near surface by well documented clastic rocks (with low shear velocities compared to adjacent regions), the velocity character of the THZ below 8 km suggests that mafic, igneous rocks are predominant at depth. The THZ therefore likely began as the locus of major rift-related magmatism initiated around ~ 830 Ma, before the rift became progressively by-passed from ~ 600 - 580 Ma onwards. Younger, sub-parallel rift branches (Crawford et al., 1997) developed farther east as the locus for final Rodinian separation (Direen and Crawford, 2003b).

The Gawler Craton is interpreted to thin east beneath the THZ and the rest of the Delamerian Fold Belt to form a buried "Tasman Toe" (Scheibner, 1998). To the east, the Escondida Fault (Cayley and Taylor, 1997) could be the surface expression of this eastern limit of PreCambrian crust. The presence and east-dipping geometry of this fault have so far been largely inferred from deep seismic data (Korsch et al., 2002; Cayley et al., 2011a) and magnetics (Moore, 1996; Cayley and Taylor, 1997), as there is minimal surface exposure. Farther north, any along-strike extension to the Escondida Fault is buried beneath the Cenozoic Murray Basin, and its location becomes equivocal. In southern Victoria, the east-dipping Moyston Fault lies close to, and subparallel with, the Escondida Fault, and appears to extend to the Moho and possibly beyond (Graeber et al., 2002). Another candidate for the Tasman Toeline (Cayley et al., 2011b), the Moyston fault has been nominated as the boundary between the Delamerian and Lachlan fold belts within the Tasmanides system (Cayley et al., 2011b; Glen, 2013).

Both the Moyston and Escondida faults lie in the vicinity of the east-dipping lateral velocity change that is readily apparent in the shear velocity model (Figure 2). However, the location of the Escondida Fault corresponds much more closely with the abrupt change in mid-lower crustal shear velocities. Therefore, we conclude that it is the most likely surface expression of this velocity anomaly. Additionally, magnetic

trends in the Escondida Fault hangingwall in SA continue north, eventually swinging toward the northeast and passing into NSW - a path followed closely by the lateral shear wave velocity change. The eastward dipping orientation of this velocity transition is consistent with the eastward dip of the southern section of the fault (Cayley et al., 2011a). It is therefore possible that the Escondida Fault represents the surface expression of inverted passive margin basins developed during the Rodinia breakup and that the elevated shear velocities to the east of the fault reflect an abundance of high velocity mafic igneous rift fill.

Linking the Escondida Fault to the lateral change in shear velocity data means that its position and existence can be interpreted with increased confidence farther north, where it becomes progressively more difficult to trace in magnetic data. The shear velocity model gives confidence that the Escondida Fault is persistent and trends northeast towards the southern margin of the Curnamona Craton. It has previously been speculated that this northeast orientation, almost orthogonal to much of the De-lamerian Gondwana margin, may represent a transform fault (Finn et al., 1999).

The Bootheragandra Fault is a north-trending terrane boundary between the Stawell, Hay-Booligal, and Tabberabbera zones on the west and the rest of the eastern Lachlan Orogen to the east. A west-east decrease in the shear wave velocity (Figure 2b) coincides with the near-surface trace of the Bootheragandra Fault in NSW as defined by magnetic data (Musgrave and Rawlinson, 2010). However, our model implies that the Bootheragandra fault is subvertical to at least the base of the mid crust. This differs from the interpretation of Musgrave and Rawlinson (2010) and instead suggests the Bootheragandra Fault is a northward extension beneath the Murray Basin of a large, Late-Silurian aged strike-slip structure further south in Victoria (Morand et al., 2003).

5.6 Conclusions

In this study we obtain a high resolution 3D shear wave velocity model for the south-east Australian crust down to 30 km depth using ambient noise data recorded by the WOMBAT transportable array. The transdimensional, hierarchical Bayesian inversion methods applied to the phase dispersion data recover structure to a level of detail that is unmatched by more conventional linearized techniques. Major features of the model are the striking velocity anomalies seen along the Escondida and Bootheragandra faults and the Torrens Hinge Zone (THZ). Furthermore, upper-crustal shear velocity variation correlates with the known distribution of intracratonic rift and basin successions within the Tasmanides.

The results confirm the THZ as a major steep-sided, crustal-scale rift structure that likely formed due to protracted Neoproterozoic rifting during the break-up of Rodinia. Intermediate shear velocities consistent with craton-related rocks extend east towards the Escondida Fault, where they abruptly change to higher velocities along this east-dipping structure, possibly forming the Tasman Toeline. The revelation of the precise

geometry and location of these structures is important to understanding the tectonic evolution of the east Gondwana margin in southeast Australia.

Global P-wave tomography of Earth's lowermost mantle from partition modeling

6.1 Foreword

This final chapter presents the application of Bayesian statistics to a global-scale problem. Namely, we present a novel view of heterogeneity in the Earth's lowermost mantle using partition modeling within a hierarchical and transdimensional Bayesian framework. We apply our method to high quality, hand-picked body wave measurements, and our resulting global-scale lowermost mantle P-wave velocity model has strong geophysical implications for the current debate concerning the strength of heterogeneity in the lowermost mantle. Achieving data noise estimates is a major step forward, as traditionally, absolute uncertainty information is difficult to obtain from travel time measurements. Although more conventional inverse methods often employ ad hoc error estimation techniques, the P-wave velocity model determined here is complete with velocity standard deviations as a result of our ensemble inference approach. An impressive outcome is a reliable estimate of the strength of the P-wave velocity heterogeneity in the lowermost mantle. Our estimates for that heterogeneity are three times greater than those of previous workers. This discrepancy is related to our circumvention of the typical smoothing and damping procedures utilized by tomographers using more conventional approaches. These findings will help to significantly refine allowable lowermost mantle thermo-chemical models. This work was published in the *Journal of Geophysical Research*:

Young, M., H. Tkalčić, T. Bodin and M. Sambridge (2013). Global P-wave tomography of Earth's lowermost mantle from partition modeling, *Journal of Geophysical Research*, 118, 5467-5486.

6.2 Abstract

Determining the scale-length, magnitude, and distribution of heterogeneity in the lowermost mantle is crucial to understanding whole mantle dynamics, and yet it remains a much debated and ongoing challenge in geophysics. Common shortcomings of current seismically-derived lowermost mantle models are incomplete raypath coverage, arbitrary model parameterization, inaccurate uncertainty estimates, and an ad hoc definition of the misfit function in the optimization framework. In response, we present a new approach to global tomography. Apart from improving the existing raypath coverage using only high quality cross-correlated waveforms, the problem is addressed within a Bayesian framework where explicit regularization of model parameters is not required. We obtain high resolution images, complete with uncertainty estimates, of the lowermost mantle P-wave velocity structure using a hand-picked dataset of PKPab-df, PKPbc-df, and PcP-P differential traveltimes. Most importantly, our results demonstrate that the root mean square of the P-wave velocity variations in the lowermost mantle is approximately 0.87%, which is three times larger than previous global-scale estimates.

6.3 Introduction

The lowermost mantle is one of the most intriguing and important layers of the Earth. Extreme contrasts in velocity, density, and viscosity are seen at the core mantle boundary, where the solid mantle meets the liquid core. Additionally, the lowermost mantle is heterogeneous in terms of viscosity, seismic velocity, density, chemistry and temperature. The pattern of velocity heterogeneity has been studied at a variety of scale-lengths, for example global models clearly reveal long-wavelength velocity patterns (e.g. Wyssession (1996), Antolik et al. (2003), Lei and Zhao (2006), Li et al. (2008), Ritsema et al. (2011)). In those studies, regions of higher wave speeds are typically attributed to cool subducted slabs while regions of slower wave speeds are regarded as the signature of hot, upwelling material. A pattern of large areas of low velocity under the southwest Pacific and southern Africa is well established in the deep Earth community (e.g. Su et al. (1994), Li and Romanowicz (1996), Wyssession (1996), Grand et al. (1997), Mégnin and Romanowicz (2000), Gu et al. (2001), Antolik et al. (2003), Lei and Zhao (2006), Houser et al. (2008), Li et al. (2008), Della Mora et al. (2011), and Soldati et al. (2012)). The African anomaly extends about 1000 km above the core mantle boundary (e.g. Ritsema et al. (2011)) and is likely both thermal and chemical in nature (e.g. Ni and Helmberger (2001a), Simmons et al. (2007)). There is increasing evidence that the Pacific anomaly is also at least partially chemical in origin (e.g. Tkalčić and Romanowicz (2002), Trampert et al. (2004), Ishii and Tromp (2004), He and Wen (2009)). Meanwhile, local studies of core phases and their precursors indicate the presence of short-scale heterogeneity (e.g. Doornbos (1974), Bataille and

Flatte (1988), Vidale and Hedlin (1998), Bréger and Romanowicz (1998), Cormier (1999), Bréger et al. (2000) Rost and Earle (2010), Earle et al. (2011)). A goal of this study is to investigate the strength of the velocity perturbations, as there is evidence that this amplitude is far greater than the level implied by current global tomographic models (e.g. Ritsema et al. (1998), Garcia et al. (2009)).

There is increasing research to support a fine-scale and complex nature of heterogeneity at the base of the mantle. Developing a global model of lowermost mantle structure may prove vital to a more precise understanding of magnetic field generation, deep mantle flow, and other geodynamical processes. Common impediments to a reliable model include limited sampling due to the natural global seismicity pattern and seismic station availability, questionable quality of large datasets, influence by crustal and mid-upper mantle structure, artificially coarse model parameterizations, and inadequate quantification of data noise. Nonetheless, considerable advances in seismic tomography have been made since early global mantle studies (Dziewonski et al., 1977; Nakanishi and Anderson, 1982; Dziewonski, 1984), which almost exclusively depended on absolute, P-wave travel times and a simple block or spherical harmonic parameterization. Differential traveltimes are less sensitive to source mislocation and heterogeneities near the source and receiver. Cormier and Choy (1986) demonstrated this advantage and used differential PKP wave measurements to assess velocity heterogeneity in and near the inner core. Woodward and Masters (1991) then applied the differential traveltime method to the mantle and used PP-P and SS-S measurements to map global upper mantle structure. It then became common to combine different datasets to improve spatial coverage and depth resolution. Su et al. (1994) used a synthesis of full waveform data, absolute S arrivals, and SS-S and ScS-S differential travel times to invert for a 3D map of mantle shear velocity structure.

6.3.1 Advances in data quality

Over the last couple of decades, many global models of P-wave velocity in the mantle have been produced (e.g. Inoue et al. (1990), Vasco et al. (1995), van der Hilst et al. (1997), Vasco and Johnson (1998), Antolik et al. (2003), Fukao et al. (2003), Montelli et al. (2004), Lei and Zhao (2006), Houser et al. (2008), Li et al. (2008), Zhao (2009), Della Mora et al. (2011), Zhao et al. (2012)). Nonetheless, P-wave mantle models are still less common than S-wave mantle models as a result of the relative difficulty in measuring P-wave arrivals. The challenge of accruing a collection of P-wave arrivals is due to several factors. First, the source mechanism radiation pattern of strike slip earthquakes does not produce much P-wave energy down to the core mantle boundary. Also, the conversion from P-waves to S-waves is often more efficient than the conversion of S-waves to P-waves. Additionally, S-waves can be viewed on both the transverse and radial component of the seismogram, whereas P-waves are best observed on just the vertical component (at epicentral distances beyond 145° and often

close to antipodal distances, the vertical and radial components of a seismogram are almost the same due to the steep incident angle of PKP waves). Finally, S wave models are typically derived from lower frequency data, which is more conducive to waveform modeling and inversion. P-waves, especially PcP, on the other hand must be observed at higher frequencies, often leaving them buried in noise and susceptible to dispersion in the lowermost mantle.

By inverting for the entire mantle structure instead of the lowermost mantle alone, mid-upper mantle heterogeneity is less likely to be erroneously mapped onto the bottom-most layer. These whole mantle models are also useful for assessing heterogeneity at the base of the mantle in the sense that they reveal any vertical continuity of structure, such is especially pertinent when investigating the presence of plumes (Zhao, 2004). The chief drawback of entire mantle models, however, is the quality of the data; it is far too time consuming to manually pick a dataset for whole mantle imaging. Therefore, researchers generally use International Seismological Center (ISC) or EHB (as in Li et al. (2008)) datasets, which are of questionable quality for many phases (Inoue et al., 1990; Vasco et al., 1995; van der Hilst et al., 1997; Vasco and Johnson, 1998; Boschi and Dziewonski, 2000; Fukao et al., 2003; Zhao, 2004; Montelli et al., 2004; Lei and Zhao, 2006; Zhao, 2009; Della Mora et al., 2011; Zhao et al., 2012). Despite the potentially enormous datasets, model resolution in the lowermost mantle is often limited due to the computational costs associated with the whole-mantle model parameterization.

The heterogeneity pattern above the core mantle boundary is frequently better retrieved when inverting for the lowermost mantle region alone. By reducing unwanted crustal and mid-upper mantle effects, differential travel times of body waves are especially helpful when deciphering the complexities of the mantle's bottom-most layer. For example, Sylvander and Souriau (1996) used PKPab-bc differential traveltimes to retrieve P-velocity structure in the lowermost mantle. A limitation of this approach, however, is incomplete raypath sampling due to the unfavorable configuration of earthquakes and land-based seismic stations. This situation can in part be ameliorated by using multiple seismic phases with different sampling patterns. For example, Kárason and van der Hilst (2001) used P, pP, and pwP, coupled with PKPab-df, PKPab-bc, and PKPdf-Pdiff differential travel times, and Tkalčić et al. (2002) used cross-correlated PKPab-df and PcP-P data to invert for lowermost mantle structure. In this study we augment the datasets of Tkalčić et al. (2002) and Tkalčić (2010) by adding new PKPab-df, PKPbc-df, and PcP-P differential travel times with the intent of patching the spatial gaps in sampling.

6.3.2 Advances in inverse methods

In addition to the steady improvement in data quality and quantity, in large part thanks to accumulated recordings of the Global Seismographic Network that the Incorporated

Research Institutions for Seismology (IRIS) initiated in 1984, there has also been improvement in inversion methods. This progress is to a great degree a reflection of an increase in computing power. Irregular-sized block parameterization was first introduced by Inoue et al. (1990), which helped reduce over parameterization while at the same time allowing the resolution of small-scale structures where justified by the data. Tkalčić et al. (2002) also employed a variable size block inversion method and introduced an algorithm to restrict the aspect ratios of the blocks. Antolik et al. (2003) used a horizontal tessellation of spherical splines that provided the equivalent resolution as spherical harmonic degree 18 for a joint inversion of P-wave and S-wave velocity in the mantle. Sambridge and Faletić (2003) presented a self-adaptive inversion technique in which the initial parameterization, based on spherical triangles and Delaunay tetrahedra, is refined throughout the inversion. Recently, Simons et al. (2011) and Chevrot et al. (2012) proposed a spherical wavelet approach to global tomographic inversions whose multi-resolution potential is ideal for spatially ill-distributed datasets. Zhao et al. (2012) adopted a flexible-grid parameterization for whole-mantle tomography that was designed to better express mantle structure under the polar regions.

In addition to increasingly sophisticated model parameterizations, inversion algorithms have also been improved. Beghein et al. (2002) used the neighborhood algorithm of Sambridge (1999) to invert for spherical harmonic degree two P and S wave velocity structure in the mantle. Garcia et al. (2009) approached lowermost mantle heterogeneity from a different perspective and used stochastic analysis to relate differential travel time measurements to the correlation function of velocity heterogeneity. Using PKP travel times they inverted for the statistical properties of velocity perturbations in the lowermost mantle and provided valuable constraints on the scale-length and magnitude of P-wave heterogeneity that are unbiased by smoothing, damping, or model parameterization. More modern tomography methods began to step away from classical ray theory when Montelli et al. (2004) implemented a finite-frequency approach to traveltimes tomography and demonstrated that wavefront healing cannot be ignored when using long-period P and PP waves. Finite frequency effects were demonstrated to be especially important for PKP phases in the lowermost mantle (Calvet and Chevrot, 2005), although only recently were the first exact and complete finite-frequency kernels for short period PKP waves computed (Fuji et al., 2012). Garcia et al. (2004, 2006) introduced another method known as Simulated Annealing Waveform Inversion of Body waves (SAWIB), which resolved the interference between direct PKP waves and their corresponding depth phases, thereby allowing the use of recordings from triplication distances and shallow earthquakes.

If we are to accurately depict the scale-length of heterogeneity at the core mantle boundary, we must ensure that the results are minimally influenced by arbitrary choices about model parameterization, smoothing, and damping. Such intervention is often the downfall of traditional linearized inversion methods, where models are artificially parameterized and either resolution is lost due to unnecessary smoothing or

noise is misinterpreted as data complexity. In response to these pitfalls, we implement a fully non-linear Bayesian partition-modeling technique for our tomographic inversion. This is an ensemble inference approach in which model space is sampled via Reversible Jump Markov Chain Monte Carlo sampling (Green, 1995, 2003). Model parameters, including the level of data noise, are treated as unknowns in the problem and are represented by probability distribution functions rather than single values. Therefore, the complexity and amplitude of the velocity variations in our final model, which results from a complete ensemble of hundreds of thousands of sampled models, depend almost exclusively on the data itself and there is no need to apply explicit smoothing or damping procedures (Bodin et al., 2012a). This method provides the statistical robustness of Beghein et al. (2002) and Garcia et al. (2009) and the multi-scale resolution capabilities of Simons et al. (2011) and Chevrot et al. (2012) while introducing a novel approach to handling data noise and model parametrization.

Conventional approaches to global tomography have two major drawbacks, both of which we seek to address in this study. The first is ad-hoc data noise estimation and the subjective choice of smoothing and damping parameters. This can lead to the loss of valuable information, especially about model discontinuities, in an effort to avoid the over-interpretation of noise. We instead invert for the data uncertainty, and the level of complexity and strength of perturbations in the final model are appropriately limited by the noise content of the data (e.g. Bodin et al. (2012a)). The second disadvantage is arbitrary model parameterization, often governed by equal-sized block cells (e.g. Sylvander and Souriau (1996), Tkalčić et al. (2002), Houser et al. (2008)) or limited-degree spherical harmonic expansions (e.g. Tanaka (2010), Ritsema et al. (2011)). Such rigid parameterizations prevent full utilization of data content while either oversimplifying and over-smoothing the model or adding unjustified complexity and artificial discontinuities. In this study we partition the lowermost mantle into a mosaic of Voronoi polygons whose size, location, velocity, and number vary throughout the inversion according to the information content of the data. This probabilistic, partition modeling based approach enables us to present a global-scale model of P-wave velocity variations in the lowermost mantle together with uncertainty estimates. Our choice of inversion method also allows valuable estimates of the scale-length and strength of velocity heterogeneity in the lowermost mantle.

6.4 Data

As a starting point, we use 1408 PKPab-df, 1068 PKPbc-df, and 399 PcP-P differential travel times taken from the handpicked datasets of Tkalčić et al. (2002) and Tkalčić (2010). Hand-picking allows the alignment of the onsets of the phases rather than the peaks or troughs of greatest amplitude, as is the tendency of automatic cross-correlation. We have automated cross-correlation estimates for a large portion of the dataset, and in most cases the difference is less than 0.5 s. We do not use measure-

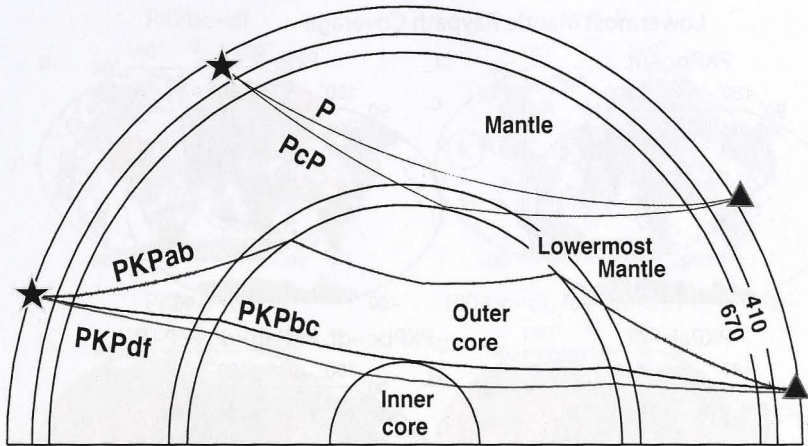


Figure 6.1: Raypaths of PKPab, PKPbc, PKPdf, PcP and P body waves for the epicentral distance of 155° and 65° .

ments from diffracted raypaths or epicentral distances less than 55° (in the case of PcP-P) to improve accuracy in forward modeling. The benefit of using differential travel times versus absolute travel times is that biases due to source mislocation and near surface structure are greatly reduced due to the nearness of the two raypaths in the crust and upper mantle (Figure A.1). To further reduce mantle effects, we experiment with correcting for mantle structure using current mantle models, as is further discussed in the next section. After assessing the gaps in the lowermost mantle sampling, we in part fill them by hand-picking an additional 463 PKPab-df, 224 PKPbc-df, and 281 PcP-P differential travel times. We use data recorded between the years 1965 and 2010 inclusive, mostly coming from large ($M_b > 6$) events with depths greater than 35 km. See Figure 2 for a demonstration of the improvement in raypath coverage. This 34% increase in travel time measurements greatly improves coverage in many areas, most notably Africa, the southwest Indian Ocean, the north Atlantic, and north Australia/Indonesia.

6.4.1 PKPab-df dataset

The differential PKPab-df travel time measurements are in part taken from the hand-picked dataset of Tkalčić et al. (2002). We have expanded this collection to improve spatial coverage (Figures 6.2b, 6.3b), although our measurement techniques remain much the same. First, we relocate earthquakes according to Engdahl et al. (1998), as a 10 km error in either source or receiver location will result in a differential travel

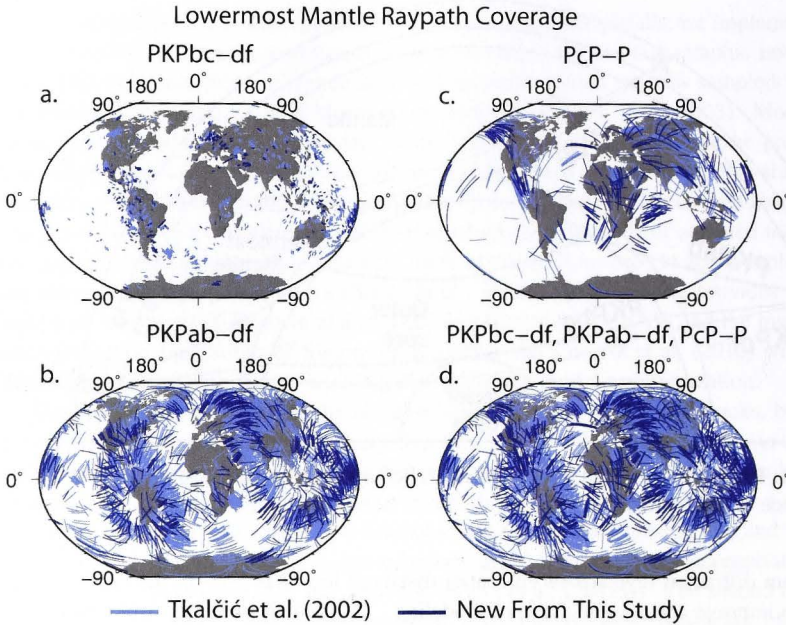


Figure 6.2: (a) PKPbc raypaths through the lowermost 300 km of the mantle associated with the PKPbc-df dataset. (b) PKPab raypaths associated with the PKPab-df dataset. (c) PcP raypaths associated with the PcP-P dataset. (d) raypaths associated with all three datasets. The raypaths from the datasets of Tkalčić et al. (2002) and Tkalčić (2010) are shown in light blue and those of this study are shown in dark blue.

time measurement error of between approximately 0.2 and 0.4 s. Then after a Hilbert transform is applied to the unfiltered PKPab waveform, the onsets of the seismic phase are aligned manually rather than by an automated cross-correlation technique (Figure 6.4a). Once precisely aligned, the travel time residual is calculated relative to the global reference model ak135 (Kennett et al., 1995) and corrections are made to account for the Earth's ellipticity (Kennett and Gudmundsson, 1996). Final, corrected residuals range from -4 to +6 s (Figure 6.5b), although most of this range results from a small cluster of very anomalous paths of ξ (angle between PKPdf leg and rotation axis of the Earth) between 20 and 30° originating in the South Sandwich Islands (SSI). The majority of residuals range between ± 2 s when the SSI data is excluded (see section 6.5.6 for further details).

Most of the dataset (1871 individually measured differential travel times) comes from large ($M_b > 5.8$) earthquakes of depths greater than 30 km recorded on the verti-

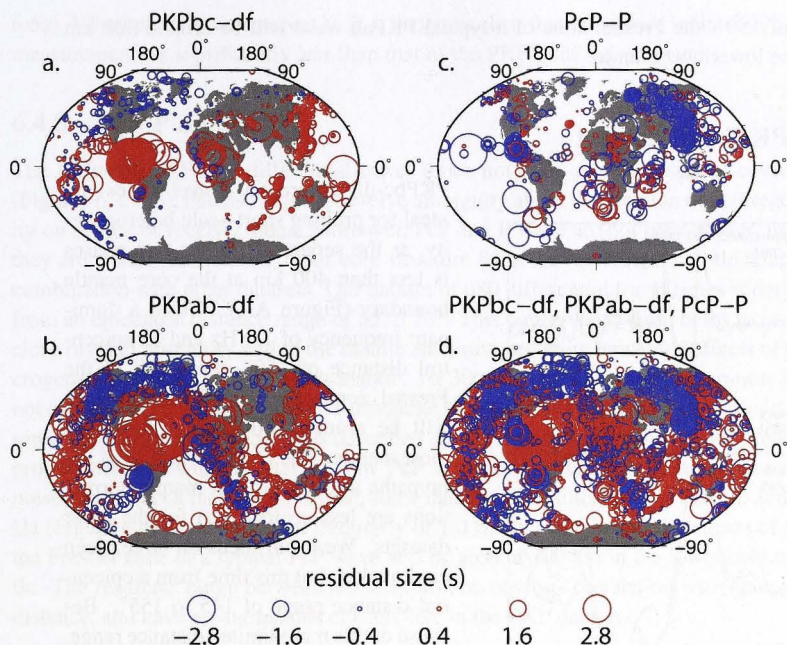


Figure 6.3: (a) PKPbc-df and (b) PKPab-df differential travel time residuals plotted at the surface projection of the bottoming point of the PKPdf raypath. (c) PcP-P differential travel time residuals plotted at the surface projection of the bottoming point of the PcP raypath. (d) differential travel time residuals of all three datasets. Positive residuals are shown by red circles; negative residuals are shown by blue circles.

cal component of primarily digital broadband instruments between 145 and 175° from the source. Although we use unfiltered data for measurement, PKP waves are in general best accentuated when filtered between 0.5 and 3.0 Hz. Data from large, deep earthquakes generally yield seismograms of good signal to noise ratios. Nonetheless, we only reserve measurements for the final inversion if the uncertainty associated with the temporal location of the phase onset is less than 0.5 s upon visual inspection. The PKPdf phase samples the inner core while the PKPab bottoms less deep and only samples the outer core (Figure A.1). The two phases are very similar in the crust and upper mantle (less than ~ 7 km separation at 30 km depth), which helps to remove most of the unwanted effects of heterogeneity near the source or receiver. The differences in raypath geometry of the two phases is, however, very sensitive to heterogeneity in the lowermost mantle, as the path separation ranges from $12 - 47^\circ$, or 720 to 2820 km, at the core mantle boundary. Given a dominant frequency of 1.0 Hz and an epicentral

distance of 150° , the Fresnel zone of a typical PKPab wave will be around 300 km wide in the lowermost mantle.

6.4.2 PKPbc-df dataset

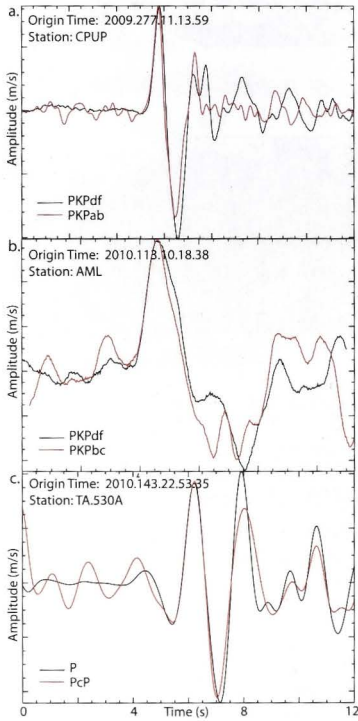


Figure 6.4: (a.) Plot of the final alignment of PKPdf and PKPab phases used to measure the differential traveltimes PKPab-df. A Hilbert transform and polarity reversal have been applied to the PKPab phase. (b.) Plot of the final alignment of PKPdf and PKPbc phases used to measure the differential traveltimes PKPbc-df. (c.) Plot of the final alignment of P and PcP phases used to measure the differential traveltimes PcP-P.

PKPbc-df differential travel times are ideal for probing short-scale heterogeneity, as the separation of the two phases is less than 400 km at the core mantle boundary (Figure A.1). Given a dominant frequency of 1.0 Hz and an epicentral distance of 150° , the width of the Fresnel zone of a typical PKPbc wave will be around 300 km in the lowermost mantle. The close proximity of the raypaths also means that mantle corrections are less critical than for the other datasets. We again focus on large, deep earthquakes, but this time from an epicentral distance range of 145 to 155° . Because of this more limited distance range, the PKPbc-df dataset is smaller than the PKPab-df dataset (1292 vs. 1871). Less measurements and shorter raypaths in the lowermost mantle makes the PKPbc-df sampling poor in comparison to the PKPab-df dataset (Figures 6.2, 6.3). ng poor in comparison to the PKPab-df dataset (Figures 6.2, 6.3).

Measurements are performed in much the same manner as with PKPab-df but without the application of the Hilbert transform. Relative phase offset times are carefully measured relative to ak135 after event relocation and ellipticity corrections are applied. The resulting residuals range from -1.5 to $+5$ s, however like in the PKPab-df case, this larger range results from a small cluster of anomalous paths from the SSI; the majority of the residuals range between ± 1 s (Figure

6.5a). When plotted with respect to ξ , it becomes clear that the spread in the PKPbc-df measurements is significantly less than that of the PKPab-df measurements.

6.4.3 PcP-P dataset

The inclusion of PcP-P differential travel times not only enhances spatial coverage (Figures 6.2, 6.3), but also helps to resolve ambiguity about the location of heterogeneity on source or receiver sides. Moreover, PcP and P wave are not core phases, hence they are useful for isolating inner core structure from the lowermost mantle when in combination with other datasets. Our dataset of 680 differential travel times is derived from an epicentral distance range of 55 to 70° . This conservative limit helps to ensure close raypath proximity within the mantle and crust, reducing unwanted effects of heterogeneity outside the lowermost mantle. At 300 km depth, raypath separation does not exceed 0.93° , or 98 km, for an earthquake with a surface depth of focus. Again, the same measurement procedures as described earlier are applied. Although we prefer to process the data without filtering, raw PcP arrivals are often buried in microseismic noise. To extract a measurable signal, some data required filtering between 1.0 and 3.0 Hz (Figure 6.4). At a dominant frequency of 1.0 Hz and an epicentral distance of 55° , the Fresnel zone of a typical PcP wave will be around 300 km in the lowermost mantle. The residuals range between ± 3 s, exhibit no obvious correlation with epicentral distance, and have no anomalous clusters like in the PKP datasets.

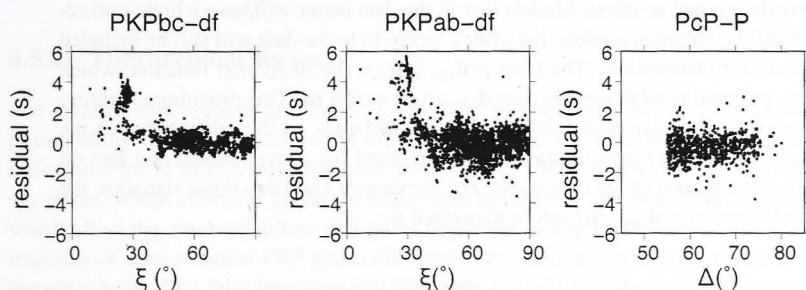


Figure 6.5: (left) The PKPbc-df, (middle) PKPab-df, and (right) PcP-P differential travel time datasets used in this study. Travel time residuals are plotted with respect to ξ ($^\circ$) (left, middle) or epicentral distance Δ ($^\circ$) (right).

6.5 Inversion method

In this paper we present a new approach to global tomography. We use a Bayesian inversion technique (e.g. Box and Tiao (1973), Tarantola and Valette (1982), Bernardo

and Smith (1994)) to invert for lowermost mantle P-wave velocity structure, as it is ideal for reliably representing model complexity and perturbation amplitude. This approach has been applied to a variety of seismological problems, including tomography (Zollo et al., 2002; Bodin and Sambridge, 2009; Khan et al., 2011; Bodin et al., 2012a; Mosca et al., 2012), receiver function inversion (Piana Agostinetti and Malinverno, 2010; Bodin et al., 2012b), and seismic source parameter estimation (Myers et al., 2007; Monelli and Mai, 2008). For a more complete description of Bayesian analysis refer to Bodin and Sambridge (2009), Bodin et al. (2012b), Bodin et al. (2012a), and Sambridge et al. (2013).

6.5.1 Transdimensional Bayes

The method relies on Bayes' theorem (Bayes, 1763), which provides the solution to the general inverse problem $\mathbf{d} = g(\mathbf{m})$, where \mathbf{d} is the data vector and g maps the model parameter vector \mathbf{m} into data, and can be stated mathematically as

$$p(\mathbf{m} | \mathbf{d}_{obs}) \propto p(\mathbf{d}_{obs} | \mathbf{m})p(\mathbf{m}), \quad (6.1)$$

where $p(\mathbf{m} | \mathbf{d}_{obs})$ is the posterior probability distribution function of the unknown model parameters \mathbf{m} solving the inverse problem given the data \mathbf{d}_{obs} . Solutions are described by a joint probability distribution function over all model parameters rather than a single optimal solution. Models that fit the data better will have a higher posterior probability, although models that offer a worse fit to the data will still be included in the posterior distribution. The term $p(\mathbf{d}_{obs} | \mathbf{m})$ is the likelihood function, which yields the probability of observing data \mathbf{d}_{obs} given model \mathbf{m} . This provides a measure of how well a particular model fits the data and depends on the misfit between the observed data and the synthetic traveltimes computed for a given model and also on the estimated variance of the data noise. For the case of Gaussian noise statistics, the likelihood function $p(\mathbf{d}_{obs} | \mathbf{m})$ can be expressed as:

$$p(\mathbf{d} | \mathbf{m}) = \frac{1}{\sqrt{(2\pi)^N | \mathbf{C}_e |}} \times \exp\left\{-\frac{1}{2} \{[g(\mathbf{m}) - \mathbf{d}]^T \mathbf{C}_e^{-1} [g(\mathbf{m}) - \mathbf{d}]\}, \quad (6.2)$$

In our case, \mathbf{d} is the vector of N observed differential travel times, $g(\mathbf{m})$ is the vector of N predicted differential travel times given the current lowermost mantle model \mathbf{m} . The method is transdimensional in the sense that model \mathbf{m} can have a variable number of defining parameters. In all inverse problems, the number of model parameters, and hence model complexity, is dependent on the level of data noise. Since the number of the model parameters can change, the required number of cells to fit the data can be expressed as a posterior probability distribution function. The term \mathbf{C}_e is the data noise covariance matrix, and $|\mathbf{C}_e|$ is its determinant. If the estimated error is

low, the required number of model parameters to fit the data will be relatively large, whereas high uncertainty will yield a simpler model of fewer parameters. By allowing a flexible number of unknowns, or a model of variable dimension, we appropriately leave model complexity to be determined by the data (Bodin et al., 2012a). Although it may seem that an overly complicated model would result in order to minimize data variance, the parsimonious nature of the Bayesian approach promotes the preservation of the simplest models that fit the data, thus preventing unjustified model complexity (Malinverno, 2002).

Going back to equation A.1, our prior information about model \mathbf{m} is represented by the a priori probability distribution $p(\mathbf{m})$. This is a mathematical representation of what we think we know about the model prior to performing the inversion. In order to minimally affect the inversion outcome, we employ a uniform distribution between -5% and +5% perturbation from the global reference model ak135 (Kennett et al., 1995) as part of our prior information. So $p(v_i) = 1/(v_{max} - v_{min})$ for values of v_i between v_{min} and v_{max} , and $p(v) = 0$ for all velocity values outside that range. Because the shape of any distribution multiplied by a uniform distribution will be unaffected, the prior information acts only as a lower and upper bound to the allowed velocity perturbations. Similarly, we impose prior assumptions about the number of Voronoi cells n needed to represent the data. We allow between 4 and 5000 cells, so $p(n) = 1/(n_{max} - n_{min})$ for all values of n between n_{min} and n_{max} , and $p(n) = 0$ otherwise.

6.5.2 Hierarchical Bayes

The level of data noise is an important unknown in modeling. In our case “noise” is everything that contributes to the difference between the observed and predicted differential travel time residuals (Scales and Snieder, 1998); this includes either theory errors, which affect the predicted differential travel times, or measurement errors, which affect the observed differential travel times. An example of a theory error is the mapping of core-sensitive PKP phase differential travel times exclusively to the lowermost mantle. In a joint inversion that also includes PcP-P differential travel times, which do not sample the core, the inner core effects on core-sensitive phases will not be coherent and will hence be accounted for as “data noise” (Bodin et al., 2012a). Another source for theory error is assuming a uniform thickness of 300 km for the lowermost mantle. Additionally, raypath geometries were not iteratively updated and ray theory instead of finite-frequency theory was utilized due to the prohibitive computational cost involved. For a typical PcP-P (epicentral distance of 55°) a 1% homogeneous increase in P-wave velocity in the lowermost 300 km of the mantle would create a ~ 0.12 s error if the raypath is not perturbed accordingly. This error may play a part in the differences between the PcP and PKP datasets (see section 6.6.2). For a PKPab-df raypath geometry with an epicentral distance range of 150° the error is less,

at around .02 s. For a PKPbc-df raypath geometry of the same epicentral distance, the error is even smaller, at around 0.001 s. The finite-frequency effects are in part diminished by the fact that the application of various bandpass filters suggests the dominant period of the datasets is approximately 1 s. Additionally, we use differential travel times rather than absolute times. Finally, the reference model is derived from data in which the finite frequency approximation was used. A more significant source of error would likely stem from the use of catalog data, such as the ISC datasets employed by many previous workers, due to triplication effects, forgoing the Hilbert transform of the PKPab phase, and not accounting for the source time function (in the case of absolute arrival times). An example of a source of measurement error is event mislocation, even though we use the event catalog presented by Engdahl et al. (1998), which uses ISC relocation algorithms. These approximations contribute to the misfit and are also accounted for as data noise. It is not possible, however, to estimate the ratio of theory errors to measurement errors. Similarly, it is not possible to estimate the relative contribution of each error source, whether it be theory- or measurement-based. Noise essentially represents the difference between the true residuals and the residuals able to be explained by our model.

We represent the data noise with the matrix \mathbf{C}_e , which for N data is a symmetric $N \times N$ matrix. We assume invariant, uncorrelated Gaussian random noise that is dependent only on the data type (i.e. whether it is a PKPab-df, PKPbc-df, or PcP-P differential travel time measurement). Therefore, the noise correlation matrix \mathbf{C}_e in equation A.2 is diagonal and can be expressed as follows (Gouveia and Scales, 1998):

$$\mathbf{C}_e = \begin{vmatrix} \sigma_1^2 & 0 & \dots & 0 \\ 0 & \sigma_2^2 & \dots & 0 \\ \vdots & \vdots & \ddots & \vdots \\ 0 & 0 & \dots & \sigma_i^2 \end{vmatrix} \quad (6.3)$$

where $\sigma_i = \sigma_1$ for PKPbc-df data, $\sigma_i = \sigma_2$ for PKPab-df data, and $\sigma_i = \sigma_3$ for PcP-P data. Each data type is represented by a single hyperparameter σ that is representative of the standard deviation of the data errors (measured in seconds). We invert for three different parameters to characterize the data uncertainty of the PKPab-df, PKPbc-df, and PcP-P datasets, as these datasets would not be expected to have the same level of noise; the raypaths, signal to noise ratios of the seismograms, and sensitivity to lowermost mantle structure and core mantle boundary topography are quite different. Although we predetermine the form of the matrix \mathbf{C}_e , the actual entry values are left as unknowns in the problem (Malinverno and Briggs, 2004; Malinverno and Parker, 2006). We do, however, impose the prior assumption that the data noise values will range between 0.01 s and 2.0 s for each dataset. The maximum of the posterior probability distribution functions of the σ values is used as the estimated noise level for each dataset. The relative uncertainty of the datasets determines their relative contribution to the inversion process (Bodin et al., 2012a,b), thereby removing any need

for ad hoc weighting factors.

6.5.3 Model parameterization

The lowermost mantle is modeled as an ensemble of Voronoi cells of variable size and shape (Figure 6.6). The positions of these non-overlapping polygons are defined by their Voronoi nuclei. Each point within a cell is closer to that cell's nucleus than to any other nucleus. Therefore, the cell walls are perpendicular bisectors of adjacent nuclei. For each cell, we have three unknowns: its position (defined by its latitude and longitude) and its velocity. The total number of these Voronoi cells is an unknown as well. A given model iteration is also parameterized by the σ values within the data noise correlation matrix C_e .

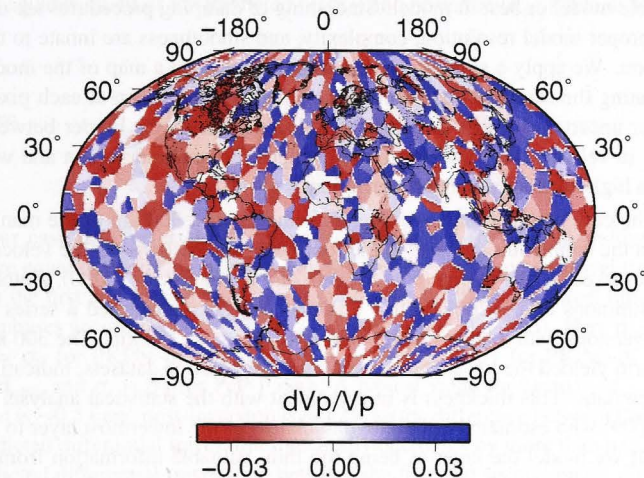


Figure 6.6: Example of a Voronoi P-wave velocity model realization in the lowermost 300 km of the mantle, which consists of an irregular, interlocking set of polygons. Each Voronoi cell encompasses all the points within the 2D space that are closer to its center than to any other Voronoi cell center.

Previous global tomographic studies invert for velocity structure using models based on blocks (e.g. Tkalčić et al. (2002), Vasco et al. (2006), Houser et al. (2008), Soldati et al. (2012)) or spherical harmonic expansions (e.g. Su et al. (1994), Antolik et al. (2003), Ritsema et al. (2011)). The problem with block parameterization is that arbitrary and fictitious velocity boundaries arise between the blocks. Ad-hoc error estimation and its consequent requirement for arbitrary smoothing and damping regularization are also issues, as the model is often overly-complex in regions of poor

sampling or high data noise. On the other hand, a spherical harmonic representation limits the resolution of fine-scale structure as might be expected of subducting slabs and mantle plumes. With a Bayesian approach, however, model parameterization is flexible and almost fully data-dependent. Large, small, smooth, and discontinuous structures can be imaged with appropriate levels of resolution.

Since the Voronoi cells can occupy an infinite range of configurations, we can take the average of a large number of post-convergence realizations to generate a continuous final model. We do this by taking the spatial mean of the distribution of velocity values at each point (we sample at every 1° in latitude and longitude) across the 2D region of interest. The grid of points for which we calculate an average velocity can be as fine as desired to enable visual evaluation of the model. This average model is both more complex and smoother than any one individual model. It is not, however, the most probable model or best fit model. Smoothing or damping procedures are unnecessary, for proper model resolution, complexity, and smoothness are innate to the averaged solution. We apply a similar procedure to approximate a map of the model error by calculating the standard deviation of the velocity distribution at each pixel. Areas of greater uncertainty, such as poorly sampled regions or the border between a sharp change in velocity, will undergo more changes in parameterization and will therefore have a higher velocity standard deviation.

We model the core mantle boundary layer as being the last 300 km of the mantle in part based on the significant increase in the root mean square (rms) of the velocity perturbations observed in this region (e.g. Mégnin and Romanowicz (2000), Antolik et al. (2003), Simmons et al. (2009), Zhao (2009)). We also performed a series of tomographic inversions with a layer thickness of 250, 300, and 350 km. The 300 km thickness scenario yielded the lowest noise estimates for the three datasets, indicating a better fit to the data. This thickness is in agreement with the statistical analysis of Garcia et al. (2009) who estimated the average thickness of the lowermost layer to be 350 ± 50 km. If we model the layer as being too thin, valuable information from P ray paths with bottoming depths above the 300 km level may be lost. On the other hand, an erroneously thick lowermost layer can potentially result in underestimated heterogeneity. An extended Bayesian scheme where layer thickness is variable would quantify the trade-off between layer thickness and the amplitude of perturbations, and is the subject of future research. Nonetheless, for this study, the perceived noise in the datasets for the most part includes effects of this approximation.

As discussed in Section 3.1, velocity perturbations (relative to an average ak_{135} velocity of 13.61 km/s in the lowermost 300 km of the mantle) are allowed to range between $\pm 5\%$. This conservative limit is necessary to properly assess the noise in the data. When the prior is too unrestrictive, the true variations in the data are misinterpreted as noise and a nearly laterally homogeneous model results.

Because the Voronoi cell generation is based on a rectangular grid, the global model is flattened from 3D to 2D. To ensure that the model agrees with itself along

the edges when wrapped around to form a sphere once again, the dataset is duplicated and shifted by 360° . The model space is made to range from -360 to $+360^\circ$ and when cropped back to -180 to $+180^\circ$ and wrapped around, the "seam" matches perfectly. Nonetheless, the models will remain somewhat "smeared" at the poles since the space is defined on a flat projection. Work to greatly improve this aspect of the model parameterization by implementing a spherical Voronoi cell grid is in progress.

6.5.4 Misfit evaluation

The Markov chain algorithm requires calculation of the likelihood for every model iteration. The likelihood function $p(\mathbf{d}_{obs} | \mathbf{m})$ describes quantitatively to what level the current model \mathbf{m} can reproduce the observed data, and as in Equation A.2 is related to the least squares misfit of the predicted ($g(\mathbf{m})$) and observed (\mathbf{d}_{obs}) data as follows:

$$p(\mathbf{d}_{obs} | \mathbf{m}) \propto \exp\left(-\frac{\phi(\mathbf{m})}{2}\right), \quad (6.4)$$

where

$$\phi(\mathbf{m}) = \left\| \frac{g(\mathbf{m}) - \mathbf{d}_{obs_i}}{\sigma_i} \right\|^2. \quad (6.5)$$

In our case \mathbf{d}_{obs_i} refers to the observed differential travel time residuals ($\Delta\delta\mathbf{t}$), which are equal to the difference between the observed differential travel time ($\delta\mathbf{t}_{obs}$) between the first and second phase and the predicted differential travel time between the two phases according to ak135 ($\delta\mathbf{t}_{ak135}$) (Kennett et al., 1995). Here $\mathbf{d}_{obs_i} = \mathbf{d}_{obs_1}$ and $\sigma_i = \sigma_1$ for PKPbc-df data, $\mathbf{d}_{obs_i} = \mathbf{d}_{obs_2}$ and $\sigma_i = \sigma_2$ for PKPab-df data, and $\mathbf{d}_{obs_i} = \mathbf{d}_{obs_3}$ and $\sigma_i = \sigma_3$ for PcP-P data. A typical value for $\|g(\mathbf{m}) - \mathbf{d}_{obs}\|$ prior to inversion is ~ 0.5 s and post-inversion is ~ 0.2 s, so the difference between the observed and predicted differential travel times generally decreases by more than half. If $\delta\mathbf{t}_m$ is the predicted differential travel time between the first and second phase given model \mathbf{m} ,

$$\phi(\mathbf{m}) = \left\{ \left\| (\delta\mathbf{t}_m - \delta\mathbf{t}_{ak135}) - (\Delta\delta\mathbf{t}_{obs}) \right\| / \sigma_d \right\}^2. \quad (6.6)$$

Using the simple relationship $\mathbf{d} = \mathbf{v}\mathbf{t}$ and the fact that we use fixed raypaths according to ak135,

$$\phi(\mathbf{m}) = \left\{ \left\| \frac{\delta\mathbf{d}(\mathbf{m})}{v_{ak135}[1 + \mathbf{p}(\mathbf{m})]} - \frac{\delta\mathbf{d}(\mathbf{m})}{v_{ak135}} - (\Delta\delta\mathbf{t}_{obs}) \right\| / \sigma_d \right\}^2, \quad (6.7)$$

where $\mathbf{p}(\mathbf{m})$ is equal to the velocity perturbation relative to the average velocity of the reference model ak135 in the lowermost 300 km of the mantle (13.61 km/s). The vector $\delta\mathbf{d}(\mathbf{m})$ is the difference in raypath distance between the first and second phase across each Voronoi cell of model \mathbf{m} . We integrate $\phi(\mathbf{m})$ over all Voronoi cells.

Each path length difference is calculated by sampling the raypaths at increments on the order of 10 km and determining to which cell the midpoint of the ray segment belongs. Segment lengths belonging to the same cell are then added together prior to integrating along the raypath. As explained in more detail in section 3.2, σ_d is dependent on the phase type and is therefore represented by one of three unknowns, σ_1 for PKPbc-df, σ_2 for PKPab-df, and σ_3 for PcP-P.

6.5.5 Sampling of the model space

The Bayesian class of inversion is based on ensemble inference, meaning that a large number of models are generated, each with varying parameters, according to the generalized version of Markov chain Monte Carlo (MCMC) sampling called Reversible Jump MCMC (Green, 1995, 2003), which is based on the Metropolis-Hasting algorithm of Metropolis et al. (1953) and Hastings (1970). Prior to producing the first model, which is randomly created by selecting values from the prior distributions, raypaths are determined according to ak135 (Kennett et al., 1995) using TauP (Crotwell et al., 1999). At each step in the inversion, a proposed model is created from a random perturbation of the current model (Mosegaard and Tarantola, 1995). The perturbation can result from one of five possible changes. First, a new set of σ values can be selected to represent the data noise; this change is applied at every iteration. At every odd iteration the second type of change is performed, which is that the velocity value of one randomly selected Voronoi cell is changed. This new velocity value v' is chosen such that

$$v' = v + u\lambda, \quad (6.8)$$

where v is the original velocity of the cell, u is a random number selected from a normal distribution between -1 and 1, and λ is the standard deviation of the proposal. The λ value is determined by the user and will affect the rate of convergence, but not the end result of the inversion. At every even iteration, one of the three remaining types of change is chosen at random to occur: (1) the position of one randomly selected Voronoi cell is perturbed according to a 2D Gaussian proposal probability density centered at the current position, (2) a new Voronoi cell is added at a randomly selected location with a velocity chosen from a Gaussian proposal probability centered on the current velocity value where the "birth" takes place (same form as equation 6.8), or (3) a randomly selected Voronoi cell is deleted.

After the model is updated, the differential traveltimes are recomputed and compared with the observed differential travel times. The new model is then either accepted or rejected according to certain acceptance criteria (Bodin and Sambridge, 2009). The probability of accepting a proposed model \mathbf{m}' given the current model \mathbf{m} is $\alpha(\mathbf{m}' | \mathbf{m})$, which Green (1995, 2003) equates to the following in order to ensure convergence of the models toward the posterior distribution:

$$\alpha(\mathbf{m}' | \mathbf{m}) = \min\left\{1, \frac{p(\mathbf{m}')}{p(\mathbf{m})} \times \frac{p(\mathbf{d}_{obs} | \mathbf{m}')}{p(\mathbf{d}_{obs} | \mathbf{m})} \times \frac{q(\mathbf{m} | \mathbf{m}')}{q(\mathbf{m}' | \mathbf{m})} \times |\mathbf{J}|\right\}, \quad (6.9)$$

where $p(\mathbf{m}')$ and $p(\mathbf{m})$ are the prior for the proposed and current model, $p(\mathbf{d} | \mathbf{m}')$ and $p(\mathbf{d} | \mathbf{m})$ are the likelihood functions (Equation A.2) for the proposed and current model, and $q(\mathbf{m} | \mathbf{m}')$ and $q(\mathbf{m}' | \mathbf{m})$ are the forward and reverse proposal functions. The term $|\mathbf{J}|$ is the Jacobian, which enables a transformation between models of different dimension or parameterization. In the case of changes that do not affect model dimension (velocity change or cell move), $q(\mathbf{m}' | \mathbf{m})$ is equal to $q(\mathbf{m} | \mathbf{m}')$, meaning that it is equally probable that we generate a proposed model \mathbf{m}' if we start with model \mathbf{m} as it is that we generate model \mathbf{m} if we start with model \mathbf{m}' . In the case of a birth or death of a cell, however, the model dimension changes and the proposal functions encourage changes to the model. So in the event of a cell birth, the proposed cell's velocity is encouraged to deviate from the velocity of the cell that was in that position in the original model. Likewise, a cell death is favored if the velocity of the deleted cell varies considerably from the velocity of the cell that will replace its position upon removal. These trends are of course subdued once combined with the likelihood and prior ratios of equation 6.9. One end result is that uneven raypath sampling is reflected in the relative size of Voronoi cells of an individual model. Larger cells will persist or form (via cell death) in regions of sparser sampling while much smaller cells can be justified and created (via cell birth) in regions of densest sampling (Bodin and Sambridge, 2009).

To determine if the proposed model \mathbf{m}' is accepted or rejected, we generate a uniformly distributed random number u between 0 and 1. If $u(\mathbf{m}')$ is greater than $\alpha(\mathbf{m}')$, then the model \mathbf{m}' is rejected and model \mathbf{m} is retained for the next step in the chain. Otherwise, model \mathbf{m}' is accepted and forms the new basis to which the next perturbation will occur. According to equation 6.9, if model \mathbf{m}' fits the data better than model \mathbf{m} , it will always be accepted. Models that fit the data almost as well as the previous model will be accepted most of the time, and models that fit very poorly in comparison to the previous model will be accepted only very rarely. In this manner the chain's path will be guided towards parameter space of high target density; the sampling distribution will mimic the target posterior distribution.

The first portion of unstable, "burn-in" iterations (usually around 2 million for the inversions considered here) is discarded, while the remaining, post-convergence portion is deemed representative of the posterior distribution (Green, 1995, 2003). We define post-convergence as the point at which average data misfit, average number of cells, and all velocity parameters cease to fluctuate beyond that of a normal white noise process and the solution map stabilizes. Once we acquire a large ensemble of independent models, we can extract useful properties, such as the average, median, or best model (Smith, 1991). To ensure model independence, we "thin" this second part of the chain by only retaining every 50th or 100th model for the final ensemble from

which we calculate a point-wise spatial average model, so usually around 800,000 post-convergence models are generated.

6.5.6 Measurement corrections

Creager (1999) suggested that the inner core is strongly cylindrically anisotropic throughout most of the western hemisphere with the fast direction aligned with or near the spin axis. Although a simple model of cylindrical inner core anisotropy with the fast axis aligned with the Earth's rotation axis has been disputed (e.g. Tkalčić (2010), here we test whether such a scenario may be affecting our lowermost mantle model inversion results by inverting the PKPab-df, PKPbc-df, and PcP-P differential travel times for two cases: 1. all raypaths (Figure 6.14) and 2. all raypaths excepting those recorded from events in the South Sandwich Islands (SSI), which are strongly polar (Figure 6.13). The total number of PKPab-df data points decreases from 1871 to 1786, and the number of PKPbc-df data points decreases from 1291 to 1042. The exclusion of these very polar paths (angle $\xi < 30^\circ$) does not significantly affect the pattern of the velocity variations of P-wave velocity model of the lowermost mantle; however, the rms of the velocity perturbations does change significantly. By removing SSI data, the rms reduces from 1.00% to 0.87%. In addition, when excluding the SSI data, the noise estimates for each dataset decrease by approximately 5%, indicating a higher quality dataset is achieved by removing these anomalous paths. When removing the relatively few polar paths not associated with the SSI, similar effects on data noise estimates and the strength of perturbations are not seen. Therefore, our preferred average model (Figure 6.13) includes polar paths except for those coming from the SSI, which may be influenced by strong mantle heterogeneity related to slabs or fragments (Tkalčić, 2010). Consequently, we also exclude SSI data from all inversions using the PKPbc-df and PKPab-df datasets (Figures 6.9, 6.11, 6.12, 6.13).

Despite our preventative measures of removing SSI data, there will still be some mapping of core structure to the lowermost mantle. We further mitigate this effect by including PcP-P measurements, which do not sample the core. These differential travel times help to remove the ambiguity between lowermost mantle and inner core contributions to core phase arrival times. We also use a hierarchical Bayesian model, which allows everything that cannot be explained by our model to be treated as data noise. If there are inner core effects, they will imply incoherency between different data types and will therefore be treated as "theory errors". The overall agreement between areas of adequate coverage by all three datasets helps to confirm that core structure can only have a minor effect on the differential travel times (Figures 6.10, 6.11).

Mantle effects are corrected for using the 3D mantle model of Della Mora et al. (2011), which results from the inversion of direct P-wave arrival times using a regularized least-squares framework. This model is based on $\sim 620,000$ measurements

from the ISC bulletin and is undoubtedly biased by inconsistent measurement quality, exclusive use of direct arrivals, smoothing and damping, and block parametrization. Nonetheless, it provides a reasonable approximation of upper mantle P-wave velocity perturbations, which is where the power of heterogeneity is greatest and therefore most important for us to consider. Della Mora et al. (2011) importantly correct for crustal structure and relocate sources according to Antolik et al. (2003).

6.6 Results

6.6.1 Resolution tests

Each dataset uniquely contributes to the retrieval of a lowermost mantle P-wave velocity model due to the different sampling patterns of the raypaths. This is illustrated through two sets of resolution tests (Figures 6.7 and 6.8). For each test in the first set, synthetic data is calculated according to the raypath geometry of the actual dataset for a known velocity model consisting of 20° squares alternating between -2% and $+2\%$ velocity variation perturbations (relative to ak135). Gaussian random noise with a standard deviation of 0.5 s is added to the synthetic data. The synthetic travel times are inverted using the same Bayesian technique as is used for the real data, and the retrieved model is compared to the actual model to assess the resolution potential given the data and method. Figure 6.7f shows the actual model used to produce the synthetic travel times. The retrieved model of the first test (Figure 6.7a) is a visual representation of the resolution potential of the PKPab-df dataset alone. As expected, the best model recovery is obtained in regions of best sampling, in particular Africa, the Atlantic, and east Asia/Indonesia. The resolution test is performed for the PKPbc-df and PcP-P datasets as well (Figure 6.7b, c). From these results it is clear that the PKPbc-df data alone cannot provide reliable information about the velocity structure for most of the globe; for this reason we only use PKPbc-df measurements when in combination with other datasets.

Finally, we join all three datasets. Now the PcP-P raypaths geometries help attribute the PKPab-df and PKPbc-df residuals to either the source or receiver side of the raypaths and much improvement is seen in the recovered model (Figure 6.7d). These tests show that in general, structure on the order of 20° in diameter is easily resolved given the method and data sampling. Areas where some smearing and damping of actual perturbation amplitude should be expected, however, include the mid-Pacific, the north Atlantic, the south Indian ocean, and the poles. The poorly resolved areas coincide with spatial gaps in raypath coverage. In these areas, there is either no sampling, or given the noise in the data, insufficient sampling to recover the true model.

Figure 6.7e demonstrates the effect of neglecting mantle effects in the data corrections. Here we display the recovered model using all three datasets with additional noise added that is equal to the travel time corrections associated with the Della Mora

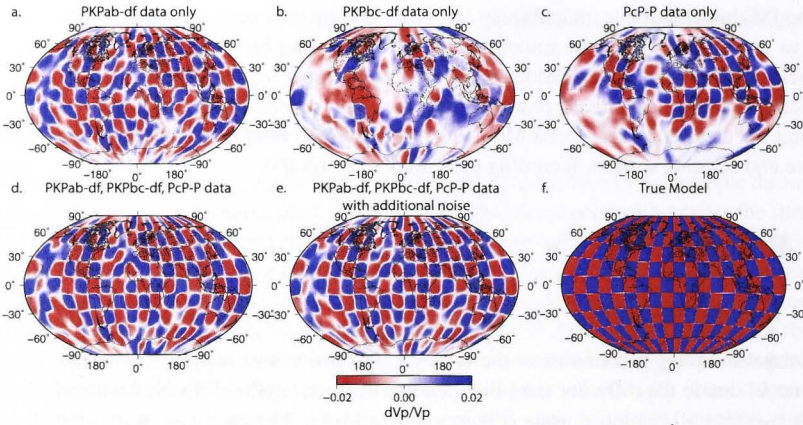


Figure 6.7: The recovered model using the PKPab-df dataset only (a), the PKPbc-df dataset only (b), the PcP-P dataset only (c), all three datasets (d), and all three datasets with additional noise added (e). Also shown is the true model (f) used in the checkerboard resolution tests to produce synthetic data. This input model (f) has alternating 20° squares of $\pm 2\%$ velocity perturbations.

et al. (2011) mantle model. These noise values range from -0.7 s to 1.2 s depending on the ray path geometry. From this figure it is evident that mantle corrections have very little effect on the final model, as the recovered models in Figures 6.7d and 6.7e are nearly indistinguishable. When mantle corrections are considered (Figure 6.7d), however, the rms of the velocity variations is slightly more accurately recovered (1.38% vs. 1.32%).

The second set of synthetic tests is designed to compare our Bayesian inversion approach to that of a more traditional linearized inversion method, namely one that uses a lower triangular-upper triangular decomposition algorithm (e.g. Tkalcic et al. (2002)). The true model of this second test has structure of varying size, shape, and orientation (Figure 6.8) as to test the limits of the resolution potential of the complete dataset (PKPab-df, PKPbc-df, and PcP-P) given each inversion method. The positive anomalies are 2% faster than the ak135 average velocity and the negative anomalies are 2% slower. This time, no noise is added to the synthetics. For the Bayesian inversion, we allow the perturbations to range between $\pm 5\%$. In areas of good raypath coverage, the method is able to retrieve the pattern and strength of the velocity pattern with reasonable accuracy (Figure 6.8). The rms of the velocity perturbations is 1.44% (actual rms is 2%). The method fails only to retrieve the structures of the finest scale (small circles of 6° (~ 360 km) diameter). The Bayesian approach is clearly able to retrieve sharp velocity contrasts and both small and large scale features in areas of

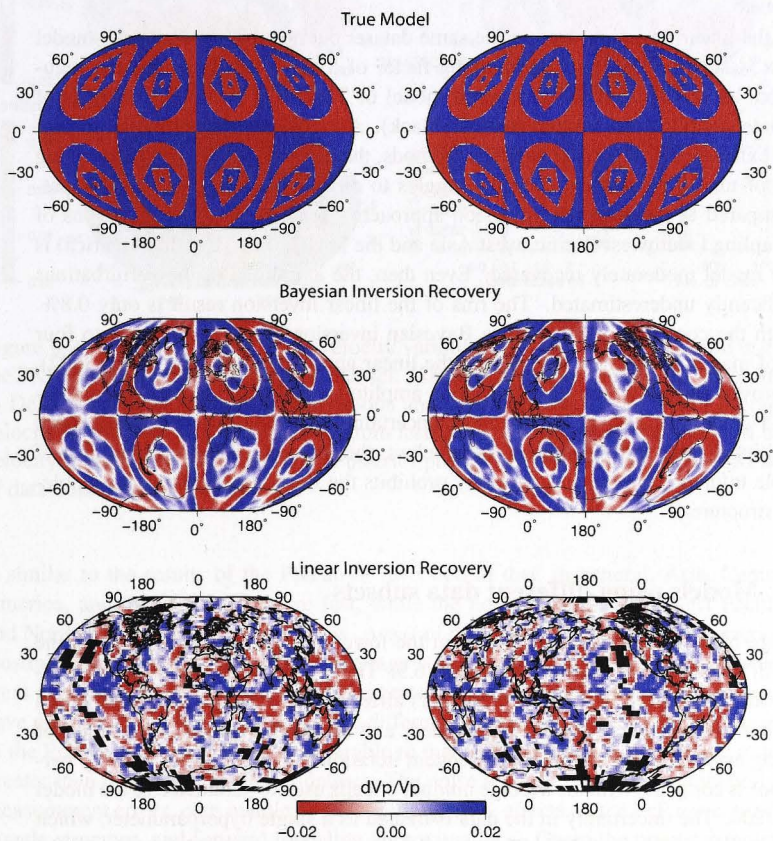


Figure 6.8: Synthetic resolution test using an irregular true model (top). The positive anomalies are 2% faster than the ak135 average velocity and the negative anomalies are 2% slower. (middle) The recovered model using a Bayesian inversion of the PKPab-df, PKPbc-df, and PcP-P datasets. (bottom) The recovered model using a more traditional linearized inversion method from Tkalčić et al. (2002).

adequate raypath sampling. The method is also shown to be fully capable of recovering curved discontinuities despite the fact that Voronoi cells have only straight edges; after averaging many differently-positioned straight-sided polygons, curved lines can be retrieved.

For the linear inversion, we use the same dataset but now parameterize the model into $5^\circ \times 5^\circ$ squares. We apply a damping factor of 5×10^5 , but no smoothing regularization, as was applied to the favored model of Tkalčić et al. (2002). Blocks of inadequate sampling are omitted (colored black). Although we do not intend to provide an exhaustive comparison between methods, the linear inversion technique using this set of tuning parameters clearly struggles to recover the complex velocity pattern compared to the Bayesian inversion approach (Figure 6.8). Only in regions of best sampling (southwest Pacific, west Asia and the Middle East, Central America) is the true model moderately recovered. Even then, the amplitude of the perturbations is significantly underestimated. The rms of the linear inversion result is only 0.8%. Although the computational cost of a Bayesian inversion is in general three to four orders of magnitude greater than that of the linear approach of Tkalčić et al. (2002), the improved ability to recover perturbation amplitudes and both velocity discontinuities and gradations and the provision of uncertainty and data error estimates merit the additional time and resources. Nonetheless, the immense computational cost of ensemble inference approaches currently prohibits the Bayesian inversion for whole-mantle structure.

6.6.2 Models using different data subsets

An image of P-wave velocity variations in the lowermost mantle resulting from the PKPab-df dataset alone is shown in Figure 6.9. There were 3.5 million model iterations produced on each of 60 CPU processors after running for 200 hours. The initial 2.5 million burn-in iterations were discarded, and the model shown is the result of averaging every 50th model of the subsequent iterations. The pattern of velocity perturbations is complex, with the average number of cells used to parameterize the model being ~ 200 . The uncertainty in the data is treated as a single hyperparameter, which after inversion peaks at ~ 0.60 s. The rms of the perturbations is 1.07%, although the maximum perturbation is 4.74%. This figure is several times larger than previous estimates (e.g. Tkalčić et al. (2002), Antolik et al. (2003), Lei and Zhao (2006), Houser et al. (2008), Li et al. (2008), Della Mora et al. (2011), and Soldati et al. (2012)), which were driven by subjective choices for damping. Because our method does not require explicit damping of the final model and such strong velocity perturbations are required by the data, we are able to justify a large variance reduction. The final rms of the residuals is 0.58 s, which is 59% less than the rms of the residuals resulting from a homogeneous lowermost mantle layer with a velocity of 13.61 km/s.

Next we invert the PcP-P dataset alone (Figure 6.10). The resulting average model

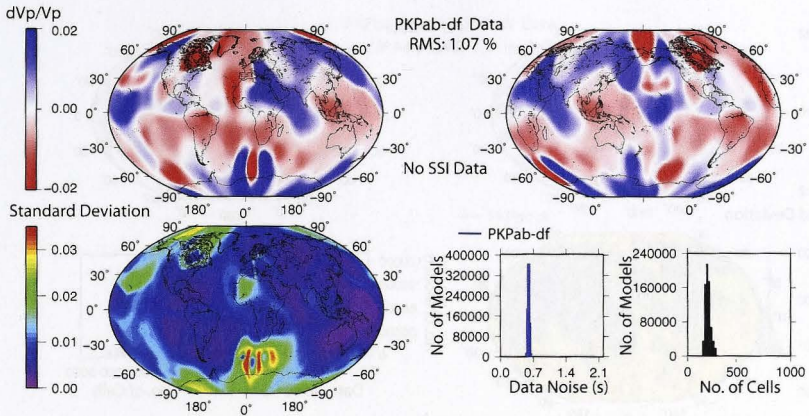


Figure 6.9: (top) Model of P-wave velocity variations in the lowermost mantle using the PKPab-df differential travel time dataset. Mantle corrections are applied according to Della Mora et al. (2011). Perturbations are shown relative to the ak135 average velocity of the layer (13.61 km/s). (bottom left) Map of the standard deviation of the velocity perturbation. (bottom right) Posterior probability distributions of the PKPab-df data noise and number of cells.

is similar to the results of the PKPab-df inversion in that, in general, Asia, Central America, and the Middle East are fast, while the north Atlantic, southwest Pacific, and North America are in general slow. Areas of discrepancy include South America, Australia, and Africa, where PcP-P coverage is poor. The basic congruency between areas of adequate coverage, however, suggests that the inner and outer core structure have no more than a minor effect on the differential travel times. The estimated noise in the PcP-P dataset (0.57 s) is comparable to that of the PKPab-df dataset and much greater than that of the PKPbc-df dataset. The noise is likely due to a combination of measurement errors, core mantle boundary topography effects on the PcP travel times, mantle structure, and forward modeling approximations. Given the poorer sampling and much greater sensitivity to mantle structure, the PcP-P dataset is less coherent than the PKP datasets. Moreover, the PcP data only sample the lowermost mantle once, whereas PKPbc and PKPab rays sample it on both the source and receiver side. The resulting lack of flexibility in redistribution of the residual times to either the source or receiver side combined with the aforesaid poorer coherency means that many Voronoi cells are required to achieve the 55% decrease in residual variance. The hierarchical Bayes approach of this study accounts for this effect when jointly inverting different data types, as less weight is naturally given to the more inconsistent datasets.

When the PKPab-df and PKPbc-df datasets are combined (Figure 6.11), the reso-

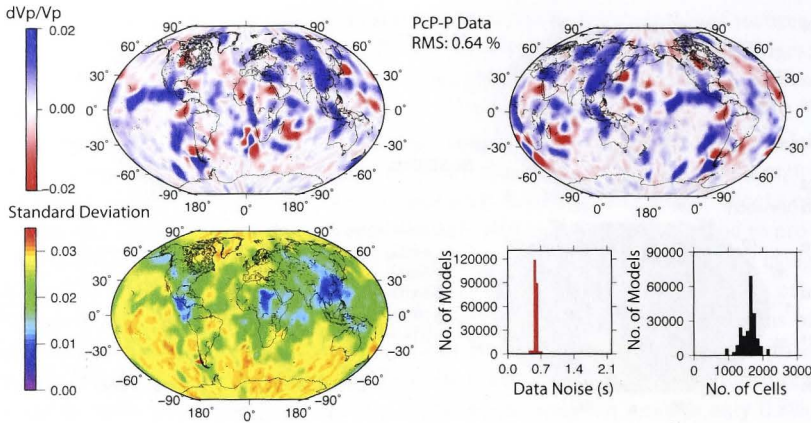


Figure 6.10: As for Figure 6.9 but for the PcP-P dataset.

lution improves relative to when PKPab-df is used alone, and the average number of cells used to parameterize the models is ~ 800 . This general increase in the required number of cells is reflected in the obvious increase in model resolution (Figure 6.7), although the main features of PKPab-df-only and the PKPab-df + PKPbc-df models are in excellent agreement, indicating a strong compatibility between the two datasets. The resulting average model explains 51% of the PKPab-df residuals and 49% of the PKPbc-df residuals, and the rms of the perturbations is 1.02%. The estimated noise of the PKPab-df dataset is significantly greater than that of the PKPbc-df dataset (0.62 vs. 0.34 s). This difference is likely a reflection of multiple factors, one of which is the decrease in scatter of the PKPbc-df residual data compared to the PKPab-df residual data (Figure 6.5). Another consideration is that PKPbc waves sample much shallower in the inner core, which means they are less attenuated, and therefore more easily and accurately measured than the deeper-sampling PKPab waves. Additionally, one must apply a Hilbert transform to the PKPab waveforms prior to comparison with the PKPdf waveform; this procedure can result in approximations and errors in the measurements. Finally, the PKPbc and PKPdf raypaths travel much closer together throughout the mantle than the PKPab and PKPdf raypaths, meaning that unwanted mantle effects will be greatly diminished. Nonetheless, the PKPab-df dataset is critical to the inversion as it provides significantly better spatial coverage than the smaller PKPbc-df dataset. The noise estimates of the two datasets act as relative weights in the inversion. Even though the PKPbc-df dataset is smaller, it has less associated error, and will therefore have a similar impact on the final model as the PKPab-df dataset.

Next we add the PcP-P differential travel times to the PKPab-df times (Figure 6.12b). The two datasets have similar noise estimates (0.76 s for PcP-P and 0.61 s

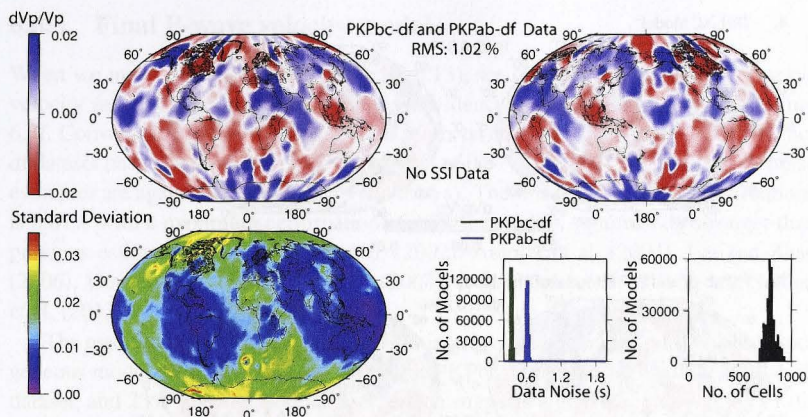


Figure 6.11: As for Figure 6.9 but for the PKPab-df and PKPbc-df datasets combined.

for PKPab-df) and so have comparable weight in the inversion. Figure 6.12a shows the tomographic model TRH_KC from the work of Tkalčić et al. (2002) for comparison. In this case, a linear inversion of PKPab-df and PcP-P travel time residuals was performed on a grid of variable-size blocks. Blocks of inadequate sampling are colored black. Since damping and smoothing procedures were applied, the amplitude variations of model TRH_KC (rms of 0.31%) are about a third as strong as the amplitudes retrieved by our modeling (rms of 0.88%). The absence of block parameterization and smoothing procedures and the increase in spatial sampling all contribute to the increased resolution of our final model. Despite the vast differences in inversion method, the large-scale features of the two models are in good agreement. For example, Canada, the southwest Pacific, most of South America and the south Atlantic are slow, while Asia, Central America, Antarctica, and the Middle East are fast. Even some of the finer-scale features are congruous, such as the sharp transition from fast to slow velocities at the eastern Alaskan border. Besides improvements in resolution, our model is noteworthy in that we are able to retrieve the strength of perturbations as well as the model uncertainty (Figure 6.12c). Model uncertainty is expressed visually by plotting the standard deviation of the velocity distribution at each pixel. Another appealing feature is that, because the variable nature of both the parameterization and the data noise, the resolution of the final model is automatically controlled by the information content of the data.

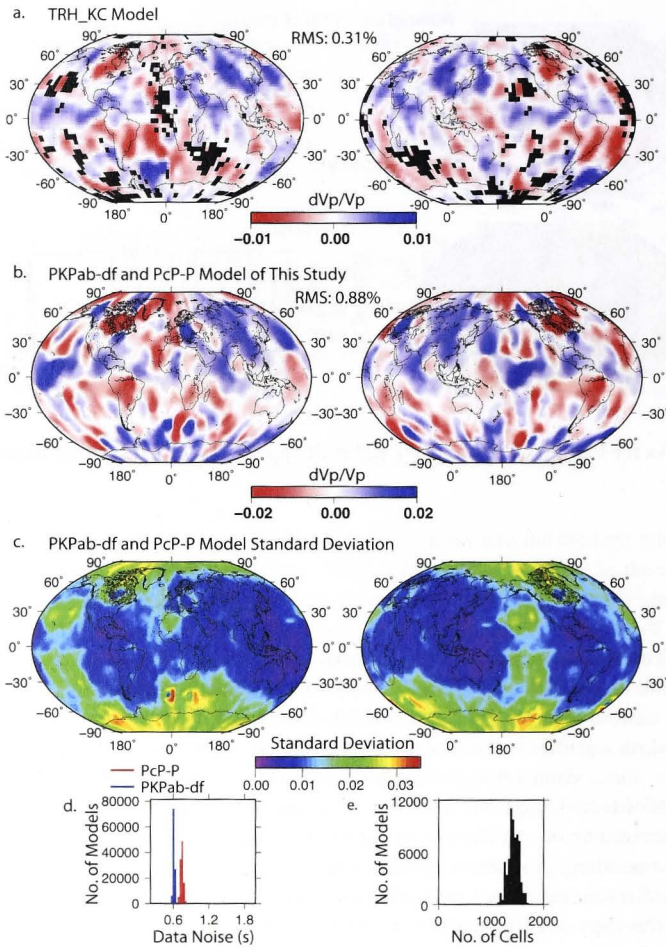


Figure 6.12: (a) The result (model TRH_KC) of the previous high-quality dataset of PKPab-df and PcP-P differential travel times from Tkalčić et al. (2002) who performed a linear inversion for the P-wave velocity structure of the lowermost mantle. Areas of insufficient data coverage are shown by black squares. (b) Bayesian inversion results for the PKPab-df and PcP-P datasets of this study. Note the difference between the color scale ranges and the root mean square values of the velocity perturbations between the two models. (c) A map of the standard deviations of the velocity distributions for each latitude/longitude pair of the model in (b). (d) Posterior probability distribution of the PKPab-df and PcP-P noise, and (e) Posterior probability distribution of the number of cells used to describe the model.

6.6.3 Final P-wave velocity model

When we invert all three datasets (Figure 6.13), we obtain a high resolution P-wave velocity model of the lowermost mantle as evidenced by the resolution test in Figure 6.7f. Convergence requires over 500 CPU hours on each of 60 processors. The PKPbc-df dataset has the lowest estimated noise level of 0.37 s; the PcP-P and PKPab-df noise estimates are again very close (0.78 s and 0.66 s). The rms of the velocity perturbations is 0.87% with a maximum perturbation of 4.74%, which is significantly stronger than previous estimates (e.g. Tkalčić et al. (2002), Antolik et al. (2003), Lei and Zhao (2006), Houser et al. (2008), Li et al. (2008), Della Mora et al. (2011), and Soldati et al. (2012)).

The resulting model reduces the differential travel time variance relative to a homogeneous model of 13.61 km/s by 45% for the PKPbc-df dataset, 49% for the PKPab-df dataset, and 23% for the PcP-P dataset, which suggests a general compatibility of the three datasets. The noise, sampling, and size of each dataset prevents further reduction of data misfit. Traditional linear inversions seek to produce a single model that minimizes the variance of the data; the Bayesian method, however, produces an ensemble of solutions whose complexity is reflected by the interpreted noise in the data. The data uncertainty determines how accurately the measurements are fit. Consequently, one should not consider the variance reductions given in the study in quite the same light as would be done for a linearized inversion, as data noise and unmodeled effects are also accounted for. Furthermore, the average model is only one measure of the ensemble of solutions, and it is often possible to select individual models that yield greater reductions in data variance (e.g. Shapiro and Campillo (2004), Moschetti et al. (2010), Behr et al. (2010)).

The large scale patterns inferred here are consistently seen in other traveltimes tomography models (e.g. van der Hilst and Kárason (1999), Tkalčić et al. (2002), Antolik et al. (2003), Vasco et al. (2006), Zhao (2004), Lei and Zhao (2006), Li et al. (2008), Houser et al. (2008), Zhao (2009), Soldati et al. (2012)), as there is agreement about the presence of fast velocities beneath Central America and East Asia and slow velocities beneath south Africa and the southwest Pacific. Common areas of discrepancy include North America, Australia, and Europe, which could be a result of poorer sampling, systematic errors in travel time picks, inversion method, and/or data noise. The chief advantage of our model over previous models is that because there is no arbitrary smoothing, damping, or grid-spacing, the scale-size and amplitude of the velocity heterogeneity are controlled directly by the data.

6.7 Discussion

The primary goal of this work is to invert for the P-wave velocity heterogeneity in the lowermost mantle as can be reliably retrieved from body wave differential trav-

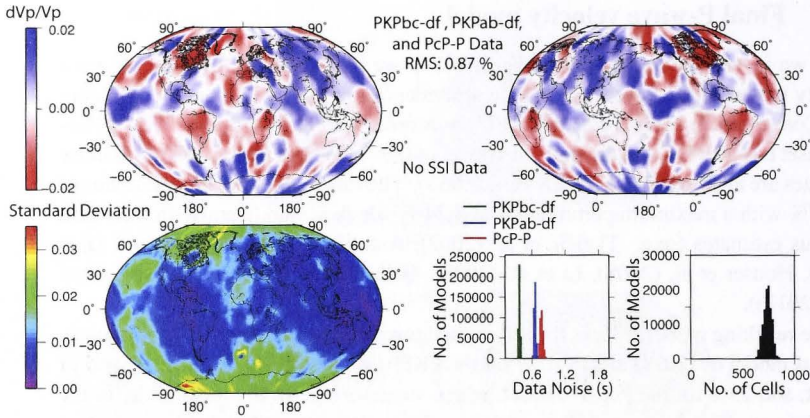


Figure 6.13: As for Figure 6.9 but for the PKPbc-df, PKPab-df, and PcP-P datasets combined. The South Sandwich Islands earthquakes are excluded from the dataset prior to inversion.

eltimes. The scale-length of the heterogeneity depends on the dataset(s) used, but invariably structure ranging from wavelengths of hundreds to thousands of kilometers is revealed. Lowermost mantle heterogeneity at even smaller scales is almost certainly present, however, (e.g. Cormier (1999), Helffrich (2002), Margerin and Nolet (2003), Garcia et al. (2009)), but its resolution is not justified by the inferred noise levels of our datasets. It is important to note that no single dataset, or even pair of datasets, produces as high resolution a map as does the combination of all three datasets (Figure 6.7). Each dataset provides unique and invaluable information that is critical to revealing the complexities of the lowermost layer. The PKPbc-df dataset is crucial to identifying the exact location of anomaly edges, as the PKPbc and PKPdf raypaths are very close within the lowermost mantle (raypath separation $< 3^\circ$). The PKPab-df dataset is the largest and provides the best spatial coverage. However, the PKPab waves sample deeper in the inner core, making them more attenuated and more difficult to measure than the more shallow-sampling PKPbc waves. The PKPab-df dataset also suffers from small errors resulting from the application of the Hilbert transform prior to alignment of the PKPab waveform with the PKPdf waveform. Finally, the PcP-P dataset is important because it is not subject to inner core effects and because of its ability to resolve ambiguity about the location of heterogeneity on source or receiver sides. The capabilities of our inversion approach combined with an exceptionally high-quality dataset enables the inversion for a global velocity model of the lowermost mantle with unprecedented reliability. The difference between our results and previous models is likely due to our evasion of block parameterization, truncation

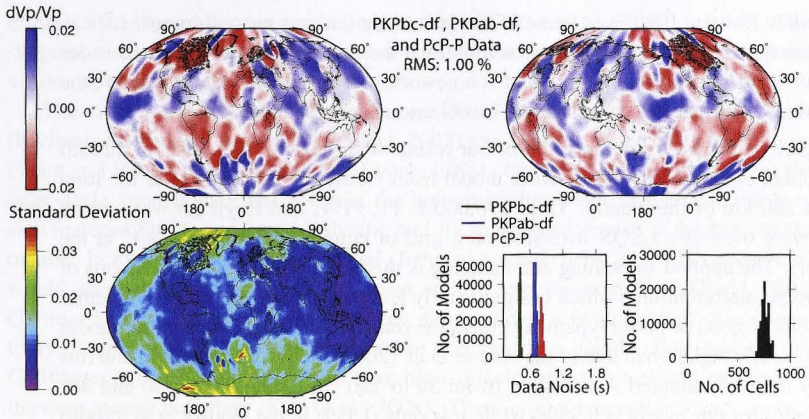


Figure 6.14: As for Figure 6.13 but with South Sandwich Islands data included.

of spherical harmonic expansions, and smoothing and damping regularization and our improvements to spatial coverage and data quality.

The rms heterogeneity level of 0.87% from our final tomographic model is significantly larger than the majority of previous estimates obtained from body wave travel time analysis (Tkalčić et al., 2002; Zhao, 2004; Lei and Zhao, 2006; Zhao, 2009; Houser et al., 2008; Soldati et al., 2012). Garcia et al. (2009), who performed a statistical analysis of P-wave heterogeneity in the lowermost mantle also obtained a higher estimate ($1.2 \pm 0.3\%$). This can be explained by the fact that like in our study, Garcia et al. (2009) did not use the damping procedures typically employed in other inversion approaches. There is evidence, however, that P-wave velocity variations in the lowermost mantle can reach even greater extremes than are revealed in our study. For example, in ultra-low velocity zones (ULVZs) P-wave anomalies can be up to 10% (Ni and Helmberger, 2001b; Garnero et al., 1998). We can not expect to reveal such features, however, for the thickness of ULVZs is on the order of tens of kilometers (Wen and Helmberger, 1998; Garnero et al., 1998), whereas our model presents a depth-averaged image of the lowermost 300 km.

Distinguishing between the possible origins of the imaged P-wave velocity anomalies is difficult, but our maps indicate that the cause(s) must correspond to lateral dimensions on the order of hundreds to a few thousand kilometers. This is an important constraint which supports the findings of both large-scale tomographic models (e.g. Sylvander et al. (1997), Zhao (2004)) and work on localized regions (e.g. Garnero and Lay (2003)). The large-scale features of our final model agree well with the results of Tkalčić et al. (2002). For example, Canada, the southwest Pacific, most of South America and the south Atlantic are slow, while Asia, Central America, Antarctica, and

the Middle East are fast. Even some of the finer-scale features are congruous, such as the sharp transition from fast to slow velocities at the eastern Alaskan border. Besides improvements in resolution, our model is noteworthy in that we are able to retrieve the strength of perturbations as well as the model uncertainty (Figure 6.12c).

Figure 6.15 shows a comparison of our results with those of Houser et al. (2008) and Soldati et al. (2012). The P-wave model from Houser et al. (2008) is of the lowermost 200 km of the mantle. Over 290,000 P, PP, PP-P, and Rayleigh wave travel times were used in a LSQR inversion on a grid of equal area blocks ($4^\circ \times 4^\circ$ at the equator). The applied smoothing and damping is the likely cause of the 0.42% rms of the velocity perturbations, which is significantly less than that of our model. Whether in regions of good or poor raypath coverage, the rms of the perturbations in our model is consistently higher than that of the Houser et al. (2008) model. For example, the rms of only the well-sampled Asia region (from 30 to 120° in longitude and 30 and 80° in latitude) for our model is 0.98%, while it is only 0.53% in the Houser et al. (2008) model. The rms of the more poorly sampled southeast Pacific region (from -180 to -100° in longitude and 0 to -60° in latitude) is 0.64 and 0.49 respectively. The areas of best coverage in the Houser et al. (2008) model include Asia, the northwest Pacific, and the north Atlantic. These areas agree with our results, and it is only in areas of poor resolution (as determined by the checkerboard resolution tests of Houser et al. (2008)), that we see significant discrepancies. Our model is slow beneath Canada, south Australia, and mid-South America and fast beneath the mid-east Pacific whereas the opposite holds true in the Houser et al. (2008) model. Because very few P, PP, and PP-P ray path geometries are sensitive to lowermost mantle structure, the resolving power in the lowermost mantle of the Houser et al. (2008) study is much weaker than that of our study. Since we employ a variety of seismic phase measurements that sample the lowermost mantle and use differential travel times, our resolution is such that most areas of the globe in the lowermost mantle layer can be reliably retrieved.

The P-wave model of the lowermost 200 km of the mantle from Soldati et al. (2012) is shown in Figure 6.15c. Over 880,000 ISC PcP, PKPbc, PKPdf, and P travel times along with a viscosity profile of the mantle were used in a least squares inversion on a grid of equal area blocks ($5^\circ \times 5^\circ$ at the equator). Here the rms of the perturbations is even lower (0.27% overall, 0.32% in the well-sampled Asia region, and 0.36% in the poorly sampled southeast Pacific region), but we see more agreement with the distribution of perturbations. This is likely due to the overall increase in data number and data type. There are strikingly similar features in Africa and Asia; however, there are also differences elsewhere, such as the mid-Pacific, Australia, and North America. Again, this is attributable to differences in data quality, spatial coverage, and handling of data noise. For example, there are likely to be systematic biases in the PKP catalog data due to the fact that no Hilbert transform is applied when calculating differential travel times. The cross-correlation coefficient between the Houser et al. (2008) and the Soldati et al. (2012) models is 0.224; that between ours and that of Houser et al.

(2008) is 0.149, and that between ours and that of Soldati et al. (2012) is 0.146. This suggests a reasonable level of agreement with our model, especially considering that we do not apply any smoothing regularization.

The lowermost mantle has long been considered the graveyard of subducted slabs (Richards and Engebretson, 1992; Grand, 2002) and the birth place of mantle plumes (Yuen and Peltier, 1980; Stacey and Loper, 1983). One possible explanation for the large-scale anomalously fast zones at the bottom of the mantle is the penetration of slab material into the lowermost mantle and its subsequent repose at the base of the mantle. In this manner, the thermal and chemical heterogeneity of a “slab graveyard” would account for some of the lowermost mantle velocity anomalies (Grand, 2002; Garnero and Lay, 2003). There has been some evidence in support of the connectivity of slabs from the surface down to the bottom of the mantle. For example, the Caribbean is consistently shown to have high-velocity structures extending down to the core mantle boundary (Kito et al., 2008). There is geochemical evidence as well that crustal material can descend to the lowermost mantle. Hirose et al. (1999) argue that former basaltic crust with perovskite lithology would gravitationally sink to the deep mantle.

Whether chemical or thermal in nature, the causes of the velocity heterogeneity in the lowermost mantle must be considered to have a larger impact on P-wave velocity than previously suggested by global tomographic models, as evidenced by the significant increase in the rms of the velocity anomalies predicted by our results. This is in line with the strong lateral velocity gradients across compositionally varying domains discovered previously from a direct comparison of PcP-P and ScS-S data (Tkalčić and Romanowicz, 2002). Furthermore, velocity variations up to 4.74%, as seen in our study, is unlikely merely an effect of the core mantle boundary topography, and we instead favor lateral variations in temperature and/or chemistry as explanation for the observed compressional wave velocity variations. A joint inversion for velocity structure and topography is needed to test this interpretation.

6.8 Conclusions

We present a new approach to global tomography using a hand-picked dataset of PKPab-df, PKPbc-df, and PcP-P differential traveltimes. We use a probabilistic, fully non-linear Bayesian inversion scheme to invert for lowermost mantle structure and obtain a new model of the distribution and amplitude of the P-wave velocity heterogeneity in the lowermost mantle. Model parameters, including the level of data noise, are treated as unknowns in the inversion problem and are therefore driven by the information content of the data. The resulting P-wave velocity model reveals heterogeneity on a range of scale-lengths and provides an important bridge between the long-wavelength images produced from previous global models and the very short-scale mapping of localized scattering studies. The root mean square of the velocity

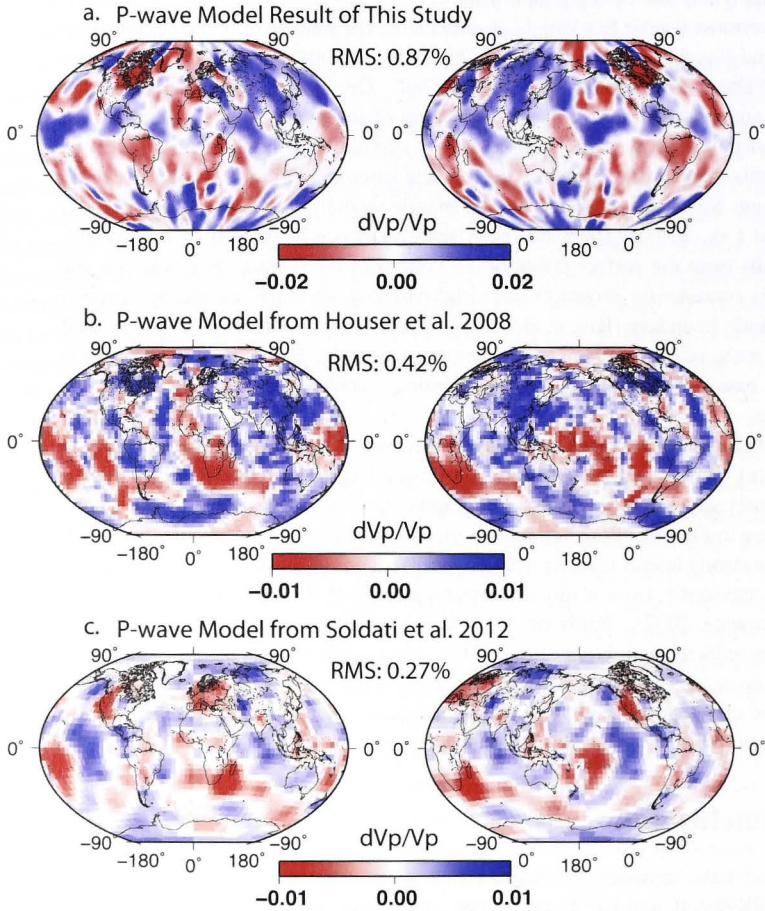


Figure 6.15: (a.) The P-wave model of the lowermost 300 km of the mantle from this study. (b.) The P-wave model of the lowermost 200 km of the mantle from Houser et al. (2008). (c.) The P-wave model of the lowermost 200 km of the mantle from Soldati et al. (2012). Note the differences in the color scale ranges for the different models. The root mean square (rms) value of each model is noted.

perturbations in our final tomographic model is 0.87%, which is significantly larger than previous estimates obtained from a global-scale analysis of body wave travel times. Importantly, model uncertainty is also retrieved, which is a major step forward for global-scale tomographic inversions.

Our results provide a unique view of the lowermost mantle, as the resolving capability is better than that of previous global models, yet is not limited spatially to a local or regional context as are current high-resolution images based on scattering or array seismology methods. The most dominant features of our preferred model include fast velocities beneath Central America and east Asia and slow velocities beneath southern Africa and the southwest Pacific. These large scale patterns agree with other traveltimes tomography models (e.g. van der Hilst and Káráson (1999), Tkalčić et al. (2002), Antolik et al. (2003), Vasco et al. (2006), Zhao (2004), Lei and Zhao (2006), Li et al. (2008), Houser et al. (2008), Zhao (2009), Soldati et al. (2012)). Our model also includes new insights on the P-wave velocity structure of more difficult to image regions such as Africa, Canada, South America and Australia. Most of these regions are slower than average in our model; however, the opposite holds true in the models of some previous studies (e.g. Houser et al. (2008), Soldati et al. (2012)).

A further consideration includes accounting for the possible effects of topography on the travel time residuals, which will involve a joint inversion for topography and velocity. This inclusion will likely decrease the data variance and increase the reliability of our velocity model. In this paper, we made the assumption that the lowermost mantle can be modeled as a single layer. Forthcoming work also includes allowing for multiple layers in the lowermost mantle model, where the thickness of these layers is an unknown. Given the continual increase in available computing power and data records, the Bayesian approach to inversion should enable an ever-improving understanding of lowermost mantle heterogeneity and its geodynamical implications.

6.9 Acknowledgments

We thank Christine Houser and Lapo Boschi for providing their mantle models. Calculations were performed on the Terrawulf cluster, a computational facility supported through the AuScope Australian Geophysical Observing System (AGOS). AuScope is funded under the National Collaborative Research Infrastructure Strategy (NCRIS), and the Education investment Fund (EIF3) both Australian Commonwealth Government Programs. We appreciate Caroline Bartlett for her contributions to the PcP-P dataset. Mallory Young was supported by an Australian National University Research Scholarship. We also thank two anonymous reviewers.

The shuffling rotation of the Earth's inner core revealed by earthquake doublets

A.1 Foreward

The following research is a modified version of the paper by Tkalčić et al. (2013b) published in *Nature Geoscience*. I have modified it such that the relevant parts of the Supplementary Information are now inserted directly into the main text where applicable. These excerpts from the Supplementary Information focus on the work I performed on the project, namely the measurement and processing of doublets. I have also included a few sections on the inversion method. The work in this chapter provides yet another example of the method's ability to excel in geophysical inversion problems and is therefore much inline with the broader goals of this thesis. This research was published in *Nature Geoscience*:

Tkalčić, H., Young, M. K., Bodin, T., and Sambridge, M. (2013), The shuffling rotation of the Earth's inner core revealed by earthquake doublets, *Nature Geoscience*, 6, 497-502.

Work is also described from the following paper:

Tkalčić, H., Bodin, T., Young, M. K. and Sambridge, M. (2013), On the nature of the P-wave velocity gradient in the inner core beneath central America, *Journal of Earth Sciences - Special Volume on Core Dynamics*, 24(5), 699-705.

A.2 Abstract

Geodynamical models and seismic observations suggest that the Earth's solid inner core rotates at a different rate than the mantle. However, discrepancies exist in rotation rate estimates based on seismic waves produced by earthquakes. Here we investigate the inherent assumption of a constant rotation rate using earthquake doublets - repeating earthquakes that produce similar waveforms. We detect that the rotation rate

of the Earth's inner core with respect to the mantle varies with time. We perform an inverse analysis of 7 doublets observed at the College station, Alaska, as well as 17 previously reported doublets, and reconstruct a history of differential inner-core rotation between 1961 and 2007. We find that the observed doublets are consistent with a model of an inner core with an average differential rotation rate of $0.25\text{--}0.48^\circ\text{yr}^{-1}$ and decadal fluctuations of the order of 1°yr^{-1} around the mean. The decadal fluctuations explain discrepancies between previous core rotation models and are in concordance with recent geodynamical simulations.

A.3 Introduction

The differential rotation of the solid inner core with respect to the mantle emerges in geodynamo modelling, but its strength and direction is very sensitive to the imposed viscous boundary conditions at the inner core boundary (Glatzmaier and Roberts, 1996; Gubbins, 1981; Kuang and Bloxham, 1997; Olson, 1997) and the balance between the gravitational and electromagnetic torques (Aurnou and Olson, 2000). The discovery of systematic variations over time in travel times of core-sensitive PKP_{df} waves (Song and Richards, 1996) (Figure A.1c) from earthquakes with similar ray paths through the Earth confirmed geodynamical predictions about the differentially rotating inner core. The estimated rotation rate of $1.1\text{--}3^\circ\text{yr}^{-1}$ in the eastward (prograde) direction (Song and Richards, 1996; Su et al., 1996; Souriau, 2007) relied on the assumption that the fast axis of cylindrical anisotropy is tilted with respect to the Earth's rotation axis. However, since these initial studies, both the assumption that the direction of the fast axis of anisotropy can be uniquely determined and the assumption that a cylindrical anisotropy prevails in the inner core have been disputed (Su and Dziewonski, 1998; Souriau et al., 1997) (see also Souriau (2007) and Tkalčić and Kennett (2008)).

Another method of detecting a differential rotation of the inner core abandoned the need for uniform cylindrical anisotropy (Creager, 1997). According to this method a fixed source-receiver path will sample a volume of the inner core with increasing velocity as a function of time as the inner core spins with a different rate than the mantle, causing PKP_{df} waves of more recent earthquakes to traverse the inner core faster. The obtained differential rotation was about 0.3° in the eastward direction. These results were criticized on the grounds that there are significant uncertainties in the earthquake location parameters, and that the contribution to travel times from short-scale inhomogeneities in the crust and mantle is significant in comparison with the resulting time

Table A.1: Rows indicating new doublets are printed in bold font. No.: doublet number; Doublet: doublet ID, indicating the year of the first and the second event (if multiple events occurred in the same year, they are marked by a,b, and c); Zhang et al. (2005): PKPdf time-difference (s) from Zhang et al. (2005); M1: PKPdf time-difference from Method 1; M2: PKPdf time-difference from Method 2; M3: PKPdf time-difference from Method 3; N1: normalized PKPdf time-difference from Method 1. The normalization was done according to Zhang et al. (2005) - the observed travel time shift between PKPdf phases is multiplied by the time through the inner core at a distance of 151° at the average of two depths of each of the events, divided by the time in the inner core at the average location of the two events and average depth; N2: normalized PKPdf time-difference from Method 2; N3: normalized PKPdf time-difference from Method 3; cc1 cross-correlation coefficient from the comparison of waveforms containing PKPbc and PKPab onsets (12s after the onset of PKPbc); cc2: cross-correlation coefficient from the comparison of PKPdf waveforms before the alignment; cc3: cross-correlation coefficient from the comparison of PKPdf waveforms (Method 1); cc4: cross-correlation coefficient from the comparison of PKPdf and PKPbc waveforms of the first event of a doublet (Method 2); cc5: cross-correlation coefficient from the comparison of PKPdf and PKPbc waveforms of the second event of a doublet (Method 2); cc6: the resulting cross-correlation coefficient of the PKPdf waveforms after the shift obtained from Method 2 is applied.

No.	Doublet	Zhang et al. (2005)	M1	M2	M3	N1	N2	N3	cc1	cc2	cc3	cc4	cc5	cc6
#01	86a.86b	0.00	0.03	-0.02	0.11	-0.029	-0.020	0.107	0.90	0.94	0.95	0.88	0.80	0.92
#02	86b.87c	0.02	0.01	0.05	-0.05	0.010	0.049	-0.049	0.89	0.91	0.92	0.80	0.71	0.90
#03	86a.87b	0.02	0.04	0.02	0.05	0.039	0.012	0.049	0.93	0.92	0.94	0.89	0.70	0.93
#04	97a.99	0.01	0.04	0.02	0.04	0.043	0.021	0.043	0.99	0.95	0.97	0.52	0.54	0.97
#05	87a.90	0.03	0.03	0.01	-0.05	0.032	0.011	-0.054	0.91	0.73	0.74	0.70	0.78	0.74
#06	98.02b	0.00	-0.05	-0.08	0.03	-0.050	-0.080	0.023	0.89	0.79	0.82	0.74	0.66	0.81
#07	01.07a	N.A.	0.09	0.10	0.08	0.088	0.097	0.078	0.87	0.76	0.85	0.85	0.73	0.84
#08	99.05a	N.A.	0.33	0.28	0.32	0.352	0.299	0.341	0.96	0.38	0.70	0.79	0.58	0.69
#09	95c.02a	0.06	0.08	0.09	0.04	0.080	0.090	0.040	0.99	0.60	0.86	0.69	0.78	0.85
#10	86d.93a	0.08	0.08	0.14	-0.04	0.079	0.138	-0.040	0.87	0.50	0.56	0.81	0.69	0.53
#11	87c.95	N.A.	0.01	0.09	-0.18	0.010	0.093	-0.186	0.96	0.92	0.92	0.70	0.68	0.87
#12	97.05a	N.A.	0.18	0.13	0.37	0.192	0.139	0.395	0.85	0.52	0.82	0.68	0.62	0.81
#13	87b.95b	0.14	0.16	0.15	0.13	0.171	0.161	0.139	0.98	0.25	0.82	0.73	0.59	0.81
#14	93b.03	0.11	0.11	0.05	0.10	0.116	0.053	0.105	0.92	0.68	0.92	0.59	0.65	0.85
#15	87e.98a	N.A.	0.20	0.14	0.14	0.189	0.133	0.133	0.81	0.53	0.86	0.69	0.90	0.83
#16	87d.98b	N.A.	0.16	0.14	-0.04	0.156	0.137	-0.039	0.86	0.66	0.84	0.51	0.80	0.83
#17	82b.95a	0.07	0.08	0.03	0.11	0.079	0.030	0.109	0.90	0.82	0.91	0.86	0.78	0.87
#18	94.07b	N.A.	0.02	0.07	0.02	0.020	0.069	0.020	0.96	0.86	0.86	0.82	0.61	0.82
#19	86c.04	0.17	0.17	0.18	0.26	0.182	0.192	0.276	0.85	0.25	0.60	0.78	0.82	0.60
#20	64.82a	0.20	0.22	0.27	0.27	0.216	0.265	0.265	0.92	0.36	0.89	0.70	0.80	0.86
#21	61.84	0.17	0.13	0.18	0.18	0.138	0.190	0.190	0.90	0.75	0.84	0.56	0.53	0.83
#22	70.93b	0.24	0.22	0.21	0.23	0.231	0.221	0.242	0.90	0.17	0.70	0.41	0.71	0.70
#23	70.03	0.34	0.31	0.28	0.32	0.327	0.295	0.337	0.86	-0.40	0.62	0.43	0.76	0.61
#24	62.97b	0.34	0.35	0.32	0.37	0.348	0.318	0.368	0.78	0.00	0.57	0.85	0.70	0.56

Table A.2: Rows indicating new doublets are printed in bold font. No.: doublet number; Doublet: doublet ID, indicating the year of the first and the second event (if multiple events occurred in the same year, they are marked by a,b, and c); Latitude: the average latitude of the two of the events in the doublet; Longitude: the average longitude of the two of the events in the doublet; Depth: the average depth of the two of the events in the doublet; Distance: epicentral distance (in degrees) between the average location of the doublet and station College, Alaska; Azimuth: azimuth (in degrees) between the average location of the doublet and station College, Alaska; ξ : angle in the inner core between the ray path of the average PKPdf and the Earth's rotation axis; IC Depth: the depth of the bottoming point of the average PKPdf of the doublet below ICB (in kilometers); IC Time: the time that the average PKPdf spends in the inner core (in seconds).

No.	Doublet	Latitude	Longitude	Depth	Distance	Azimuth	ξ	IC Depth	Time
#01	86a_86b	55.971	27.550	125.2	150.32	311.92	26.26	129.1	126.6
#02	86b_87c	56.032	27.613	143.2	150.33	311.85	26.23	129.9	126.8
#03	86a_87b	56.044	27.563	126.5	150.36	311.82	26.23	130.2	126.8
#04	97a_99	58.047	25.657	51.2	152.47	308.58	25.50	180.0	138.3
#05	87a_90	58.008	25.275	32.4	152.59	308.63	25.54	182.5	138.8
#06	98_02b	56.531	27.450	106.8	150.75	311.09	26.03	139.5	129.1
#07	01_07a	56.041	27.768	148.2	150.29	311.80	26.22	129.1	126.5
#08	99_05a	57.941	25.712	52.5	152.38	308.75	25.54	177.7	137.8
#09	95c_02a	56.342	26.745	88.3	150.90	311.29	26.17	142.8	129.9
#10	86d_93a	56.225	27.320	132.8	150.58	311.54	26.17	136.0	128.2
#11	87c_95	56.609	25.659	24.0	151.53	310.73	26.16	156.9	133.1
#12	97_05a	57.944	25.648	52.6	152.41	308.73	25.55	178.5	138.0
#13	87b_95b	58.013	25.517	60.6	152.49	308.67	25.51	180.7	138.4
#14	93b_03	57.544	25.811	67.8	152.08	309.39	25.71	170.4	136.2
#15	87e_98a	55.593	28.294	23.8	149.76	312.50	26.37	112.1	122.4
#16	87d_98b	56.124	27.704	142.2	150.36	311.71	26.18	130.8	126.9
#17	82b_95a	56.297	27.485	136.6	150.56	311.48	26.11	135.6	128.2
#18	94_07b	56.229	27.223	104.0	150.64	311.49	26.18	136.5	128.4
#19	86c_04	57.962	25.588	67.7	152.44	308.73	25.54	179.5	138.2
#20	64_82a	56.150	27.581	151.3	150.42	311.69	26.17	132.5	127.4
#21	61_84	56.858	24.522	43.9	152.17	310.19	26.17	172.1	136.6
#22	70_93b	57.535	25.884	62.7	152.03	309.45	25.70	169.2	136.0
#23	70_03	57.551	25.756	71.7	152.11	309.37	25.72	171.2	136.4
#24	62_97b	56.306	27.145	67.3	150.72	311.37	26.16	137.7	128.6

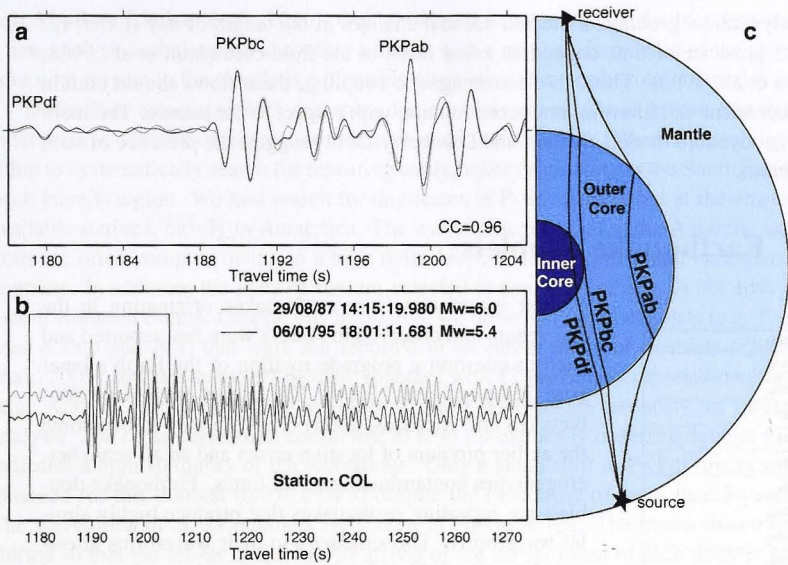


Figure A.1: Newly observed doublet and PKP waves. A newly observed doublet at the College station, Alaska (doublet #11; Table A.1; row 11). The more recently recorded waveform (06/01/1995) is shown with black. a, Enlarged 3 branches of PKP waveforms marked by a rectangle in b. Traces are aligned on the BC phase and filtered between 0.5 and 1.0 Hz. c, A schematic representation of Earth's cross-section and ray paths of seismic waves PKPdf, PKPbc and PKPab used in the study of doublets. Note that only PKPdf waves traverse the Earth's inner core.

shift in the PKPdf arrival (Souriau, 1998). A subsequent joint inversion for inner-core rotation and mantle heterogeneity confirmed a very robust lateral velocity gradient in the inner core and found an eastward differential rotation of between 0.3 and 1.1 yr^{-1} (Song, 2000). This result was contrasted, however, by a study of earthquakes from 1977 to 1998, which found small temporal variations in the splitting functions of the normal modes sensitive to the Earth's core indicating a low differential rotation rate of $0.13 \pm 0.11^\circ \text{ yr}^{-1}$ (Laske and Masters, 2003).

The discrepancy between the body wave and normal mode results seems to reflect an inherent difficulty in obtaining accurate estimates of inner-core rotation. However, it may also indicate that the underlying assumption of a steady differential inner-core rotation is incorrect. If one instead allows for a time-variable inner-core rotation, different studies sampling different time intervals would be expected to yield different rotation rates. In fact, decadal fluctuations in inner-core rotation are indeed expected

on geodynamical grounds. Detected decadal changes in the length of day (LOD) reflect the presence of time-dependent zonal flows in the fluid core (Jault et al., 1988; Jackson et al., 1993). Through electromagnetic coupling, these flows should entrain time-dependent variations in inner-core rotation with respect to the mantle. The more recent geodynamo models (Aubert and Dumberry, 2011) suggest the presence of such fluctuations.

A.4 Earthquake doublets

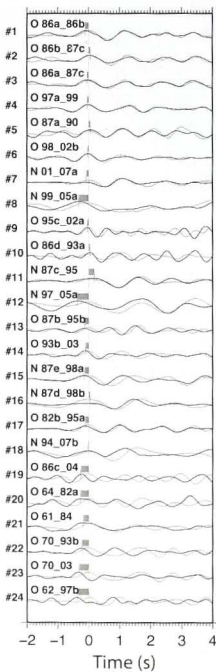


Figure A.2: Method 3; Enlarged PKPdf segments for each doublet marked by ticks in Figure A.10a. The traces have been shifted to align the PKPdf arrivals of the earlier event of each doublet. The gray horizontal bars indicate the measured difference in PKPdf travel times.

Similar waveforms from earthquakes originating in the SSI region and observed in Alaska were first reported and used to question a prograde rotation of the Earth's inner core (Poupinet et al., 2000). The use of earthquake doublets (Li and Richards, 2003) offered a way to overcome the earlier problem of location errors and small-scale heterogeneities contaminating travel times. Earthquake doublets are repeating earthquakes that produce highly similar waveforms. The similarity in their waveforms attests that the waves initiated at the same location and traversed through the same Earth structure. In practice, this means that the separation of the two sources is smaller than the typical wavelength at which the waveforms are observed. Indeed, a recent relocation of the SSI earthquakes using improved algorithms verifies that they occur in tight spatial clusters (Bondár and Storchak, 2011). Using a number of earthquake doublets, a significant and steady differential rotation of the inner core in the eastward direction was robustly determined to be about $0.4\text{--}1.0^\circ\text{yr}^{-1}$ (Li and Richards, 2003) and $0.3\text{--}0.5^\circ\text{yr}^{-1}$ (Zhang et al., 2005).

Here we present results of a new search for earthquake doublets using the College station (the station with the most complete continuous recording) and perform an analysis of their travel times. A common feature of all previous seismological studies using earthquake doublets was the assumption that the rate of inner-core differential rotation is constant with time. Using data less reliable than earthquake doublets, evidence for a fluctuation in the inner core rotation rate has been found from a statistical-based spectral analysis (Collier and Hellfrich, 2001) and an event pair travel time analysis (Song and Poupinet, 2007). Furthermore, a non-zero acceleration has been suggested for the

past 55 years (Lindner et al., 2010). On the basis of new earthquake doublet data and a new analysis technique, we show that a model with a non-steady rotation of the inner core with respect to the mantle is a plausible alternative to a steady-rotation model.

Difficulties associated with searching for doublets are escalated by the fact that most seismic stations of interest do not have continuous records. We design an algorithm to systematically search for repeating earthquakes originating in the South Sandwich Islands region. We first search for duplicates in P-waves recorded at the closest available stations, mostly in Antarctica. The waveforms recorded at the Antarctic stations are often complex owing to a high noise level, concealing potential earthquake doublets. In addition, the pairs of stations selected to confirm doublets do not always record common events. Despite this limitation, we observe 12 new doublets (e.g. Figures A.1a,b and A.4) that were not reported in an earlier study of doublets (Zhang et al., 2005), and we analyse 7 of them together with 17 previously reported doublets (e.g. A.3 and A.5). The PKPdf waveforms of five doublets are too noisy for further analysis. The cross-correlation coefficient of 0.96 for the newly observed doublet #11 indicates a high similarity of the waveforms. Only a small shift in PKPdf onsets was obtained for this doublet (0.05 ± 0.04 s) despite the time lapse of more than 7 years. The waveforms of all 24 doublets are shown in Figure A.10a. The traces shown are shifted so that the onsets of the PKPdf arrival of the earlier event of each doublet are roughly aligned. The measurement alignments for several previously reported and new doublets are featured in Figures A.6, A.7, A.8, A.9.

A.5 PKPdf differential travel times measurements

In this study, we employ three different methods of measuring the differences in PKPdf wave onset time. The first method (Method 1) consists of measuring onsets of the PKPdf waves of the earlier and later event of a doublet by cross-correlation (column 12 of Table A.1) after the waveforms are aligned on the PKPbc phase. The time shift (differential travel time) can be described as:

$$dT = PKPdf_1 - PKPdf_2, \quad (\text{A.1})$$

where the subscript 1 refers to the travel time of the earlier event and the subscript 2 refers to the travel time of the later event. A positive differential travel time indicates that the PKPdf waves of the later event arrived earlier than those of the earlier event. Figure A.10b shows the time segments used for calculating the cross-correlation coefficients of the PKPdf waveforms and the resulting time shifts (blue bars). These measurements are reported in column 5 of Table A.1. The alignment of the PKPdf waves after applying the shift calculated using Method 1 is shown in the middle right section in Figures A.6, A.7, A.8, and A.9.

In Method 2 the cross-correlation is computed between the PKPdf and PKPbc

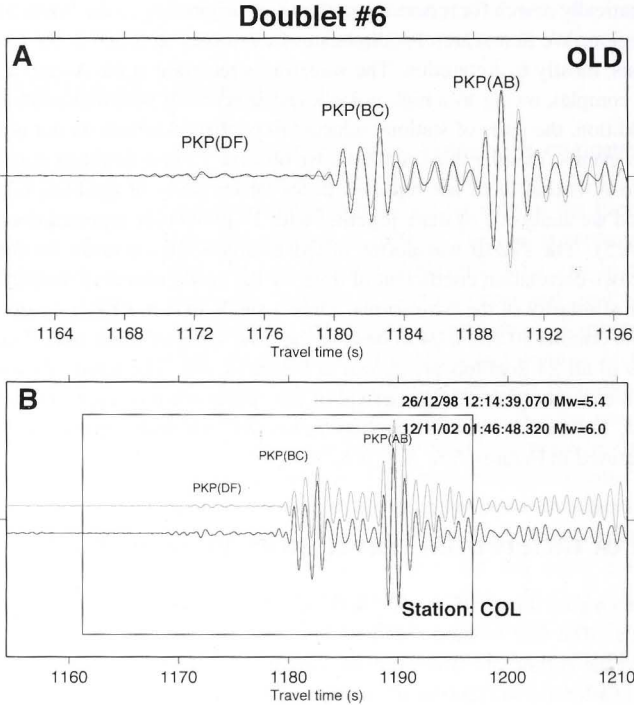


Figure A.3: An example of a previously observed doublet at College Station, Alaska (Doublet #6; Tables A.1, A.2; row 6). The more recently recorded waveform is shown with black. (A) Enlarged three branches of PKP waveforms marked by a rectangle in (B), where longer records are shown (noise preceding DF and coda following AB phases). Traces (grey for the earlier event and black for the more recent event) are aligned on the BC phase and filtered between 0.8 and 1.5 Hz. In the top right corner, it is indicated that the doublet is a previously observed doublet (OLD).

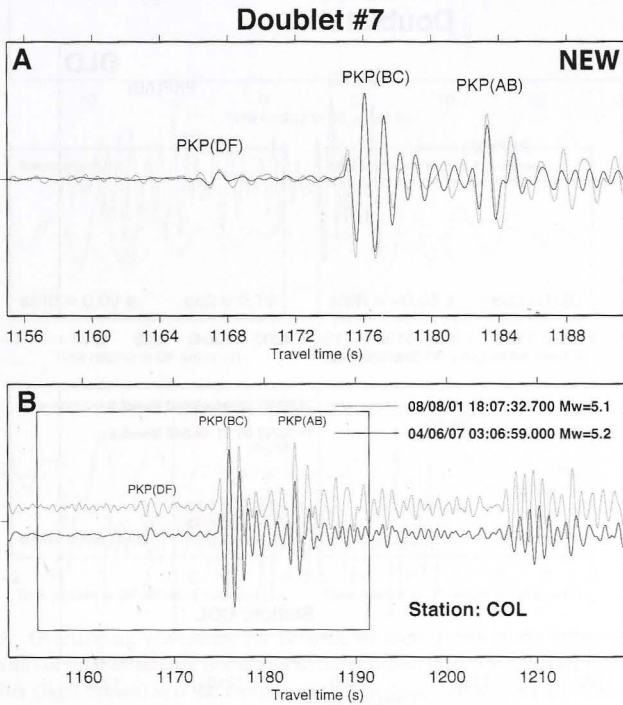


Figure A.4: Doublet #7. See description for Figure A.3.

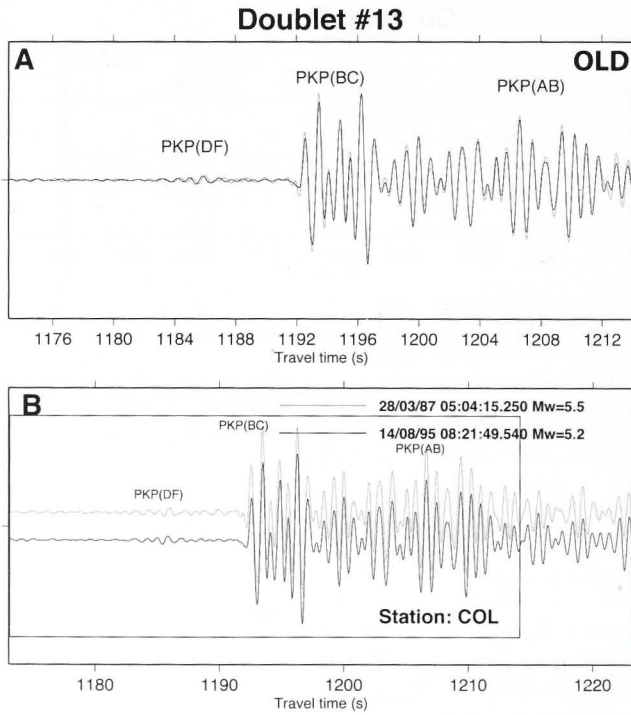


Figure A.5: Doublet #13. See description for Figure A.3.

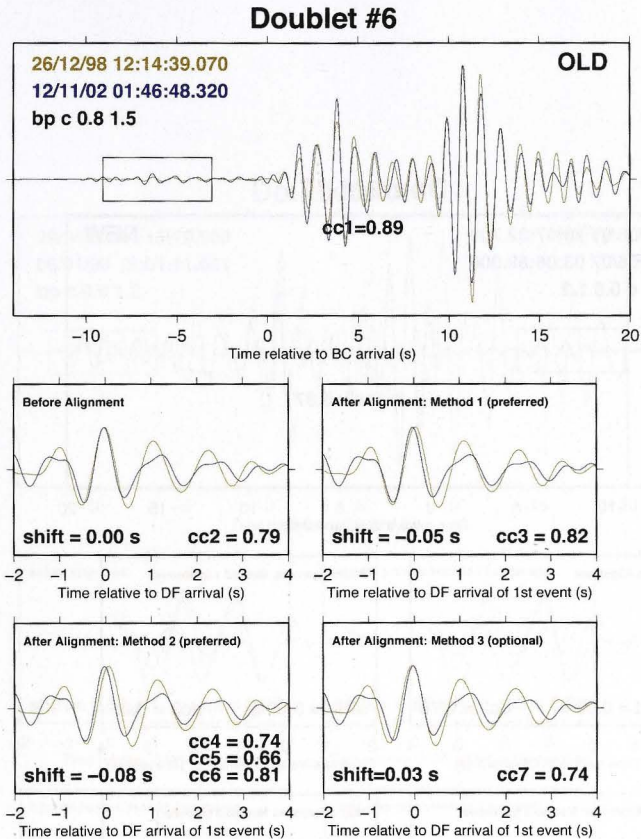


Figure A.6: Overlapping waveforms for Doublet #6 used in this study before and after the measurements of time-difference in the PKPdf onset times. (Top) Overlapped PKP waveforms of the earlier (light brown) and the more recent event (blue), containing all three branches of PKP waves aligned on PKPbc phase. The time interval around the PKPdf waves is marked by a rectangle. Also shown is the band-pass filter applied prior to measuring (for example, bp c 0.8 1.5 means: band-pass filter with corner frequencies of 0.8 and 1.5 Hz) and the obtained cross-correlation coefficient for the entire waveform before and after the alignment. In the top right corner, it is indicated whether the doublet has already been reported (OLD) or if it is a newly observed doublet (NEW); (Middle) The waveforms around the PKPdf onsets are incised by a rectangle in the top panel and are enlarged to clearly show the alignment of the PKPdf phases before (left) and after (right) the time shift obtained by cross-correlation is applied (Method 1). Also shown are the cross-correlation coefficient and the shift in seconds; (Bottom) Alignment of PKPdf phases after the shifts obtained from Method 2 (left) and 3 (right) are applied. Also shown are the cross-correlation coefficient and the shift in seconds for Method 2 and the shift in seconds for Method 3. Compare with Table A.1.

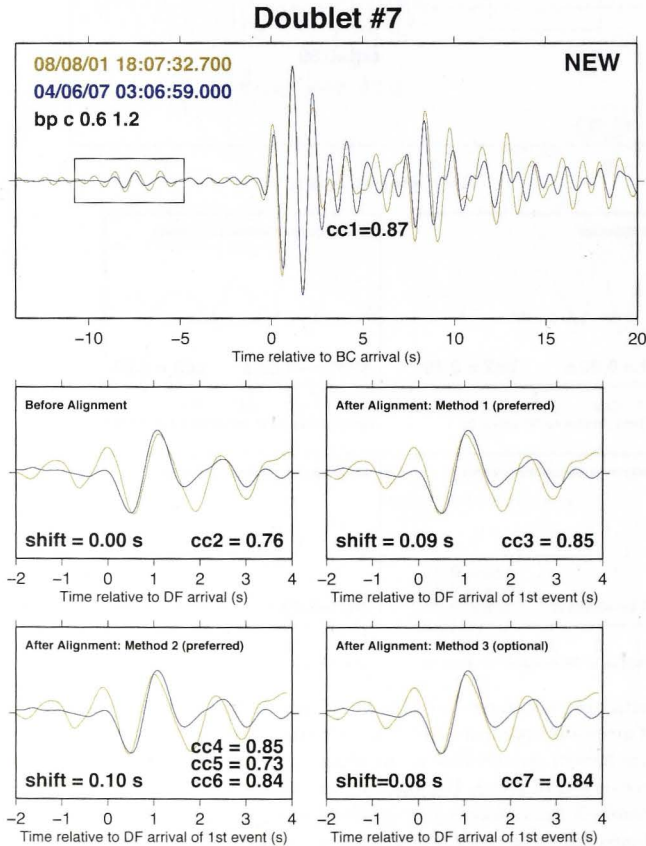


Figure A.7: Doublet #7. See description for Figure A.6.

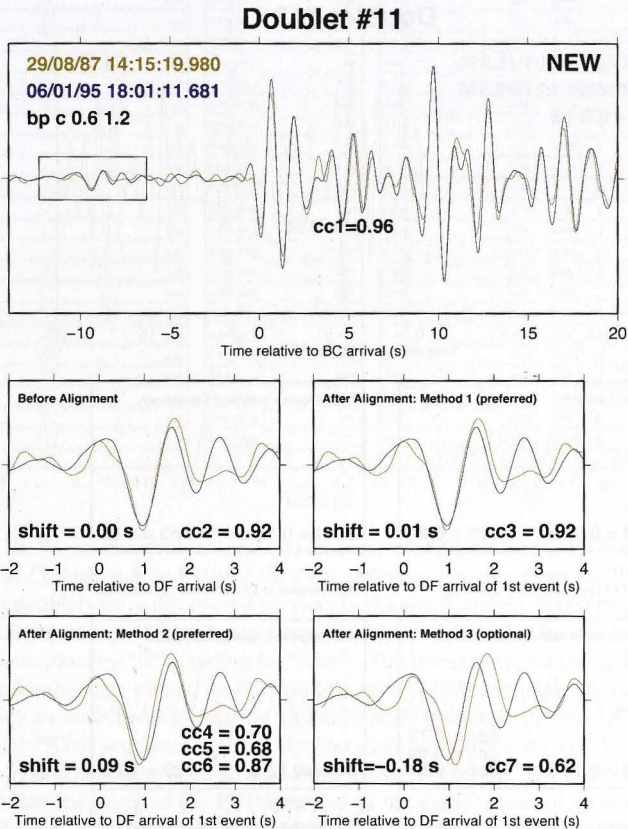


Figure A.8: Doublet #11. See description for Figure A.6.

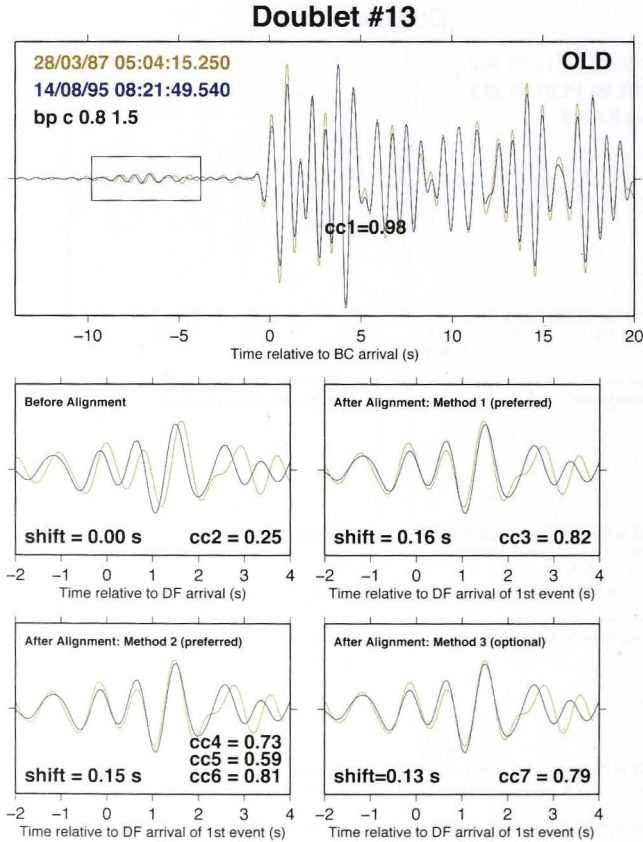


Figure A.9: Doublet #13. See description for Figure A.6.

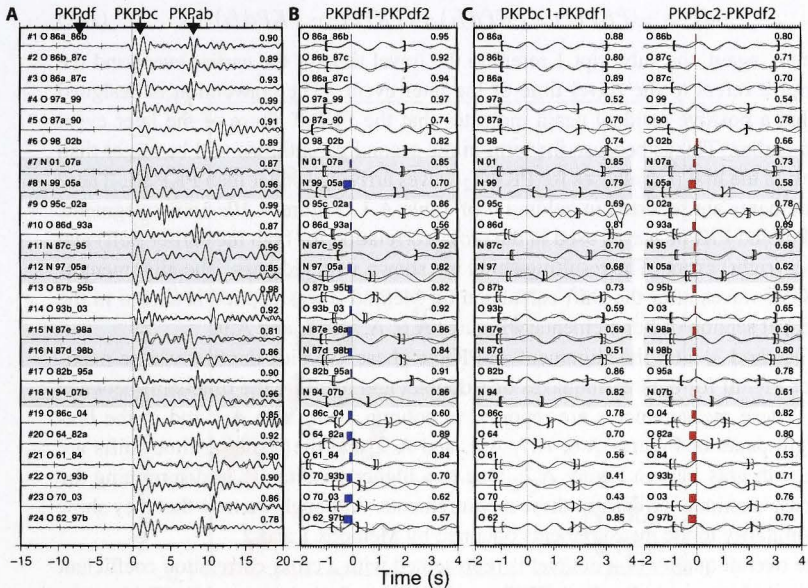


Figure A.10: Waveform doublets and two measurement methods. (A) PKP waveforms observed at College station, Alaska for 24 doublets originating from the SSI region. Seventeen doublets were discovered previously (Li and Richards, 2003) (also marked by “O” standing for “old”) and seven new doublets are reported in this study (grey shade; also marked by “N” standing for “new”). The traces (gray for the earlier events and black for the later events, as in Li and Richards (2003) are aligned with the BC phase. They are sorted with increasing time separation from top to bottom. (B) Method 1: Enlarged PKPdf segments for each doublet marked by ticks in (A). The segments indicated by brackets have been aligned using cross-correlation. The traces have been shifted so that the onset of the PKPdf arrival of the earlier event of each doublet is roughly aligned. The blue horizontal bars indicate the measured difference of PKPbc-PKPpdf travel times. (C) Method 2: Enlarged PKPdf and PKPbc segments of the first event of a doublet (left) and the second event of a doublet (right). The traces indicated by brackets have been aligned using cross-correlation. The red horizontal bars indicate the measured difference of PKPbc-PKPpdf travel times.

phases of both events of a doublet (columns 13 and 14 of Table A.1), and the differential travel time is computed by:

$$dT = -(PKPbc_1 - PKPdf_1) + (PKPbc_2 - PKPdf_2), \quad (A.2)$$

where, again, the subscript 1 refers to the travel time of the earlier event and the subscript 2 refers to the travel time of the later event. The convention is designed such that a positive residual again indicates that the PKPdf phase of the later event arrived earlier. This is because the term in the second parentheses will be larger than the term in the first parentheses for PKPdf₂ waves arriving sooner than PKPdf₁. These measurements are reported in column 6 of Table A.1. Figure A.10c shows segments of PKPdf and PKPbc waves used in the cross-correlation for both the earlier (left) and the later (right) event. The resulting shifts are shown with red bars. The alignment of the PKPdf waves after the shift calculated by Method 2 was applied is shown in the bottom left section of Supplementary Figures A.6, A.7, A.8, and A.9.

In Method 3, after the alignment on PKPbc phase, we pick the first visible maximum of PKPdf for both earthquakes of a doublet and measure the time-shift between them. These measurements are reported in column 7 of Table A.1 and in the bottom right panel of Figures A.6, A.7, A.8, and A.9, and the resulting time-shifts are shown with gray bars in Figure A.2. Due to a higher uncertainty in determining the first phase maxima, we discard these measurements. Although we note that they show great similarity to the measurements obtained by Methods 1 and 2.

The overall quality of a doublet is represented with a cross-correlation coefficient for the waveforms including both PKPbc and PKPab arrivals (column 11 of Table A.1). These values are more objective than the values obtained from the cross-correlation of the PKPdf waves since the time-window length is a constant length (12 s). We also calculate cross-correlation coefficients for longer time-windows (30 s from the beginning of PKPbc onsets, as done by Waszek et al. (2011)) and confirm that all 24 doublet-waveforms have high cross-correlation coefficients. For example, two newly identified doublets (Doublet #8 and Doublet #11), which have a significant bearing on the results, have cross-correlation coefficients as high as 0.95. Among previously reported doublets, only Doublets #4, #9 and #13 have values greater than 0.95.

The averaged measurements obtained using Method 1 and Method 2 are plotted as a function of time lapse between detected earthquake doublets in Figure A.11. In this figure, we emphasize the doublets with similar time lapses (indicated by numbers), but with very different differential travel times. Considering our central premise that the inner core rotates differentially, this implies varying rotation rates of the inner core with respect to the mantle. Instead of plotting differential travel times as a function of time lapse as in previous studies, we represent each doublet with 2 end-points (marked by triangles), join them with a line, and plot them against the absolute time. It becomes clear that the variation in differential travel times revealed this way can not be explained with a linear fit.

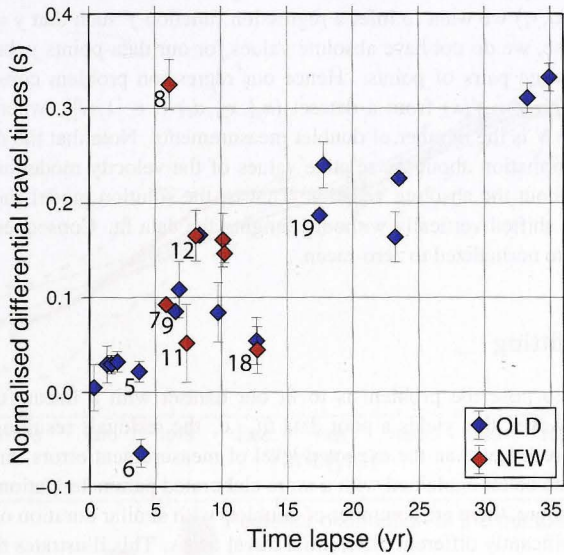


Figure A.11: PKPdf differential travel times averaged from two different methods of measurements (Method 1 and Method 2). Differential travel times are normalised with respect to the total amount of time the PKPdf waves spend in the inner core. See Table A.1 for a more detailed description of how the normalisation was performed. New doublets are shown in red. Doublet numbers (in the lower left corner next to the symbol) are shown for the doublets with similar time lapse, but with very different differential travel times, some of which are discussed in the text. Similar time lapses with dissimilar differential travel times indicate a non-steady rotation of the inner core. This plot also illustrates the need to present differential travel times obtained from doublets as a function of real time, instead of a function of time lapse.

A.6 Regression problem

Our doublet measurements reflect the difference in P-wave velocity within a given volume (i.e. that sampled by the PKPdf ray-path) in the inner-core at two given times. The goal of the inversion is to infer the variation of P-wave speed along this ray as a function of time. The problem is then similar to a regression problem, where from a set of data points (x_i, y_i) we want to infer a regression function f such that $y = f(x)$. However, in our case, we do not have absolute values for our data-points y_i but only relative values between pairs of points. Hence our regression problem consists of recovering a function $y = f(x)$ from a dataset (x_{1i}, x_{2i}, d_i) ($i \in [1, N]$), where $d_i = y_{2i} - y_{1i}$, and where N is the number of doublet measurements. Note that the doublet data only carry information about the relative values of the velocity model and that nothing is known about the absolute velocity. That is, the solution model shown in Figure A.12 can be shifted vertically without changing the data fit. Consequently, in this study models are normalized to zero-mean.

A.6.1 Linear fitting

The simplest way to pose the problem is to fit our dataset with a linear function $f(x) = ax + b$. However, this yields a poor data fit, i.e. the residuals resulting from such an inversion are larger than the expected level of measurement errors, meaning that the data could be better explained with a more elaborated parameterization of the function f . Furthermore, there are a number of doublets with similar duration of time-lapse, but with significantly different differential travel times. This illustrates that the PKPdf differential travel time data could be explained with another function other than a simple linear trend.

A.6.2 Model parameterization

In this study we propose parameterising the regression model with a variable number of B-splines. Hence, the unknown parameters in the inversion are the number of B-spline nodes and the values of their coefficients. Contrary to the classical regression problem, two different models can perfectly fit the same dataset, and hence the solution is non-unique. However, as we increase the number of doublets as well as the variability of time-lapse between pairs of events, we expect the solution to become more unique, and an inference can be made on the time variability of our P-wave velocity model. We also tested different types of parameterization. Most notably, we used Partition Modelling with a variable number of piecewise constant Voronoi cells. Although this yields a similar fit to the data and allows us to invert for the noise in the data, it is deemed "less physical" in describing the underlying physical model.

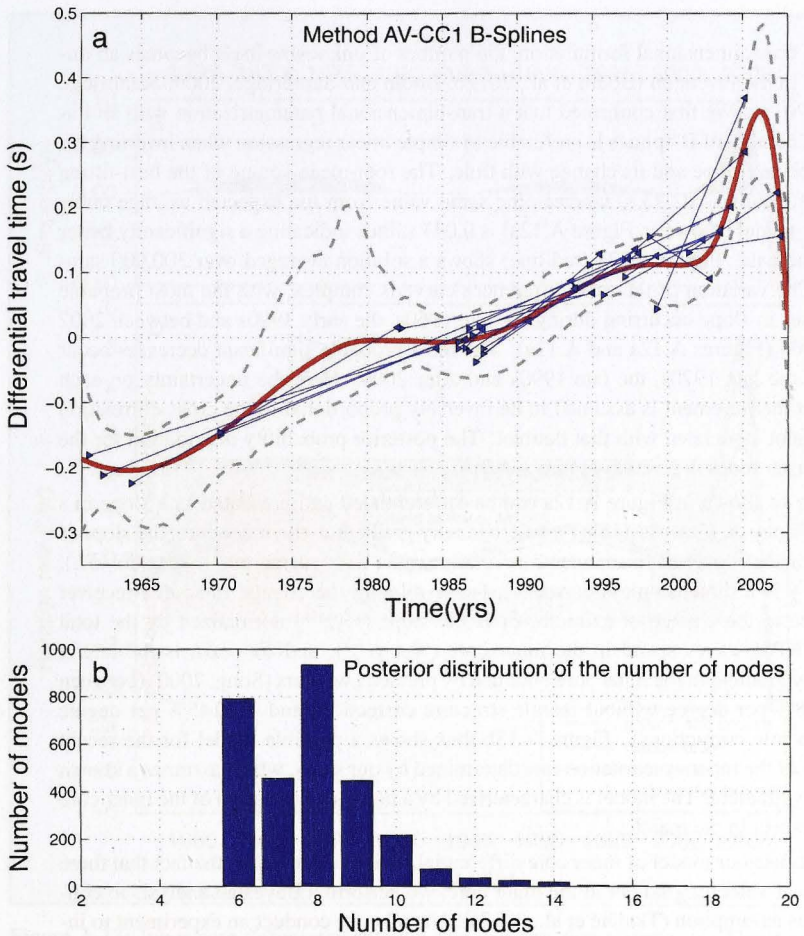


Figure A.12: Solution model and posterior distribution of the number of nodes. a, Doublet measurements (blue triangles represent measurements for each earthquake of a doublet and they are joined with straight lines) are fitted with a variable slope model using a Bayesian transdimensional inversion derived as an average over the ensemble of collected models. The red line shows the expected solution model (normalized to zero mean). The dashed grey line is an average solution ± 1 standard deviation. b, Posterior distribution for the number of B-spline nodes across the ensemble solution.

A.7 Variable rates of inner-core rotation

With a transdimensional formulation, the number of unknowns itself becomes an unknown in the inversion (Bodin et al., 2012b; Bodin and Sambridge, 2009; Sambridge et al., 2013). We first confirmed that a transdimensional parametrization with an unknown number of B-splines is preferable to simple linear regression when inverting for the expected slope and its change with time. The root-mean-square of the best-fitting linear function is 0.073 s, whereas the same value from the expected average cubic splines model (shown in Figure A.12a) is 0.047 s, thus indicating a significantly better fit to the data. Figure A.12a (red line) shows a solution averaged over 300,000 samples. The variation of the time differences curve is complex, with the most probable increases in slope occurring during the late 1960s, the early 1990s and between 2002 and 2004 (Figures A.12a and A.13a). The most probable significant decreases occur during the late 1970s, the late 1990s and after 2004. Here the uncertainty on each doublet measurement is assumed to be inversely proportional to the cross-correlation coefficient associated with that doublet. The posterior probability distribution for the number of nodes is given in Figure A.12b.

The fit shown in Figure A.12a can be differentiated and presented as a slope in yr^{-1} (Figure A.13a). Assuming a heterogeneity gradient in the inner core, the slope (s yr^{-1}) can be converted to an inner-core rotation rate ($^{\circ}\text{yr}^{-1}$) using $\alpha = -\gamma\delta t / (\delta v / \delta L)$, where γ is a dimensionless correction factor relating the change in source-receiver distance to the change of azimuth, δt is the slope (s yr^{-1}) normalized by the total time PKPdf waves spend in the inner core ($\%, \text{s yr}^{-1}$), and $\delta v = \delta L$ is the lateral velocity gradient in the inner core obtained by previous workers (Song, 2000) (between -0.0278% per degree without mantle structure corrections and -0.0145% per degree with mantle corrections). Figure A.13b thus shows a possible model for the recent history of the inner-core rotation rate determined by our study, which assumes a known velocity gradient. The model is characterized by a non-steady rotation of the inner core with respect to the mantle.

Because our model of inner core differential rotation relies upon the fact that there is a linear velocity gradient in the inner core, we perform a Bayesian analysis to confirm this assumption (Tkalčić et al., 2013a). Namely, we conduct an experiment to investigate whether linearity in the observed velocity gradient in the volume of the inner core sampled by the PKP raypaths beneath Central America is a robust approximation. Instead of solving an optimization problem, we approach it within the Bayesian inference. Since this is an ensemble approach, model specification is relaxed so that instead of only one solution, groups of reasonable models are acceptable. As with previous transdimensional inversions discussed in this thesis, the number of basis functions needed to model observations is by itself an unknown. Our modeling reveals that in the ensemble of models, the most likely are those containing only 2 nodes (linear trend). Thus this result justifies the assumption used for the determination of inner core

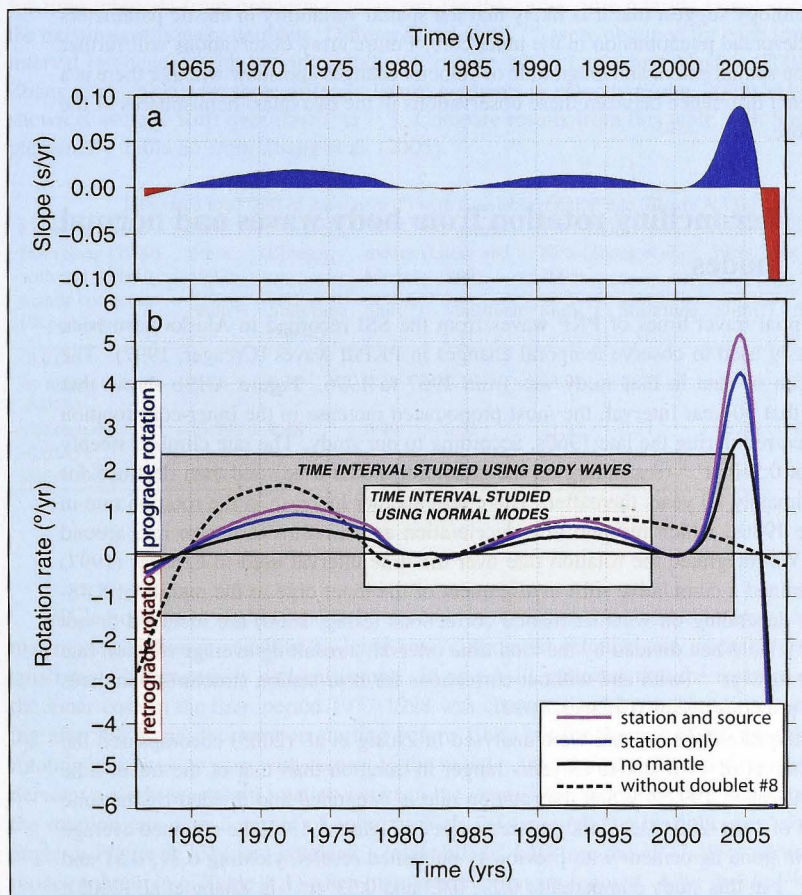


Figure A.13: Inner core differential rotation rate as a function of time. (a) The slope parameter determined by the inversion (Figure A.12). Blue areas indicate an eastward rotation whereas red areas indicate a westward rotation. (b) Differential rotation rate determined from the slope for 3 different values of the velocity gradient (Song, 2000). The dark grey and the light grey rectangles delineate the time intervals used in the study of doublets (Zhang et al., 2005) and normal modes (Laske and Masters, 2003). The areas under these curves were integrated to estimate the total shift (Table A.1). The dashed line is the solution obtained when Doublet #8 is omitted from the inversion.

rotation that the observed gradient is constant in nature (linear). Recent observations in seismology suggest that it is likely that the spatial variability in elastic parameters is a widespread phenomenon in the inner core. Future array observations will further constrain spatial extent and magnitude of velocity changes and show whether there is a significant difference between these observations in the two quasi-hemispheres of the inner core.

A.8 Reconciling rotation from body waves and normal modes

Differential travel times of PKP waves from the SSI recorded in Alaska have been previously used to observe temporal changes in PKP waves (Creager, 1997). The time span of data in that study was from 1967 to 1996. Figure A.13b shows that during that 30-year interval, the most pronounced increase in the inner-core rotation rate occurred during the late 1960s, according to our study. The rate climbed steeply to about $0.5\text{-}1^\circ\text{yr}^{-1}$ (depending on the structural model used) and then declined for approximately 10 years thereafter. There was another increase in the rotation rate in the late 1980s, which resulted in a deceleration and a return to a zero rate around 2000. We integrated the rotation rate over the time interval used in Creager (1997) and obtained a cumulative shift in alignment of the inner core to the mantle of $8.48\text{-}16.26^\circ$, depending on whether mantle corrections (Song, 2000) are included or not (Table A.1). When divided by the total time interval, a resulting average rotation rate of $0.30\text{-}0.58^\circ\text{yr}^{-1}$ (with and without corrections for near-station structure) compares well to previous results (Creager, 1997).

Earthquake doublets that were analysed in Zhang et al. (2005) encompassed the time interval of 1961-2004, 15 years longer in duration than that of the travel time study (Creager, 1997). When the rotation rate is integrated and divided by the time interval of 1961-2004 (see dark grey rectangle in Figure A.13b), the obtained average rate is in good agreement with previously published results, yielding 0.31, 0.51 and 0.63°yr^{-1} in this study compared to 0.27, 0.43 and 0.53°yr^{-1} in Zhang et al. (2005); compare the 1961-2004 doublets column of Table A.3 with Supplementary Table S5 from Zhang et al. (2005). After interpreting Figure A.13, it becomes clear that the larger differential rotation rate value compared with that obtained in the travel-time study comes from two additional increases in the rotation rate: one occurring during the late 1960s and one occurring between 2002 and 2005. We note that during the 1971-1974 time interval a small inner-core rotation rate of 0.15°yr^{-1} was obtained from an independent study of scattering (Vidale and Earle, 2005). Although this time interval is relatively short, the high, however decelerating, inner-core rotation rates of $0.5\text{-}1^\circ\text{yr}^{-1}$ of our model (Figure A.13) are in apparent disagreement with this scattering study.

Table A.3: Integrated shift in alignment of the inner core with respect to the mantle for time intervals from previous studies and for the entire time-interval sampled by the existing earthquake doublets. Different total shifts ($^{\circ}$) were obtained for each time interval (associated with previous studies (Creager, 1997; Laske and Masters, 2003; Zhang et al., 2005)) for three different lateral gradients in velocity (Song, 2000). Also shown is average shift over time ($^{\circ}\text{yr}^{-1}$). Compare results from this table with Supplementary Table S5 from Zhang et al. (2005).

Integrated total shift of inner core ($^{\circ}$) with a variable rotation rate (Figure A.13b)								
Lateral gradient from Song (2000) with and without mantle correction (% per degree)	1967-1996 travel times (Creager, 1997)		1977-1998 normal modes (Laske and Masters, 1999)		1961-2004 doublets (Zhang et al., 2005)		1961-2007 doublets, This study	
	Shift($^{\circ}$)	Shift/time ($^{\circ}\text{yr}^{-1}$)	Shift($^{\circ}$)	Shift/time ($^{\circ}\text{yr}^{-1}$)	Shift($^{\circ}$)	Shift/time ($^{\circ}\text{yr}^{-1}$)	Shift($^{\circ}$)	Shift/time ($^{\circ}\text{yr}^{-1}$)
-0.0278								
no mantle corr.	8.48	0.30	4.10	0.19	13.27	0.31	11.43	0.25
-0.0176								
station only	13.39	0.48	6.49	0.31	21.97	0.51	18.05	0.39
-0.0145								
station and source	16.26	0.58	7.88	0.38	26.66	0.62	21.91	0.48

While body wave studies tend to be superior in revealing short-scale features, normal modes, although sensitive to inner-core differential rotation, are insensitive to small-scale heterogeneity and anisotropy. Figure A.13 indicates that the rotation of the inner core in the time period 1977-1998 was characterized by acceleration starting after 1985 and deceleration starting before 1995, but for the rest of the time the rotation was close to zero with respect to the mantle. Interestingly, the inner core underwent a slight westward rotation between the years 1981 and 1985. We integrated the rotation rate over a period of approximately 20 years (shown by light grey rectangle in Figure A.13b) and obtained a total shift of 4.10° (see the 1977-1998 normal modes column in of Table A.1) when mantle correction are ignored. After dividing by the total time interval, we retrieved an average rate of $0.19^{\circ}\text{yr}^{-1}$, in agreement with normal modes from the same time interval (Laske and Masters, 2003). Slightly higher values were obtained when the station and source corrections were applied (0.31 and $0.38^{\circ}\text{yr}^{-1}$). Overall, our averaged rate obtained from the normal modes time interval is significantly smaller than that resulting from the doublets time interval.

The above calculations thus provide a quantitative explanation for and an elegant resolution to the long-standing discrepancy between differential rotation rates derived from either body waves (Song and Richards, 1996; Creager, 1997; Song, 2000; Li and Richards, 2003; Zhang et al., 2005) or normal modes (Laske and Masters, 2003) alone (Figure A.13b).

A.9 Geodynamical implications

Our results reveal that although at times the angular alignment of the inner core and the mantle remains negligibly small or even negative (retrograde rotation), the inner core exhibits cumulative rotation in the eastward direction (prograde rotation) with a mean rate of $0.25\text{--}0.48^\circ\text{yr}^{-1}$, depending on the Earth model used for travel time corrections (Table A.1). This produces a total eastward shuffle between about 11 and 22° over the time interval of 1961–mid 2007 (Table A.1). Our study provides an alternative to the steady rotation model and suggests that superimposed on this average motion are decadal fluctuations. The most striking feature of the recovered differential rotation time history is the large fluctuation starting after 2000 characterized by a sharp acceleration and then a deceleration that leads to a retrograde rotation. Its magnitude is uncertain owing to the edge effects imposed by the B-spline parametrization and disappears completely when doublet #8 is excluded from the inversion, as shown by our bootstrap test (Figure A.13b). Although the error associated with doublet #8 is not larger than that of other doublets, additional data are required to further constrain the inner-core rotational dynamics for these more recent years. In the meantime, a more conservative model should be considered (dashed line in Figure A.13b) while noting that the exclusion of doublet #8 does not change the main conclusions about the shuffling rotation of the inner core.

Present constraints on the amplitude of fluctuation in the differential rotation rate of the inner core are based on LOD variations not exceeding those observed. These constraints depend on the assumptions about the relative strength of electromagnetic coupling at the core-mantle boundary and gravitational coupling. In a previous study (Dumberry, 2007), the inner-core-mantle gravitational coupling strength was required to be quite large to explain the 6 yr mode in LOD. However, a more recent study (Gillet et al., 2010) suggests a different source for this mode, thereby making a weaker gravitational coupling strength viable. When inner-core differential rotation is approached from an angular momentum perspective as in Dumberry and Mound (2010), a rate of about 0.25°yr^{-1} at all periods of fluctuation does not violate the observed LOD so long as the product of Γ and τ is smaller than 5×10^{19} Nmyr, where Γ is the gravitational coupling factor and τ is the viscous relaxation time of the inner core. Keeping in mind the uncertainties in estimates of electromagnetic coupling at the core-mantle boundary (Dumberry and Mound, 2010), the observed inner-core fluctuations shown in Figure A.13b can be used to place upper bounds on the gravitational coupling.

Although other mechanisms, such as variable inner-core topography (Wen, 2006; Cao et al., 2007) or rapidly changing structure in the inner or outer core (Makinen and Deuss, 2011), have been suggested to explain seismic observations, the inferred acceleration of the inner core is in agreement with geodynamical simulations. Using a torque balance equation such as in Aubert and Dumberry (2011) and a previous gravitational torque estimate (Dumberry and Mound, 2010), the exciting electromagnetic

torque required to explain the observed accelerations in our model of inner-core rotation is $\sim 1.19 \times 10^{20}$ Nm, which agrees with published values (Aurnou and Olson, 2000).

Recent numerical geodynamo simulations suggest that present-day seismically inferred mean rotation rates of several tenths of a degree per year could be a fragment of a time-varying signal rather than a steady super rotation (Aubert and Dumberry, 2011). If, on the one hand, the mantle has a major influence on the core dynamics, it would take a very slow rotation of 1°Myr^{-1} , assuming an inner core growth rate of 1mmyr^{-1} (Dumberry and Mound, 2010), to preserve a degree-one longitudinal signature at the top 100 km of the inner core, as seismological evidence suggests there exists (Tanaka and Hamaguchi, 1997; Niu and Wen, 2009). We note that despite attempts to map the slow to fast transition as a function of depth (Waszek et al., 2011), the present core-sensitive seismological data do not provide dense enough spatial sampling to constrain a sharp transition from the slow to the fast hemisphere of the inner core. If, on the other hand, the core dynamics are minimally influenced by the mantle, a development of a hemispherical structure at the top of the inner core is possible through a much faster dynamical mechanism, such as degree-one convection (Monnereau et al., 2010; Alboussière et al., 2010).

Chapter 2 supplementary information

What follows are figures not included in the Young et al. (2012) paper, yet are nonetheless important to the research of Chapter 2.

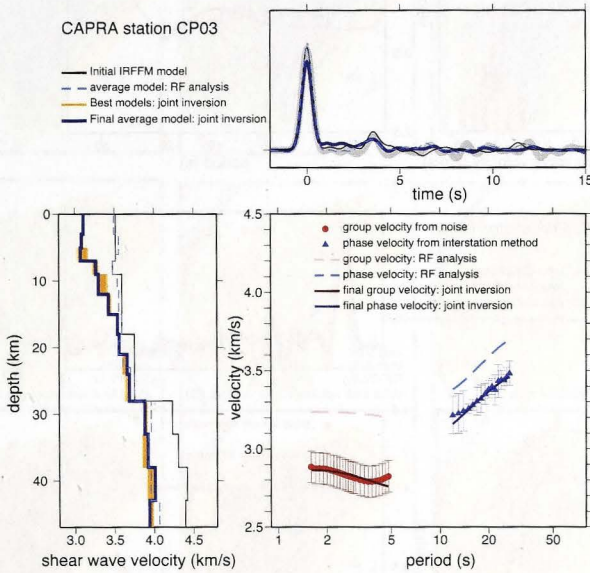


Figure B.1: Inversion information for station CP03 as shown for stations CP14 and CP08 (Figure 2.6) in Chapter 2. 1-D shear wave velocity models are shown in the lower left. An ensemble of best models (yellow) comprise 279 individual models, which include 3 weight values, 3 damping values, and 31 iterations. Error bars for the dispersion curves show one standard deviation of the velocities (see bottom right).

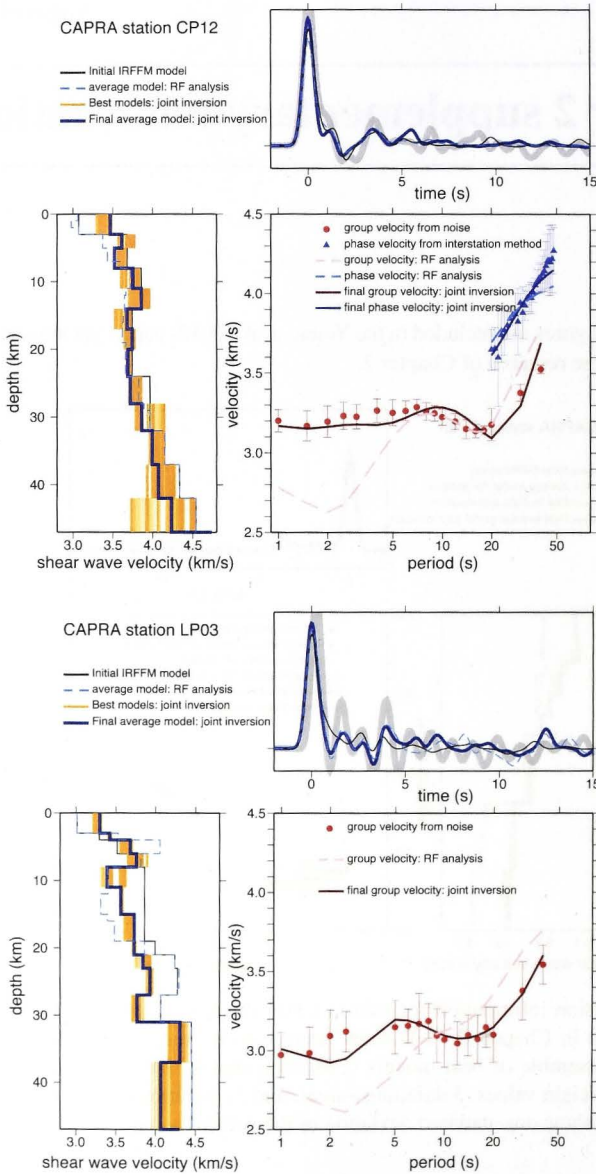


Figure B.2: As in Figure B.1, but for stations CP12 and LP03.

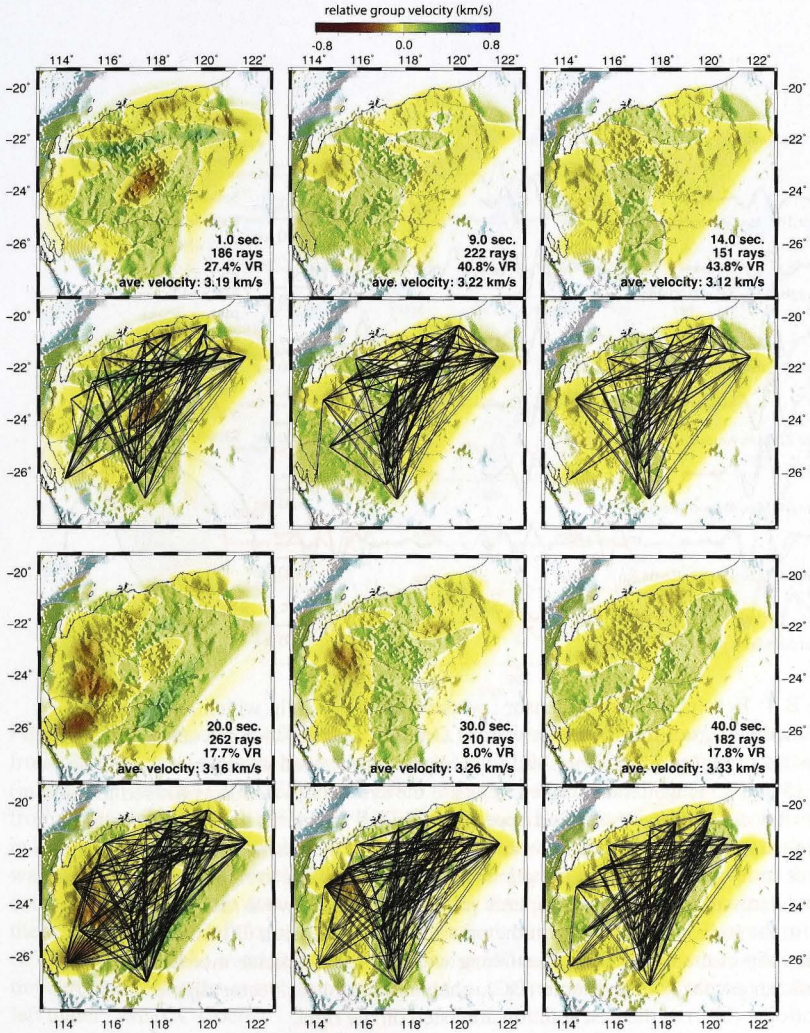


Figure B.3: Group velocity and raypath coverage maps in Western Australia for periods of 1, 9, 14, 20, 30, and 40 s. Period, number of raypaths, variance reduction, and the average velocity are shown in the lower left corners. The “relative group velocity” of the color scale is relative to the average velocity for each period.

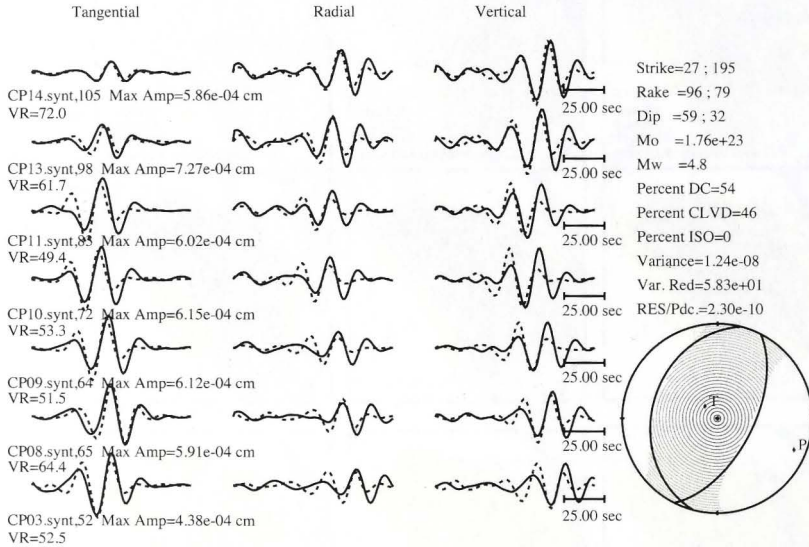


Figure B.4: Results of moment tensor inversion for the case in which our final composite model is used to produce structural Green's functions for the seven selected stations (as in Figure 2.8b). The solid lines show the observed waveforms filtered between 15 and 35 s, whilst the dashed lines are the synthetic waveforms filtered in the same manner. The data are shifted approximately 9 s further in time with respect to the synthetics than in Figure 2.8a, where a normal fault mechanism results. The three different components of the seismograms are shown from left to right: tangential, radial, and vertical. The lower-hemisphere projection of the P-wave radiation pattern is shown in the lower right along with the pressure (P) and tension (T) axis. The strike, rake, and dip of the two nodal planes along with the scalar seismic moment, moment magnitude, percent double couple (DC), compensated linear vector dipole (CLVD), and isotropic (ISO) of the best solution are listed on the right.

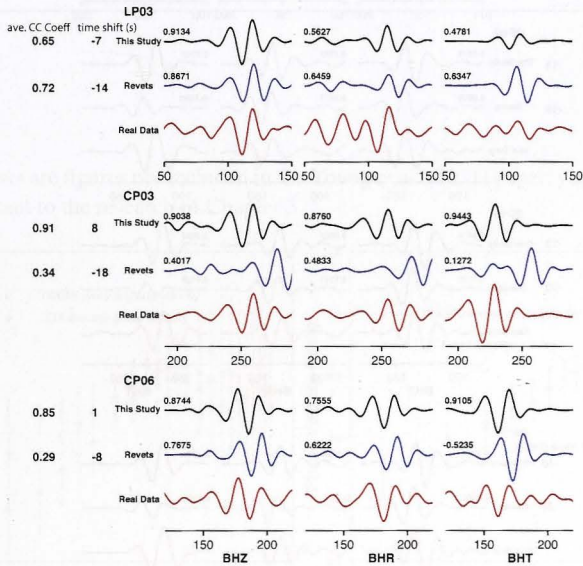


Figure B.5: A comparison of the data (in black) to the synthetic waveforms produced from our preferred focal mechanism (in red) and from that given in Revets et al. (2009) (in blue) for stations CP06, CP03, and LP03. The three station components are shown from left to right as BHZ, BHR, and BHT. The synthetic waveforms have been shifted in time according to the number of seconds listed under “time shift” on the left of the waveforms. The cross correlation coefficient of each component resulting from the comparison of synthetic data with the data for the time interval shown is listed above the waveform on the left for each component for both our solution and the Revets et al. (2009) solution. The average cross-correlation coefficient, which is the mean of the three component cross-correlation coefficients for a given station, is given on the far left under “ave. CC Coeff”.

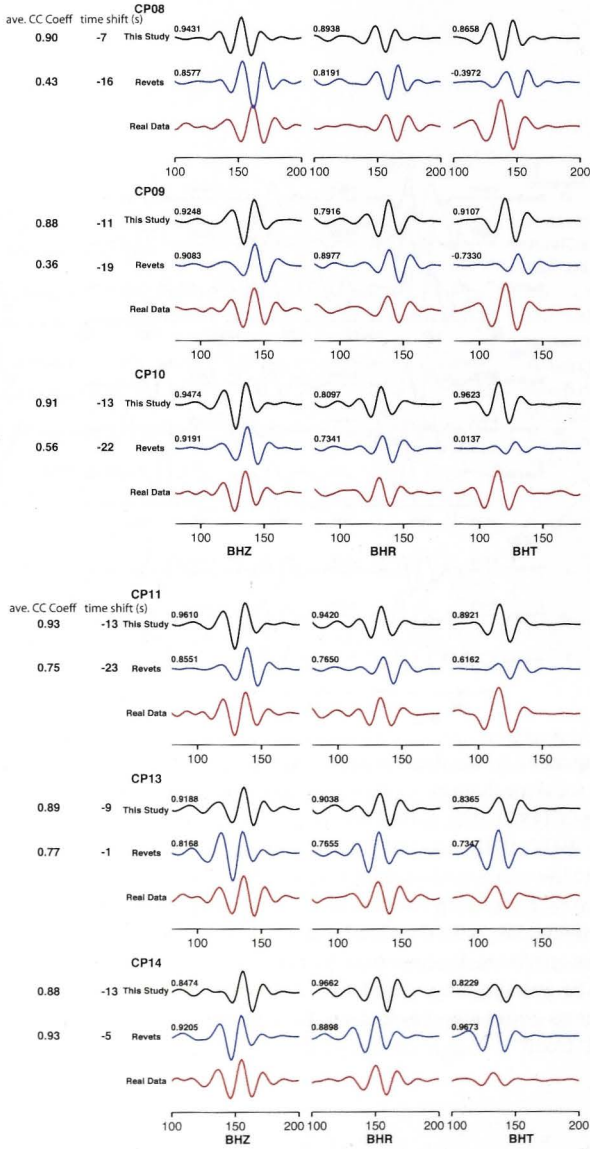


Figure B.6: As for Figure B.5, but for stations CP08, CP09, CP10, CP11, CP13, and CP14.

Chapter 3 supplementary information

What follows are figures not included in the Young et al. (2011) paper, yet are nonetheless important to the research of Chapter 3.

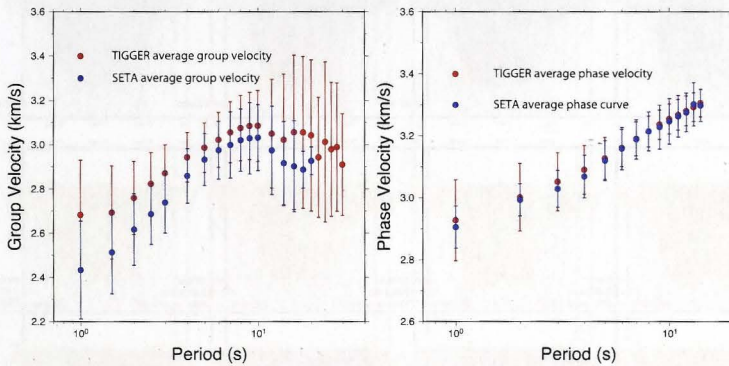


Figure C.1: Average group (left) and phase (right) velocity curves and standard deviations for the SETA and TIGGER subarrays.

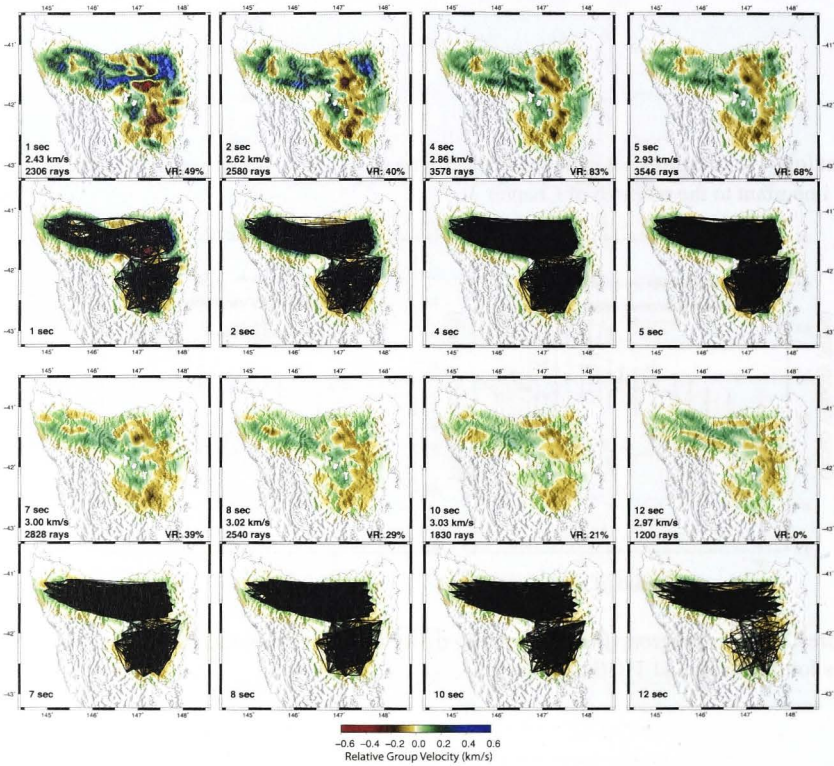


Figure C.2: Group velocity maps and their corresponding raypath coverage maps for periods of 1, 2, 4, 5, 7, 8, 10, and 12 s. Period, background velocity, and number of ray paths are shown in the lower left corners.

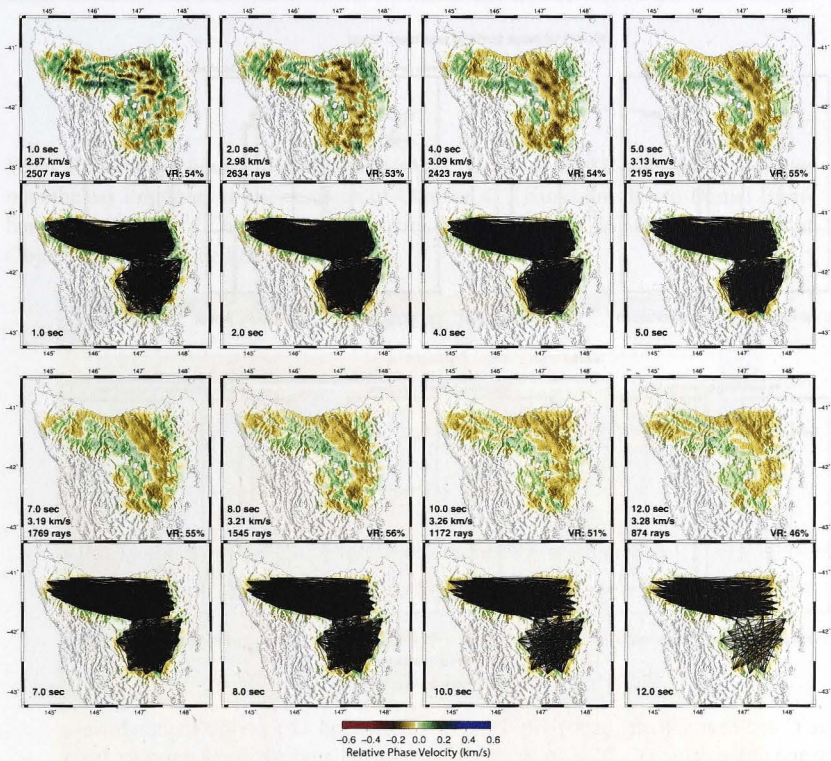


Figure C.3: Phase velocity maps and their corresponding raypath coverage maps for periods of 1, 2, 4, 5, 7, 8, 10, and 12 s. Period, background velocity, and number of ray paths are shown in the lower left corners.

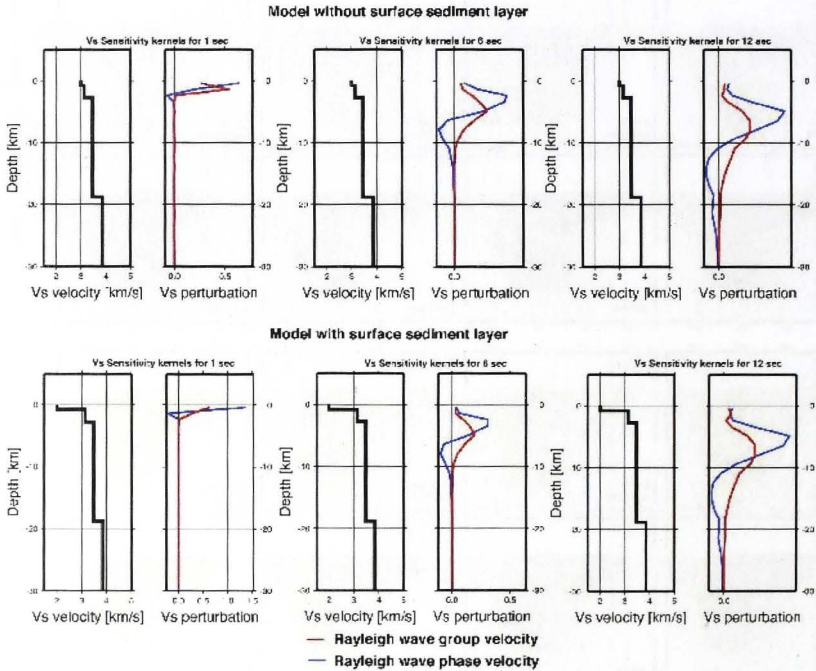


Figure C.4: Shear velocity sensitivity kernels for 1, 6, and 12 s period Rayleigh wave group and phase velocities. The upper row is for a crustal model without a surface layer of sediments and the lower row is calculated assuming a decrease in shear velocity by 1 km/s in the uppermost 0.8 km of the crust. Note that the presence of a 0.8 km surface layer of decreased velocities does not significantly affect the sensitivity kernels.

Chapter 4 supplementary information

What follows are figures not included in the Young et al. (2013b) paper, yet are nonetheless important to the research of Chapter 4. Thanks are due to Daniel Bombardieri and Richard Chopping for help with figure creation using Gocad (Geological Object Computer Aided Design) software.

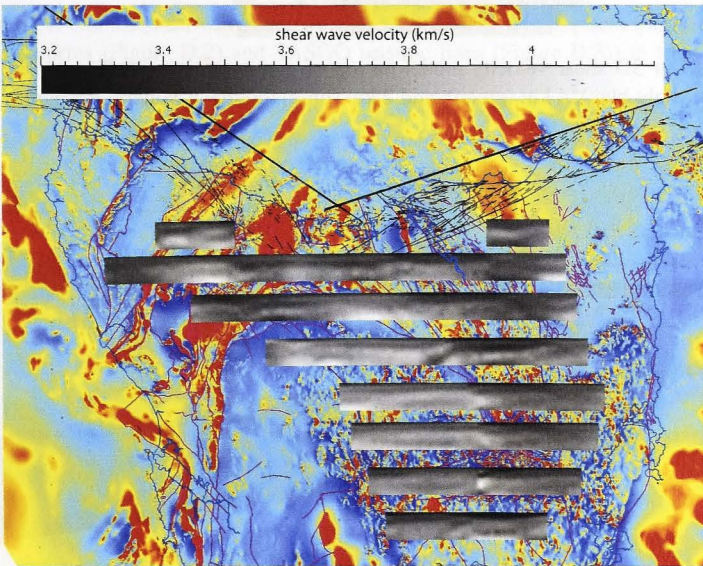


Figure D.1: Our 3D shear velocity model on top of total magnetic intensity (courtesy Mineral Resources Tasmania).

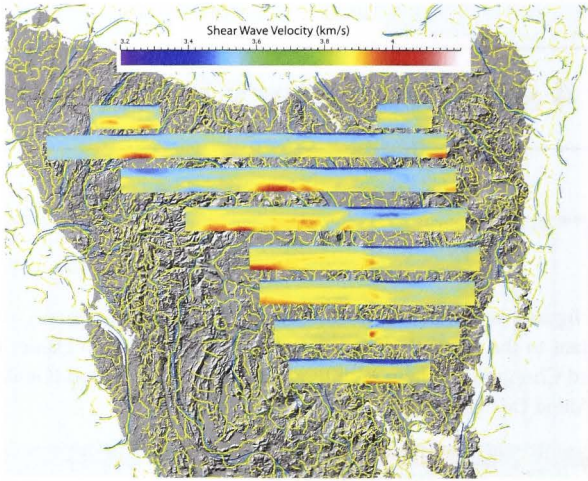


Figure D.2: Our 3D shear velocity model on top of gravity worms for 7 km (dark blue), 13 km (light blue), 4 km (green), and 2 km (lime) (courtesy Mineral Resources Tasmania).

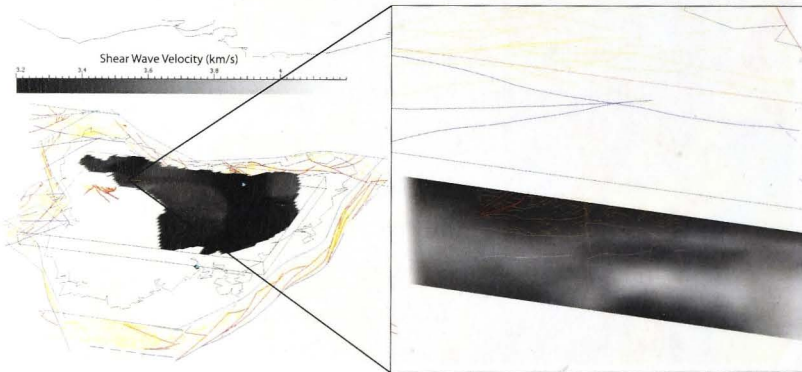


Figure D.3: TASGO seismic survey (1995) lines (left) and zoom on line in northwest Tasmania on top of our 3D shear wave velocity model (courtesy Mineral Resources Tasmania and Geoscience Australia).

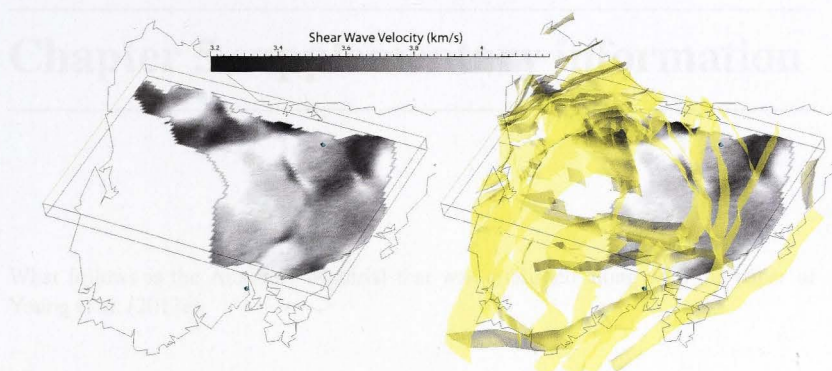


Figure D.4: Our 3D shear wave velocity model with major fault surfaces (derived from gravity worms (Figure D.2) and TASGO seismic lines (Figure D.3)) in transparent yellow.

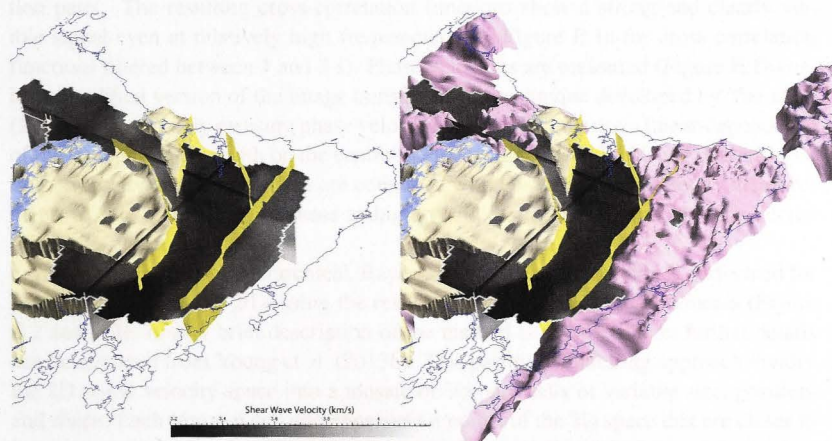


Figure D.5: (left) Concealed Tyennan Block material (straw colored), Tyennan metasediments at surface (blue colored), and major fault structures (yellow surfaces). (right) Intrusive Devonian granites shown by pink structure (courtesy Mineral Resources Tasmania) (Courtesy Geoscience Australia).



Figure 4.1: [Illegible text describing the figure]



Figure 4.2: [Illegible text describing the figure]

Chapter 5 supplementary information

What follows is the Auxiliary Material that was published along with the paper of Young et al. (2013a).

E.1 Data analysis and inversion scheme

The data for this study come from the WOMBAT transportable seismic array project. To produce the highest quality Green's functions (Figure E.1a), the noise recordings are divided into 40-min segments with 75% overlap (Seats et al., 2012). Vertical-component data are cross-correlated and stacked for all simultaneously recording station pairs. The resulting cross-correlation functions show a strong and clearly visible signal even at relatively high frequencies (see Figure E.1a for cross-correlation functions filtered between 1 and 3 s). Phase velocities are measured (Figure E.1b) using a modified version of the image transformation technique developed by Yao et al. (2006). To accurately measure phase velocities up to 1 Hz, we use a linear-dependence of the bandpass filter width on the central period as introduced by Young et al. (2011). Phase velocity dispersion curves are compared with observed group velocity measurements to help resolve the 2π phase ambiguity and ensure the correct curve is selected (Figure E.1b).

A transdimensional, hierarchical, Bayesian tomographic inversion is performed for periods between 1 and 20 s using the resulting phase velocity measurements (Figure E.2 and E.3). A very brief description of the method is provided here; further details can be obtained from Young et al. (2013b). This partition modelling approach divides the 2D phase velocity space into a mosaic of Voronoi cells of variable size, position, and shape. Each Voronoi cell encompasses all points of the 2D space that are closer to its center than to any other Voronoi cell center. The transdimensionality of the method enables the number of cells to vary throughout the course of the inversion. In addition to solving for the number of cells, the data noise is also left as an unknown. Here, data "noise" refers to whatever our model cannot explain (Scales and Snieder, 1998; Bodin et al., 2012a), which can be attributed to measurement errors, shortcomings of the forward model, and mathematical or theoretical approximations. We assume that

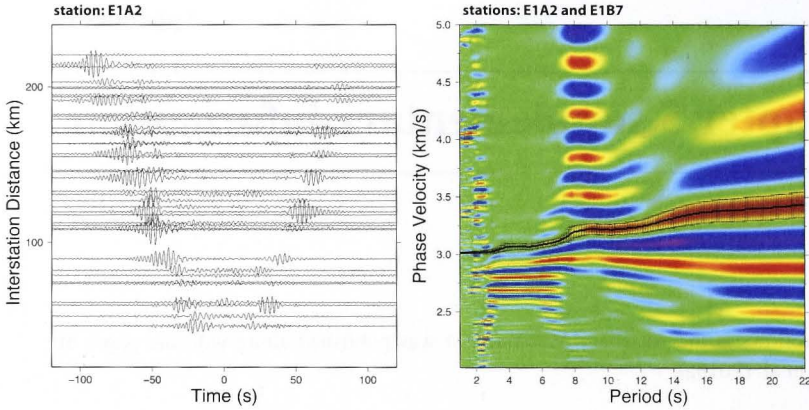


Figure E.1: (a) Cross-correlograms calculated from the EAL1 WOMBAT subarray with respect to station E1A2. Record sections are bandpass filtered between 1 and 3 s to illustrate the clear visibility of the Rayleigh waves at high frequencies. (b) Example frequency-time diagram for the EAL1 station pair E1A2 and E1B7. The dotted black line represents the chosen phase curve for this pair.

all phase velocity curves have the same level of uncertainty, or noise, for each given period.

As required by the Bayesian method, we impose prior information; namely, we use a uniform prior distribution 2.4 km/s wide and centered on the average phase velocity observed for that period. These bounds are wide enough such that the final recovered model is not hampered by the upper and lower limits.

A posterior probability distribution is acquired for the data noise and for each Voronoi cell location (nucleus latitude and longitude), Voronoi cell velocity, and the total number of cells (Figures E.2 and E.3). These posterior probability distributions are generated using a generalized version of MCMC sampling called reversible jump MCMC (rj-MCMC; Green (1995), Green (2003)). We can extract meaningful quantities from the posterior probability distributions such as the mean, median, or maximum. The average models, such as we show in Figures E.2 and E.3, contains more detail than any one individual model but none of the artificial discontinuities inherent to the base parametrization. Model complexity is greatest for periods between 3 and 12 s. This is likely due to the fact that (1) data for periods longer than 12 s have slightly higher noise estimates (see posterior probability distributions in Figures E.2 and E.3), (2) raypath coverage decreases with increasing period, since the interstation spacing is required to be at least three wavelengths (Bensen et al., 2008), (3) the short period stations (1 Hz sensors) will have more self-noise at longer periods, (4) data for periods shorter than 3 s also have higher noise estimates as a likely result of unresolvable

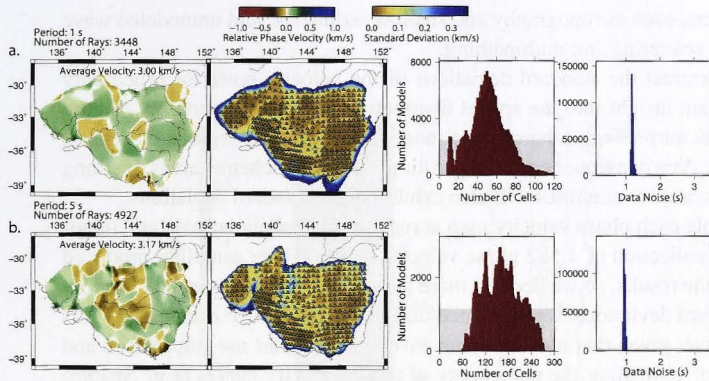


Figure E.2: Phase velocity maps for periods of (a) 1.0 and (b) 5.0 s are shown with their corresponding standard deviation plots. Phase velocities are relative to the “average velocity” given at the top of each map. Phase velocity and standard deviation maps are trimmed according to the contour line when standard deviation is equal to 0.3 km/s. Posterior probability distribution histograms for the number of cells (red columns) and data noise (blue columns) are also shown (right). The prior distributions are indicated by shaded gray rectangles.

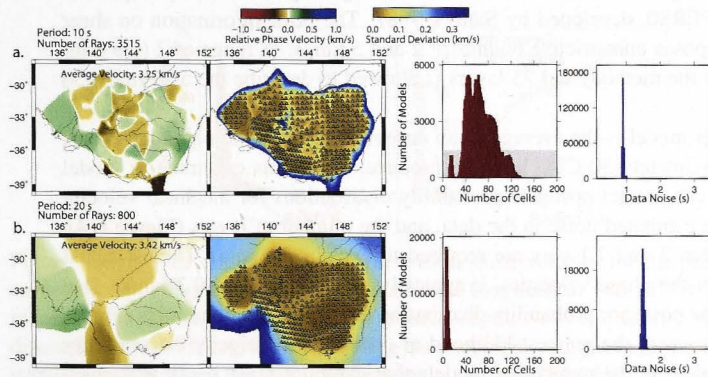


Figure E.3: Phase velocity maps for periods of (a) 10.0 and (b) 20.0 s are shown with their corresponding standard deviation plots. Phase velocities are relative to the “average velocity” given at the top of each map. Phase velocity and standard deviation maps are trimmed according to the contour line when standard deviation is equal to 0.3 km/s. Posterior probability distribution histograms for the number of cells (red columns) and data noise (blue columns) are also shown (right). The prior distributions are indicated by shaded gray rectangles.

near-surface effects, such as topography and shallow sediments, and unmodeled wave behavior, such as scattering and multipathing.

We can also extract the standard deviations of the velocity posterior probability distributions to gain insight into the spatial distribution of model uncertainty (Figure E.2 and E.3). Not surprisingly, there is the most certainty in the regions of densest raypath coverage. As a consequence of the partition modelling scheme, areas of strong velocity contrasts or discontinuities will also exhibit larger standard deviations.

We then sample each phase velocity map at regular intervals in latitude and longitude to acquire a collection of 1,572 phase velocity curves. Finer sampling produced essentially the same results, so we deemed more curves to be unnecessary. By also extracting the standard deviations, we gain uncertainty information for each curve. This is important to note, given that most previous inversion schemes use improvised and ad hoc methods of estimating the uncertainty of phase velocity curves (e.g. Shapiro and Ritzwoller (2002) and Bensen et al. (2009)).

Each phase velocity curve is inverted for a 1D shear velocity model using the Bayesian techniques described by Young et al. (2013b) (Figure E.4). The uncertainty of each phase velocity value is assumed to be proportional to the standard deviation associated with that value, with the constant of proportionality serving as an unknown in the problem. Each model is defined by a variable number of homogeneous horizontal layers, where the number, position, and velocity of the layers are all unknowns in the inverse problem. The forward method of calculating the phase velocity dispersion curves uses DISPER80, developed by Saito (1988). The prior information on shear wave velocity imposes unrestrictive bounds of 2 and 5 km/s. A range of 2 (the minimum allowed by the method) and 25 layers is allowed to describe the uppermost 30 km of the crust.

Each 1D shear model is the average of an ensemble of 100,000 model iterations, which take approximately 30 CPU hours to produce. From this ensemble of model realizations, one can extract posterior probability distributions for the shear velocity at each depth, the estimated noise in the data, and the number of layers (Figure E.4). In general, between 3 and 7 layers are required to explain the data. The estimated noise, or errors in the phase velocities, is typically between 0.1 and 0.3 km/s. One can also extract the posterior probability distribution for model discontinuities (Figure E.4c). The regions with the greatest likelihood of containing a velocity discontinuity are revealed by plotting the number of models that exhibit a layer break at a given depth. From Figure E.4c, it is apparent that a discontinuity is most probable at shallow depths.

E.2 Final 3D shear wave velocity model

Once we have inverted for the 1,572 unique 1D shear velocity models, we can represent each point in our final pseudo-3D shear wave velocity model by a shear velocity

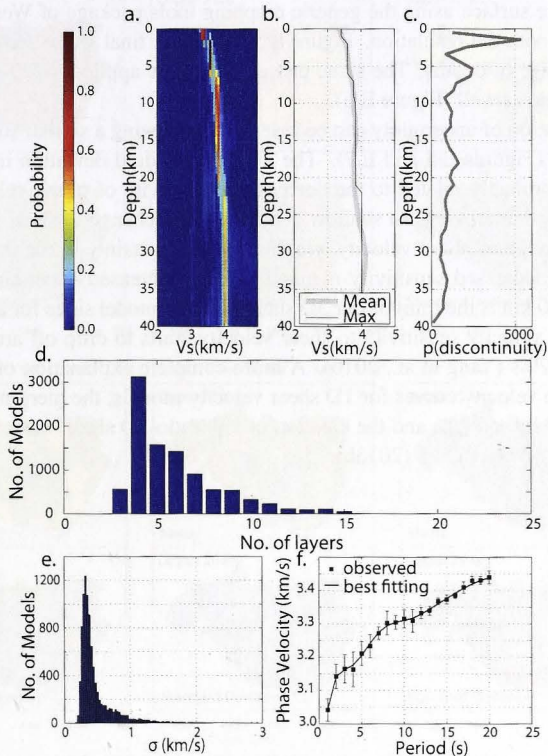


Figure E.4: (a.) Ensemble solutions for crustal shear velocity for the phase velocity curve corresponding to a latitude of -30.64° and longitude of 140.13° . (b.) Mean and maximum of the velocity distribution at each depth. (c.) Probability of a velocity discontinuity. (d.) Histogram representing the accompanying posterior probability distribution functions for the number of layers in the models. (e.) Histogram representing the accompanying posterior probability distribution functions for the noise associated with the data. (f.) Also shown are the phase velocity curves associated with the best fitting shear velocity model (black line) overlaid on the actual phase velocity values of the curve (small black squares). Standard deviations are shown by black error bars.

posterior probability distribution. To visualize the results, the average of the posterior probability distribution at a given depth is plotted at its respective geographic location. For aesthetic purposes, the resulting grid of velocity pixels is transformed into a continuous curvature surface using the generic mapping tools package of Wessel and Smith (1995) to smooth the pixelation. Figure E.5 shows the final shear wave velocity model over a range of depths. The same procedure can be applied to 2D slices in longitude and latitude as well (Figure E.6).

The spatial variation of uncertainty can be assessed by viewing a similar surface of standard deviations (Figures E.5 and E.7). The average standard deviation increases with depth; this is probably related to the decreasing sensitivity of phase velocity to shear velocity as depth increases. At shallow depths, a small change in shear velocity produces a large change in phase velocity, yielding greater certainty in the inversion. On the other hand, decreased sensitivity is manifested by increased uncertainty estimates. A depth of 30 km is the limit of our 3D shear velocity model since for a typical Earth model, phase velocity sensitivity to shear velocity starts to drop off around 35 km for a period of 20 s (Yang et al., 2010). A more complete explanation of the inversion of the phase velocity curves for 1D shear velocity models, the merging of the resulting shear velocity models, and the creation of a pseudo-3D shear wave velocity model is provided by Young et al. (2013b).

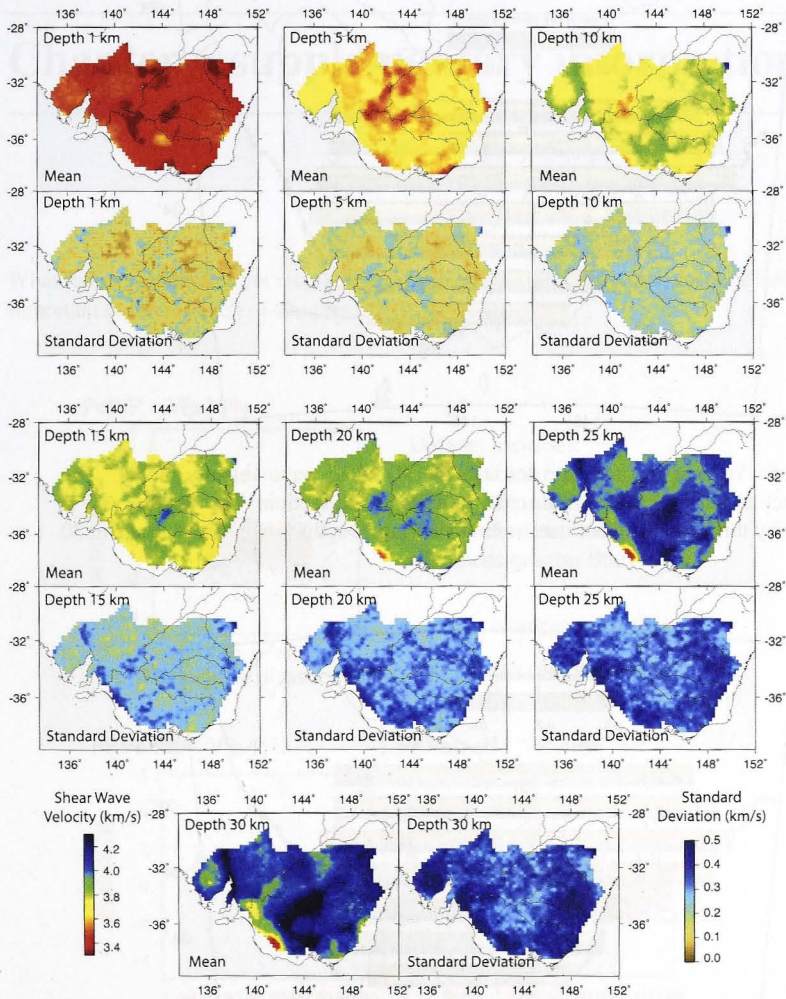


Figure E.5: Horizontal cross-sections showing the mean and standard deviation of the final ensemble of the pseudo-3D shear wave velocity models for depths of 1, 5, 10, 15, 20, 25, and 30 km.

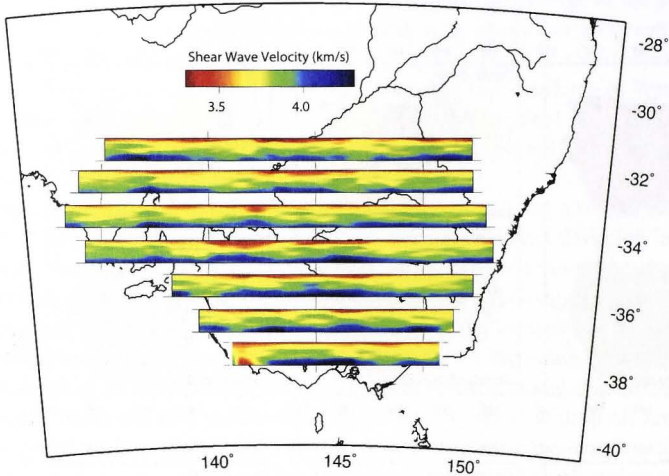


Figure E.6: Vertical cross-section through the 3D shear wave velocity model. The top of each cross-section is at the actual latitude of the section. The vertical axis is stretched by three times to facilitate ease of viewing. Depths range from surface to 30 km.

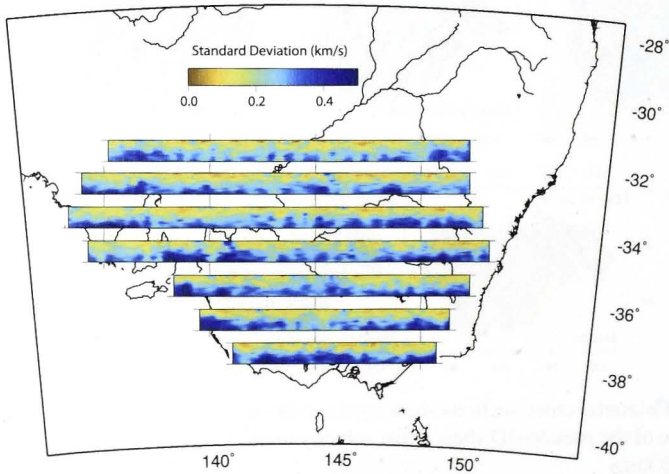


Figure E.7: Accompanying standard deviations for Figure E.6.

Chapter 6 supplementary information

What follows are figures not included in the Young et al. (2013c) paper, yet nonetheless important to the research of Chapter 6.

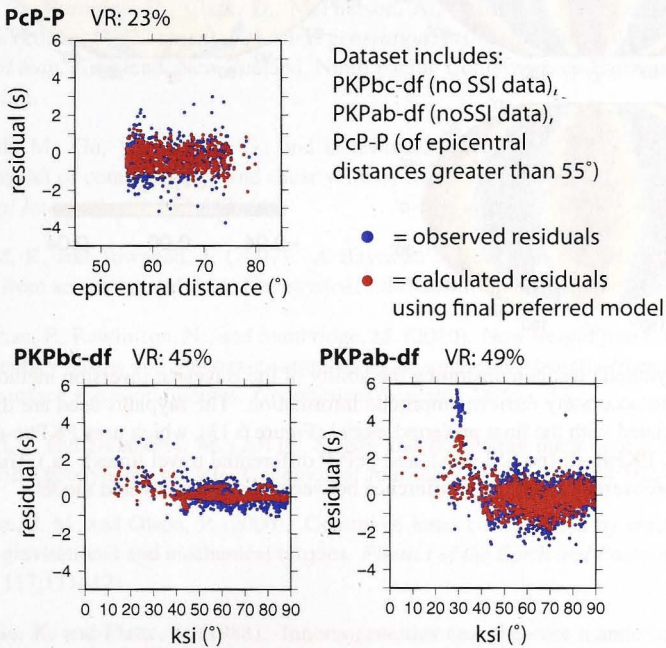


Figure F.1: Comparison of observed PKPbc-df, PKPab-df, and PcP-P differential travel time residuals and the forward-calculated residuals using our final preferred model from Chapter 4 (Figure 6.13).

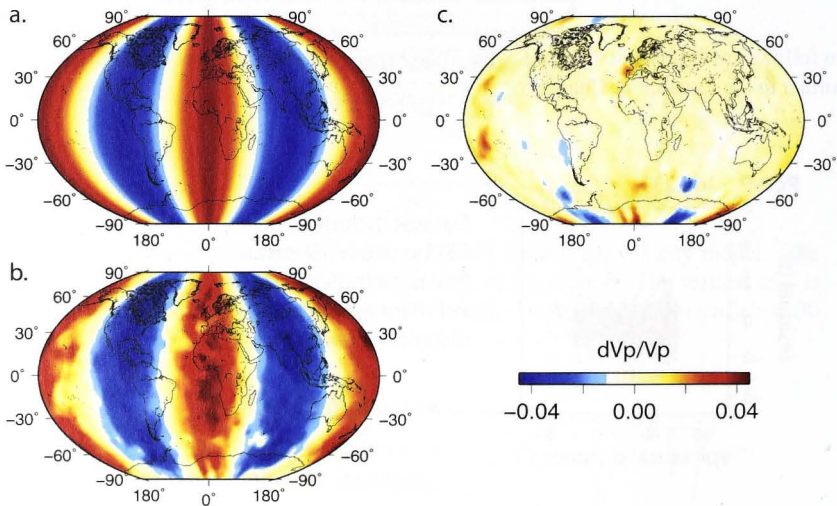


Figure F.2: Synthetic test demonstrating the ability of the Bayesian inversion method of this study to accurately retrieve amplitude information. The raypaths used are the same as associated with the final preferred model (Figure 6.13), which uses PKPbc-df (no SSI data), PKPab-df (no SSI data), and PcP-P differential travel times. (a.) True model. (b.) Recovered model. (c.) Difference between true and recovered model.

Bibliography

- Abdulah, A. (2007). *Seismic body wave attenuation tomography beneath Australasian region*. PhD thesis, The Australian National University, Canberra, ACT.
- Aki, K. and Richards, P., editors (2002). *Quantitative Seismology: Theory and Methods*. University Science Books, Sausalito, CA, 2nd edition.
- Alboussière, T., Deguen, R., and Melzani, M. (2010). Melting-induced stratification above the Earth's inner core due to convective translation. *Nature*, 466:744–747.
- Allen, T., Burbidge, D., Clark, D., McPherson, A., Collins, C., and Leonard, M., editors (2011). *Development of the next generation Australian National Earthquake Hazard map*, Auckland, New Zealand. Ninth Pacific Conference on Earthquake Engineering.
- Antolik, M., Gu, Y., Elström, G., and Dziewonski, A. (2003). J362D28: A new joint model of compressional and shear velocity in the Earth's mantle. *Geophysical Journal International*, 153:443–446.
- Arnold, R. and Townend, J. (2007). A Bayesian approach to estimating tectonic stress from seismological data. *Geophysical Journal International*, 170:1336–1356.
- Arroucau, P., Rawlinson, N., and Sambridge, M. (2010). New insight into Cainozoic sedimentary basins and Paleozoic suture zones in southeast Australia from ambient noise surface wave tomography. *Geophysical Research Letters*, 37.
- Aubert, J. and Dumberry, M. (2011). Steady and fluctuating inner core rotation in numerical geodynamo models. *Geophysical Journal International*, 184:162–170.
- Aurnou, J. M. and Olson, P. (2000). Control of inner core rotation by electromagnetic, gravitational and mechanical torques. *Physics of the Earth and Planetary Interiors*, 117:111–121.
- Bataille, K. and Flatte, S. (1988). Inhomogeneities near the core-mantle boundary inferred from short-period scattered PKP waves recorded at the Global Digital Seismograph Network. *Journal of Geophysical Research*, 93:15,057–15,064.
- Bayes, T. (1763). An essay towards solving a problem in the doctrine of chances. *Philosophical Transactions of the Royal Society of London*, 53:370–418.

Beghein, C., Resovsky, J. S., and Trampert, J. (2002). P and S tomography using normal-mode and surface waves data with a neighbourhood algorithm. *Geophysical Journal International*, 149:646–658.

Behr, Y., Townend, J., Bannister, S., and Savage, M. (2010). Shear velocity structure of the Northland Peninsula, New Zealand, inferred from ambient noise correlations. *Journal of Geophysical Research*, 115.

Behr, Y., Townend, J., Bannister, S., and Savage, M. K. (2011). Crustal shear wave tomography of the Taupo Volcanic Zone, New Zealand, via ambient noise correlation between multiple three-component networks. *Geochemistry, Geophysics, Geosystems*.

Belperio, A. P. and Flint, R. B. (1993). Geological note: The southeast margin of the Gawler Craton. *Australian Journal of Earth Sciences*, 40:4:423–426.

Bensen, G., Ritzwoller, M., and Yang, Y. (2009). A 3-D shear velocity model of the crust and uppermost mantle beneath the United States from ambient seismic noise. *Geophysical Journal International*, 177:1177–1196.

Bensen, G. D., Ritzwoller, M. H., Barmin, M. P., Levshin, A. L., Lin, F., Moschetti, M. P., Shapiro, N. M., and Yang, Y. (2007). Processing seismic ambient noise data to obtain reliable broad-band surface wave dispersion measurements. *Geophysical Journal International*, 169:1239–1260.

Bensen, G. D., Ritzwoller, M. H., and Shapiro, N. M. (2008). Broadband ambient noise surface wave tomography across the United States. *Journal of Geophysical Research*, 113.

Bernardo, J. and Smith, A. (1994). *Bayesian Theory*. John Wiley & Sons, Ltd.

Berry, R. F., Steele, D. A., and Meffre, S. (2008). Proterozoic metamorphism in Tasmania: Implications for tectonic reconstructions. *Precambrian Research*, 166:387–396.

Betts, P., Giles, D., Lister, G., and Frick, L. (2002). Evolution of the Australian lithosphere. *Australian Journal of Earth Sciences*, 49:661–695.

Bijwaard, H., Spakman, W., and Engdahl, E. R. (1998). Closing the gap between regional and global travel time tomography. *Journal of Geophysical Research*, 103:30055–30078.

Bodin, T. and Sambridge, M. (2009). Seismic tomography with the reversible jump algorithm. *Geophysical Journal International*, 173(3):1411–1436.

- Bodin, T., Sambridge, M., Rawlinson, N., and Arroucau, P. (2012a). Transdimensional tomography with unknown data noise. *Geophysical Journal International*, 189:1536–1556.
- Bodin, T., Sambridge, M., Tkalčić, H., Arroucau, P., Gallagher, K., and Rawlinson, N. (2012b). Transdimensional inversion of receiver functions and surface wave dispersion. *Journal of Geophysical Research*, 117.
- Bondár, I. and Storchak, D. (2011). Improved location procedure at the International Seismological Centre. *Geophysical Journal International*, 186:1220–1244.
- Boschi, L. and Dziewonski, A. M. (2000). Whole Earth tomography from delay times of P, PcP, and PKP phases: Lateral heterogeneities in the outer core or radial anisotropy in the mantle? *Journal of Geophysical Research*, 105:13675–13696.
- Box, G. and Tiao, G. (1973). *Bayesian inference in statistical analysis*. John Wiley & Sons, Inc.
- Brauns, C. M., Hergt, J. M., Woodhead, J. D., and Maas, R. (2000). Os isotopes and the origin of the Tasmanian dolerites. *Journal of Petrology*, 41:905–918.
- Bréger, L. and Romanowicz, B. (1998). Three-dimensional structure at the base of the mantle beneath the central Pacific. *Science*, 282:718–720.
- Bréger, L., Tkalčić, H., and Romanowicz, B. (2000). The effect of D'' on PKP(AB-DF) travel time residuals and possible implications for inner core structure. *Earth and Planetary Science Letters*, 175:133–143.
- Calvet, M. and Chevrot, S. (2005). Traveltime sensitivity kernels for PKP phases in the mantle. *Physics of the Earth and Planetary Interiors*, 153:21–31.
- Campillo, M. (2006). Phase and correlation in 'random' seismic fields and the reconstruction of the Green's function. *Pure Applied Geophysics*, 163:475–502.
- Cao, A., Masson, Y., and Romanowicz, B. (2007). Short wavelength topography on the inner-core boundary. *Proceedings of the National Academy of Sciences USA*, 104:31–35.
- Cassidy, K., Champion, D., Krapez, B., Barley, M., Brown, S., Blewett, R., Groenewald, P., and Tyler, I. (2006). A revised geological framework for the Yilgarn Craton, Western Australia. *Geological Survey of Western Australia Record*, 2006/8.
- Cawood, P. (2005). Terra Australia Orogen: Rodinia breakup and development of the Pacific and Iapetus margins of Gondwana during the Neoproterozoic and Paleozoic. *Earth-Science Reviews*, 69:249–279.

Cawood, P. and Tyler, I. (2004). Assembling and reactivating the Proterozoic Capricorn Orogen: Lithotectonic elements, orogenies, and significance. *Precambrian Research*, 128:201–218.

Cayley, R. (2011). Exotic crustal block accretion to the eastern Gondwanaland margin in the Late Cambrian - Tasmania, the Selwyn Block, and implications for the Cambrian-Silurian evolution of the Ross, Delamerian, and Lachlan orogens. *Gondwana Research*, 19:628–649.

Cayley, R. A., Korsch, R. J., Kennett, B. L. N., Skladzien, P., Jones, L., Morand, V., Gibson, G., Rawling, T., and Betts, P. (2011a). Results of deep seismic reflection imaging of the eastern Delamerian Orogen, South Australia and western Victoria, Australia. Data CD version, GeoScience Department of Primary Industries, Victoria.

Cayley, R. A., Korsch, R. J., Moore, D. H., Costelloe, R. D., Nakamura, A., Willman, C. E., Rawling, T. J., Morand, V. J., Skladzien, P. B., and O'Shea, P. J. (2011b). Crustal architecture of central Victoria: Results from the 2006 deep crustal reflection seismic survey. *Australian Journal of Earth Sciences*, 58:113–156.

Cayley, R. A. and Taylor, D. H. (1997). Grampians special map area geological report. Technical Report 107, Geological Survey of Victoria Report.

Cayley, R. A., Taylor, D. H., VandenBerg, A. H. M., and Moore, D. H. (2002). Proterozoic - Early Palaeozoic rocks and the Tyennan Orogeny in central Victoria: The Selwyn Block and its tectonic implications. *Australian Journal of Earth Sciences*, 49:225–254.

Chevrot, S., Martin, R., and Komatitsch, D. (2012). Optimized discrete wavelet sphere with the lifting scheme - implications for global finite-frequency tomography. *Geophysical Journal International*, 191:1391–1402.

Clark, D. and Leonard, M. (2003). Principle stress orientations from multiple focal-plane solutions: New insight into Australian intraplate stress field. *Special Publications - Geological Society of Australia*, 22:91–105.

Clarke, G. L. and Powell, R. (1989). Basement-cover interaction in the Adelaide Foldbelt, South Australia: The development of an arcuate foldbelt. *Tectonophysics*, 158:209–226.

Clitheroe, G., Gudmundsson, O., and Kennett, B. (2000). The crustal thickness of Australia. *Journal of Geophysical Research*, 105:13,697–13,713.

Clitheroe, G., Gudmundsson, O., and Kennett, B. (2001). Sedimentary and upper crustal structure of Australia from receiver functions. *Australian Journal of Earth Sciences*, 47:209–216.

- Coblentz, D., Zhou, S., Hillis, R., Richardson, R., and Sandiford, M. (1998). Topography, boundary forces, and the Indo-Australian intraplate stress field. *Journal of Geophysical Research*, 103:919–931.
- Collier, J. D. and Hellfrich, G. (2001). Estimate of inner core rotation rate from United Kingdom regional seismic network data and consequences for inner core dynamical behaviour. *Earth and Planetary Science Letters*, 193:523–537.
- Collins, C., Drummond, B., and Nicoll, M. (2003). Crustal thickness patterns in the Australian continent. *Special Paper - Geological Society of America*, 372:121–128.
- Cormier, V. (1999). Anisotropy of heterogeneity scale lengths in the lower mantle from PKIKP precursors. *Geophysical Journal International*, 136:373–384.
- Cormier, V. and Choy, G. L. (1986). A search for lateral heterogeneity in the inner core from differential travel times near PKP-D and PKP-C. *Geophysical Research Letters*, 13:1553–1556.
- Crawford, A. J., Meffre, S., and Symonds, P. A. (2003). 120 to 0 Ma tectonic evolution of the southwest Pacific and analogous geological evolution of the 600 to 220 Ma Tasman Fold Belt System. In Hillis, R. R. and Miller, R. D., editors, *The evolution and dynamics of the Australian plate*, pages 25–40. Special Publications - Geological Society of Australia.
- Crawford, A. J., Stevens, B. P. J., and Fanning, M. (1997). Geochemistry and tectonic setting of some Neoproterozoic and early Cambrian volcanics in western New South Wales. *Australian Journal of Earth Sciences*, 44(6):831–852.
- Creager, K. (1997). Inner core rotation rate from small-scale heterogeneity and time-varying travel times. *Science*, 278:1284–1288.
- Creager, K. (1999). Large-scale variations in inner core anisotropy. *Journal of Geophysical Research*, 104:23127–23139.
- Crotwell, H. P., Owens, T. J., and Ritsema, J. (1999). The TauP Toolkit: Flexible seismic travel-time and ray-path utilities. *Seismological Research Letters*, 70:154–160.
- Curtis, A., Gerstoft, P., Sato, H., Snieder, R., and Wapenaar, K. (2006). Seismic interferometry - turning noise into signal. *The Leading Edge*, 25(9):1082–1092.
- Dahlen, F. and Tromp, J., editors (1998). *Theoretical Global Seismology*. Princeton University Press, Princeton, NJ.

Della Mora, L., Boschi, L., Tackley, P. J., Nakagawa, T., and Giardini, D. (2011). Low seismic resolution cannot explain S/P decorrelation in the lower mantle. *Geophysical Research Letters*, 38.

Diehl, T. and Kissling, E. (2007). Users guide for consistent phase picking at local to regional scales. Inst. of Geophys., ETH Zurich, Switzerland.

Direen, N. G. and Crawford, A. J. (2003a). Fossil seaward-dipping reflector sequences preserved in southeastern Australia: A 600 Ma volcanic passive margin in eastern Gondwanaland. *Journal of the Geological Society (London)*, 160:985–990.

Direen, N. G. and Crawford, A. J. (2003b). The Tasman Line: Where is it, what is it, and is it Australia's Rodinian breakup boundary? *Australian Journal of Earth Sciences*, 50:491–502.

Direen, N. G. and Leaman, D. E. (1997). Geophysical modelling of structure and tectonostratigraphic history of the Longford Basin, northern Tasmania. *Exploration Geophysics*, 28:29–33.

Doornbos, D. (1974). Seismic wave scattering near caustics: Observations of PKKP precursors. *Nature*, 247:352–353.

Dorman, J. and Ewing, M. (1962). Numerical inversion of seismic surface wave dispersion data and crust-mantle structure in the New York - Pennsylvania area. *Journal of Geophysical Research*, 67:5227–5241.

Dreger, D. and Helmberger, D. (1993). Determination of source parameters at regional distances with three-component sparse network data. *Journal of Geophysical Research*, 98:8107–8125.

Drummond, B. (1988). A review of crust/upper mantle structure in the Precambrian areas of Australia. *Precambrian Research*, 40/41:101–116.

Drummond, B. J., Barton, T. J., Korsch, R. J., Rawlinson, N., Yeates, A. N., Collins, C. D. N., and Brown, A. V. (2003). Evidence for crustal extension and inversion in eastern Tasmania, Australia, during the Neoproterozoic and Early Palaeozoic. *Tectonophysics*, 329:1–21.

Du, Z. and Foulger, G. (1999). The crustal structure beneath the northwest fjords, Iceland, from receiver functions and surface waves. *Geophysical Journal International*, 139:419–432.

Dumberry, M. (2007). Geodynamic constraints on the steady and time dependent inner core axial rotation. *Geophysical Journal International*, 170:886–895.

- Dumberry, M. and Mound, J. (2010). Inner core-mantle gravitational locking and the super-rotation of the inner core. *Geophysical Journal International*, 181:806–817.
- Dziewonski, A. (1984). Mapping the lower mantle: Determination of lateral heterogeneity in P wave velocity up to degree and order 6. *Journal of Geophysical Research*, 89(7):5929–5952.
- Dziewonski, A., Bloch, S., and Landisman, M. (1969). A technique for the analysis of transient seismic signals. *Bulletin of the Seismological Society of America*, 59(1):427–444.
- Dziewonski, A. and Gilbert, F. (1976). The effect of small, aspherical perturbations on travel times and a re-examination of the corrections for ellipticity. *Geophysical Journal of the Royal Astronomical Society*, 44:7–17.
- Dziewonski, A., Hager, B. H., and O'Connell, R. J. (1977). Large-scale heterogeneities in the lower mantle. *Journal of Geophysical Research*, 82(2):239–255.
- Earle, P. S., Rost, S., Shearer, P. M., and Thomas, C. (2011). Scattered P'P' waves observed at short distances. *Bulletin of the Seismological Society of America*, 101:2843–2854.
- Earle, P. S. and Shearer, P. M. (1997). Observations of PKKP precursors used to estimate small-scale topography on the core-mantle boundary. *Science*, 227:667–670.
- Eberhart-Phillips, D. and Reyners, M. (1999). Plate interface properties in the northeast Hikurangi subduction zone, New Zealand, from converted seismic waves. *Geophysical Research Letters*, 26:2565–2568.
- Engdahl, E., Van der Hilst, R. D., and Buland, R. (1998). Global teleseismic earthquake relocation with improved travel times and procedures for depth determination. *Bulletin of the Seismological Society of America*, 88:722–743.
- Fergusson, C. L. (2003). Ordovician-Silurian accretion of the Lachlan Fold Belt, southeastern Australia. *Australian Journal of Earth Sciences*, 50:475–490.
- Finn, C., Moore, D., Damake, D., and Mackey, T. (1999). Aeromagnetic legacy of early Palaeozoic subduction along the Pacific margin of Gondwana. *Geology*, 27:1087–1090.
- Fitzsimons, I. (2003). Proterozoic basement provinces of southern and southwestern Australia, and their correlation with Antarctica. *Special Publications - Geological Society of London*, 206:93–130.

Foster, D. A. and Gray, D. R. (2000). Evolution and structure of the Lachlan Fold Belt (Orogen) of eastern Australia. *Annual Review of Earth and Planetary Sciences*, 28:47–80.

Foster, D. A., Gray, D. R., and Spaggiari, C. (2005). Timing of subduction and exhumation along the Cambrian East Gondwana margin, and the formation of Paleozoic backarc basins. *Bulletin of the Seismological Society of America*, 117:105–116.

Friedrich, A., Krüger, F., and Klinge, K. (1998). Ocean-generated microseismic noise located with the Gräfenberg array. *Journal of Seismology*, 2:47–64.

Fuji, N., Chevrot, S., Zhao, L., Geller, R. J., and Kawai, K. (2012). Finite-frequency structural sensitivities of short-period compressional body waves. *Geophysical Journal International*, 190:522–540.

Fukao, Y., To, A., and Obayashi, M. (2003). Whole mantle P wave tomography using P and PP-P data. *Journal of Geophysical Research*, 108.

Gallagher, K., Charvin, K., Nielsen, S., Sambridge, M., and Stephenson, J. (2009). Markov chain Monte Carlo (MCMC) sampling methods to determine optimal models, model resolution and model choice for Earth science problems. *Marine and Petroleum Geology*, 26(4):525–535.

Garcia, R., Chevrot, S., and Calvet, M. (2009). Statistical study of seismic heterogeneities at the base of the mantle from PKP differential traveltimes. *Geophysical Journal International*, 179:1607–1616.

Garcia, R., Revenaugh, J., and Weber, M. (2004). Nonlinear waveform and delay time analysis of triplicated core phases. *Geophysical Journal International*, 109.

Garcia, R., Tkalčić, H., and Chevrot, S. (2006). A new global PKP dataset to study Earth's core and deep mantle. *Physics of the Earth and Planetary Interiors*, 159:15–31.

Garnero, E. and Lay, T. (2003). D'' shear velocity heterogeneity, anisotropy and discontinuity structure beneath the Caribbean and Central America. *Physics of the Earth and Planetary Interiors*, 140:219–242.

Garnero, E., Revenaugh, J., Williams, Q., Lay, T., and Kellogg, L. (1998). Ultralow velocity zone at the core-mantle boundary. *Geodynamics*, 28:319–334.

Gelman, A., Carlin, J., Stern, H., and Rubin, D. (1995). *Texts in Statistical Science. Bayesian data analysis*. Chapman & Hall.

- Gibson, G., Morse, M., Ireland, T., and Nayak, G. (2010). Arc-continent collision and orogenesis in western Tasmanides: Insights from reactivated basement structures and formation of an ocean-continent transform boundary off western Tasmania. *Gondwana Research*, 19:608–627.
- Gillet, N., Jault, D., Canet, E., and Fournier, A. (2010). Fast torsional waves and strong magnetic field within the Earth's core. *Nature*, 465:74–77.
- Glatzmaier, G. H. and Roberts, P. H. (1996). Rotation and magnetism of Earth's inner core. *Science*, 274:1887–1891.
- Glen, R. (2005). The Tasmanides of eastern Australia. In Vaughan, A., Leat, P., and Pankhurst, R., editors, *Terrane Processes at the Margins of Gondwana*, pages 23–96. Geological Society Special Publications, London.
- Glen, R. A. (2013). Refining accretionary orogen models for the Tasmanides of eastern Australia. *Australian Journal of Earth Sciences*, 60:315–370.
- Gouveia, W. and Scales, J. (1998). Bayesian seismic waveform inversion - Parameter estimation and uncertainty analysis. *Journal of Geophysical Research*, 103:2759–2780.
- Graeber, F. M., Houseman, G. A., and Greenhalgh, S. A. (2002). Regional teleseismic tomography of the western Lachlan Orogen and the Newer Volcanic Province, southeast Australia. *Geophysical Journal International*, 149:249–266.
- Grand, S. (2002). Mantle shear-wave tomography and the fate of subducted slabs. *Philosophical Transactions of the Royal Society A*, 360:2475–2491.
- Grand, S., van der Hilst, R. D., and Widiyantoro, S. (1997). High resolution global tomography: a snapshot of convection in the Earth. *Geological Society of America TODAY*, 7:1–7.
- Green, P. J. (1995). Reversible jump Markov chain Monte Carlo computation and Bayesian model determination. *Biometrika*, 82:711–732.
- Green, P. J. (2003). Transdimensional Markov chain Monte Carlo. In Green, P. J., Hjort, N., and Richardson, S., editors, *Highly Structured Stochastic Systems*, pages 179–196. Oxford Statistical Sciences Series.
- Greene, D. C. (2010). Neoproterozoic rifting in the southern Georgina Basin, central Australia: Implications for reconstructing Australia in Rodinia. *Tectonics*, 29.
- Gu, Y. J., Dziewonski, A. M., Su, W., and Ekström, G. (2001). Models of the mantle shear velocity and discontinuities in the pattern of lateral heterogeneities. *Journal of Geophysical Research*, 106:11169–11199.

Gubbins, D. (1981). Rotation of the inner core. *Journal of Geophysical Research*, 86:11695–11699.

Hardebeck, J. and Shearer, P. (2003). Using S/P amplitude ratios to constrain the focal mechanisms of small earthquakes. *Bulletin of the Seismological Society of America*, 93:2434–2444.

Hastings, W. K. (1970). Monte Carlo sampling methods using Markov chains and their applications. *Biometrika*, 57:97–109.

He, Y. and Wen, L. (2009). Structural features and shear-velocity structure of the “Pacific Anomaly”. *Journal of Geophysical Research*, 114.

Helfrich, G. (2002). Chemical and seismological constraints on mantle heterogeneity. *Phil. Trans. R. Soc. Lond. A*, 360:2493–2505.

Herrmann, R. (2004). Computer programs in seismology, Version 3.30.

Hickman, A. (2004). Two contrasting granite-greenstone terranes in the Pilbara Craton, Australia: Evidence for vertical and horizontal tectonic regimes prior to 2900 Ma. *Precambrian Research*, 131:153–172.

Hirose, K., Fei, Y., Ma, Y., and Mao, H. (1999). The fate of subducted basaltic crust in the Earth’s lower mantle. *Nature*, 397:53–56.

Houser, C., Masters, G., Shearer, P., and Laske, G. (2008). Shear and compressional velocity models of the mantle from cluster analysis of long-period waveforms. *Geophysical Journal International*, 174:195–212.

Huang, Y., H. Yao, B. H., Van der Hilst, R. D., K. Wen, W. H., and Chen, C. (2010). Phase velocity variation at periods of 0.5–3 seconds in the Taipei Basin of Taiwan from correlation of ambient seismic noise. *Bulletin of the Seismological Society of America*, 100:2250–2263.

Inoue, H., Fukao, Y., Tanabe, K., and Ogata, Y. (1990). Whole mantle P-wave travel time tomography. *Physics of the Earth and Planetary Interiors*, 59:294–328.

Ishii, M. and Tromp, J. (2004). Constraining large-scale mantle heterogeneity using mantle and inner-core sensitive normal modes. *Physics of the Earth and Planetary Interiors*, 146:113–124.

Ivanic, T., Wingate, M., Kirkland, C., Kranendonk, M. V., and Wyche, S. (2010). Age and significance of voluminous mafic-ultramafic magmatic events in the Murchison Domain, Yilgarn Craton. *Australian Journal of Earth Sciences*, 57:597–614.

- Jackson, A., Bloxham, J., and Gubbins, D. (1993). Dynamics of Earth's deep interior and Earth rotation. In Mouel, J.-L. L., Smylie, D., and Herring, T., editors, *Geophysical Monograph Series*, volume 72, pages 97–107. AGU.
- Jault, D., Gire, C., and Mouel, J.-L. L. (1988). Westward drift, core motions and exchanges of angular momentum between core and mantle. *Nature*, 333:353–356.
- Julia, J., Ammon, C., and Herrmann, R. (2003). Lithospheric structure of the Arabian Shield from the joint inversion of receiver functions and surface-wave group velocities. *Tectonophysics*, 37:1–21.
- Julia, J., Ammon, C., Herrmann, R., and Correig, A. (2000). Joint inversion of receiver function and surface wave dispersion observations. *Geophysical Journal International*, 143:99–112.
- Julian, B. and Foulger, G. (1996). Earthquake mechanisms from linear-programming inversion of seismic-wave amplitude ratios. *Bulletin of the Seismological Society of America*, 86:972–980.
- Julian, B., Miller, A., and Foulger, G. (1997). Non-double-couple earthquake mechanism at the Hengill-Grensdalur volcanic complex, southwest Iceland. *Geophysical Research Letters*, 24:743–746.
- Kagan, Y. (1992). Correlations of earthquake focal mechanisms. *Geophysical Journal International*, 110:305–320.
- Káráson, H. and van der Hilst, R. D. (2001). Tomographic imaging of the lowermost mantle with differential times of refracted and diffracted core phases (PKP, Pdiff). *Journal of Geophysical Research*, 106(B4):6569–6587.
- Karato, S. (1993). Importance of anelasticity in the interpretation of seismic tomography. *Geophysical Research Letters*, 20:1623–1626.
- Kennett, B., Engdahl, E., and Buland, R. (1995). Constraints on seismic velocities in the Earth from traveltimes. *Geophysical Journal International*, 122:108–124.
- Kennett, B. L. N. and Gudmundsson, O. (1996). Ellipticity corrections for seismic phases. *Geophysical Journal International*, 127:40–48.
- Khan, A., Zunino, A., and Deschamps, F. (2011). The thermo-chemical and physical structure beneath the North American continent from Bayesian inversion of surface-wave phase velocities. *Journal of Geophysical Research*, 116.
- Kilb, D. and Hardebeck, J. (2006). Fault parameter constraints using relocated earthquakes: A validation of first-motion focal-mechanism data. *Bulletin of the Seismological Society of America*, 96:1140–1158.

- Kissling, E. (1998). Geotomography with local earthquake data. *Reviews of Geophysics*, 26:659–698.
- Kito, T., Thomas, C., Rietbrock, A., Garnero, E., Nippress, S., and Heath, A. (2008). Mantle shear-wave tomography and the fate of subducted slabs. *Geophysical Journal International*, 174:1019–1028.
- Knopoff, L., Muller, S., and Pilant, W. (1966). Structure of the crust and upper mantle in the Alps from the phase velocity of Rayleigh waves. *Bulletin of the Seismological Society of America*, 56:1009–1044.
- Koelemeijer, P. J., Deuss, A., and Trampert, J. (2012). Normal mode sensitivity to Earth's D'' layer and topography on the core-mantle boundary: what we can and cannot see. *Geophysical Journal International*, 190:553–568.
- Koper, K. D., Pyle, M. L., and Franks, J. M. (2003). Constraints on aspherical core structure from PKiKP-PcP differential travel-times. *Science*, 283:1881–1884.
- Korsch, R. J., Barton, T. J., Gray, D. R., Owen, A. J., and Foster, D. A. (2002). Geological interpretation of a deep seismic-reflection transect across the boundary between the Delamerian and Lachlan Orogens, in the vicinity of the Grampians, western Victoria. *Australian Journal of Earth Sciences*, 49:1057–1075.
- Kuang, W. and Bloxham, J. (1997). An Earth-like numerical dynamo model. *Nature*, 389:371–374.
- KUTh Energy (2012). KUTh Energy. www.kuthenergy.com. accessed 20 July 2012.
- Langston, C. (1979). Structure under Mount Rainier, Washington, inferred from teleseismic body waves. *Journal of Geophysical Research*, 84:4749–4762.
- Larsen, S. and Schultz, C. (1992). E3D: 2D/3D elastic finite-difference wave propagation code. Lawrence Livermore National Laboratory.
- Laske, G. and Masters, G. (1999). Limits on differential rotation of the inner core from an analysis of the Earth's free oscillations. *Nature*, 402:66–69.
- Laske, G. and Masters, G. (2003). The Earth's free oscillations and the differential rotation of the inner core. In Dehant, V., Creager, K. C., Karato, S.-I., and Zatman, S., editors, *Earth's Core: Dynamics, Structure, Rotation*, volume 31, pages 5–21. AGU.
- Leaman, D. E. (1994). The Tamar Fracture System in Tasmania: Does it exist? *Australian Journal of Earth Sciences*, 41:73–74.

- Leaman, D. E., Baillie, P. W., and Powell, C. M. (1994). Precambrian Tasmania: A thin-skinned devil. *Exploration Geophysics*, 25:19–23.
- Leaman, D. E., Symonds, P. A., and Shirley, J. E. (1973). Gravity survey of the Tamar region, northern Tasmania. *Geological Survey of Tasmania Paper*, 1.
- Lei, J. and Zhao, D. (2006). Global P-wave tomography: On the effect of various mantle and core phases. *Physics of the Earth and Planetary Interiors*, 154:44–69.
- Levshin, A., Pisarenko, V. F., and Pogrebinsky, G. A. (1972). On a frequency-time analysis of oscillations. *Annals of Geophysics*, 28:211–218.
- Levshin, A. L. and Ritzwoller, M. H. (2001). Automated detection, extraction, and measurement, of regional surface waves. *Pure Applied Geophysics*, 158:1531–1545.
- Li, A. and Richards, P. G. (2003). Using earthquake doublets to study inner core rotation and seismicity catalog precision. *Geochemistry, Geophysics, Geosystems*, 4:1–23.
- Li, C., van der Hilst, R. D., Engdahl, E. R., and Burdick, S. (2008). A new global model for P wave speed variations in Earth's mantle. *Geochemistry, Geophysics, Geosystems*, 9.
- Li, X.-D. and Romanowicz, B. (1996). Global mantle shear velocity model developed using nonlinear asymptotic coupling theory. *Journal of Geophysical Research*, 101(B10):22245–22272.
- Ligorriá, J. and Ammon, C. (1999). Iterative deconvolution and receiver-function estimation. *Bulletin of the Seismological Society of America*, 89:1395–1400.
- Lin, F., Moschetti, M. P., and Ritzwoller, M. H. (2008). Surface wave tomography of the western United States from ambient seismic noise: Rayleigh and Love wave phase velocity maps. *Geophysical Journal International*, 173:281–298.
- Lin, F., Ritzwoller, M., Townend, J., Bannister, S., and Savage, M. (2007). Ambient noise Rayleigh wave tomography of New Zealand. *Geophysical Journal International*, 170:649–666.
- Lindner, D., Song, X., Ma, P., and Christensen, D. H. (2010). Inner core rotation and its variability from nonparametric modeling. *Journal of Geophysical Research*, 115.
- Lobkis, O. I. and Weaver, R. L. (2001). On the emergence of the Green's function in the correlations of a diffuse field. *Journal of Acoustical Society of America*, 110.
- Makinen, A. M. and Deuss, A. (2011). Global seismic body-wave observations of temporal variations in the Earth's inner core, and implications for its differential rotation. *Geophysical Journal International*, 187:355–370.

Malinverno, A. (2002). Parsimonious Bayesian Markov chain Monte Carlo inversion in a nonlinear geophysical problem. *Geophysical Journal International*, 151(3):675–688.

Malinverno, A. and Briggs, V. (2004). Expanded uncertainty quantification in inverse problems: Hierarchical Bayes and empirical Bayes. *Geophysics*, 69:1005–1016.

Malinverno, A. and Leaney, W. (2000). A Monte Carlo method to quantify uncertainty in the inversion of zero-offset VSP data. In *Expanded Abstracts*. SEG 70th Annual Meeting, The Society of Exploration Geophysicists, Calgary, Alberta.

Malinverno, A. and Parker, R. (2006). Two ways to quantify uncertainty in geophysical inverse problems. *Geophysics*, 71:W15–W27.

Margerin, L. and Nolet, G. (2003). Multiple scattering of high-frequency seismic waves in the deep Earth: PKP precursor analysis and inversion for mantle granularity. *Journal of Geophysical Research*, 108.

McClenaghan, M. P. (2006). The geochemistry of Tasmanian Devonian-Carboniferous granites and implications for the composition of their source rocks. *Mineral Resources Tasmania Record*, 6.

McCue, K. (1990). Australia's large earthquakes and recent fault scarps. *Journal of Structural Geology*, 12:761–766.

Meffre, S., Berry, R. F., and Hall, M. (2000). Cambrian metamorphic complexes in Tasmania: Tectonic implications. *Australian Journal of Earth Sciences*, 47:971–985.

Mégnin, C. and Romanowicz, B. (2000). The three-dimensional shear velocity structure of the mantle from the inversion of body, surface, and higher-mode waveforms. *Geophysical Journal International*, 143:709–728.

Metropolis, N., Rosenbluth, A. W., Rosenbluth, M. N., Teller, A. H., and Teller, E. (1953). Equation of state calculations by fast computing machines. *Journal of Chemical Physics*, 21:1087–1093.

Mitra, S., Kainkaryam, S., Padhi, A., Rai, S., and Bhattacharya, S. (2011). The Himalayan foreland basin crust and upper mantle. *Physics of the Earth and Planetary Interiors*, 184:34–40.

Monelli, D. and Mai, P. M. (2008). Bayesian inference of kinematic earthquake rupture parameters through fitting of strong motion data. *Geophysical Journal International*, 173:220–232.

Monnereau, M., Calvet, M., Mergerin, L., and Souriau, A. (2010). Lopsided growth of Earth's inner core. *Science*, 328:1014–1017.

- Montelli, R., Nolet, G., Dahlen, A., Engdahl, E. R., and Hung, S.-H. (2004). Finite-frequency tomography reveals a variety of plumes in the mantle. *Science*, 303:338–343.
- Moore, D. H. (1996). A geological interpretation of the geophysical data for the Horsham 1:250 000 map sheet area. Technical Report 24, Victorian Initiative for Minerals & Petroleum Report. Department of Natural Resources and Environment.
- Morand, V. J., Wohlt, K. E., Cayley, R. A., Taylor, D. H., Kemp, A. I. S., Simons, B. A., and Magart, A. P. M. (2003). Glenelg Special Map Area Geological Report. Geological Survey of Victoria Report 123, Geological Survey of Victoria.
- Morelli, A. and Dziewonski, A. (1987). Topography of the core-mantle boundary and lateral homogeneity of the liquid core. *Nature*, 325:678–683.
- Mosca, I., Cobden, L., Deuss, A., Ritsema, J., and Trampert, J. (2012). Seismic and mineralogical structures of the lower mantle from probabilistic tomography. *Journal of Geophysical Research*, 117.
- Moschetti, M. P., Ritzwoller, M. H., Lin, F.-C., and Yang, Y. (2010). Crustal shear wave velocity structure of the western United States inferred from ambient seismic noise and earthquake data. *Journal of Geophysical Research*, 115.
- Mosegaard, K. and Tarantola, A. (1995). Monte Carlo sampling of solutions to inverse problems. *Journal of Geophysical Research*, 100(B7):12431–12447.
- Musgrave, R. and Rawlinson, N. (2010). Linking the upper crust to the upper mantle: comparison of teleseismic tomography with long-wavelength features of the gravity and magnetic fields of southeastern Australia. *Exploration Geophysics*, 41(5435):155–162.
- Myers, J. (1993). Precambrian history of the West Australian craton and adjacent orogens. *Annual Review of Earth and Planetary Sciences*, 21:453–485.
- Myers, J., Shaw, R., and Tyler, I. (1996). Tectonic evolution of Proterozoic Australia. *Tectonics*, 15:1431–1446.
- Myers, S. C., Johannesson, G., and Hanley, W. (2007). A Bayesian hierarchical method for multiple-event seismic location. *Geophysical Journal International*, 171:1049–1063.
- Nakanishi, I. and Anderson, D. L. (1982). Worldwide distribution of group velocity of mantle Rayleigh waves as determined by spherical harmonic inversion. *Bulletin of the Seismological Society of America*, 72(4):1185–1194.

Ni, S. and Helmberger, D. V. (2001a). Horizontal transition from fast to slow structures at the core-mantle boundary; south Atlantic. *Earth and Planetary Science Letters*, 187(3-4):301–310.

Ni, S. and Helmberger, D. V. (2001b). Probing an ultra-low velocity zone at the core mantle boundary with P and S waves. *Geophysical Research Letters*, 28(12):2345–2348.

Niu, F. and Wen, L. (2009). Hemispherical variations in seismic velocity at the top of the Earth's inner core. *Nature*, 410:1607–1616.

Obayashi, M. and Fukao, Y. (1997). P and PcP travel time tomography for the core-mantle boundary. *Journal of Geophysical Research*, 102(B8):17825–17841.

Okabe, A., Boots, B., and Sugihara, K. (1992). *Spatial tessellations: concepts and applications of Voronoi diagrams*. John Wiley & Sons, Inc., New York, NY, USA.

Olson, P. (1997). Probing Earth's dynamo. *Nature*, 389:337–338.

Ozalaybey, S., Savage, M., Sheehan, A., Louie, J., and Brune, J. (1997). Shear-wave velocity structure in the northern Basin and Range province from the combined analysis of receiver functions and surface waves. *Bulletin of the Seismological Society of America*, 87:183–199.

Parkinson, W., Hermanto, R., Sayers, J., Bindoff, N., Dosso, H., and Nienaber, W. (1988). The Tamar conductivity anomaly. *Physics of the Earth and Planetary Interiors*, 52:8–22.

Pasyanos, M., Dreger, D., and Romanowicz, B. (1996). Towards real-time determination of regional moment tensor. *Bulletin of the Seismological Society of America*, 86:1255–1269.

Patison, N. L., Berry, R. F., Davidson, G. J., Taylor, B. P., Bottrill, R. S., Manzi, B., Ryba, J., and Shepherd, R. E. (2001). Regional metamorphism of the Mathina Group, northeast Tasmania. *Australian Journal of Earth Sciences*, 48:281–292.

Piana Agostinetti, N. and Malinverno, A. (2010). Receiver function inversion by trans-dimensional Monte Carlo sampling. *Geophysical Journal International*, 181:858–872.

Picozzi, M., Parolai, S., Bindi, D., and Strollo, A. (2008). Characterization of shallow geology by high-frequency seismic noise tomography. *Geophysical Journal International*, 176:164–174.

Poli, P., Campillo, M., Pedersen, H., and Group, L. W. (2012). Body-wave imaging of Earth's mantle discontinuities from ambient seismic noise. *Science*, 23:1063–1065.

- Poupinet, G., Souriau, A., and Coutant, O. (2000). The existence of an inner core super-rotation questioned by teleseismic doublets. *Physics of the Earth and Planetary Interiors*, 118:77–88.
- Powell, C. M. and Baillie, P. W. (1992). Tectonic affinity of the Mathinna Group in the Lachlan Fold Belt. *Tectonophysics*, 214:193–209.
- Powell, C. M., Preiss, W. V., Gatehouse, C. G., Krapez, B., and Li, Z. X. (1994). South Australian record of a Rodinian epicontinental basin and its mid-Neoproterozoic breakup (~700 Ma) to form the Palao-Pacific Ocean. *Tectonophysics*, 237:113–140.
- Preiss, W. V. (2000). The Adelaide Geosyncline of South Australia and its significance in Neoproterozoic continental reconstruction. *Precambrian Research*, 100:21–63.
- Rawlinson, N., Houseman, G. A., Collins, C. D. N., and Drummond, B. J. (2001). New evidence of Tasmania's tectonic history from a novel seismic experiment. *Geophysical Research Letters*, 28:3337–3340.
- Rawlinson, N., Kennett, B. L. N., Vanacore, E., Glen, R. A., and Fishwick, S. (2011). The structure of the upper mantle beneath the Delamerian and Lachlan orogens from simultaneous inversion of multiple teleseismic datasets. *Gondwana Research*, 19.
- Rawlinson, N., Pozgay, S., and Fishwick, S. (2010a). Seismic tomography: A window into deep Earth. *Physics of the Earth and Planetary Interiors*, 178:101–135.
- Rawlinson, N., Reading, A. M., and Kennett, B. L. N. (2006). Lithospheric structure of Tasmania from a novel form of teleseismic tomography. *Journal of Geophysical Research*, 111.
- Rawlinson, N. and Sambridge, M. (2004a). Multiple reflection and transmission phases in complex layered media using a multistage fast marching method. *Geophysics*, 69:1338–1350.
- Rawlinson, N. and Sambridge, M. (2004b). Wavefront evolution in strongly heterogeneous layered media using the fast marching method. *Geophysical Journal International*, 156:631–647.
- Rawlinson, N., Sambridge, M., and Saygin, E. (2008). A dynamic objective function technique for generating multiple solution models in seismic tomography. *Geophysical Journal International*, 174:295–308.
- Rawlinson, N., Tkalčić, H., and Reading, A. M. (2010b). Structure of the Tasmanian lithosphere from 3D seismic tomography. *Australian Journal of Earth Sciences*, 57:381–394.

- Rawlinson, N. and Urvoy, M. (2006). Simultaneous inversion of active and passive source datasets for 3-D seismic structure with application to Tasmania. *Geophysical Research Letters*, 33.
- Reading, A. and Kennett, B. (2003). Lithospheric structure of the Pilbara Craton, Capricorn Orogen and northern Yilgarn Craton, Western Australia from teleseismic receiver functions. *Australian Journal of Earth Sciences*, 50:439–445.
- Reading, A., Tkalčić, H., Kennett, B., Johnson, S., and Sheppard, S. (2012). Seismic structure of the crust and uppermost mantle of the Capricorn and Paterson orogens and adjacent cratons, Western Australia, from passive seismic transects. *Precambrian Research*, 196–197:295–308.
- Reasenber, P. and Oppenheimer, D. (1985). FPFIT, FPLOT and FPPAGE: Fortran computer programs for calculating and displaying earthquake fault-plane solutions. *U.S. Geological Survey Open-File Report*, 85-739:1–109.
- Reed, A. R. (2001). Pre-Tabberabberan deformation in eastern Tasmania: A southern extension of the Benambran Orogeny. *Australian Journal of Earth Sciences*, 48:785–7964.
- Reed, A. R., Calver, C., and Bottrill, R. S. (2002). Palaeozoic suturing of eastern and western Tasmania in the west Tamar region: Implications for the tectonic evolution of southeast Australia. *Australian Journal of Earth Sciences*, 49:809–830.
- Revs, S., Keep, M., and Kennett, B. (2009). NW Australian intraplate seismicity and stress regime. *Journal of Geophysical Research*, 114.
- Reynolds, S., Coblenz, D., and Hillis, R. (2002). Tectonic forces controlling the regional intraplate stress field in continental Australia: Results from new finite element modeling. *Journal of Geophysical Research*, 107(B7).
- Reynolds, S., Coblenz, D., and Hillis, R. (2003). Influences of plate-boundary forces on the regional intraplate stress field of continental Australia. *Special Paper - Geological Society of America*, 372:59–70.
- Rhie, J. and Romanowicz, B. (2004). Excitation of Earth's continuous free oscillations by atmosphere-ocean-seafloor coupling. *Nature*, 431:552–556.
- Richards, M. A. and Engebretson, D. C. (1992). Large-scale mantle convection and the history of subduction. *Nature*, 355:437–440.
- Ritsema, J., Deuss, A., van Heijst, H., and Woodhouse, J. (2011). S40RTS: A degree-40 shear-velocity model for the mantle from new Rayleigh wave dispersion, teleseismic traveltimes and normal-mode splitting function measurements. *Geophysical Journal International*, 184:1223–1236.

- Ritsema, J., Ni, S., Helmberger, D., and Crotwell, H. (1998). Evidence for strong shear velocity reductions and velocity gradients in the lower mantle beneath Africa. *Geophysical Research Letters*, 24:4245–4248.
- Rodgers, A. and Wahr, J. (1993). Inference of core-mantle boundary topography from ISC PcP and PKP traveltimes. *Geophysical Journal International*, 115:991–1011.
- Rost, S. and Earle, P. S. (2010). Identifying regions of strong scattering at the core-mantle boundary from analysis of PKKP precursor energy. *Earth and Planetary Science Letters*, 297:616–626.
- Roux, P., Sabra, K. G., Gerstoft, P., Kuperman, W. A., and Fehler, C. (2005a). P-waves from cross-correlation of seismic noise. *Geophysical Research Letters*, 32.
- Roux, P., Sabra, K. G., Kuperman, W. A., and Roux, A. (2005b). Ambient noise cross correlation in free space: theoretical approach. *Journal of Acoustical Society of America*, 117:79–84.
- Ryberg, T. (2011). Body wave observations from cross-correlations of ambient seismic noise: A case study from the Karoo, RSA. *Geophysical Research Letters*, 38.
- Saikia, C. (1994). Modified frequency-wavenumber algorithm for regional seismograms using Filon's quadrature: Modelling of Lg waves in eastern North America. *Geophysical Journal International*, 118:142–158.
- Saito, M. (1988). DISPER80: A subroutine package for the calculation of seismic normal mode solutions. In Doornbos, D., editor, *Seismological algorithms: Computational methods and computer programs*, pages 293–319. Academic Press.
- Sambridge, M. (1999). Geophysical inversion with a neighbourhood algorithm I. Searching a parameter space. *Geophysical Journal International*, 103:4839–4878.
- Sambridge, M., Bodin, T., Gallagher, K., and Tkalčić, H. (2013). Transdimensional inference in the geosciences. *Philosophical Transactions of the Royal Society A*, 371.
- Sambridge, M., Braun, J., and McQueen, H. (1995). Geophysical parametrization and interpolation of irregular data using natural neighbours. *Geophysical Journal International*, 122(3):837–857.
- Sambridge, M. and Faletić, R. (2003). Adaptive whole Earth tomography. *Geochemistry, Geophysics, Geosystems*, 4(3).
- Sambridge, M., Gallagher, K., Jackson, A., and Rickwood, P. (2006). Transdimensional inverse problems, model comparison and the evidence. *Geophysical Journal International*, 167(2):528–542.

- Sambridge, M. and Mosegaard, K. (2002). Monte Carlo methods in geophysical inverse problems. *Reviews of Geophysics*, 40(3):1–29.
- Saygin, E. and Kennett, B. L. N. (2010). Ambient seismic tomography of the Australian continent. *Tectonophysics*, 481:116–125.
- Saygin, E. and Kennett, B. L. N. (2012). Crustal structure of Australia from ambient seismic noise tomography. *Journal of Geophysical Research*, 117.
- Scales, J. and Snieder, R. (1998). What is noise? *Geophysics*, 63:1122–1124.
- Scheibner, E. (1998). Introductory Notes. In Scheibner, E. and Basden, H., editors, *Geology of New South Wales - Synthesis*, volume 2, pages 3–21. Geological Survey of New South Wales Memoir, Geology.
- Schmidt, P. W. and Williams, G. E. (1995). The Neoproterozoic climatic paradox: Equatorial palaeolatitute Marinoan glaciation near sea level in South Australia. *Earth Planet. Sci. Lett.*, 134:107–124.
- Seats, K. J., Lawrence, J. F., and Prieto, G. A. (2012). Improved ambient noise correlation functions using Welch's method. *Geophysical Journal International*, 188:513–523.
- Seymour, D. B., Green, G. R., and Calver, C. R. (2007). The geology and mineral deposits of Tasmania: A summary. *Geological Survey Bulletin of Tasmania*, 72.
- Shapiro, N. M. and Campillo, M. (2004). Emergence of broadband Rayleigh waves from correlations of the ambient seismic noise. *Geophysical Research Letters*, 31.
- Shapiro, N. M., Campillo, M., Stehly, L., and Ritzwoller, M. H. (2005). High-resolution surface-wave tomography from ambient seismic noise. *Science*, 307:1615–1618.
- Shapiro, N. M. and Ritzwoller, M. H. (2002). Monte-Carlo inversion for a global shear-velocity model of the crust and upper mantle. *Geophysical Journal International*, 151:88–105.
- Shapiro, N. M., Ritzwoller, M. H., Mareschal, J. C., and Jaupart, C. (2004). Lithospheric structure of the Canadian Shield inferred from inversion of surface-wave dispersion with thermodynamic a priori constraints. In Curtis, A. and Wood, R., editors, *Geological Prior Information: Informing Science and Engineering*, pages 175–194. Geological Society, London, Special Publications, London.
- Shaw, R. D., Wellman, P., Gunn, P., Whitaker, A. J., Tarlowski, C., and Morse, M. (1996). *Australian Crustal Elements based on the distribution of geophysical domains (1:5 000 000 scale map; version 2.4, ArcGIS dataset)*. Geoscience Australia, Canberra.

- Sheppard, S., Johnson, S., Wingate, M., and Kirkland, C. (2010). The Paleoproterozoic Capricorn Orogeny: Intracontinental reworking not continent-continent collision. *Geological Survey of Western Australia Record*, 2010/108:1–33.
- Simmons, N., Forte, A., and Grand, S. (2007). Thermochemical structure and dynamics of the African superplume. *Geophysical Research Letters*, 34.
- Simmons, N., Forte, A., and Grand, S. (2009). Joint seismic, geodynamic and mineral physical constraints on three-dimensional mantle heterogeneity: Implications for the relative importance of thermal versus compositional heterogeneity. *Geophysical Journal International*, 177:1284–1304.
- Simons, F. J., Loris, I., Nolet, G., Daubehies, I. C., Voronin, S., Judd, J. S., Vetter, P. A., Charley, J., and Vonesch, C. (2011). Solving or resolving global tomographic models with spherical wavelets, and the scale and sparsity of seismic heterogeneity. *Geophysical Journal International*, 187(2):969–988.
- Sisson, S. (2005). Transdimensional Markov chains: A decade of progress and future perspectives. *Journal of the American Statistical Association*, 100(471):1077–1090.
- Smith, A. (1991). Bayesian computational methods. *Philosophical Transactions of the Royal Society A*, 337(1647):369–386.
- Snieder, R. (2004). Extracting the Green's function from the correlation of coda waves: A derivation based on stationary phase. *Physical Review E*, 69.
- Snoke, A. (2003). Focal mechanism determination software (FOCMEC package). <http://www.geol.vt.edu/outreach/vtso/focmec>.
- Soldati, G., Boschi, L., and Forte, A. (2012). Tomography of core-mantle boundary and lowermost mantle coupled by geodynamics. *Geophysical Journal International*, 189:730–746.
- Song, X. (2000). Joint inversion for inner core rotation, inner core anisotropy, and mantle heterogeneity. *Journal of Geophysical Research*, 105:7931–7943.
- Song, X. and Poupinet, G. (2007). Inner core rotation from event-pair analysis. *Earth and Planetary Science Letters*, 261:259–266.
- Song, X. and Richards, P. (1996). Seismological evidence for differential rotation of the Earth's inner core. *Nature*, 382:221–224.
- Souriau, A. (1998). New seismological constraints on differential rotation of the inner core from Novaya Zemlya events recorded at DRV, Antarctica. *Geophysical Journal International*, 134:F1–F5.

- Souriau, A. (2007). Deep Earth structure - the Earth's cores. In Schubert, G., editor, *Seismology and Structure of the Earth*, volume 1, pages 655–693. Treatise on Geophysics.
- Souriau, A., Roudil, P., and Moynot, B. (1997). Inner core differential rotation: Facts and artefacts. *Geophysical Research Letters*, 24:2103–2106.
- Spaggiari, C., Wartho, J., and Wilde, S. (2008). Proterozoic deformation in the northwest of the Archean Yilgarn Craton, Western Australia. *Precambrian Research*, 162:354–384.
- Spaggiari, C. V., Gray, D. R., Foster, D. A., and McKnight, S. (2003). Evolution of the boundary between the western and central Lachlan Orogen: Implications for Tasmanide tectonics. *Australian Journal of Earth Sciences*, 50:725–749.
- Stacey, F. and Loper, D. (1983). The thermal boundary interpretation of D and its role as a plume source. *Physics of the Earth and Planetary Interiors*, 33:45–55.
- Stankiewicz, J., Ryberg, T., Haberland, C., Fauzi, and Natawidjaja, D. (2010). Lake Toba volcano magma chamber imaged by ambient seismic noise tomography. *Geophysical Research Letters*, 37.
- Stehly, L., Fry, B., Campillo, M., Shapiro, N. M., Guilbert, J., Boschi, L., and Gardini, D. (2009). Tomography of the Alpine region from observations of seismic ambient noise. *Geophysical Journal International*, 178:338–350.
- Stein, S. (2007). Approaches to continental intraplate earthquake issues. *Special Publications - Geological Society of Australia*, 425:1–16.
- Su, W., Woodward, R., and Dziewonski, A. (1994). Degree 12 model of shear velocity heterogeneity in the mantle. *Journal of Geophysical Research*, 99:6945–6980.
- Su, W.-J. and Dziewonski, A. M. (1998). A local anomaly in the inner core. *Eos Transaction AGU (Spring Meeting Supplement)*, 79:S218.
- Su, W.-J., Dziewonski, A. M., and Jeanloz, R. (1996). Planet within a planet: Rotation of the inner core of Earth. *Science*, 274:1883–1887.
- Sylvander, M., Ponce, B., and Souriau, A. (1997). Seismic velocities at the core-mantle boundary inferred from P waves diffracted around the core. *Physics of the Earth and Planetary Interiors*, 101:189–202.
- Sylvander, M. and Souriau, A. (1996). P-velocity structure of the core-mantle boundary region inferred from PKP(AB)-PKP(BC) differential travel times. *Geophysical Research Letters*, 23:853–856.

- Sze, E. K. M. and van der Hilst, R. D. (2003). Core mantle boundary topography from short period PcP, PKP, and PKKP data. *Physics of the Earth and Planetary Interiors*, 101:27–46.
- Talent, J. A. and Banks, M. R. (1967). Devonian of Victoria and Tasmania. In Oswald, D. H., editor, *International Symposium on the Devonian System*, pages 147–163. Alberta Society of Petroleum Geologists, Calgary.
- Tanaka, S. (2010). Constraints on the core-mantle boundary topography from P4KP-PcP differential travel times. *Journal of Geophysical Research*, 115.
- Tanaka, S. and Hamaguchi, H. (1997). Degree one heterogeneity and hemispherical variation of anisotropy in the inner core from PKP(BC)-PKP(DF) times. *Journal of Geophysical Research*, 102:2925–2938.
- Tanimoto, T. (1999). Excitation of normal modes by atmospheric turbulence: source of long-period seismic noise. *Geophysical Journal International*, 136:395–402.
- Tarantola, T. and Valette, B. (1982). Inverse problems = Quest for information. *Journal of Geophysics*, 50:159–170.
- Thurber, C. H. (1992). Hypocenter-velocity structure coupling in local earthquake tomography. *Physics of the Earth and Planetary Interiors*, 75:55–62.
- Tierney, L. (1994). Markov chains for exploring posterior distributions. *The Annals of Statistics*, 22(4):1701–1728.
- Tkalčić, H. (2010). Large variations in travel times of mantle-sensitive seismic waves from the South Sandwich Islands: Is the Earth's inner core a conglomerate of anisotropic domains? *Geophysical Research Letters*, 37.
- Tkalčić, H., Bodin, T., Young, M. K., and Sambridge, M. (2013a). On the nature of the P-wave velocity gradient in the inner core beneath Central America. *Journal of Earth Sciences*, 24(5):699–705.
- Tkalčić, H., Chen, Y., Liu, R., Huang, Z., Sun, L., and Chan, W. (2011). Multi-step modeling of teleseismic receiver functions combined with constraints from seismic tomography: Crustal structure beneath southeast China. *Geophysical Journal International*, 187:303–326.
- Tkalčić, H., Dreger, D., Foulger, G., and Julian, B. (2009). The puzzle of the 1996 Bárðarbunga, Iceland, earthquake: No volumetric component in the source mechanism. *Bulletin of the Seismological Society of America*, 99:3077–3085.
- Tkalčić, H. and Kennett, B. (2008). Core structure and heterogeneity: A seismological perspective. *Australian Journal of Earth Sciences*, 55:419–431.

Tkalčić, H., Pasyanos, M., Rodgers, A., Gok, R., Walter, W., and Al-Amri, A. (2006). A multistep approach for joint modeling of surface wave dispersion and teleseismic receiver functions: Implications for lithospheric structure of the Arabian Peninsula. *Journal of Geophysical Research*, 111.

Tkalčić, H., Rawlinson, N., Arroucau, P., Kumar, A., and Kennett, B. (2012). Multi-step modeling of receiver-based seismic and ambient noise data from WOMBAT array: Crustal structure beneath southeast Australia. *Geophysical Journal International*, 189:1681–1700.

Tkalčić, H. and Romanowicz, B. (2002). Short scale heterogeneity in the lowermost mantle: Insights from PcP-P and ScS-S data. *Earth and Planetary Science Letters*, 201:57–68.

Tkalčić, H., Romanowicz, B., and Houy, N. (2002). Constraints on D'' structure using PKP(AB-DF), PKP(BC-DF) and PcP-P traveltimes data from broad-band records. *Geophysical Journal International*, 148:599–616.

Tkalčić, H., Young, M. K., Bodin, T., and Sambridge, M. (2013b). The shuffling rotation of the Earth's inner core revealed by earthquake doublets. *Nature Geoscience*, 6:497–502.

Trampert, J., Deschamps, F., Resovsky, J., and Yuen, D. (2004). Probabilistic tomography maps chemical heterogeneities throughout the lower mantle. *Science*, 306:853–856.

Turner, N. J., Black, L. P., and Kamperman, M. (1998). Dating of Neoproterozoic and Cambrian orogenies in Tasmania. *Australian Journal of Earth Sciences*, 45:789–806.

Tyler, I. and Thorne, A. (1990). The northern margin of the Capricorn Orogen, Western Australia - an example of an early Proterozoic collision zone. *Journal of Structural Geology*, 12:685–701.

van der Hilst, R. and Kárason, H. (1999). Compositional heterogeneity in the bottom 1000 kilometers of Earth's mantle: Toward a hybrid convection model. *Science*, 283:1885–1888.

van der Hilst, R. S., Widiyantoro, S., and Engdahl, E. R. (1997). Evidence for deep mantle circulation from global tomography. *Nature*, 386:578–584.

Van Kranendonk, M., Smithies, R., Hickman, A., and Champion, D. (2007). Review: Secular tectonic evolution of Archean continental crust: Interplay between horizontal and vertical processes in the formation of the Pilbara Craton, Australia. *Terra Nova*, 19:1–38.

- VandenBerg, A. H. M., Willman, C. E., Maher, S., Simons, B. A., Cayley, R. A., Taylor, D. H., Morand, V. J., Moore, D. H., and Radojkovic, A. (2000). The Tasman Fold Belt System in Victoria. *Geological Survey of Victoria Special Publication*.
- Vasco, D. and Johnson, L. (1998). Whole Earth structure estimated from seismic arrival times. *Journal of Geophysical Research*, 103:2633–2671.
- Vasco, D., Johnson, L., and Marques, O. (2006). Resolution, uncertainty, and whole Earth tomography. *Journal of Geophysical Research*, 108(B1).
- Vasco, D., Johnson, L., and Pulliam, J. (1995). Lateral variations in mantle velocity structure and discontinuities determined from P, PP, S, SS, and SS-SdS travel time residuals. *Journal of Geophysical Research*, 100:24037–24059.
- Vidale, J. E. and Earle, P. S. (2005). Evidence for inner core rotation from possible changes with time in PKP coda. *Geophysical Research Letters*, 32.
- Vidale, J. E. and Hedlin, M. (1998). Evidence for partial melt at the core-mantle boundary north of Tonga from the strong scattering of seismic waves. *Nature*, 391:682–685.
- Villaseñor, A., Ritzwoller, M., Levshin, A., Barmin, M., Engdahl, E., Spakman, W., and Trampert, J. (2001). Shear velocity structure of central Europe from inversion of surface wave velocities. *Physics of the Earth and Planetary Interiors*, 123:169–184.
- Villaseñor, A., Yang, Y., Ritzwoller, M. H., and Gallert, J. (2007). Ambient noise surface wave tomography of the Iberian Peninsula: Implications for shallow seismic structure. *Geophysical Research Letters*, 34.
- Voronoi, G. (1908). Nouvelles applications des parametres continus a la theorie des formes quadratiques. *Journal für die reine und angewandte Mathematik*, 134:198–287.
- Šilený, J., Campus, P., and Panza, G. (1996). Seismic moment tensor resolution by waveform inversion of few local noisy records - I. Synthetic tests. *Geophysical Journal International*, 126:605–619.
- Walck, M. C. and Clayton, R. W. (1987). P wave velocity variations in the Coso Region, California, derived from local earthquake travel times. *Journal of Geophysical Research*, 92:393–405.
- Walsh, D., Arnold, R., and Townend, J. (2009). A Bayesian approach to determining and parameterizing earthquake focal mechanisms. *Geophysical Journal International*, 176:235–255.

Wang, C., Chan, W., and Mooney, W. (2003). Three-dimensional velocity structure of crust and upper mantle in southwestern China and its tectonic implications. *Journal of Geophysical Research*, 108.

Wapenaar, K. (2004). Retrieving the elastodynamic Green's function of an arbitrary inhomogeneous medium by cross correlation. *Physical Review Letters*, 93(25).

Wapenaar, K. (2006). Green's function retrieval by cross-correlation in case of one-sided illumination. *Geophysical Research Letters*, 33(19).

Waszek, A., Irving, J., and Deuss, A. (2011). Reconciling the hemispherical structure of Earth's inner core with its super-rotation. *Nature Geoscience*, 4:264–267.

Wathelet, M. (2008). An improved neighborhood algorithm: Parameter conditions and dynamic scaling. *Geophysical Research Letters*, 35.

Weaver, R., Hadziioannou, C., Larose, E., and Campillo, M. (2011). On the precision of noise correlation interferometry. *Geophysical Journal International*, 185:1384–1392.

Wellman, P. (2000). Upper crust of the Pilbara Craton, Australia; 3D geometry of a granite/greenstone terrain. *Precambrian Research*, 104:175–186.

Wen, L. (2006). Localized temporal change of the Earth's inner core boundary. *Science*, 314:967–970.

Wen, L. and Helmberger, D. V. (1998). Ultra-low velocity zones near the core-mantle boundary from broadband PKP precursors. *Science*, 279:1701–1703.

Wessel, P. and Smith, W. (1995). New version of the Generic Mapping Tools released. *Eos (Transactions, American Geophysical Union)*, 76:329.

Williams, E. (1989). Summary and synthesis. In Burrett, C. F. and Martin, E. L., editors, *Geology and mineral resources of Tasmania*, pages 468–499. Geological Society Special Publications, Australia.

Woodward, R. L. and Masters, G. (1991). Global upper mantle structure from long-period differential travel times. *Journal of Geophysical Research*, 96(B4):6351–6377.

Wysession, M. E. (1996). Large-scale structure at the core-mantle boundary from diffracted waves. *Nature*, 382:244–248.

Xu, L., Rondenay, S., and Van der Hilst, R. D. (2007). Structure of the crust beneath the southeastern Tibetan Plateau from teleseismic receiver functions. *Physics of the Earth and Planetary Interiors*, 165:176–193.

- Yang, Y., Li, A., and Ritzwoller, M. H. (2008a). Crustal and uppermost mantle structure in southern Africa revealed from ambient noise and teleseismic tomography. *Geophysical Journal International*, 174:235–248.
- Yang, Y., Ritzwoller, M., Levshin, A., and Shapiro, N. (2007). Ambient noise Rayleigh wave tomography across Europe. *Geophysical Journal International*, 168:259–274.
- Yang, Y. and Ritzwoller, M. H. (2008). Characteristics of ambient seismic noise as a source for surface wave tomography. *Geochemistry, Geophysics, Geosystems*, 9.
- Yang, Y., Ritzwoller, M. H., Lin, F. C., Moschetti, M. P., and Shapiro, N. M. (2008b). Structure of the crust and uppermost mantle beneath the western United States revealed by ambient noise and earthquake tomography. *Journal of Geophysical Research*, 113.
- Yang, Y., Zheng, Y., Chen, J., Zhou, S., Ceylan, S., Sandvol, E., Tilmann, F., Priestley, K., Hearn, T. M., Ni, J. F., Brown, L. D., and Ritzwoller, M. H. (2010). Rayleigh wave phase velocity maps of Tibet and the surrounding regions from ambient seismic noise tomography. *Geochemistry, Geophysics, Geosystems*, 11.
- Yao, H., Beghein, C., and Van der Hilst, R. D. (2008). Surface wave array tomography in SE Tibet from ambient seismic noise and two-station analysis - II. Crustal and upper-mantle structure. *Geophysical Journal International*, 173:205–219.
- Yao, H. and Van der Hilst, R. D. (2009). Analysis of ambient noise energy distribution and phase velocity bias in ambient noise tomography, with application to SE Tibet. *Geophysical Journal International*, 179:1113–1132.
- Yao, H., Van der Hilst, R. D., and de Hoop, M. V. (2006). Surface-wave array tomography in SE Tibet from ambient seismic noise and two-station analysis - I. Phase velocity maps. *Geophysical Journal International*, 166:732–744.
- Yolsal-Çevikbilen, S., Biryol, C., Beck, S., Zandt, G., Taymaz, T., Adiyaman, H., and Ozacar, A. (2012). 3-D crustal structure along the North Anatolian Fault Zone in north-central Anatolia revealed by local earthquake tomography. *Geophysical Journal International*, 188:819–849.
- Young, M. K., Cayley, R. A., Mclean, M. A., Rawlinson, N., Arroucau, P., and Salmon, M. (2013a). Crustal structure of the east Gondwana margin in southeast Australia revealed by transdimensional ambient seismic noise tomography. *Geophysical Research Letters*, 40:4266–4271.
- Young, M. K., Rawlinson, N., Arroucau, P., Reading, A., and Tkalčić, H. (2011). High-frequency ambient noise tomography of southeast Australia: New constraints on Tasmania's tectonic past. *Geophysical Research Letters*, 38.

Young, M. K., Rawlinson, N., and Bodin, T. (2013b). Transdimensional inversion of ambient seismic noise for 3D shear velocity structure of the Tasmanian crust. *Geophysics*, 78(3):49–62.

Young, M. K., Tkalčić, H., Bodin, T., and Sambridge, M. (2013c). Global P-wave tomography of Earth's lowermost mantle from partition modeling. *Journal of Geophysical Research*, 118:5467–5486.

Young, M. K., Tkalčić, H., Rawlinson, N., and Reading, A. (2012). Exploiting seismic signal and noise in an intracratonic environment to constrain crustal structure and source parameters of infrequent earthquakes. *Geophysical Journal International*, 188:1303–1321.

Yuen, D. A. and Peltier, W. R. (1980). Mantle plumes and thermal stability of the D layer. *Geophysical Research Letters*, 7:625–628.

Zhang, J., Song, X., Li, Y., Richards, P. G., and Sun, X. (2005). Inner core differential motion confirmed by earthquake waveform doublets. *Science*, 309:1357–1360.

Zhao, D. (2004). Global tomographic images of mantle plumes and subducting slabs: Insight into deep Earth dynamics. *Physics of the Earth and Planetary Interiors*, 146:3–34.

Zhao, D. (2009). Multiscale seismic tomography and mantle dynamics. *Gondwana Research*, 15:297–323.

Zhao, D., Yamamoto, Y., and Yanada, Y. (2012). Global mantle heterogeneity and its influence on teleseismic regional tomography. *Gondwana Research*, 23:595–616.

Zhao, S. and Muller, R. (2003). Three-dimensional finite-element modelling of the tectonic stress field in continental Australia. *Special Paper - Geological Society of America*, 372:71–89.

Zollo, A., D'Auria, L., Matteis, R. D., Herrero, A., Virieux, H., and Gasparini, P. (2002). Bayesian estimation of 2-D P-velocity models from active seismic arrival time data: Imaging of the shallow structure of Mt. Vesuvius (Southern Italy). *Geophysical Journal International*, 151:566–582.